PNNL-12030
UC-2010

STOMP

Subsurface Transport Over Multiple Phases
Version 2.0

Theory Guide

M. D. White
M. Oostrom

March 2000

Disclaimer on back side of cover

PNNL-12030
UC-2010

STOMP
Subsurface Transport Over Multiple Phases
Version 2.0
Theory Guide

M. D. White
M. Oostrom

March 2000

Prepared for the U.S. Department of Energy
under Contract DE-AC06-76RLO 1830

This work is funded by the Office of Science and Technology, within the U.S. Department of Energy's Office of Environmental Management, under the Plumes Focus Area.

Pacific Northwest National Laboratory
Richland, Washington 99352

Preface

This guide describes the simulator's governing equations, constitutive functions and numerical solution algorithms of the STOMP (Subsurface Transport Over Multiple Phases) Version 2.0 simulator, a scientific tool for analyzing multiple phase subsurface flow and transport. Examples of the STOMP simulator applied to classical groundwater problems are provided in a companion application guide [Nichols et al. 2000]. A description of the general use, input file formatting, compilation and execution are provided in an updated user's guide [White and Oostrom 2000]. The latest STOMP version includes new operational modes (Water-Oil-Dissolved Oil and Water-Oil-Dissolved Oil-Surfactant), several changes to existing modes, and expanded options for solute transport. For additional information, the reader is referred to the STOMP web page at http://www.pnl.gov/etd/stomp/.

In writing this guide for the STOMP simulator, the authors have assumed that the reader comprehends concepts and theories associated with (multiple-phase) hydrology, heat transfer, thermodynamics, radioactive chain decay, and relative permeability-saturation-capillary pressure constitutive functions. The authors further assume that the reader is familiar with the computing environment on which they plan to compile and execute the STOMP simulator.

The STOMP simulator requires an ANSI FORTRAN 77 compiler to generate an executable code. The memory requirements for executing the simulator are dependent on the complexity of physical system to be modeled and the size and dimensionality of the computational domain. Likewise execution speed depends on the problem complexity, size and dimensionality of the computational domain, and computer performance. One-dimensional problems of moderate complexity can be solved on conventional desktop computers, but multidimensional problems involving complex flow and transport phenomena typically require the power and memory capabilities of workstation or mainframe type computer systems.

Summary

The U. S. Department of Energy, through the Office of Technology Development, has requested the demonstration of remediation technologies for the cleanup of volatile organic compounds and associated radionuclides within the soil and groundwater at arid sites. This demonstration program, called the VOC-Arid Soils Integrated Demonstration Program (Arid-ID), has been initially directed at a volume of unsaturated and saturated soil contaminated with carbon tetrachloride, on the Hanford Site near Richland, Washington. A principal subtask of the Arid-ID program involves the development of an integrated engineering simulator for evaluating the effectiveness and efficiency of various remediation technologies. The engineering simulator's intended users include scientists and engineers who are investigating subsurface phenomena associated with remediation technologies. Principal design goals for the engineer simulator include broad applicability, verified algorithms, quality assurance controls, and validated simulations against laboratory and field-scale experiments. An important goal for the simulator development subtask involves the ability to scale laboratory and field-scale experiments to full-scale remediation technologies, and to transfer acquired technology to other arid sites. The STOMP (Subsurface Transport Over Multiple Phases) simulator has been developed by the Pacific Northwest National Laboratory(a) for modeling remediation technologies. Information on the use, application, and theoretical basis of the STOMP simulator are documented in three companion guide manuals. This manual, the Theory Guide (Version 2.0), provides the most recent theory and discussions on the governing equations, constitutive relations, and numerical solution algorithms for the STOMP simulator.

The STOMP simulator's fundamental purpose is to produce numerical predictions of thermal and hydrogeologic flow and transport phenomena in variably saturated subsurface environments, which are contaminated with volatile or nonvolatile organic compounds. Auxiliary applications include numerical predictions of solute transport processes including radioactive chain decay processes. Quantitative predictions from the STOMP simulator are generated from the numerical solution of partial differential equations that describe subsurface environment transport phenomena. Description of the contaminated subsurface environment is founded on governing conservation equations and constitutive functions. Governing coupled flow equations are partial differential equations for the conservation of water mass, air mass, (dissolved) organic compound mass and thermal energy. Equations for the conservation of salt or surfactant mass have also been included. Constitutive functions relate primary variables to secondary variables. Solution of the governing partial differential equations occurs by the integral volume finite difference method. The governing equations that describe thermal and hydrogeological flow

---

(a) Pacific Northwest National Laboratory is operated for the U.S. Department of Energy by Battelle Memorial Institute

processes are solved simultaneously using Newton-Raphson iteration to resolve the nonlinearities in the governing equations. Governing transport equations are partial differential equations for the conservation of solute mass. Solute mass conservation governing equations are solved sequentially, following the solution of the coupled flow equations, by a direct application of the integral volume finite difference method. The STOMP simulator is written in the FORTRAN 77 language, following American National Standards Institute (ANSI) standards. The simulator utilizes a variable source code configuration, which allows the execution memory and speed be tailored to the problem specifics, and essentially requires that the source code be assembled and compiled through a software maintenance utility.

KEYWORDS: subsurface, porous media, multiple phase, groundwater, nonaqueous phase liquid (NAPL), volatile organic compound (VOC), variably saturated, frozen-soil conditions, brines, nonequilibrium kinetics, solute transport, radioactive chain decay, hysteresis, fluid entrapment, finite-difference, Langmuir, Freundlich, Monod, mobilization, solubilization, dissolution, Newton-Raphson, nonlinear, modeling, TVD transport, banded linear system solver, conjugate gradient solver

Acknowledgements

The initial development of the simulator was funded by the Office of Science and Technology, within the Department of Energy's Office of Environmental Management, under the Subsurface Contaminants Focus Area, with the support of the following contributors:

Headquarters: Office of Science and Technology
Skip Chamberlain

Focus Area/Program: Subsurface Contaminants Focus Area
James A. Wright

Operations Office: Richland Operations Office
Science and Technology Programs Division
John P. Neath, Technical Program Officer

Contractor: Pacific Northwest National Laboratory
Environmental Management
Technology Development Program
Rod K. Quinn, Manager

Glossary of Symbols

Roman Symbols

a	generic function coefficient
a_n^o	activity for liquid of oil component o
$a_1 , \ldots , a_{12}$	liquid water primary constant (Table A.4)
a_ς	solute mass conservation equation coefficient for node ς
$a_{\gamma\,\varsigma}$	phase component of the solute mass conservation equation coefficient for phase γ for node ς
a_s^C	effective solute diffusion coefficient parameter
A	area, m^2
A_r	product constituent
A_{pr}	primary reactant constituent
A_r	secondary reactant constituent
A_ς	area of surface ς , m^2
$A_0 , \ldots, A_{22}$	liquid water primary constant (Table A.4)
b	generic function coefficient
$b_0 , \ldots, b_{82}$	water-vapor primary constant (Table A.6)
b_s^C	effective solute diffusion coefficient parameter
$B_0 , \ldots, B_{96}$	water-vapor primary constant (Table A.6)

Roman Symbols (Continued)

c	generic function coefficient
$c_{p_n}^{c}$	isobaric specific heat for liquid of oil component o , J/kg K
$\bar{c}_{p_n}^{c}$	ref. isobaric specific heat for liquid of oil component o , J/kg K
c_v^c	constant volume specific heat for component j , J/kg K
c_{10} ,…, c_{33}	liquid water thermal conductivity constants (Table A.9)
C	solute concentration , 1/m^3
$\bar{C}_l^{do}$	dissolved oil equilibrium concentration, 1/m^3
C_l^i	component concentration in aqueous phase, 1/m^3
C_p	product concentration, 1/m^3
C_{pr}	primary reactant concentration, 1/m^3
C_r	secondary reactant concentration, 1/m^3
C_γ	solute concentration in phase γ , 1/m^3
CMC	critical micelle concentration, 1/m^3
d	generic function coefficient
d_p	particle diameter, m
D_g^{jk}	vapor binary diffusion coefficient for component pair jk , m^2/s
$\bar{D}_g^{jk}$	reference vapor binary diffusion coefficient for component pair jk , m^2/s

Roman Symbols (Continued)

$D_{h\gamma_x}$, $D_{h\gamma_y}$, $D_{h\gamma_z}$	hydraulic dispersion coefficient for phase γ (x-direction component, y–direction component, z–direction component).
$D^{C}_{\ell e}$	effective solute diffusion coefficient for the aqueous phase, m^2/s
D^{j}_{ml}	molecular diffusion coefficient of component i in aqueous phase, m^2/s
D_n^{jk}	NAPL binary diffusion coefficient for dissolved component pair jk , m^2/s
${}^{o}D_n^{jk}$	NAPL binary diffusion coefficient at infinite dilution for dissolved component pair jk , m^2/s
D_γ^j	diffusion coefficient of component j for phase γ , m^2/s
$\mathbf{D}_\gamma^j$	diffusion-dispersion tensor of component j for phase γ , m^2/s
D_γ^C	solute diffusion coefficient for phase γ , m^2/s
$\overline{D}_\gamma^C$	reference solute diffusion coefficient for phase γ , m^2/s
D_γ^S	salt diffusion coefficient for phase γ , m^2/s
$\mathbf{D}_{h\gamma}$	hydraulic dispersion tensor for phase γ , m^2/s
e	generic function coefficient
$\overline{E}$	energy accumulation term, J/m^3
f_{pr}	reaction rate factor
F^{jk}	chain decay fraction for radionuclide pair jk

Roman Symbols (Continued)

F_p^j	polarity correction factor of component j

$\mathbf{F}_{\ell}^{S}$ osmotic flux of the aqueous phase, kg/m^2 s

$\mathbf{F}_{\gamma}^{j}$ advective flux of component j in phase γ, kg/m^2 s

g acceleration of gravity, m/s^2

g_{pr} component of reaction rate factor

G^{jk} Grunberg interaction parameter for component pair jk

$G_{\gamma\,\varsigma}^{C}$ solute flux for phase γ across surface ς, 1/m^2 s

h capillary head, m

h^{j} enthalpy of component j, J/kg

h_{γ} enthalpy of phase γ, J/kg

h_{g}^{j} vapor enthalpy of component j, J/kg

$h_{g\ell}$ gas-aqueous water equivalent capillary head, m

h_{gn} gas-NAPL water equivalent capillary head, m

h_{n}^{o} liquid enthalpy of oil component o, J/kg

$h_{n\ell}$ NAPL-aqueous water equivalent capillary head, m

h_{od} oven-dried head, 10^9 m

h_{vap}^{o} heat of vaporization of oil component o, J/kg

Roman Symbols (Continued)

$h_{vap_b}^{o}$ heat of vaporization at normal boiling of oil component o, J/kg

h_{wi} water-ice heat of fusion, J/kg

$h_1, \ldots, h_{11}$ Hankinson-Brobst-Thomson liquid density function constants (Table A.5)

$H_{g\ell}^{j}$ Henry's coefficient vapor-aqueous phase of component j, 1/Pa

$\mathbf{J}_g^j$ diffusive-dispersive flux of component j for the gas phase, kg/m^2 s

$\mathbf{J}_\ell^j$ diffusive-dispersive flux of component j for the aqueous phase, kg/m^2 s

$\mathbf{J}_n^j$ diffusive-dispersive flux of component j for the NAPL phase, kg/m^2 s

$\mathbf{J}_\gamma^S$ pressure dispersion flux of salt for phase γ, kg/m^2 s

k^{jk} thermal conductivity interaction parameter for component pair jk, W/m K

k_f, k_m intrinsic permeability (fracture, matrix), m^2

k_γ thermal conductivity of phase γ, W/m K

k_n^o liquid thermal conductivity of oil component o, W/m K

$k_{n,l}^{do}$ NAPL-aqueous interface transfer coefficient, 1/s

$k_{\max}$ maximum utilization rate in Monod reactions,1/m^3 s

k_s half-velocity coefficient in Monod reactions, 1/m^3

$k_{r\gamma}$ fluid relative permeability of phase γ

k_{rg_f}, k_{rg_m} gas relative permeability (fracture, matrix)

Roman Symbols (Continued)

$k_{r\ell_f}$, $k_{r\ell_m}$ aqueous relative permeability (fracture, matrix)

$k_{r\ell_b}$ aqueous relative permeability (bulk)

$k_1, \ldots, k_9$ saturated water vapor pressure function constants (Table A.2)

$K_{g\ell}$	solute gas-aqueous distribution coefficient, m^3 aqu/m^3 gas
$K_{\ell n}$	solute aqueous-NAPL distribution coefficient, m^3 NAPL/m^3 aqu
$K_{s\ell}$	solute solid-aqueous distribution coefficient, m^3 aqu/kg solid
K_{sl}^{i}	solid-aqueous distribution coefficient of component i, m^3 aqu/kg solid
K_{γ}^{S}	pressure dispersion coefficient for salt through phase γ , m^2
$\mathbf{k}$	intrinsic permeability tensor, m^2
$\mathbf{k}_e$	equivalent thermal conductivity tensor, W/m K
$\mathbf{k}_{e\,sat}$	equivalent thermal conductivity tensor (saturated conditions), W/m K
$\mathbf{k}_{e_{un}}$	equivalent thermal conductivity tensor (unsaturated conditions), W/m K
$\mathbf{k}_s$	porous media thermal conductivity tensor, W/m K
$l(j)$	numerical index (Table A.8)
L_g	Land's parameter for gas-NAPL and gas-aqueous interfaces
L_n	Land's parameter for NAPL-aqueous interfaces
L_0 ,..., L_2	water vapor derived constants (Table A.7)

Roman Symbols (Continued)

m	van Genuchten function parameter
$\dot{m}^{j}$	mass source rate of component j , kg/s
$\dot{m}^{C}$	solute source rate, 1/s
$\dot{m}^{S}$	salt mass source rate, kg/s
M^{C}	molecular weight of solute C , kg/kgmol

M^j	molecular weight of component j, kg/kgmol
$\overline{M}^j$	mass accumulation term for component j, kg/m^3
M^{ij}	mean molecular weight of component pair jk, kg/kgmol
M_γ	molecular weight of phase γ, kg/kgmol
n	van Genuchten function parameter
N_b, N_c, N_t	Bond, capillary, and total trapping number
N_t^c	critical trapping number
N_p	moles of product p
N_{pr}	moles of primary reactant pr
N_r	moles of secondary reactant r
n	surface normal vector
$n(j)$	numerical index (Table A.8)
n_D, n_T	porosity (diffusive, total)

Roman Symbols (Continued)

$\bar{n}_D$, $\bar{n}_T$	reference porosity (diffusive, total)
n_{D_f}, n_{D_m}	diffusive porosity (fracture, matrix)
P	pressure, Pa
$\overline{P}$	reference pressure, Pa
P_{atm}	atmospheric pressure, Pa
P_c^C	critical pressure of solute C, Pa

P_c^j	critical pressure of component j, Pa
P_c^n	critical pressure for NAPL phase mixture, Pa
P_{cap}	capillary pressure, Pa
$Pe_{\gamma\varsigma}$	Peclet number for phase γ on surface ς
P_γ	pressure of phase γ, Pa
P_g^j	vapor pressure of component j, Pa
P_r	reduced pressure, Pa
P_r^j	reduced pressure of component j, Pa
P_{sat}^j	saturated vapor pressure of component j, Pa
P_{tp}	total potential pressure, Pa
$\dot{q}$	thermal energy source, W

Roman Symbols (Continued)

$Q_{\gamma\varsigma}$	heat flux for phase γ across surface ς, W/m^2
R	universal gas constant, J/kg K
Re	Reynolds number
R^j	gas constant of component j, J/kg K
$\overline{R}^e$	residual for energy conservation equation, W
$\overline{R}^j$	residual for mass conservation equation of component j, kg/s
$\dot{R}^C$	solute decay rate constant, 1/s

R_D	retardation factor
R_γ	gas constant of phase γ , J/kg K
Sc	Schmidt number
Sh	Sherwood number
$s\ (\ )$	generic saturation-capillary pressure function
s_g , $\bar{s}_g$, $\bar{\bar{s}}_g$	gas saturation (actual, effective, apparent)
$\bar{s}_{g_f}$	free gas saturation (effective)
$\bar{s}_{g_r}$	residual gas saturation (effective)
${}^i\bar{s}_{g_r}$	maximum residual gas saturation (effective)
$\bar{s}_{g_t}$	trapped gas saturation (effective)

Roman Symbols (Continued)

$s_{g_{t\ell}}$, $\bar{s}_{g_{t\ell}}$	gas saturation trapped by aqueous phase (actual, effective)
$\bar{s}_{g_{tn}}$	gas saturation trapped by NAPL phase (effective)
s_i , $\bar{s}_i$	ice saturation (actual)
s_ℓ , $\bar{s}_\ell$, $\bar{\bar{s}}_\ell$	aqueous saturation (actual, effective, apparent)
s_{ℓ_f} , $\bar{s}_{\ell_f}$	fracture aqueous saturation (actual, effective)
s_{ℓ_m} , $\bar{s}_{\ell_m}$	matrix aqueous saturation (actual, effective)
$\bar{s}_l^{\min}$	minimum aqueous saturation (effective)
s_m , $\bar{s}_m$	irreducible saturation (actual, effective)

s_{m_f}	fracture irreducible saturation (actual)
s_{m_m}	matrix irreducible saturation (actual)
s_n , $\bar{s}_n$, $\bar{\bar{s}}_n$	NAPL saturation (actual, effective, apparent)
$\bar{s}_{n_f}$	free NAPL saturation (effective)
$\bar{s}_{n_r}$	residual NAPL saturation (effective)
${}^{i}\bar{s}_{n_r}$	maximum residual NAPL saturation (effective)
$\bar{s}_{n_t}$	trapped NAPL saturation (effective)
$\bar{s}_{nr}^{\max}$	maximum residual NAPL saturation
s_t , $\bar{s}_t$, $\bar{\bar{s}}_t$	total-liquid saturation (actual, effective, apparent)

Roman Symbols (Continued)

$\bar{s}_t^{\min}$	minimum total-liquid saturation (effective)
s_{uf}	unfrozen water fraction
S	salt concentration, kg/m^3
S_s	coefficient of specific storage, 1/m, or solute sorbed on solid phase, 1/kg
S_γ	salt concentration in phase γ , kg/m^3
t	time, s
T	temperature, K
$\bar{T}$	reference temperature, K
T^{jk}	dimensionless temperature for component pair jk , K

$T_{1/2}^{C}$ radioactive decay half-life, s

T_{b}^{j} normal boiling temperature of component j, K

T_{c}^{C} critical temperature for solute C, K

T_{c}^{j} critical temperature for component j, K

T_{c}^{jk} critical temperature for component pair jk, K

T_{c}^{n} critical temperature of NAPL mixture, K

T_{fp}^{j} freezing point temperature for component j, K

$\bar{T}_{n}^{o}$ reference temperature of oil component o, K

Roman Symbols (Continued)

T_{r} reduced temperature, K

T_{r}^{j} reduced temperature of component j, K

$\bar{T}_{r}^{j}$ reduced reference temperature of component j, K

u_{γ} internal energy of phase γ, J/kg

u_{g}^{j} vapor internal energy of component j, J/kg

u_{n}^{o} liquid internal energy of oil component o, J/kg

u_{s} porous media internal energy, J/kg

v_{γ} specific volume of phase γ, m^3/kg

v_{c}^{j} critical specific volume of component j, m^3/kg

$\bar{V}$ volume, m^3

$V_{\gamma x}, V_{\gamma y}, V_{\gamma z}$ Darcy velocity of phase γ (x- or r-direction component, y- or Q-direction component, z-direction component), m/s

$V'_{\gamma x}, V'_{\gamma y}, V'_{\gamma z}$ Normalized Darcy velocity of phase γ (x- or r-direction component, y- or Q-direction component, z-direction component), m/s

$\hat{V}_{\gamma x}, \hat{V}_{\gamma y}, \hat{V}_{\gamma z}$ Pore velocity of phase γ (x- or r-direction component, y- or Q-direction component, z-direction component), m/s

$\hat{V}'_{\gamma x}, \hat{V}'_{\gamma y}, \hat{V}'_{\gamma z}$ Normalized pore velocity of phase γ (x- or r-direction component, y- or Q-direction component, z-direction component), m/s

$\mathbf{V}_{\gamma}$ Darcy velocity vector of phase γ , m/s

Roman Symbols (Continued)

$x(j,i)$ numerical index (Table A.8)

X reduced temperature factor

Y reduced temperature factor

Y' reduced temperature factor

$z(j,i)$ numerical index (Table A.8)

Z reduced temperature and pressure factor

Z_c^o critical compressibility factor of oil component o

Z_{RA}^j Rackett compressibility factor of component j

Z_{RA}^n Rackett compressibility factor for NAPL mixture

$\mathbf{z}_g$ unit gravitational direction vector

Greek Symbols

α van Genuchten function parameter, 1/m

α_d van Genuchten function parameter for drainage, 1/m

α_i van Genuchten function parameter for imbibition, 1/m

α_L longitudinal dispersivity, m

α_P porous media coefficient of pressure compressibility, 1/Pa

α_q thermodynamic correction factor

α_T porous media coefficient of thermal compressibility, 1/K or transverse dispersivity, m

α_γ DeVries thermal conductivity weighting factor

$\beta_{g\ell}$ gas-aqueous capillary pressure scaling factor

β_{gn} gas-NAPL capillary pressure scaling factor

$\beta_{i\ell}$ ice-aqueous capillary pressure scaling factor

$\beta_{n\ell}$ NAPL-aqueous capillary pressure scaling factor

β_L reduced temperature factor

β_L' reduced temperature factor

β_P liquid water coefficient of pressure compressibility, 1/Pa

δt time step, s

δx_ς node spacing across surface ς , m

δ_j^k Kronecker delta for component pair jk

Greek Symbols (Continued)

ζ integration variable

η^o dipole moment of oil component o, debyes

η_r^o reduced dipole moment of oil component o, debyes

λ Brooks and Corey function parameter

λ^C reaction (radioactive decay) constant, 1/s

μ_γ kinematic viscosity of phase γ, Pa s

$\bar{\mu}_\gamma$ reference kinematic viscosity of phase γ, Pa s

μ_g^j vapor component kinematic viscosity of component j, Pa s

μ_ℓ^S brine viscosity, Pa s

μ_n^o liquid kinematic viscosity of oil component o, Pa s

$\bar{\mu}_n^o$ reference liquid kinematic viscosity of oil component o, Pa s

ξ^j inverse viscosity of component j, $(\text{Pa s})^{-1}$

π osmotic potential, Pa

ρ_γ phase density for phase γ, kg/m^3

ρ_g^j component vapor density of component j, kg/m^3

$\bar{\rho}_\ell$ reference aqueous density, kg/m^3

ρ_n^o liquid density of oil component o, kg/m^3

Greek Symbols (Continued)

ρ_s porous media grain density, kg/m^3

ρ_{sat}^j saturated liquid density of component j, kg/m^3

$\bar{\rho}_{sat}^{j}$ reference saturated liquid density of component j, kg/m^3

σ^{jk} scale parameter for component pair jk

$\sigma_{g\ell}$ gas-aqueous interfacial surface tension, N/m

σ_{gn} gas-NAPL interfacial surface tension, N/m

$\sigma_{i\ell}$ ice-aqueous interfacial surface tension, N/m

$\sigma_{n\ell}$ NAPL-aqueous interfacial surface tension, N/m

$\bar{\sigma}_{g\ell}$ reference gas-aqueous interfacial surface tension, N/m

$\bar{\sigma}_{gn}$ reference gas-NAPL interfacial surface tension, N/m

$\bar{\sigma}_{n\ell}$ reference NAPL-aqueous interfacial surface tension, N/m

ς surface or node index

ς^{-} negative surface (west, south, bottom)

ς^{+} positive surface (east, north, top)

τ_{γ} phase tortuosity for phase γ

υ_{b}^{C} molar volume of solute at its normal boiling temperature, m^3/mol

υ_{c}^{j} critical molar volume of component j, m^3/mol

Greek Symbols (Continued)

υ_{n}^{o} liquid molar specific volume of oil component o, m^3/mol

ϕ^{j} volume fraction of component j

ϕ^{jk} association factor for component pair jk

ϕ_{γ} association factor for solvent γ

Φ^{jk} binary interaction parameter for component pair jk

Φ_{g}^{jk} vapor binary interaction parameter for component pair jk

χ_{γ}^{j} mole fraction of component j in phase γ

ψ Brooks and Corey function nonwetting fluid entry head, m

ψ_{d} Brooks and Corey function nonwetting fluid entry head for drainage, m

ψ_{i} Brooks and Corey function nonwetting fluid entry head for imbibition, m

ω_{γ}^{j} mass fraction of component j in phase γ

ω_{s}^{o} mass fraction of organic compound sorbed on the rock/soil phase

ω_{P}^{j} Pitzner acentric factor of component j

Ω_{D} collision integral for diffusion

Subscripts

B	bottom
BB	bottom boundary surface
E	east
EB	east boundary surface
g	gas phase
i	ice phase
ℓ	aqueous phase
n	NAPL phase
N	north
NB	north boundary surface
P	center or local node
s	rock/soil or solid phase
S	south
SB	south boundary surface
T	top
TB	top boundary surface
W	west
WB	west boundary surface
γ	generic phase or phase index

Superscripts

a	air component
j	generic component or component index
k	generic component or component index
o	oil component
w	water component

Mathematical Symbols

∂	partial differential operator
	divergence operator
$\sum$	summation operator
$\sum_{j \text{ or } k}^{o}$	summation over oil components
$\sum_{j=w,a,o}$	summation over water, air, and oil components
$\sum_{\gamma=\ell,g}$	summation over aqueous and gas phases
$\sum_{\gamma=\ell,g,i}$	summation over aqueous, gas, and ice phases
$\sum_{\gamma=\ell,g,n,i}$	summation over aqueous, gas, NAPL, and ice phases
$\sum_{\gamma=\ell,g,n}$	summation over aqueous, gas, and NAPL phases
$\sum_{\varsigma=W,E,S,N,B,T}$	summation over all node surfaces
$\int_{\bar{V}} d\bar{V}$	volume integral
$\int_{\Gamma} d\Gamma$	surface integral
$x\big\|_{y}$	x evaluated at y

Mathematical Symbols (Continued)

$\langle\ \rangle_{\varsigma}^{a}$	arithmetic interfacial averaging at surface ς
$\langle\ \rangle_{\varsigma}^{h}$	harmonic interfacial averaging at surface ς
$\langle\ \rangle_{\varsigma}^{uw}$	upwind or donor cell interfacial averaging at surface ς
$\{\ \}^{t}$	evaluated at time t (previous time step)
$\{\ \}^{t+\delta t}$	evaluated at time $t + \delta t$ (current time step)
$\{\ \}^{t+\frac{\delta t}{2}}$	evaluated at time $t + \frac{\delta t}{2}$ (intermediate time)
$\max[\ ,\ ]$	maximum value
$\lvert\ \rvert$	absolute value

Contents

Figures

Tables

1.0 Introduction

An engineering simulator named STOMP, an acronym for Subsurface Transport Over Multiple Phases, has been developed by the Pacific Northwest National Laboratory[1] in the framework of the VOC-Arid Soils Integration Demonstration Program, (Arid-ID) and funded by the U.S. Department of Energy (DOE), Office of Technology Development (OTD). The Arid-ID project was directed at the cleanup of volatile organic compounds (VOC) and associated radionuclides and heavy metals in soils and groundwater at arid sites. The initial demonstration site is located within the 200 West Area on the Hanford Site near Richland, Washington. The site contains a volume of soil contaminated with carbon tetrachloride, which includes approximately 200 vertical feet of contaminated unsaturated sediments underlying inactive disposal sites and overlying a 7-square-mile plume of contaminated groundwater. A critical component of the Arid-ID program involves assessing the impact of spatial heterogeneity of subsurface materials on remediation processes and evaluating the effectiveness and efficiency of demonstrated remedial technologies. Because of the complexity of subsurface flow and heat transport phenomena, these assessments and evaluations will require complex numerical tools for their completion. Numerical tools allow scientists and engineers to integrate the current knowledge of contaminant behavior in the subsurface environment to predict and evaluate the performance of proposed remediation methods against established technologies.

A principal subtask of the Arid-ID program involves the development of an engineering simulator (numerical tool), which is capable of numerically simulating proposed remediation processes. The design goals are that the engineering simulator will 1) be accessible and exploitable to scientists and engineers familiar with subsurface environment phenomena, but not necessarily numerical modeling technicalities, 2) have enough general applicability to recruit a user group that is capable of supporting training, maintenance, and enhancement activities, 3) be verified by comparisons to analytical solutions and benchmarked against existing simulators, 4) be validated against germane laboratory and field experiments, and 5) have controlled configuration and documentation under an appropriate quality assurance program. The STOMP simulator attempts to achieve the five design goals described above.

This document, an updated Theory Guide, is one of three companion documents. It has been written to provide users of the STOMP simulator with information about the solved governing and constitutive equations, numerical algorithms, and solution techniques. The second companion document, the STOMP Applications Guide [Nichols et al. 2000], provides users of the STOMP simulator with applications of the simulator to classical groundwater problems. The third companion document, the STOMP User Guide [White and Oostrom 2000], provides users

[1]Pacific Northwest National Laboratory is operated by Battelle for the U.S. Department of Energy under Contract DE-A-C06-76RLO 1830.

of the STOMP simulator with necessary information for selecting an appropriate operational mode, understanding the code flow path and design, creating input files, dimensioning the executable, compiling and executing, and interpreting simulation outputs.

Numerical models for subsurface flow and transport generate quantitative descriptions of physical processes in porous media. These numerical models are frequently classified as empirical, semi-empirical, or fundamental. Empirical models typically are developed from experimental measurements and functionally describe a specific relationship between intrinsic properties (e.g., saturation-capillary pressure relation). Semi-empirical models are typically developed from observed or experimentally measured quantities and are generally used to predict the response of a particular system. Fundamental models describe flow and transport phenomena through accepted physical laws (e.g., conservation equations, Darcy flow equation). Generally, fundamental models have a broader range of applicability than semi-empirical models. The STOMP simulator primarily comprises fundamental and empirical models. Fundamental models are used to describe subsurface flow and transport phenomena through the governing conservation equations for mass and energy. Empirical models and semi-empirical models, to a lesser degree, are used to define relationships among the primary and secondary variables.

This document describes the application of the fundamental, empirical, and semi-empirical models to the solution of subsurface flow and transport problems as formulated in the STOMP simulator. Following a capabilities overview discussion, the organization of this document proceeds from theory to practice. Theory discussions begin with descriptions of the fundamental models of the simulator, which are the conservation equations for component mass, salt mass, energy, and solute mass. These governing equations for subsurface flow and transport are presented in partial differential form. Following this introduction of the fundamental equations, are discussions of the empirical and semi-empirical models which comprise the constitutive relations. The constitutive relations provide functional links between the primary and secondary variables of the governing equations. These equations also provide the means for completely specifying the thermodynamic and hydrologic state within a porous media system given a sufficient number of independent intensive property values. The next section describes the relationships between thermodynamic and hydrologic states and primary variables. This section specifically describes the criteria for choosing primary variable sets as a function of the operational mode and phase condition and precedes the discussions on numerical solution techniques. The numerical solution discussions completely document the transformation of the fundamental and empirical equations into nonlinear algebraic equations using discretization and linear algebraic equations using Newton-Raphson iteration. These discussions also include descriptions of the solution techniques for linear systems available with the STOMP simulator. This guide concludes with an overview of the code architecture which provides the final link between theory and practice. This section specifically describes the sequence of numerical solution stages and iterative loops. Flow diagrams for the coupled flow and transport solution and the secondary solute transport solution are also included.

The fundamental equations presented in this guide will probably remain unchanged throughout the life of the simulator, with the exception of specialty modules added to address unique problems or processes. The empirical equations, in particular the constitutive relations, however, are undoubtedly expected to change over time with the development of new theoretical models from experimental research. The modular form and numerical solution scheme of the STOMP simulator is suited for these types of changes. Advances in numerical solution schemes for nonlinear systems, in particular those involving phase transitions, are anticipated during the life of the STOMP simulator. Adapting the simulator to incorporate these advances will probably occur, because execution speed is a primary concern with users. With these code modifications on the horizon, this document will necessarily change and experience several editions.

2.0 Fundamentals

2.1 Introduction

The STOMP simulator has been designed to solve a wide variety of nonlinear, single- or multi-phase, flow and transport problems for variably saturated geologic media. Partial differential conservation equations for component mass, energy, and solute mass comprise the fundamental equations for the simulator. Coefficients within the fundamental equations are related to the primary variables through a set of constitutive relations. The conservation equations for component mass and energy are solved simultaneously, whereas the solute transport equations are solved sequentially after the coupled flow solution. The variable source code configuration allows the user to select the combination of solved fundamental equations. The current version (Version 2.0) of the STOMP simulator recognizes ten coupled flow equation combinations and the single-phase Water mode (Table 2.1). Each coupled flow equation combination is referred to as an operational mode and may additionally include the solution of a number of transported solutes. The associated constitutive relations for each recognized operational mode are automatically incorporated into the source code as required.

In reading this document, it is important to distinguish between phases and components, which comprise phases. The terms aqueous, gas, nonaqueous phase liquid (NAPL), ice, and solid will be used exclusively in referring to phases. The terms water, air, oil, salt and surfactants will be used to refer to components. The aqueous phase will be primarily comprised of liquid water with dissolved air, oil, salt and surfactant. The gas phase composition can been highly variable containing air, water vapor, and oil vapor. The NAPL phase will primarily be comprised of one oil with negligible amounts of dissolved water and air. The ice phase is assumed to be comprised of frozen water with small amounts of dissolved air and oil. The solid phase refers to the rock/soil matrix. Oil, salt, surfactant, and transported solutes can be sorbed onto the solid phase.

The STOMP simulations are limited in application scope according to the solved fundamental equations, the associated constitutive theory, inherent assumptions, computer execution speed and memory, and the user's creativity. A critical component to correct application of the STOMP simulator and comprehension of output results requires an understanding of the assumptions taken to develop the various flow and transport algorithms. The simulator is capable of predicting flow and transport behavior for a variety of subsurface systems; however, application of the simulator to problems which violate an inherent assumption in the simulator's design or fundamental equations could yield incorrect results. STOMP is principally limited to flow through variably saturated porous media, which can be characterized with an extended form of Darcy's law. Additionally, the simulator is limited to a maximum of three immiscible phases: aqueous, nonaqueous liquid, and gas. Low solubilities are assumed for the liquid phases. Interphase mass transfer assumes equilibrium conditions or first-

order kinetics. Specific to the energy equation, the principal assumptions are that heat transport by gas-phase conduction and the kinetic nature of thermodynamic processes are neglected. Solute transport solutions are computed sequentially to the coupled flow equations. This approach requires the assumption that solutes are passive scalars with respect to the flow equations, which is equivalent to assuming solute concentrations are dilute.

The STOMP simulator solves transient flow and transport problems in the subsurface environment in one, two, or three dimensions. Coordinate systems must be orthogonal and currently are limited to Cartesian, tilted Cartesian, and cylindrical, where the vertical coordinate of the cylindrical system must be aligned with the gravitational vector. The STOMP simulator solves steady-state problems either directly or through false-transients starting from a user-specified initial state. Direct solutions to steady-state problems are possible for initial conditions sufficiently close to the solution; therefore, transient solutions to steady-state conditions are the recommended approach. All boundary conditions, sources, and sinks are time variant and allow the user considerable control over transient simulations. Hydrogeologic properties can be spatially varied throughout the computational domain within the resolution of a node volume. Hydraulic and thermal transport properties for the porous medium can be anisotropic, where the diagonal tensor elements are assumed to be aligned with the principal axes of the coordinate system. Coupled flow solutions can be obtained for selected one-, two-, or three-phase systems under isothermal or nonisothermal conditions. Transport of radioactive solutes with chain-decay tracking can be coupled to all transport solutions with the assumption of dilute solute concentrations. A variety of boundary conditions are available for each operational mode, which may be applied selectively over the boundary surfaces. Unspecified boundary surfaces are always assumed to be zero flux surfaces. Inactive nodes can be specified by the user and boundary conditions can be applied to surfaces separating active (computational) and inactive (noncomputational) nodes. Selected operational modes allow the user to invoke a dynamic domain option which temporarily sets quiescent nodes to an inactive set, thus removing them from the computational domain.

The fundamental coupled flow equations are solved following an integral volume finite-difference approach with the nonlinearities in the discretized equations resolved through Newton-Raphson iteration. Linear systems which result from the Newton-Raphson linearization or the solute transport solution can be solved with a direct banded matrix solver or an indirect conjugate gradient-based solver. these linear system solvers are commercially available software products that have been adapted for the particulars of the STOMP simulator. The STOMP simulator allows considerable control over simulation parameters related to convergence, time stepping, solution techniques, and execution limits. A single simulation can be divided into multiple execution periods, each with a different set of solution control parameters. Restart capabilities have also been included in the simulator, which can resume a simulation from user-defined points with or without alterations to input parameters. Output from the simulator can be completely controlled by the user and is written both to files and to the standard input/output device (e.g.,

screen). Output forms include time histories of selected variables, time "snapshots" of selected variables across the computational domain, and variable integrals for sources and fluxes across boundary and internode surfaces.

The dominant nonlinear functions within the STOMP simulator are the relative permeability-saturation-capillary pressure ($k–s–P$) relations. The STOMP simulator allows the user to specify these relations through a large variety of retention functions. Two-phase (water-air) $k–s–P$ relations can be specified with nonhysteretic functions, nonhysteretic tabular data, or relations that account for gas entrapment. Two-phase $k–s–P$ relations span both saturated and unsaturated conditions. The aqueous phase is assumed to never completely disappear through extensions to the $s–P$ function below the residual saturation and a vapor pressure lowering scheme. Three-phase (aqueous-NAPL-gas) $k–s–P$ relations can be specified with nonhysteretic functions or relations that account for gas/NAPL entrapment. Tabular three-phase $k–s–P$ relations are not currently available. The wettability order for fluids in the STOMP simulator is assumed to follow the descending order aqueous to NAPL to gas. Three-phase $k–s–P$ relations span both total-liquid saturated and unsaturated conditions and aqueous saturated and unsaturated conditions. Phase appearances and disappearances are possible for the gas and NAPL phases; however, the aqueous phase is assumed to never completely disappear through extensions to the $s–P$ function below the residual saturation and a vapor pressure lowering scheme.

2.2 Operational Modes

The STOMP simulator operational modes do not comprise all of the possible combinations of coupled governing equations. The combination sets of coupled governing equations selected for inclusion in the list of operational modes represent those with the greatest utility for physical systems. For example, a Water-Energy operational mode could be envisioned, which solved the water mass and energy conservation equations. This operational mode would invoke the assumption of a nonparticipating gas phase. Two-phase flow and transport through porous media under thermal gradients, however, strongly depends on the diffusion, dispersion, and advection transport through gas phase, even for low thermal gradients. Therefore, this operational mode, while capable of functioning and producing converged solutions, would have limited utility because of its premise that gas phase transport could be neglected. Other combinations of governing equation sets with associated assumptions have considerable utility for specific systems or problems and have been coded, but have not been selected for inclusion in the STOMP guide manuals. For example, an operational mode has been created that solves the water mass, air mass, oil mass, and/or energy equation with the assumption that oil concentrations remain below the aqueous solubility limit. This operational mode has utility in the investigation of the remediation of oil contaminants in dissolved plumes. This operational mode differs from one which models the oil as a dilute solute because 1) the oil

mass equation is solved simultaneously with the other coupled flow equations and 2) fluid properties have a dependence on the oil concentration.

Operational modes support solute transport calculations and are identified according to the coupled conservation equations that are solved. The solved conservation equations and primary assumptions are summarized in Table 2.1 for each operational mode. Beyond the set of solved coupled equations, some of the operational modes have unique features developed for specific applications. The Water operational mode contains an optional dynamic domain feature. This feature converts relatively invariant nodes into noncomputational or inactive nodes, therefore improving execution performance. With this feature, all active nodes are included in the computational set during the initial iteration. If the residual for the water mass conservation equation for a particular node is less than a specified limit, then that node becomes inactive for the remainder of iterations within the time step. The Water operational mode additionally contains two algorithms for computing the partitioning of transported solutes between the solid and aqueous phases. The first approach assumes that the solid surface is continuously wet independent of the aqueous saturation; whereas the second approach assumes that the wetted surface is proportional to the aqueous saturation. This operational mode also includes a feature for solute-dependent retardation. With this feature solid-aqueous partition coefficient for one solute is dependent on the concentration of another solute. The feature allows the modeling of surfactant type reactions between solvents. The Water-Air operational mode contains a unique hysteretic air entrapment constitutive theory that allows dissolution and expansion of entrapped air. This feature was developed specifically to examine mechanisms for entrapped gas release from a declining water table. The Water-Air-Energy operational mode contains models for computing ice saturations under soil freezing conditions but does not include soil stress processes necessary to compute mounding and heaving. This operational mode additionally contains a feature to correct water vapor pressures for vapor pressure lowering through capillary forces. Aqueous saturations less than the residual saturation can occur through application of an extension to the capillary pressure-saturation constitutive model. Enhanced vapor diffusion from thermal gradients can be considered as a function of the thermal gradient, moisture content, soil-moisture retention function, and soil clay fraction.

Table 2.1. Operational Mode Summary

Operational Mode with Options	Solved Coupled Equations	Primary Assumptions
Water	water mass	isothermal conditions passive gas phase no NAPL phase no dissolved oil no brine no surfactant local thermodynamic equilibrium
Water-Air	water mass air mass	isothermal conditions no NAPL phase no dissolved oil no brine no surfactant local thermodynamic equilibrium
Water-Air-Energy w/ Ice	water mass air mass thermal energy	no NAPL phase no dissolved oil no brine no surfactant local thermodynamic equilibrium
Water-Oil	water mass oil mass	isothermal conditions single component NAPL phase passive gas phase no brine no surfactant local thermodynamic equilibrium
Water-Oil-Air	water mass oil mass air mass	isothermal conditions single component NAPL phase no brine no surfactant local thermodynamic equilibrium

Table 2.1. (Continued)

Operational Mode with Options	Solved Coupled Equations	Primary Assumptions
Water-Oil-Air-Energy	water mass oil mass air mass thermal energy	single component NAPL phase no brine no surfactant local thermodynamic equilibrium
Water-Oil-Dissolved Oil	water mass oil mass dissolved oil mass	isothermal conditions single component NAPL phase passive gas phase no brine no surfactant kinetic oil dissolution
Water-Oil-Dissolved Oil-Surfactant	water mass oil mass dissolved oil mass surfactant mas	isothermal conditions single component NAPL phase passive gas phase no brine kinetic oil dissolution
Water-Salt	water mass salt mass	isothermal conditions passive gas phase no NAPL phase no dissolved oil no surfactant local thermodynamic equilibrium
Water-Air-Salt	water mass air mass salt mass	isothermal conditions no NAPL phase no dissolved oil no surfactant local thermodynamic equilibrium
Water-Air-Energy-Salt w/ Ice	water mass air mass salt mass thermal energy	no NAPL phase no dissolved oil no surfactant local thermodynamic equilibrium

3.0 Governing Equations

3.1 Introduction

In broad terms, the STOMP simulator solves coupled conservation equations for component mass and energy that describe subsurface flow over multiple phases through variably saturated geologic media. The resulting flow fields are used to sequentially solve conservation equations for solute transport with radioactive chain decay over multiple phases through variably saturated geologic media. These conservation equations for component mass, energy, and solute are partial differential equations that mathematically describe flow and transport through porous media and are collectively referred to as the governing equations. The STOMP simulator has capabilities for modeling subsurface flow and transport over three distinct phases: aqueous, gas, and NAPL. The aqueous phase primarily comprises liquid water with small quantities of dissolved air and oils. The gas phase comprises variable amounts of air, water vapor, and oil vapors. The NAPL phase comprises liquid oil components with the amounts of dissolved air and water assumed to be negligible. Additional conservation equations, termed the salt and surfactant mass conservation equation, can be solved coupled with the component mass and energy equations to simulate brines or surfactants. Because the salt and surfactant mass conservation equation are solved coupled with the flow and energy transport equations, phase properties can be dependent on salt and surfactant concentrations. This approach allows modeling of systems with brines or surfactants, where the physical properties (e.g., density, viscosity, relative permeability) are dependent on the salt or surfactant concentration. In this respect, the terms salt and surfactant refer to a dissolved and transported solute whose concentration influences the physical properties of the solvents. Salts and surfactants differ from solutes because the primary assumption for solution of the solute transport equation is that solute concentrations are infinitely dilute.

3.2 Water Mass Conservation Equation

The water mass conservation equation, shown in Equation (3.2.1), equates the time rate of change of water mass within a control volume with the flux of water mass crossing the control volume surface. In the STOMP simulator water exists in the diffusive pore space as liquid water and water vapor, in the aqueous and gas phases, respectively. Dissolution of water in the NAPL phase is neglected. Phase partitioning of water mass is computed assuming equilibrium conditions, implying that in geologic media the time scale for thermodynamic equilibrium is significantly shorter for component transport. Water transport occurs by advection through the aqueous and gas phases and by diffusion-dispersion through the gas phase. Following the low solubility assumption for dissolved air and oil in the aqueous phase, water diffusion-dispersion

through the aqueous phase is neglected. Flow of fluid phases is computed from Darcy's law. Transport of phase components is computed from a modified form of Fick's law, where a combined diffusion-dispersion coefficient replaces the classical Fickian diffusion coefficient. Equation (3.2.1) includes an osmotic flux term, which accounts for the flow of aqueous fluid by osmotic pressure for simulations with coupled salt transport.

$$\frac{\partial}{\partial t}\left[\sum_{\gamma=\ell,g,i}\left(n_D\,\omega_\gamma^w\,\rho_\gamma\,s_\gamma\right)\right] = -\sum_{\gamma=\ell,g}\left(\mathbf{F}_\gamma^w + \mathbf{J}_\gamma^w\right) - \mathbf{F}_\ell^S + \dot{m}^w \qquad (3.2.1)$$

where,

$$\mathbf{F}_\gamma^w = -\frac{\omega_\gamma^w\,\rho_\gamma\,k_{r\gamma}\,\mathbf{k}}{\mu_\gamma}\left(P_\gamma + \rho_\gamma\,g\,\mathbf{z}_g\right) \quad \textit{for } \gamma = \ell, g$$

$$\mathbf{J}_\gamma^w = -\tau_\gamma\,n_D\,\rho_\gamma\,s_\gamma\,\frac{M^w}{M_\gamma}\,D_\gamma^w\,\chi_\gamma^w \quad \textit{for } \gamma = \ell, g$$

$$\mathbf{F}_\ell^S = D_\ell^S\,S_\ell$$

3.3 Air Mass Conservation Equation

The air mass conservation equation, shown in Equation (3.3.1), equates the time rate of change of the air mass within a control volume with the flux of air mass crossing the control volume surface. In the STOMP simulator, air exists in the diffusive pore space as a component of the gas phase and dissolved in the aqueous phase. Dissolution of air in the NAPL is neglected. Phase partitioning of air mass is computed assuming equilibrium conditions: this assumption implies that in geologic media the time scale for thermodynamic equilibrium is significantly shorter than that for component transport. Air transport occurs by advection and diffusion-dispersion through the aqueous and gas phases. Flow of fluid phases is computed from Darcy's law. Transport of phase components is computed from a modified form of Fick's law, where a combined diffusion-dispersion coefficient replaces the classical Fickian diffusion coefficient.

$$\frac{\partial}{\partial t}\left[\sum_{\gamma=\ell,g}\left(n_D\,\omega_\gamma^a\,\rho_\gamma\,s_\gamma\right)\right] = -\sum_{\gamma=\ell,g}\left(\mathbf{F}_\gamma^a + \mathbf{J}_\gamma^a\right) + \dot{m}^a \qquad (3.3.1)$$

where,

$$\mathbf{F}_\gamma^a = -\frac{\omega_\gamma^a \rho_\gamma k_{r\gamma} \mathbf{k}}{\mu_\gamma}\left(P_\gamma + \rho_\gamma g \mathbf{z}_g \right) \quad for\ \gamma = \ell, g$$

$$\mathbf{J}_\gamma^a = -\tau_\gamma n_D \rho_\gamma s_\gamma \frac{M^a}{M_\gamma} D_\gamma^a \quad \chi_\gamma^a \quad for\ \gamma = \ell, g$$

3.4 Oil Mass Conservation Equations

The oil mass conservation equation for the Water-Oil, Water-Oil-Air, and Water-Oil-Air-Energy modes is shown in Equation (3.4.1). This equation equate the time rate of change of oil mass within a control volume with the flux of oil mass crossing the control volume surface. In these four modes, oil exists in the diffusive pore space as liquid oil in the NAPL phase, dissolved oil in the aqueous phase, and as oil vapor in the gas phase. Phase partitioning of oil is computed assuming equilibrium conditions: this assumption implies that in geologic media, the time scale for thermodynamic equilibrium is significantly shorter than that for component transport. Oil transport occurs by advection and diffusion-dispersion through the aqueous, gas, and NAPL phases. Flow of fluid phases is computed from Darcy's law. Transport of phase components is computed from a modified form of Fick's law, where a combined diffusion-dispersion coefficient replaces the classical Fickian diffusion coefficient.

$$\frac{\partial}{\partial t}\left[\sum_{\gamma = \ell,g,n} \left(n_D \omega_\gamma^o \rho_\gamma s_\gamma \right) + \left(1 - n_T\right) \omega_s^o \rho_s \right] = -\sum_{\gamma = \ell,g,n} \left(\mathbf{F}_\gamma^o + \mathbf{J}_\gamma^o \right) + \dot{m}^o \qquad (3.4.1)$$

where,

$$\mathbf{F}_\gamma^o = -\frac{\omega_\gamma^o \rho_\gamma k_{r\gamma} \mathbf{k}}{\mu_\gamma}\left(P_\gamma + \rho_\gamma g \mathbf{z}_g \right) \quad for\ \gamma = \ell, g, n$$

$$\mathbf{J}_\gamma^o = -\tau_\gamma n_D \rho_\gamma s_\gamma \frac{M^o}{M_\gamma} D_\gamma^o \quad \chi_\gamma^o \quad for\ \gamma = \ell, g, n$$

In the Water-Oil-Dissolved Oil and the Water-Oil-Dissolved Oil-Surfactant mode, the continuity equation for the oil component in the NAPL phase is used, as shown in equation (3.4.2). Oil transport occurs by advection in the NAPL phase. Interphase mass transfer of oil between the NAPL and aqueous phases is computed with a convective mass transfer relation.

$$\frac{\partial}{\partial t}\left(\rho_n s_n n_D\right) = - \mathbf{F}_n + I^o_{n,l} + \dot{m}^o \qquad (3.4.2)$$

where,

$$\mathbf{F}_n = -\frac{\rho_n\, k_{rn}\, \mathbf{k}}{\mu_n}\left(P_n + \rho_n\, g\, \mathbf{z}_g\right)$$

$$I^o_{n,l} = -n_D s_l k^{do}_{n,l}\left(\overline{C}^{do}_l - C^{do}_l\right)$$

The dissolved oil conservation equation associated with equation (3.4.2) is shown in equation (3.4.3)

$$\frac{\partial}{\partial t}\left[\left(n_D\, \omega^{do}_l\, \rho_l\, s_l\right) + \left(1 - n_T\right)\omega^{do}_s\, \rho_s\right] = -\left(\mathbf{F}^{do}_l + \mathbf{J}^{do}_l\right) + I^{do}_{n,l} + \dot{m}^o \qquad (3.4.3)$$

where,

$$\mathbf{F}^{do}_l = -\frac{\omega^{do}_l\, \rho_l\, k_{rl}\, \mathbf{k}}{\mu_l}\left(P_l + \rho_l\, g\, \mathbf{z}_g\right)$$

$$\mathbf{J}^{do}_l = -\tau_l\, n_D\, \rho_l\, s_l \frac{M^{do}}{M_l} D^{do}_l \quad \chi^{do}_l$$

$$I^{do}_{n,l} = n_D s_l k^{do}_{n,l}\left(\overline{C}^{do}_l - C^{do}_l\right)$$

3.5 Energy Conservation Equation

The energy conservation equation, shown in Equation (3.5.1), equates the time rate of change of energy within a control volume with the flux of energy crossing the control volume surface. In the STOMP simulator, thermal energy is partitioned, according to thermal equilibrium conditions, among the fluid and solid phases. The thermal capacitance of unconnected pore space, represented by the difference between the total and diffusive porosity, is computed as it is filled with liquid water. Heat transfer occurs by advection of phase mass, diffusion of component mass, and thermal diffusion through the fluid and solid phases. Heat transfer by hydraulic dispersion of flowing fluid phases is neglected. Enhanced vapor transport is

incorporated through enhancement factors for component diffusion through the gas phase. Energy associated with component mass sources are included as internal heat generation sources. Reference states for enthalpy and internal energy are component dependent. Latent heat transport is considered through vapor transport through the gas phase and equilibrium thermodynamics.

$$\frac{\partial}{\partial t}\left[\sum_{\gamma=\ell,g,n,i}\left(n_D\,\rho_\gamma\,s_\gamma\,u_\gamma\right)+\left(1-n_T\right)\rho_s\,u_s+\left(n_T-n_D\right)\rho_\ell\,u_\ell\right]= -\sum_{\gamma=\ell,g,n}\left(\rho_\gamma\,h_\gamma\,\mathbf{V}_\gamma\right)+\sum_{j=w,a,o}\left(h^j\,\mathbf{J}_\gamma^j\right)+\left(\mathbf{k}_e\quad T\right)+\sum_{j=w,a,o}\left(h^j\,\dot{m}^j\right)+\dot{q} \tag{3.5.1}$$

where,

$$\mathbf{V}_\gamma = -\frac{k_{r\gamma}\,\mathbf{k}}{\mu_\gamma}\left(\quad P_\gamma+\rho_\gamma\,g\,\mathbf{z}_g\right)\quad for\ \gamma=\ell,g,n$$

$$\mathbf{J}_\gamma^j = -\tau_\gamma\,n_D\,\rho_\gamma\,s_\gamma\,\frac{M^j}{M_\gamma}\,D_\gamma^j\quad\chi_\gamma^j\quad for\ \gamma=\ell,g,n\ and\ j=w,a,o$$

3.6 Salt Mass Conservation Equation

The salt mass conservation equation, shown in Equation (3.6.1), equates the time rate of change of salt mass within a control volume with the flux of salt mass crossing the control volume surface. In the STOMP simulator, salt mass is partitioned among the fluid and solid phases assuming thermodynamic and geochemical equilibrium conditions. This assumption implies that the time scales for thermodynamic and geochemical equilibrium are short compared against those for salt transport. For geologic media, this assumption is generally appropriate. Salt transport occurs by advection and diffusion-dispersion through the aqueous phase. Solubility of salt in the gas phase is neglected. This formulation neglects an effect known as pressure diffusion [Bird et al. 1960], which accounts for dispersive salt mass flux due to phase pressure gradients.

$$\frac{\partial S}{\partial t} = -\left[S_\ell\,\mathbf{V}_\ell\right]+\left[\left(\tau_\ell\,s_\ell\,n_D\,D_\ell^S+s_\ell\,n_D\,\mathbf{D}_{h\ell}\right)\quad S_\ell\right]+\dot{m}^S \tag{3.6.1}$$

where,

$$\mathbf{V}_\ell = -\frac{k_{r\ell}\,\mathbf{k}}{\mu_\ell}\left(\nabla P_\ell + \rho_\ell\, g\, \nabla \mathbf{z}_g\right)$$

3.7 Surfactant Mass Conservation Equation

The surfactant mass conservation equation, shown in Equation (3.7.1), equates the time rate of change of surfactant mass within a control volume with the flux of surfactant mass crossing the control volume surface. In the STOMP simulator, surfactant mass is partitioned among the fluid and solid phases assuming thermodynamic and geochemical equilibrium conditions. This assumption implies that the time scales for thermodynamic and geochemical equilibrium are short compared against those for surfactant transport. For geologic media, this assumption is generally appropriate. Surfactant transport occurs by advection and diffusion-dispersion through the aqueous phase. Solubility of surfactant in the gas phase is neglected. This formulation neglects an effect known as pressure diffusion [Bird et al. 1960], which accounts for dispersive surfactant mass flux due to phase pressure gradients.

$$\frac{\partial S}{\partial t} = -\nabla\left[S_\ell\, \mathbf{V}_\ell\right] + \nabla\left[\left(\tau_\ell\, s_\ell\, n_D\, D_\ell^S + s_\ell\, n_D\, \mathbf{D}_{h\ell}\right)\nabla S_\ell\right] + \dot{m}^S \qquad (3.7.1)$$

where,

$$\mathbf{V}_\ell = -\frac{k_{r\ell}\,\mathbf{k}}{\mu_\ell}\left(\nabla P_\ell + \rho_\ell\, g\, \nabla \mathbf{z}_g\right)$$

3.8 Solute Mass Conservation Equation

The solute conservation equation, shown in Equation (3.8.1), equates the time rate of change of solute within a control volume with the flux of solute crossing the control volume surface. In the STOMP simulator, solute is partitioned among the fluid and solid phases assuming thermodynamic and geochemical equilibrium conditions. This assumption implies that the time scales for thermodynamic and geochemical equilibrium are short compared against those for solute transport. For geologic media, this assumption is generally appropriate. Solute transport occurs by advection and diffusion-dispersion through the aqueous phase, gas phase, and NAPL. Radioactive chain decay of solutes is computed using first-order decay kinetics. Progeny solute production rates are computed from parent decay rates and chain decay fractions. Chemical reactions occur according to first-order or Monod-type kinetics. Solute conservation equations are solved sequentially with progeny or product solutes preceding parent or primary

reactant solutes.

$$\frac{\partial C}{\partial t} = -\sum_{\gamma=\ell,g,n}\left(\left[C_\gamma\ \mathbf{V}_\gamma\right]\right) + \dot{m}^C - \dot{R}^C\ C + \sum_{\gamma=\ell,g,n}\left[\left(\tau_\gamma\ s_\gamma\ n_D\ D_\gamma^C + s_\gamma\ n_D\ \mathbf{D}_{h_\gamma}\right)\quad C_\gamma\right] \tag{3.8.1}$$

where,

$$\mathbf{V}_\gamma = -\frac{k_{r\gamma}\ \mathbf{k}}{\mu_\gamma}\left(\quad P_\gamma + \rho_\gamma\ g\ \mathbf{z}_g\right)\ \ for\ \gamma = \ell, g, n$$

4.0 Constitutive Relations

4.1 Introduction

Constitutive relations are functions that relate the primary unknowns of the governing equations to the associated secondary variables. Each governing equation is solved for a single variable that is referred to as the primary unknown. The remaining variables in the governing equation are referred to as secondary variables. A closed system requires that all of the secondary variables be computable from the set of primary unknowns. In the STOMP simulator primary variables (unknowns) for a particular governing equation can vary between operational modes and phase conditions; however, the set of primary unknowns is fixed for each operational mode and phase condition combination. Primary unknowns are macroscopic properties that fix the physical state of the system. The thermodynamic state of the system is independent of the path by which the system arrived at the given state; however, the saturation state of the system may be dependent on the prior saturation history. Secondary variables include intensive and extensive properties (e.g., phase saturation, phase relative permeability, porosity, tortuosity, viscosity, density, enthalpy, saturated vapor pressures, vapor mass fractions, and diffusion coefficients). Because secondary variables are often computed in terms of other secondary variables, the calculation order for secondary variables is critical to closing the thermodynamic and hydrologic system. Each operational mode and phase condition combination follows a specified sequence for computing secondary variables from the primary variables. This section documents the functions available in the STOMP simulator for computing secondary variables. The subsections are ordered in the most frequent calculation sequence for secondary variables.

4.2 Gas-Phase Pressure

For liquid-vapor equilibrium conditions the vapor pressure exerted by a component can be computed from the saturated vapor pressure of the component as a function of temperature and the component's molar concentration in the liquid phase. Because of the low solubility assumption associated with the STOMP simulator for oil solubility in the aqueous phase, the water vapor pressure equals its saturated vapor pressure. For hydrologic saturation conditions with strong capillary pressures, the saturated water vapor pressure is lowered according to the vapor pressure lowering formulation [Nitao 1988]. Compositional NAPL contains a mixture of liquid-oil components. According to Raoult's Rule for multicomponent, multiphase equilibrium [Van Wylen and Sonntag 1978] the vapor pressure for each oil is computed from its saturated vapor pressure and mole fraction in the NAPL phase, where each component's saturated vapor pressure is computed as a function of temperature.

4.2.1 Water Vapor Pressure

The STOMP simulator assumes the presence of liquid water and the equilibrium condition of liquid water and water vapor. Water vapor pressure is computed from saturated water vapor pressure as a function of temperature and the hydrologic aqueous saturation state. Saturated water vapor pressure is computed as a function of temperature from the steam table equations [ASME 1967], according to Equation (4.2.1). Numerical values of the critical properties for water and saturated water vapor pressure function constants are listed in Tables A.1 and A.2, of Appendix A, respectively. The saturated water vapor pressure function is shown graphically in Figure (4.1). The water vapor pressure is computed as a function of the saturated vapor pressure and capillary pressure from the expression for vapor pressure lowering [Nitao 1988], according to Equation (4.2.2). The vapor pressure lowering function is shown graphically in Figure (4.2). The effect of total system pressure on the vapor pressure, the Poynting effect [Wark 1995], is computed using the assumption that the gas phase behaves as an ideal solution and an ideal-gas mixture according to Equation (4.2.3). Water vapor pressure is relatively insensitive to changes in total system pressure. For example, at 20 C a total system pressure of over 1700 times the saturated vapor pressure value is required to yield a 3 percent change in the vapor pressure.

$$P_{sat}^{w} = P_c^{w} \exp\left[\frac{T_c^{w}}{T}\left(\frac{\sum_{j=1}^{5} k_j X^j}{1 + k_6 X + k_7 X^2}\right) - \left(\frac{X}{k_8 X^2 + k_9}\right)\right] \tag{4.2.1}$$

where,

$$X = 1 - \frac{T}{T_c^{w}}$$

$$\bar{P}_g^{w} = P_{sat}^{w} \exp\left[\frac{-P_{cap}}{\rho_\ell R_\ell T}\right] \tag{4.2.2}$$

$$\ln\left(\frac{P_g^{w}}{\bar{P}_g^{w}}\right) = \frac{\left(P - \bar{P}_g^{w}\right)}{R T \rho_\ell} \tag{4.2.3}$$

4.2.2 Oil Vapor Pressure

Saturated oil vapor pressure is computed as a function of temperature by the Wagner equations [Reid et al. 1987], according to Equations (4.2.4) through (4.2.7). Oil-saturated vapor pressure function constants and critical properties of pressure and temperature are determined experimentally and have been tabulated for numerous inorganic and organic compounds in Reid et al. [1987]. It should be noted that Equation (4.2.5) is nonlinear and requires an iterative solution technique. The saturated vapor pressure function for carbon tetrachloride is shown graphically in Figure (4.3), according to Equation (4.2.4). Numerical values of vapor pressure function constants and critical properties are listed in Table A.3 of Appendix A. Oil vapor pressure is computed as a function of NAPL-phase concentration according to Raoult's Law [Van Wylen and Sonntag 1978], according to Equation (4.2.7). The effect of total system pressure on the oil vapor pressure and the Poynting effect [Wark 1995], is computed using the assumption that the gas phase behaves as an ideal solution and an ideal gas mixture according to Equation (4.2.8).

$$P_{sat}^{o} = P_{c}^{o} \exp\left[\frac{a\,X + b\,X^{1.5} + c\,X^{3} + d\,X^{6}}{1 - X}\right] \tag{4.2.4}$$

where,

$$X = 1 - \frac{T}{T_{c}^{o}}$$

$$P_{sat}^{o} = \exp\left[a - \frac{b}{T} + c\,\ln(T) + \frac{d\,P_{sat}^{o}}{T^{2}}\right] \tag{4.2.5}$$

$$P_{sat}^{o} = \exp\left[a - \frac{b}{(T + c)}\right] \tag{4.2.6}$$

$$\overline{P}_{g}^{o} = \chi_{n}^{o}\; P_{sat}^{o} \tag{4.2.7}$$

$$\ln\left(\frac{P_{g}^{o}}{\overline{P}_{g}^{o}}\right) = \frac{\left(P - \overline{P}_{g}^{o}\right)}{R\,T\,\rho_{n}} \tag{4.2.8}$$

4.2.3 Air Pressure

The air pressure is computed from Dalton's partial pressure law for ideal gas mixtures [Van Wylen and Sonntag 1978], according to Equation (4.2.9).

$$P_g^a = P_g - P_g^w - P_g^o \tag{4.2.9}$$

4.2.4 Brine Vapor Pressure

The vapor pressure depression that occurs with the addition of a solute to a pure solvent for an ideal solution, is used to calculate the water vapor pressure above an aqueous solution of sodium chloride according to Equation (4.2.10).

$$P_g^{wS} = \left(1 - \chi_\ell^S\right) P_g^w \tag{4.2.10}$$

4.3 Density

Gas-phase densities are computed according to Dalton's ideal gas law for mixtures [Van Wylen and Sonntag 1978], where the sum of the gas component partial pressures equals the total gas pressure. The low solubility assumption for air and oil solubility in the aqueous phase allows the aqueous-phase density to be approximated with the density of liquid water. Compositional NAPL contains a mixture of liquid-oil components. NAPL-phase density is computed from the pure component liquid-oil densities and molar concentrations within the NAPL phase.

4.3.1 Gas-Phase Density

Component vapor densities are computed according to the ideal gas law, as shown in Equation (4.3.1). Gas-phase density equals the sum of the component densities, according to the ideal gas law shown in Equation (4.3.2).

$$\rho_g^j = \frac{P_g^j}{R^j T}, \quad for \;\; j = w,a,o \tag{4.3.1}$$

$$\rho_g = \sum_{j=w,a,o} \rho_g^j \tag{4.3.2}$$

4.3.2 Aqueous-Phase Density

Aqueous-phase density is computed as a function of temperature and pressure using the steam table formulations [ASME 1967], as shown in Equation (4.3.3). With the low solubility assumption, aqueous phase density is independent of dissolved component concentrations. Numerical values of the constants shown in Equation (4.3.3) are listed in Table A.4 of Appendix A. The aqueous-phase density function using the steam table formulation is shown graphically in Figure 4.4. Values below the freezing point are used to compute subcooled aqueous phase density for freezing conditions in the Water-Air-Energy operational mode.

$$\rho_\ell = v_c^w \left\{ A_{11}\ a_5\ Z^{-5/17} + A_{12} + A_{13}\ T_r^w + A_{14} \left(T_r^w\right)^2 \right. \tag{4.3.3}$$

$$+ A_{15} \left(a_6 - T_r^w\right)^{10} + A_{16} \left[a_7 + \left(T_r^w\right)^{19} \right]^{-1}$$

$$- \left[a_8 + \left(T_r^w\right)^{11} \right]^{-1} \left[A_{17} + 2\ A_{18}\ P_r^w + 3\ A_{19} \left(P_r^w\right)^2 \right]$$

$$- A_{20} \left(T_r^w\right)^{18} \left[a_9 + \left(T_r^w\right)^2 \right] \left[-3 \left(a_{10} + P_r^w\right)^{-4} + a_{11} \right]$$

$$\left. + 3\ A_{21} \left(a_{12} - T_r^w\right) \left(P_r^w\right)^2 + 4\ A_{22} \left(T_r^w\right)^{-20} \left(P_r^w\right)^3 \right\}^{-1}$$

where,

$$Z = Y + \left(a_3\ Y^2 - 2\ a_4\ T_r^w + 2\ a_5\ P_r^w\right)^{1/2}$$

$$Y = 1 - a_1 \left(T_r^w\right)^2 - a_2 \left(T_r^w\right)^{-6}$$

4.3.3 NAPL-Phase Density

Liquid oil density for saturated conditions is computed as a function of temperature using the Modified Rackett method [Reid et al. 1987], according to Equation (4.3.4). If an experimental value for liquid density is available, then the recommended form of the Rackett function appears as shown in Equation (4.3.5). The saturated liquid density function for carbon tetrachloride is shown graphically in Figure 4.5. A correction for compressed conditions is made following the Hankinson-Brobst-Thompson (HBT) technique [Reid et al. 1987], according to Equation (4.3.6). Numerical values for the coefficients shown in Equation (4.3.6) are listed Table A.5 of Appendix A. Compositional NAPL contains a mixture of liquid-oil components. NAPL-phase density is computed as a function of the pure component liquid densities and molar concentrations in the NAPL phase according to Equation (4.3.7). Alternatively, mixing rules for the Rackett equation have been published [Reid et al.1987] which define the critical pressure, critical temperature, and critical compressibility for a liquid mixtures, according to Equations (4.3.8) through (4.3.10) respectively. NAPL-phase density for a compositional NAPL is then computed as a function of temperature and pressure using the Modified Rackett and HBT methods shown in Equations (4.3.4) through (4.3.6) by substituting the mixture critical properties for the component critical properties.

$$\rho_{sat}^{o} = \left[\frac{R^{o}\, T_{c}^{o}}{P_{c}^{o}}\right]\left(Z_{RA}^{o}\right)^{\left[1+\left(1-T_{r}^{o}\right)^{2/7}\right]^{-1}} \tag{4.3.4}$$

where,

$$T_{r}^{o} = \frac{T}{T_{c}^{o}},\quad P_{r}^{o} = \frac{P}{P_{c}^{o}},\quad Z_{RA}^{o} = 0.29056 - 0.08775\,\omega_{P}^{o}$$

$$\rho_{sat}^{o} = \left[\frac{1}{\rho_{sat}^{o}}\right]\left(Z_{RA}^{o}\right)^{\left[\left(1-T_{r}^{o}\right)^{2/7} - \left(1-\bar{T}_{r}^{o}\right)^{2/7}\right]^{-1}} \tag{4.3.5}$$

$$\rho_{n}^{o} = \frac{\rho_{sat}^{o}}{\left[1 - h_{3}\ln\left(\frac{h_{9}+P}{h_{9}+P_{sat}^{o}}\right)\right]} \tag{4.3.6}$$

where,

$$h_9 = P_c^o \left[-1 + h_1 X^{1/3} + h_2 X^{2/3} + h_4 X + h_5 X^{4/3} \right]$$

$$h_3 = h_{10} + h_{11}\, \omega_P^o, \quad h_5 = \exp\left[h_6 + h_7\, \omega_P^o + h_8 \left(\omega_P^o \right)^2 \right]$$

$$\rho_n = \sum_j^o \chi_n^j \rho_n^j \tag{4.3.7}$$

where,

$$\phi^j = \frac{\chi_n^j \upsilon_c^j}{\sum_j^o \chi_n^j \upsilon_c^j}$$

$$T_c^{jk} = \left(1 - \Phi^{jk} \right) \left(T_c^j T_c^k \right)^{1/2}$$

$$1 - \Phi^{jk} = \frac{8 \left(\upsilon_c^j \upsilon_c^k \right)^{1/2}}{\left[\left(\upsilon_c^j \right)^3 + \left(\upsilon_c^k \right)^3 \right]^{1/3}}$$

$$T_c^n = \sum_j^o \sum_k^o \phi^j \phi^k T_c^{jk} \tag{4.3.8}$$

$$P_c^n = \sum_j^o \chi_n^j P_c^j \tag{4.3.9}$$

$$Z_{RA}^n = \sum_j^o \chi_n^j Z_{RA}^j \tag{4.3.10}$$

4.3.4 Ice Density

Ice density is computed as a function of temperature from empirical correlation of ASHRAE [1977] data, according to Equation (4.3.10). The correlation is valid over the temperature range from -100 C to 0 C.

$$\rho_i = \left[1.06472\, x\, 10^{-3} + 1.23173\, x\, 10^{-8}\, T + 3.0203\, x\, 10^{-10}\, T^2\right]^{-1} \tag{4.3.11}$$

4.3.5 Brine Density

Liquid density for an aqueous solution of sodium chloride is computed as a function of salt mass fraction from an empirical relation [Leijnse 1992] according to Equation (4.3.11), where the aqueous density is computed as a function of temperature and pressure according to Equation (4.10).

$$\rho_\ell^S = \rho_\ell \exp\left(0.7\, \omega_\ell^S\right) \tag{4.3.12}$$

4.4 Mass and Mole Fractions

Aqueous-phase component fractions are computed assuming equilibrium conditions and low solubilities of dissolved components according to Henry's Law [Reid et al. 1987]. Gas-phase component fractions are computed from the ratio of component vapor density to gas-phase density. Zero solubilities are assumed for water and air components in the NAPL phase. Compositional NAPL contains mixtures of liquid-oil components. For a compositional NAPL phase the component partial pressures are the primary unknowns for all but one oil mass conservation equation. Conversion between mass and mole fraction is computed according to Equations (4.4.1) and (4.4.2).

$$\chi_\gamma^j = \frac{\dfrac{\omega_\gamma^j}{M^j}}{\displaystyle\sum_{k=w,a,o} \frac{\omega_\gamma^k}{M^k}} \tag{4.4.1}$$

$$\omega_{\gamma}^{j} = \frac{\chi_{\gamma}^{j} M^{j}}{\sum_{k=w,a,o} \chi_{\gamma}^{k} M^{k}} \tag{4.4.2}$$

4.4.1 Gas-Phase Component Fractions

Gas-phase mass fraction is computed from the ratio of component vapor density to gas-phase density for water and oils, according to Equation (4.4.3). Component vapor density and gas-phase density are computed as a function of component partial pressure and temperature according to Equations (4.3.1) and (4.3.2), respectively. Gas-phase mass fractions sum to one; therefore, the air mass fraction is computed according to Equation (4.4.4).

$$\omega_{g}^{j} = \frac{\rho_{g}^{j}}{\rho_{g}}, \quad for \;\; j = w,o \tag{4.4.3}$$

$$\omega_{g}^{a} = 1 - \sum_{j=w,o} \omega_{g}^{j} \tag{4.4.4}$$

4.4.2 Aqueous-Phase Component Fractions

Aqueous-phase mole fraction is computed assuming equilibrium conditions and low solubilities for the dissolution of air and oils in water. Under these conditions, the partial pressure of a component in the gas phase is proportional to its mole fraction in the aqueous phase, through a temperature and pressure-dependent proportional constant known as Henry's constant [Sandler 1989]. Henry's law relates the air and oil component partial pressures to their mole fraction concentrations in the aqueous phase. Henry's law is limited to low solubilities because at moderate to high solute concentrations Henry's constant becomes dependent on solute concentration. Aqueous-phase mole fractions for air and oil components are computed according to Equation (4.4.5). The solubility of a component in water is typically a complex function of temperature which may decrease or increase with temperature. Generally, the solubility of oils increase with increasing temperature; whereas the solubility of noncondensible gases (e.g., air) decrease with increasing temperature. With adequate experimental data the functional dependence of aqueous solubility on temperature may be included, with the general form for temperature dependence shown in Equation (4.4.6). In the absence of adequate experimental solubility data, Henry's constant for a slightly soluble oil can be estimated from a single measurement of aqueous solubility and saturated vapor pressure [Reid et al 1987], according to

Equation (4.4.7). Aqueous-phase mole fractions sum to one; therefore, the water mole fraction is computed according to Equation (4.4.8).

$$\chi_\ell^j = \frac{P_g^j}{H_{g\ell}^j}, \quad for \;\; j = a, o \tag{4.4.5}$$

$$H_{g\ell}^o = \frac{P_g^o}{\chi_\ell^o} \tag{4.4.6}$$

$$\chi_\ell^o = a + b\,T + c\,T^2 + d\,T^3 \tag{4.4.7}$$

$$\chi_\ell^w = 1 - \sum_{j=a,o} \chi_\ell^j \tag{4.4.8}$$

4.4.3 NAPL-Phase Component Fractions

The solubilities of air and water in the NAPL phase are assumed to be very small and are neglected in the STOMP simulator. Compositional NAPL contains mixtures of liquid-oil components. For compositional NAPL the component partial pressures are the primary unknowns for all but one oil mass conservation equation. Conversion between component partial pressure and component mole fraction in the NAPL phase is computed assuming equilibrium conditions using Raoult's law, as shown in Equation (4.4.9). The remaining uncomputed component mole fraction in the NAPL phase is determined from the requirement that the sum of the mole fractions equals one, as shown in Equation (4.4.10).

$$P_g^o = \chi_n^o \; P_{sat}^o \tag{4.4.9}$$

$$\sum_j^o \chi_n^j = 1 \tag{4.4.10}$$

4.4.4 Salt Solubility

Saturated solubilities in aqueous solutions for solutes that ionize either completely (e.g., strong salts like sodium chloride) or partially (e.g., sulfur dioxide and acetic acid) are computed as a function of temperature from empirical fits [Reid et al. 1987] of experimental data, according to

Equation (4.4.11). Saturated solubility for salt (sodium chloride) in water as a function of temperature is shown in Figure 4.6 against experimental data [Linke 1965].

$$\ln\left(\omega_{\ell}^{S}\right) = a + \frac{b}{T_r} + c\ln\left(T_r\right) + d\ T_r \qquad (4.4.11)$$

where,

$$T_r = \frac{T}{100\ K}$$

4.5 Viscosity

Gas-phase viscosity is dependent on composition, temperature, and pressure. The STOMP simulator computes gas-phase viscosity with an extension of the Chapman-Enskog theory for multicomponent gas mixtures at low densities [Reid et al. 1987]. Aqueous-phase viscosity is assumed independent of composition, and is determined for pure water as a function of temperature and pressure from the steam table formulations [ASME 1967]. Liquid oil viscosity is determined from the Lewis-Squires chart formulation [Reid et al. 1987]. Compositional NAPL contains mixtures of liquid-oil components. For compositional NAPL the liquid viscosity is computed using the Grunberg and Nissan method for liquid mixtures [Reid et al. 1987].

4.5.1 Gas-Phase Viscosity

Gas-phase viscosity depends on composition and temperature according to an extension of the Chapman-Enskog theory, which was proposed by Wilke for multicomponent gas mixtures at low densities [Bird et al. 1960]. This semi-empirical expression combines component vapor viscosities, gas-phase mole fractions, and component molecular weights into a gas mixture viscosity. Component vapor viscosities are computed separately as a function of temperature and pressure. Air component viscosity is determined as a function of temperature from empirical correlations [ASHRAE 1977], according to Equation (4.5.1). Water vapor viscosity is computed from the steam table formulations [ASME 1967], according to Equation (4.5.2). Oil vapor viscosity is determined as a function of temperature and pressure from the Corresponding States method [Reid et al. 1987], according to Equation (4.5.3). Component vapor viscosities, expressed in Equations (4.5.1) through (4.5.3) for air, water, and carbon tetrachloride, respectively, are shown graphically in Figure 4.7. The computed component vapor viscosities are subsequently combined, according to the modified Chapman-Enskog theory, to determine the gas-phase viscosity, as shown in Equation (4.5.4).

$$\mu_g^a = 2.6693x10^{-6} \frac{\left(M^a \; T\right)^{1/2}}{13.0827 \left(1.188 - \frac{0.051 \; T}{97.0}\right)} \tag{4.5.1}$$

$$\mu_g^w = \left[0.407 \; T - 30.772 - \rho_g^w \left(3.4696\,x10^{-3} - 5.9\,x10^{-6} \; T\right)\right] \; x \; 10^{-7} \tag{4.5.2}$$

$$\mu_g^o = \frac{F_P^o}{\xi^o} \left[0.807 \left(T_r^o\right)^{0.618} - 0.357 \exp\left(-0.449 \; T_r^o\right)\right.$$

$$\left. + \; 0.340 \exp\left(-4.058 \; T_r^o\right) + \; 0.018\right] \; x \; 10^{-7} \tag{4.5.3}$$

where,

$$\xi^o = 0.176 \left[\frac{T_c^o}{\left(M^o\right)^3 \left(\frac{P_c^o}{10^5}\right)^4}\right]^{1/6}$$

$$F_p^o = 1 \quad if \;\; 0 \le \eta_r^o < 0.022$$

$$F_p^o = 1 + 30.55 \left(0.292 - Z_c^o\right)^{1.72} \quad if \;\; 0.022 \le \eta_r^o < 0.075$$

$$F_p^o = 1 + 30.55 \left(0.292 - Z_c^o\right)^{1.72} \left|0.96 + 0.1 \left(T_r^o - 0.7\right)\right| \quad if \;\; 0.075 \le \eta_r^o$$

$$\eta_r^o = 52.46 \frac{\left(\eta^o\right)^2 \left(P_c^o / 10^5\right)}{\left(T_c^o\right)^2}$$

$$T_r^o = \frac{T}{T_c^o}$$

$$\mu_g = \sum_{j=w,a,o} \frac{\chi_g^j \mu_g^j}{\sum_{k=w,a,o} \chi_g^k \Phi_g^{jk}} \tag{4.5.4}$$

where,

$$\Phi_g^{jk} = \frac{1}{\sqrt{8}} \left(1 + \frac{M^j}{M^k}\right)^{-1/2} \left[1 + \left(\frac{\mu_g^j}{\mu_g^k}\right)^{1/2} \left(\frac{M^k}{M^j}\right)^{1/4}\right]^2$$

4.5.2 Aqueous-Phase Viscosity

Aqueous phase viscosity is computed using the low solubility assumption as a function of temperature from an empirical expression for liquid water viscosity [Yaws et al. 1976], according to Equation (4.5.5). Aqueous-phase viscosity as expressed in Equation (4.5.5) is shown graphically in Figure 4.8.

$$\mu_\ell = \exp\left[-24.71 + \frac{4209.0}{T} + 0.04527\ T - 3.376x10^{-5}\ T^2\right] x\ 10^{-3} \tag{4.5.5}$$

4.5.3 NAPL-Phase Viscosity

Liquid oil viscosity is computed from empirical functions depending on the available data. If an experimentally determined value for liquid viscosity is known, then the variation with temperature is determined according to the Lewis-Squire chart formulation [Reid et al. 1987], shown in Equation (4.5.6). Errors associated with computing the liquid oil viscosity from Equation (4.5.6) can approach 15%. Constants have also been published [Reid et al. 1987], that allow the estimation of liquid oil viscosity according to the forms shown in Equations (4.5.7) through (4.5.9), where the empirical constants are determined experimentally. Few estimation techniques exist for determining NAPL-phase viscosity for a mixture of oils. Those available are limited to values of reduced temperature below 0.7. Moreover, at these temperatures NAPL-phase viscosity is sensitive to the structure of the constituent molecules, which requires estimation techniques for computing interaction parameters. The STOMP simulator uses the Grunberg and Nissan method [Reid et al. 1987] to determine NAPL-phase viscosity for a mixture of liquid oils, shown in Equation (4.5.10). NAPL-phase viscosity, expressed in Equation (4.5.9), for saturated liquid carbon tetrachloride is shown graphically in Figure 4.9.

$$\mu_n^o = \left[\left(\bar{\mu}_n^o\right)^{-0.2661} + \frac{\left(T - \bar{T}_n^o\right)}{233.0}\right]^{-3.758} x\,10^{-7} \tag{4.5.6}$$

$$\mu_n^o = \left(a\,T^b\right) x\,10^{-7} \tag{4.5.7}$$

$$\mu_n^o = \exp\left[a + \frac{b}{T}\right] x\,10^{-7} \tag{4.5.8}$$

$$\mu_n^o = \exp\left[a + \frac{b}{T} + c\,T + d\,T^2\right] x\,10^{-7} \tag{4.5.9}$$

$$\mu_n = \exp\left[\sum_j^o \left(\chi_n^j \ln\left(\mu_n^j\right)\right) + \frac{1}{2}\sum_j^o \sum_k^o \left(\left(1 - \delta_j^k\right)\chi_n^j\,\chi_n^k\,G^{jk}\right)\right] \tag{4.5.10}$$

4.5.4 Brine Viscosity

Liquid viscosity of an aqueous solution of sodium chloride is strongly dependent on the salt mass fraction and is computed as a function of salt mass fraction from an empirical relation [Leijnse 1992] according to Equation (4.5.11), where the aqueous phase viscosity is computed as a function of temperature according to Equation (4.5.5).

$$\mu_\ell^S = \mu_\ell \left[1.0 + 1.85\,\omega_\ell^S + 4.1\left(\omega_\ell^S\right)^2 + 44.5\left(\omega_\ell^S\right)^3\right] \tag{4.5.11}$$

4.6 Enthalpy and Internal Energy

Gas-phase enthalpy and internal energy are computed by combining component vapor quantities according to mass fraction weighing. The low solubility assumption for dissolved air and oils allows the aqueous-phase enthalpy and internal energy to be approximated with quantities for liquid water. Compositional NAPL contains a mixture of liquid-oil components. NAPL-phase enthalpy and internal energy are computed from liquid oil quantities and mass fractions in the NAPL phase. Reference states vary among the components, but not between phases for a particular component. For water, the internal energy of liquid water at saturated conditions and 0.01 C is assigned the reference value of 0 J/kg. For air, the internal energy at 0 C

is assigned the reference value of 0 J/kg. For oil components, the internal energy of liquid oil at saturated conditions and 0 C is assigned the reference value of 0 J/kg.

4.6.1 Gas-Phase Enthalpy and Internal Energy

Gas-phase enthalpy and internal energy are computed from component vapor quantities and gas-phase mass fractions [Falta et al. 1990a], according to Equations (4.6.1) and (4.6.2). Water vapor enthalpy is computed from the steam table formulations as a function of temperature and pressure, according to Equation (4.6.3). Numerical values of the water vapor constants are listed in Tables A.6 through A.8 of Appendix A. Water vapor internal energy is computed from its enthalpy using the thermodynamic relationship [Van Wylen and Sonntag 1978] shown in Equation (4.6.4). Water vapor enthalpy and internal energy as a function of temperature for saturated conditions according to Equations (4.6.3) and (4.6.4) are shown graphically in Figure 4.10. In the STOMP simulator, air is considered a noncondensible gas, therefore its enthalpy is computed as a function of temperature and pressure from the thermodynamic property relationship [Van Wylen and Sonntag 1978] shown in Equation (4.6.5). By neglecting the variation in the constant-volume specific heat with temperature and assigning the reference point for air as the internal energy at 0 C, the air internal energy is computed according to Equation (4.6.6).

$$h_g = \sum_{j=w,a,o} \omega_g^j \, h_g^j \tag{4.6.1}$$

$$u_g = \sum_{j=w,a,o} \omega_g^j \, u_g^j \tag{4.6.2}$$

$$h_g^w = P_c^w \, v_c^w \left[B_0 \, T_r^w - \sum_{i=1}^{5} B_{0i} \, (i-2) \left(T_r^w \right)^{i-1} \right. \tag{4.6.3}$$

$$\left. - \sum_{j=1}^{5} \left(P_r^w \right)^j \sum_{i=1}^{n(j)} B_{ji} \left(1 + z(j,i) \, b_0 \, T_r^w \right) X^{z(j,i)} \right.$$

$$-\sum_{j=6}^{8}\left(\frac{\left(\sum_{u=1}^{n(j)} B_{ji}\ X^{z(j,i)}\right)\left(1+z(j,i)\ b_0\ T_r^w\right)-\dfrac{b_0\ T_r^w\ \sum_{k=1}^{l(j)} x(j,k)\ b_{jk}\ X^{x(j,k)}}{\left(P_r^w\right)^{2-j}+\sum_{k=1}^{l(j)} b_{jk}\ X^{x(j,k)}}}{\left(P_r^w\right)^{2-j}+\sum_{k=1}^{l(j)} b_{jk}\ X^{x(j,k)}}\right)$$

$$+\ P_r^w\left(\frac{P_r^w}{\beta_L}\right)^{10}\sum_{j=0}^{6}\left[1+T_r^w\left(\frac{10\ \beta_L'}{\beta_L}\right)+j\ b_0\right]B_{9j}\ X^j$$

where,

$$T_r^w\ =\ \frac{T}{T_c^w}$$

$$P_r^w\ =\ \frac{P}{P_c^w}$$

$$X\ =\ \exp\left[b_0\ \left(1-\ T_r^w\right)\right]$$

$$\beta_L\ =\ L_0\ +\ L_1\ T_r^w\ +\ L_2\ \left(T_r^w\right)^2$$

$$\beta_L'\ =\ L_1\ +\ 2\ L_2\ T_r^w$$

$$u_g^w\ =\ h_g^w\ -\ \frac{P_g^w}{\rho_g^w}\ =\ h_g^w\ -\ R^wT \qquad (4.6.4)$$

$$h_g^a\ =\ u_g^a\ +\ \frac{P_g^a}{\rho_g^a} \qquad (4.6.5)$$

$$u_g^a = c_v^a \; T \tag{4.6.6}$$

The reference state for both liquid and vapor oil is the internal energy of liquid oil at 0 C under saturated conditions. Oil vapor enthalpy is computed as the sum of the oil liquid enthalpy and the latent heat of vaporization as shown in Equation (4.6.7). The change in vapor enthalpy between saturated conditions and superheated conditions for an ideal gas equals zero; therefore, the oil vapor enthalpy is only a function of temperature. Liquid oil enthalpy is computed as a function of temperature [Van Wylen and Sonntag 1978] according to Equation (4.6.8), where the integral is evaluated with a two-point Gauss-Legendre quadrature method [Carnahan et al. 1969]. The liquid-specific heat is computed as a function of temperature from the ideal specific heat according to the Rowlinson-Bondi method [Reid et al. 1987], as shown in Equation (4.6.9). Coefficients for the ideal liquid-specific heat are empirically determined constants, developed from the method of Joback and published for numerous organic and inorganic compounds by Reid et al. [1987]. The heat of vaporization for oils is computed in two stages. During the first stage, the heat of vaporization for the normal boiling point is computed following the method of Chen [Reid et al. 1987], according to Equation (4.6.10). In the second stage, the heat of vaporization for temperatures, other than the normal boiling point, is computed following a correction method developed by Watson [Reid et al. 1987], according to Equation (4.6.11). Oil vapor internal energy is computed from its enthalpy using the thermodynamic relationship [Van Wylen and Sonntag 1978] shown in Equation (4.6.12). Vapor enthalpy and internal energy for carbon tetrachloride as a function of temperature for saturated conditions, are presented Equations (4.6.7) and (4.6.12) and shown graphically in Figure 4.11.

$$h_g^o = h_n^o + h_{vap}^o \tag{4.6.7}$$

$$h_n^o = \int_{\bar{T}}^{T} c_{p_n}^o \; d\zeta \tag{4.6.8}$$

where,

$$h_n^o \quad \frac{\left(T-\bar{T}\right)}{2}\left[c_{p_n}^o\left|_{\left(-0.57735\left(T-\bar{T}\right)+T+\bar{T}\right)/2} + c_{p_n}^o\right|_{\left(0.57735\left(T-\bar{T}\right)+T+\bar{T}\right)/2}\right]$$

$$c_{p_n}^o = \frac{1}{M^o}\left[\bar{c}_{p_n}^o + R\left(1.45 + 0.45\left(1-T_r^o\right)^{-1}\right.\right. \tag{4.6.9}$$

$$\left.\left. + 0.25\,\omega_P^o\left(17.11 + 25.2\left(1-T_r^o\right)^{1/3}\left(T_r^o\right)^{-1} + 1.742\left(1-T_r^o\right)^{-1}\right)\right)\right]$$

$$\bar{c}_{p_n}^o \langle J/mol\ K\rangle = a + b\,T + c\,T^2 + d\,T^3$$

$$T_r^o = \frac{T}{T_c^o}$$

$$h_{vap_b}^o = R^o\,T_b^o\,\frac{\left[3.978\left(\frac{T_b^o}{T_c^o}\right) - 3.958 + 1.555\ln\left(\frac{P_c^o}{10^5}\right)\right]}{1.07 - \left(\frac{T_b^o}{T_c^o}\right)} \tag{4.6.10}$$

$$h_{vap}^o = h_{vap_b}^o\left(\frac{1 - T/T_c^o}{1 - T_b^o/T_c^o}\right)^{3/8} \tag{4.6.11}$$

$$u_g^o = h_g^o - \frac{P_g^o}{\rho_g^o} = h_g^o - R^o T \tag{4.6.12}$$

4.6.2 Aqueous-Phase Enthalpy and Internal Energy

Aqueous-phase enthalpy and internal energy are computed using the low solubility assumption as a function of temperature from the steam table formulations [ASME 1967], according to Equation (4.6.13). The reference point for the aqueous phase and water vapor enthalpy and internal energy is the internal energy of liquid water at 0.01 C. Because water is nearly incompressible, the difference between aqueous-phase enthalpy and internal energy are neglected. Numerical values of the constants shown in Equation (4.6.13) are listed in Table A.4 of Appendix A. Aqueous-phase enthalpy is shown graphically in Figure 4.12.

$$h_\ell = P_c^w \; v_c^w \left[A_0 \; T_r - \sum_{i=1}^{10} (i-2) \; A_i \; (T_r)^{(i-1)} \right. \tag{4.6.13}$$

$$+ A_{11} \left(Z^{-17} \left[\frac{Z}{29} - \frac{Y}{12} \right] + 5 \; T_r \; \frac{Y'}{12} \right) + a_4 \; T_r \; Y \; Y' \Big) \; Z^{-5/17}$$

$$+ P_r \left(A_{12} - A_{14} \; (T_r)^2 + A_{15} \; (9 \; T_r + a_6) \; (a_6 - T_r)^9 \right)$$

$$+ P_r \left(A_{16} \left(20 \; (T_r)^{19} + a_7 \right) \left(a_7 + (T_r)^{19} \right)^{-2} \right.$$

$$- \left(12 \; (T_r)^{11} + a_8 \right) \left(a_8 + (T_r)^{11} \right)^{-2} \left(A_{17} \; P_r + A_{18} \; (P_r)^2 + A_{19} \; (P_r)^3 \right)$$

$$+ A_{20} \; (T_r)^{18} \left(17 \; a_9 + 19 \; (T_r)^2 \right) \left((a_{10} + P_r)^{-3} + a_{11} \; P_r \right)$$

$$\left. + A_{21} \; a_{12} \; (P_r)^3 + 21 \; A_{22} \; (T_r)^{-20} \; (P_r)^4 \right]$$

where,

$$Z = Y + \left(a_3 \; Y^2 - 2 \; a_4 \; T_r + 2 \; a_5 \; P_r \right)^{1/2}$$

$$Y = 1 - a_1 \; (T_r)^2 - a_2 \; (T_r)^{-6}$$

$$Y' = -2 \; a_1 \; T_r + 6 \; a_2 \; (T_r)^{-7}$$

$$T_r = \frac{T}{T_c^w}$$

$$P_r = \frac{P}{P_c^w}$$

4.6.3 NAPL-Phase Enthalpy and Internal Energy

Liquid-oil enthalpy is computed as a function of temperature [Van Wylen and Sonntag 1978] according to Equation (4.6.8), where the integral is evaluated with a two-point Gauss-Legendre quadrature method [Carnahan et al. 1969]. The liquid-specific heat is computed as a function of temperature from the ideal specific heat according to the Rowlinson-Bondi method [Reid et al. 1987], as shown in Equation (4.6.9). Coefficients for the ideal liquid-specific heat are empirically determined constants, developed from the method of Joback and published for numerous organic and inorganic compounds by Reid et al. [1987]. The reference state for both liquid and vapor oil is the internal energy of liquid oil at 0 C under saturated conditions. Saturated liquid enthalpy for carbon tetrachloride, as a function of temperature according to Equation (4.6.8), is shown graphically in Figure 4.13. NAPL-phase enthalpy for a mixture of liquid oils is computed from the mass fraction weighted sum of the oil component liquid enthalpies shown in Equation (4.6.14).

$$h_n = \sum_j^o \omega_n^j \, h_n^j \tag{4.6.14}$$

4.6.4 Ice Enthalpy and Internal Energy

Ice enthalpy is computed as a function of temperature from empirical correlation of ASHRAE [1977] data, according to Equation (4.6.15). The correlation is valid over the temperature range from -100 C to 0 C. The reference point for the ice enthalpy and internal energy is the internal energy of liquid water at 0.01 C. Because ice is nearly incompressible, the difference between ice enthalpy and internal energy is neglected.

$$h_i = u_i = -6.36443 \, x 10^5 + 1.14468 \, x \, 10^2 \, T + 3.64104 \, T^2 \tag{4.6.15}$$

4.6.5 Brine Enthalpy and Internal Energy

Liquid enthalpy for a aqueous solution of sodium chloride is computed as a function of temperature and salt concentration using empirical corrections [Pitzer et al. 1984] to the ideal solution equation for enthalpy of dilution and solution according to Equation (4.6.16). The reference states for Equation (4.6.16) are the internal energy of liquid water at 0.01 C for water and crystalline solid at 298.15 K for salt (NaCl). The standard state enthalpy for salt as a function of temperature is computed from the empirical expression shown in Equation (4.6.17) and graphically in Figure 4.14. The excess enthalpy for salt, as a function of temperature and salt

concentration is computed from the empirical expression shown in Equation (4.6.18) and graphically in Figure 4.15.

$$h_\ell^S = \frac{\left(1-\chi_\ell^S\right) M^w\, h_\ell^w + \chi_\ell^S\, M^S \left(h_\ell^{S^\circ} + h_{\ell\,ex}^S + \Delta h_\ell^{S^\circ}\right)}{\left(1-\chi_\ell^S\right) M^w + \chi_\ell^S\, M^S} \tag{4.6.16}$$

where,

$$\Delta h_\ell^{S^\circ} = 3883\ J/mol = 66.4410\ J/g$$

$$\frac{h^S M^S}{RT} = 77.734 - 0.60371\,T - 0.0015662\,T^2 - 1.3913\,x\,10^{-6}\,T^3 \tag{4.6.17}$$

where,

$$R = 8.1344\ J/mol\,K$$

$$\frac{M^S\, h_{\ell\,ex}^S}{R\,T} = a + b\,T + c\,T^2 + d\,T^3 \tag{4.6.18}$$

where,

$$a = 185.116 + 71.6835\exp\left(-15.8738\,\chi_\ell^S\right) + 18.797\exp\left(-138.055\,\chi_\ell^S\right)$$

$$b = 0.685477 - 0.492508\exp\left(-20.6543\,\chi_\ell^S\right) - 0.123717\exp\left(-210.741\,\chi_\ell^S\right)$$

$$c = -0.0016534 + 0.0011433\exp\left(-22.285\,\chi_\ell^S\right) + 0.0003252\exp\left(-213.52\,\chi_\ell^S\right)$$

$$d = 1.3951\,x\,10^{-6} - 9.356\,x\,10^{-7}\exp\left(-23.291\,\chi_\ell^S\right) - 2.9154\,x\,10^{-7}\exp\left(-215.25\,\chi_\ell^S\right)$$

4.7 Thermal Conductivity

The thermal conductivity of multiple-phase geologic-media system depends on the volumetric proportions of the fluid and solid phases, the configuration and structure of the solid particles, the interfacial contact between the fluid and solid phases, and the thermal conductivities of the phase components [Jury et al. 1991]. Generally, for geologic media, the thermal conductivity of the solid phase is an order of magnitude greater than the liquid phases and another order of magnitude greater than the gas phase. NAPL-phase thermal conductivity is generally lower than that of the aqueous phase. Data collected from two-phase geologic-media systems by Jury et al. [1991] have revealed important characteristics with respect to thermal conductivity in porous media. Thermal conductivity rises with increasing surface contact between soil particles and increasing bulk density. The presence of liquid water between soil particles greatly improves the thermal contact between particles and displaces the relatively poor, thermally conductive gas phase. Thermal conductivity changes more rapidly with liquid saturation at lower saturations, whereas the change in thermal conductivity near saturated conditions is asymptotic.

4.7.1 Effective Thermal Conductivity

The STOMP simulator offers three thermal conductivity function options for two-phase systems and a single function for three-phase systems. Two-phase systems refer to geologic media containing water and air components, whereas three-phase systems refer to geologic media with either water, oil, and air components or water, ice, and air components. In both two- and three-phase systems, thermal conduction through the gas phase is neglected, because of the relatively low thermal conductivity of gas compared with the solid and liquid phases. For geologic media, the thermal conductivity of the solid phase is frequently anisotropic; therefore the effective thermal conductivity of a multiple-phase geologic-media system is computed as anisotropic. For two-phase systems, the effective thermal conductivity function options are modified DeVries, linear, and Somerton [Somerton et al. 1973,1974]. The DeVries [1966] empirical model for the thermal conductivity uses empirical weighing factors based on the soil according to Equation (4.7.1). The modified DeVries model computes the effective thermal conductivity as the phase fraction weighted sum of the phase thermal conductivities according to Equation (4.7.2), where the DeVries weighing factors equal one. The linear model computes the effective thermal conductivity as the aqueous-saturation scaled average between the unsaturated and saturated effective thermal conductivities, according to Equation (4.7.3). The Somerton mode computes the effective thermal conductivity as the square root of the aqueous-saturation scaled average between the unsaturated and saturated effective thermal conductivities, according to

Equation (4.7.4). For three-phase systems, the effective thermal conductivity is computed from a parallel model, according to Equation (4.7.5) for water, oil, and air systems and Equation (4.7.6) for water, ice, and air systems.

$$\mathbf{k}_e = \frac{\sum_{\gamma=1}^{n} \alpha_\gamma \, s_\gamma \, \mathbf{k}_\gamma}{\sum_{\gamma=1}^{n} \alpha_\gamma \, s_\gamma} \tag{4.7.1}$$

$$\mathbf{k}_e = \mathbf{k}_s \left(1 - n_T\right) + k_\ell \left[n_T - n_D \left(1 - s_\ell\right)\right] \tag{4.7.2}$$

$$\mathbf{k}_e = \mathbf{k}_{e_{un}} + s_\ell \left(\mathbf{k}_{e_{sat}} - \mathbf{k}_{e_{un}}\right) \tag{4.7.3}$$

$$\mathbf{k}_e = \mathbf{k}_{e_{un}} + \sqrt{s_\ell} \left(\mathbf{k}_{e_{sat}} - \mathbf{k}_{e_{un}}\right) \tag{4.7.4}$$

$$\mathbf{k}_e = \mathbf{k}_s \left(1 - n_T\right) + k_\ell \left[n_T - n_D \left(1 - s_\ell\right)\right] + k_n \, s_n \tag{4.7.5}$$

$$\mathbf{k}_e = \mathbf{k}_s \left(1 - n_T\right) + k_\ell \left[n_T - n_D \left(1 - s_\ell\right)\right] + k_i \, s_i \tag{4.7.6}$$

4.7.2 Liquid Thermal Conductivity

The thermal conductivity of liquid water is computed as a function of temperature and pressure from the steam table formulations [ASME 1967], according to Equation (4.7.6). Numerical values of the constants shown in Equation (4.7.6) are listed in Table A.9 of Appendix A. Liquid-oil thermal conductivity is computed as a function of temperature according to the method of Sato and Riedel [Reid et al. 1987] as shown in Equation (4.7.7). The thermal conductivities function for saturated liquid water and saturated liquid carbon tetrachloride are shown graphically in Figure 4.16. Thermal conductivities of liquid mixtures are typically less than those predicted by either mole or mass fraction averages, although the deviations are often small. NAPL-phase thermal conductivity for a mixture of liquid oils is computed according to the method of Li [Reid et al. 1987], as shown in Equation (4.7.8).

$$k_\ell = \frac{\sum_{i=0}^{4} c_{1i} \left(\frac{T}{\overline{T}}\right)^i + \left(\frac{P - P_{sat}^w}{10^5}\right) \sum_{i=0}^{3} c_{2i} \left(\frac{T}{\overline{T}}\right)^i + \left(\frac{P - P_{sat}^w}{10^5}\right)^2 \sum_{i=0}^{3} c_{3i} \left(\frac{T}{\overline{T}}\right)^i}{10^3} \tag{4.7.6}$$

$$k_n^o = \frac{\frac{1.11}{\sqrt{M^o}} \left[3 + 20 \left(1 - \frac{T}{T_c^o} \right)^{2/3} \right]}{\left[3 + 20 \left(1 - \frac{T_b^o}{T_c^o} \right)^{2/3} \right]} \tag{4.7.7}$$

$$k_n = \sum_j^o \sum_k^o \phi^j \phi^k k^{jk} \tag{4.7.8}$$

where,

$$k^{jk} = 2 \left(\frac{1}{k_n^j} + \frac{1}{k_n^k} \right)^{-1}$$

$$\phi^i = \frac{\chi_n^i \upsilon_n^i}{\sum_j^o \chi_n^j \upsilon_n^j}$$

4.7.3 Ice Thermal Conductivity

Ice thermal conductivity is computed as a function of temperature from empirical correlation of data from Dickerson et al. [1969], according to Equation (4.7.9). The correlation is valid over the temperature range from -100 C to 0 C.

$$k_i = 7.39519 - 2.86936 \, x \, 10^{-2} \, T + 3.54452 \, x \, 10^{-5} \, T^2 \tag{4.7.9}$$

4.7.4 Brine Thermal Conductivity

Thermal conductivity for aqueous solutions of sodium chloride are computed as a function of temperature, pressure, and salt concentration using an empirical correlation [Washburn et al. 1929], according to Equation (4.7.10).

$$k_\ell^S = k_\ell \left(1 - 0.248 \, \omega_\ell^S \right) \tag{4.7.10}$$

4.8 Diffusion Coefficients

Diffusion in geologic media refers to the net transport of material within a single phase in the absence of advective mixing. The diffusion described in this section refers to that which results from concentration gradients within a single phase. Diffusion coefficients represent the proportionality between the flux of a diffusing component and its gradient within a single phase. With the low solubility assumption for the aqueous phase, diffusion of air and oils through the aqueous phase is computed with binary liquid diffusion coefficients for dilute solutes. The gas phase contains variable proportions of air, water vapor, and oil vapors. Diffusion through the gas phase is computed from multicomponent diffusion coefficients which are component concentration dependent. Multicomponent diffusion coefficients for the gas phase are computed by combining the gas-phase binary diffusion coefficient at infinite dilution through a method proposed by Wilke [Reid et al. 1987]. Water and air are assumed insoluble in the NAPL phase; therefore, dissolved water and air diffusion through the NAPL phase is neglected. Diffusion of oil components through NAPL-phase mixtures of liquid oils is computed from multicomponent liquid mixture diffusion coefficients, which are dependent on the NAPL-phase composition. Multicomponent liquid mixture diffusion coefficients are computed from binary diffusion coefficients at infinite dilution with a modification of the Wilke and Chang method [Reid et al. 1987].

4.8.1 Gas-Phase Diffusion Coefficient

Gas-phase diffusion coefficients are computed from dilute binary diffusion coefficients and gas-phase mole fractions, according to the method by Wilke [Reid et al. 1987] and as shown in Equations (4.8.1) and (4.8.2), for water vapor and oil-component vapor, respectively. Air diffusion through the gas phase is computed from the mass conservation requirement that the net diffusive flux sum to zero, as shown in Equation (4.8.3). Gas-phase binary diffusion coefficients are computed as a function of temperature and pressure from reference values [Vargaftik 1975] or using the empirical method of Wilke and Lee [Reid et al. 1987]. The reference method of Vargaftik is shown in Equation (4.8.4), where association factors for air-water and air-oil of 1.8 and 1.6, respectively, are recommended. In the absence of reference diffusion coefficients, gas-phase binary diffusion coefficients are estimated using the method of Wilke and Lee [Reid et al. 1987], as shown in Equation (4.8.5). The gas-phase binary diffusion coefficient as a function of temperature for water and carbon tetrachloride vapor, is shown graphically in Figure 4.17 for 1 atm pressure.

$$D_g^w = \frac{1 - \chi_g^w}{\frac{\chi_g^a}{D_g^{aw}} + \sum_j^o \frac{\chi_g^j}{D_g^{jw}}} \tag{4.8.1}$$

$$D_g^o = \frac{1 - \chi_g^o}{\frac{\chi_g^a}{D_g^{ao}} + \frac{\chi_g^w}{D_g^{wo}} + \sum_j^o \left(1 - \delta_j^o\right) \frac{\chi_g^j}{D_g^{jo}}} \tag{4.8.2}$$

$$\sum_{j\,=\,w,a,o} \left(\tau_g \, n_D \, \rho_g \, s_g \, \frac{M^j}{M_g} \, D_g^j \quad \chi_g^j \right) = 0 \tag{4.8.3}$$

$$D_g^{jk} = \overline{D}_g^{jk} \left(\frac{\overline{P}}{P} \right) \left(\frac{T}{\overline{T}} \right)^{\phi^{jk}} \tag{4.8.4}$$

$$D_g^{jk} = \frac{\left[3.03 - \left(\frac{0.98}{\sqrt{M^{jk}}} \right) \right] \left(10^{-2}\right) \, T^{3/2}}{P \, \sqrt{M^{jk}} \, \left(\sigma^{jk}\right)^2 \, \Omega_D} \tag{4.8.5}$$

where,

$$M^{jk} = 2 \left(\frac{1}{M^j} + \frac{1}{M^k} \right)^{-1}$$

$$\sigma^{jk} = \frac{1.18 \left[0.285 \left(\frac{v_c^j}{10^3} \right)^{1.048} \right]^{1/3} + 1.18 \left[0.285 \left(\frac{v_c^k}{10^3} \right)^{1.048} \right]^{1/3}}{2}$$

$$\Omega_D = \frac{1.06036}{\left(T^{jk}\right)^{0.15610}} + \frac{0.193}{\exp\left(0.47635 \, T^{jk}\right)} + \frac{1.03587}{\exp\left(1.52996 \, T^{jk}\right)} + \frac{1.76474}{\exp\left(3.89411 \, T^{jk}\right)}$$

$$T^{jk} = \frac{T}{\sqrt{\left(1.15 \; T_b^j\right) \left(1.15 \; T_b^k\right)}}$$

4.8.2 Aqueous-Phase Diffusion Coefficient

With the low solubility assumption for air and oil dissolution in the aqueous phase, diffusion coefficients for diffusive transport through the aqueous phase are computed from binary liquid diffusion coefficients at infinite dilution. This assumption implies that each molecule of dissolved air or oil diffuses through an aqueous environment of essentially pure water. Typically engineering practices apply diffusion coefficients at infinite dilution for solute concentrations up to 10 % molar concentration. Aqueous-phase diffusion coefficients are computed from the method of Wilke and Chang [Reid et al. 1987], according to Equation (4.8.6). Water diffusion through the aqueous phase is computed from the mass conservation requirement that the net diffusive flux sum is zero, as shown in Equation (4.8.7).

$$D_\ell^j = \frac{7.4\ x\ 10^{-15}\left(2.6\ M_\ell\right)^{1/2}\ T}{\mu_\ell \left(0.285\left(\frac{v_c^j}{10^3}\right)^{1.048}\right)^{0.6}}, \quad for \quad j = a,o \tag{4.8.6}$$

$$\sum_{j\,=\,w,a,o} \left(\tau_\ell\ n_D\ \rho_\ell\ s_\ell\ \frac{M^j}{M_\ell}\ D_\ell^j\right) \chi_\ell^j = 0 \tag{4.8.7}$$

4.8.3 NAPL-Phase Diffusion Coefficient

In the STOMP simulator, air and water are considered insoluble in NAPL phase. Component diffusion occurs in the NAPL phase for mixtures of liquid oils. In a binary NAPL phase, mixture a single diffusion coefficient is sufficient to express the proportionality between diffusive component flux and the molar concentration gradient. In a compositional NAPL phase, the flux of a single oil component is dependent on the molar concentration gradients of 1 minus the number of oil components in the liquid mixture. For example, the flux of a component in a ternary system depends on the molar concentration gradients of two components. In multicomponent liquid systems, main coefficients relate the diffusion rate of a component to its gradient, whereas cross coefficients relate the diffusion rate of a component to the gradient in another component. When dealing with multicomponent systems with more than two components, there are no convenient and simple estimation methods for estimating these main and cross coefficients [Reid et al. 1987]. For binary NAPL phases, diffusion coefficients are computed from the method of Vignes [Reid et al. 1987], according to Equation (4.8.8). The thermodynamic correction factor, shown in Equation (4.8.8), corrects the expression for diffusive flux. The diffusion coefficient indicates that the flux of a diffusing component is proportional to the concentration gradient. Diffusion, however, should be expressed by the gradient in chemical

potential. The thermodynamic correction factor makes this adjustment. For gases, this correction factor is typically close to unity and neglected; however, for liquid mixtures it is generally applied.

$$D_n^{jk} = \frac{\left[{}^{o}D_n^{jk}\ \mu_n^{k} \right)^{\chi_n^{k}} + \left({}^{o}D_n^{kj}\ \mu_n^{j} \right)^{\chi_n^{j}} \right] \alpha_q}{\mu_n} \tag{4.8.8}$$

where,

$$\alpha_q = \left. \frac{\partial\ \ln\left(a_n^{j}\right)}{\partial\ \ln\left(\chi_n^{j}\right)} \right|_{T,P} = \left. \frac{\partial\ \ln\left(a_n^{k}\right)}{\partial\ \ln\left(\chi_n^{k}\right)} \right|_{T,P}$$

$${}^{o}D_n^{jk} = \frac{7.4\ x10^{-15}\ \left(2.6\ M^{k}\right)^{1/2}\ T}{\mu_n^{k}\ \left(0.285\ \left(\frac{\upsilon_c^{j}}{10^{3}}\right)^{1.048}\right)^{0.6}}$$

4.9 Porosity and Tortuosity

The STOMP simulator makes uses of three porosity types: effective, diffusive, and total. Effective porosity refers to interconnected pore spaces associated with gross fluid flow. Diffusive porosity refers to all interconnected pore spaces. Total porosity refers to both isolated and connected pore spaces. Isolated pore spaces are assumed to be filled with liquid water. All saturations are defined with respect to the diffusive porosity. The liquid contained within the pore space, represented by the difference between the diffusive and effective porosities, equals the residual moisture content. This residual moisture content is a function of capillary pressure and consequentially not strictly an immobile fluid. Changes in porosity occur through changes in system pressure [Leijnse 1992], according to Equations (4.9.1) and (4.9.2), where the porous media compressibility is computed from the coefficient of specific storage.

$$n_D = 1 - \left(1 - \bar{n}_D\right) \exp\left(-\alpha_P \left(P - \bar{P}\right)\right) \tag{4.9.1}$$

$$n_T = 1 - \left(1 - \bar{n}_T\right) \exp\left(-\alpha_P \left(P - \bar{P}\right)\right) \tag{4.9.2}$$

where,

$$\alpha_P = \frac{S_s}{\bar{\rho}_\ell \, g} - \bar{n}_D \, \beta_P$$

Diffusive flux in porous media is computed from a modified expression for Fickian diffusion using phase tortuosities [Jury et al. 1991]. In the STOMP simulator, tortuosities are computed from the methods of Millington and Quirk [1959], which were based on theoretical pore-size distribution models for partially saturated and fully saturated two-phase systems. These expressions, extended for three-phase systems are shown in Equation (4.9.3).

$$\tau_\gamma = \left(n_D\right)^{1/3} \left(s_\gamma\right)^{7/3}, \quad for \ \gamma = \ell, g, n \tag{4.9.3}$$

4.10 Saturation

Saturations are computed from scaled pressure differences between phases. These functions are collectively referred to as the soil moisture retention functions or soil moisture characteristics. Numerous empirical functions have been published that relate saturation with various capillary pressures. The soil moisture retention functions, available with the STOMP simulator, depend on the operational mode and, in particular, the system of phases. Saturation functions can be classified as hysteretic or nonhysteretic. In hysteretic functions, effects of saturation history, saturation direction (e.g., wetting or draining), and/or nonwetting fluid entrapment are considered. In nonhysteretic functions, these phenomena are neglected. In general, the hysteretic functions are numerically complex, requiring additional execution time and memory compared with their nonhysteretic counterparts. The following sections describe available nonhysteretic and simplified (fluid-entrapment only) hysteretic saturation functions according to the system of phases. In all phase systems, the summation of phase saturations equal one. Aqueous-NAPL-gas systems are assumed to have a decreasing wettability order from aqueous to NAPL to gas. In aqueous-ice-gas systems, ice is assumed to be completely entrapped by the aqueous phase with no gas-ice interfaces.

4.10.1 Aqueous-Gas Systems

The following sections describe nonhysteretic and hysteretic soil moisture retention functions for aqueous-gas systems. Beyond the listed functions, the STOMP simulator also allows the description of the saturation function for aqueous-gas systems through tabular data. Unless specifically stated, the described functions refer to nonhysteretic systems. For aqueous-gas systems, actual aqueous saturations are computed in terms of effective aqueous saturations, according to Equation (4.10.1), where the effective minimum aqueous saturation is computed as a function of aqueous-gas capillary pressure, as shown in Equation (4.10.2), according to Fayer and Simmons [1995].

$$s_\ell = \bar{s}_\ell \left(1 - \bar{s}_m\right) + \bar{s}_m \tag{4.10.1}$$

$$\bar{s}_m = \left[1 - \frac{\ln\left(\frac{P_g - P_\ell}{\bar{\rho}_\ell \, g}\right)}{\ln\left(h_{od}\right)}\right] s_m \tag{4.10.2}$$

4.10.1.1 Van Genuchten Function

The van Genuchten function [van Genuchten 1980] relates the gas-aqueous capillary pressure to the effective aqueous saturation through two correlation parameters, according to Equation (4.10.3). The n and m correlation parameters for the van Genuchten function can be related depending on the chosen function for relative permeability. Typically, these parameters are related, as shown in Equation (4.10.3). An example of the van Genuchten function is shown graphically in Figure 4.18.

$$\bar{s}_\ell = \left[1 + \left(\alpha \left|\frac{P_g - P_\ell}{\bar{\rho}_\ell \, g}\right|\right)^n\right]^{-m} \quad for \left[P_g - P_\ell\right] > 0 \tag{4.10.3}$$

$$\bar{s}_\ell = 1 \quad for \left[P_g - P_\ell\right] \leq 0$$

where,

$$m = 1 - \frac{1}{n}$$

4.10.1.2 Brooks and Corey Function

The Brooks and Corey function [Brooks and Corey 1966] for aqueous-gas systems relates the gas-aqueous capillary pressure to the effective aqueous saturation with two correlation parameters, according to Equation (4.10.4). The first parameter, ψ , is referred to as the entry head and equals the minimum drainage capillary head for which a continuous nonwetting phase (e.g., gas phase) exits. The second parameter, λ , is related to the pore-size distribution within the porous media. An example of the Brooks and Corey function for aqueous-gas systems is shown graphically in Figure 4.19.

$$\bar{s}_\ell = \left[\frac{P_g - P_\ell}{\bar{\rho}_\ell \, g \, \psi} \right]^{-\lambda} \quad for \left(P_g - P_\ell \right) \geq \psi \tag{4.10.4}$$

$$\bar{s}_\ell = 1 \quad for \left(P_g - P_\ell \right) < \psi$$

4.10.1.3 Dual Porosity Functions

Dual porosity functions or equivalent continuum models for aqueous-gas systems relate the gas-aqueous capillary pressure to the bulk aqueous saturation for fractured geologic media through two functions [Klavetter and Peters 1986; Nitao 1988]. One function relates the gas-aqueous capillary pressure to the matrix aqueous saturation and the other relates the gas-aqueous capillary pressure to the fracture aqueous saturation. The pivotal assumption associated with the dual porosity function is that the fracture and matrix pressures are in equilibrium. This assumption neglects transient fracture-matrix interactions. Fracture and matrix effective saturations can be computed with either van Genuchten or Brooks and Corey functions (Sections 4.10.1.1 and 4.10.1.2). The bulk aqueous saturation is computed by combining the fracture and matrix aqueous saturations and diffusive porosities, as shown in Equation (4.10.5), where the actual saturations are computed from effective saturations, according to Equations (4.10.6) and (4.10.7). An example of a dual porosity function, using the van Genuchten and Brooks and Corey saturation functions for aqueous-gas systems, is shown graphically in Figures 4.20 and 4.21, respectively.

$$s_\ell = \frac{s_{\ell f} \, n_{Df} + s_{\ell m} \left(1 - n_{Df} \right) n_{Dm}}{n_{Df} + \left(1 - n_{Df} \right) n_{Dm}} \tag{4.10.5}$$

$$s_{\ell_f} = \bar{s}_{\ell_f}\left(1 - s_{m_f}\right) + s_{m_f} \tag{4.10.6}$$

$$s_{\ell_m} = \bar{s}_{\ell_m}\left(1 - s_{m_m}\right) + s_{m_m} \tag{4.10.7}$$

4.10.1.4 Capillary Pressure-Saturation Functions for Systems with Gas Entrapment

A theoretical model for hysteretic saturation functions for aqueous-gas systems was developed by Parker and Lenhard [1987]. A simplified version of this model, analogous to Kaluarachchi and Parker [1992], has been implemented in the STOMP simulator. The model includes effects of gas entrapment during aqueous-phase imbibition paths. Gas entrapment during aqueous-phase imbibition will depend on the aqueous saturation and current saturation path. The amount of entrapped gas varies linearly between zero and the gas effective residual saturation with the apparent saturation, which varies between the reversal point from main drainage to one. Gas effective residual saturations are computed using an empirical relationship developed by Land [1968] for aqueous-NAPL systems. In this simplified hysteretic model for aqueous-gas systems, gas can be trapped or free, where free gas refers to continuous volumes which advect freely and trapped gas refers to discontinuous ganglia of gas occluded within the aqueous phase. Occluded gas is assumed to be immobile. The apparent aqueous saturation equals the effective aqueous saturation plus effective trapped gas saturation, as shown in Equation (4.10.8). The effective gas saturation equals the effective trapped and free gas saturations, as shown in Equation (4.10.9). In hysteretic systems, the residual saturation is independent of capillary pressure.

$$\bar{\bar{s}}_\ell = \bar{s}_\ell + \bar{s}_{g_{t\ell}} \tag{4.10.8}$$

where,

$$\bar{s}_\ell = \frac{s_\ell - s_m}{1 - s_m}$$

$$\bar{s}_g = \bar{s}_{g_f} + \bar{s}_{g_{t\ell}} = \frac{s_g}{1 - s_m} \tag{4.10.9}$$

The saturation functions relate gas-aqueous capillary pressure to apparent aqueous saturations, according to Equations (4.10.10) and (4.10.11), for the van Genuchten and Brooks and Corey functions, respectively. The effective trapped gas saturation is computed according to Equation (4.10.12), which recognizes that entrapped gas cannot exceed the gas present. Land's

parameter for gas-aqueous interfaces is computed according to Equation (4.10.13).

$$\bar{\bar{s}}_\ell = \left[1 + \left(\alpha \left[\frac{P_g - P_\ell}{\bar{\rho}_\ell\, g}\right]\right)^n\right]^{-m} \tag{4.10.10}$$

$$\bar{\bar{s}}_\ell = \left[\frac{\left(\frac{P_g - P_\ell}{\bar{\rho}_\ell\, g}\right)}{\psi}\right]^{-\lambda}, \quad for\ \left(P_g - P_\ell\right) \geq \psi \tag{4.10.11}$$

$$\bar{\bar{s}}_\ell = 1, \quad for\ \left(P_g - P_\ell\right) < \psi$$

$$\bar{s}_g = \min\left[\frac{1 - \bar{s}_l^{\min}}{1 + L_g\left(1 - \bar{s}_l^{\min}\right)} - \frac{1 - \bar{\bar{s}}_l}{1 + L_g\left(1 - \bar{\bar{s}}_l\right)}, \bar{s}_g\right], \quad for\ \bar{\bar{s}}_\ell > \bar{s}_l^{\min} \tag{4.10.12}$$

where,

$$L_g = \frac{1}{\bar{s}_{g_r}} - 1 \tag{4.10.13}$$

4.10.2 Aqueous-Ice-Gas Systems

The following sections describe nonhysteretic soil-moisture retention functions for aqueous-ice-gas systems. For these systems, ice is assumed to be occluded by the aqueous phase, with no gas-ice interfaces. The apparent aqueous saturation represents the ratio of free aqueous saturation to the normalized free pore volume, according to Equation (4.10.14). The unfrozen aqueous fraction is defined as the ratio of liquid aqueous saturation to total aqueous saturation, according to Equation (4.10.15). The effective irreducible aqueous saturation is

defined as a function of the actual irreducible aqueous saturation and the unfrozen aqueous fraction, according to Equation (4.10.16). The effective aqueous and gas saturations, used in the relative permeability functions, are defined according to Equations (4.10.17) and (4.10.18), respectively.

$$\bar{\bar{s}}_\ell = \frac{s_\ell - \bar{s}_m}{1 - s_i - \bar{s}_m} \tag{4.10.14}$$

$$s_{uf} = \frac{s_\ell}{s_\ell + s_i} \tag{4.10.15}$$

$$\bar{s}_m = s_{uf}\, s_m \tag{4.10.16}$$

$$\bar{s}_\ell = \frac{s_\ell - \bar{s}_m}{1 - \bar{s}_m} \tag{4.10.17}$$

$$\bar{s}_g = \frac{s_g}{1 - \bar{s}_m} \tag{4.10.18}$$

Under freezing conditions, an assumption is made that thermodynamic equilibrium exists between the ice and aqueous phases in porous media. An expression of thermodynamic equilibrium between the ice and aqueous phases in porous media, which accounts for the difference between the ice pressure and the total potential of the aqueous phase, has been developed by Loch [1977], according to Equation (4.10.19). The total potential of the aqueous phase is the pressure one would measure in a soil aqueous solution with a tensiometer, if the tensiometer cup were a perfect semipermeable membrane. The total pressure is defined as the difference between the aqueous phase pressure and the osmotic pressure, as shown in Equation (4.10.20). The osmotic pressure for dilute solutes is computed according to Equation (4.10.21). Combining Equations (4.10.19) through (4.10.21) yields an expression for the ice pressure as a function of temperature, aqueous pressure, and solute concentration, as shown in Equation (4.10.22).

$$v_i\, P_i - v_\ell\, P_{tp} = -h_{wi} \ln\left(1 + \frac{\left(T - T^w_{fp}\right)}{T^w_{fp}}\right) \tag{4.10.19}$$

$$P_{tp} = P_\ell - \pi \tag{4.10.20}$$

$$\pi = C_\ell \; R \; T \tag{4.10.21}$$

$$P_i = \rho_i \left[\frac{\left(P_\ell - C_\ell \, R \, T\right)}{\rho_\ell} - h_{wi} \ln\left(1 + \frac{\left(T - T_{fp}^{w}\right)}{T_{fp}^{w}}\right) \right] \tag{4.10.22}$$

The soil moisture retention function that relates gas-aqueous capillary pressures to aqueous saturations, can be used to predict the retention function of any two-phase interface by interfacial-tension dependent scaling of the capillary pressures. Under freezing conditions, the apparent aqueous saturation is computed from the gas-aqueous capillary pressure and the fraction of unfrozen water is computed from the scaled ice-aqueous capillary pressure [Panday and Corapcioglu 1994], where the scaling factor is computed from the ratios of interfacial tensions [Lenhard 1994], according to Equation (4.10.23).

$$\beta_{i\ell} = \frac{\sigma_{g\ell}}{\sigma_{i\ell}}, \quad \beta_{g\ell} = \frac{\sigma_{g\ell}}{\sigma_{g\ell}} = 1 \tag{4.10.23}$$

4.10.2.1 Van Genuchten Functions

For freezing conditions, the van Genuchten function relates the gas-aqueous capillary pressure to the apparent aqueous saturation and the scaled ice-aqueous capillary pressure to the unfrozen aqueous-phase fraction, according to Equations (4.10.24) and (4.10.25), respectively. The correlation parameters for the van Genuchten function can be determined from gas-aqueous retention data. Ice saturation, as a function of temperature using the van Genuchten soil moisture retention function, is shown graphically in Figure 4.22, for a constant total aqueous saturation of 0.9 and unfrozen solute concentrations of 0.0, 1.0, and 2.0 mol/L. The graphs in Figure 4.22 were generated by fixing the total aqueous saturation and the unfrozen or base solute concentration. Solute concentrations in the aqueous phase increased with increasing ice saturation, because of the a lack of solute absorption within the ice phase. Solute concentrations in the aqueous phase as a function of temperature for unfrozen solute concentrations of 1.0, and 2.0 mol/L, are shown graphically in Figure 4.23.

$$\bar{\bar{s}}_\ell = \left[1 + \left(\alpha \, \beta_{g\ell} \frac{P_g - P_\ell}{\bar{\rho}_\ell \, g}\right)^{n}\right]^{-m}, \quad for \left[P_g - P_\ell\right] > 0 \tag{4.10.24}$$

$$\bar{\bar{s}}_\ell = 1, \quad for \left[P_g - P_\ell\right] \le 0$$

$$s_{uf} = \left[1 + \left(\alpha \beta_{i\ell} \left[\frac{P_i - P_\ell}{\bar{\rho}_\ell g}\right]\right)^n\right]^{-m}, \quad for \left[P_i - P_\ell\right] > 0 \tag{4.10.25}$$

$$s_{uf} = 1, \quad for \left[P_i - P_\ell\right] \le 0$$

4.10.2.2 Brooks and Corey Functions

For freezing conditions, the Brooks and Corey function relates the gas-aqueous capillary pressure to the apparent aqueous saturation and the scaled ice-aqueous capillary pressure to the unfrozen aqueous fraction, according to Equations (4.10.26) and (4.10.27), respectively. The correlation parameters for the Brooks and Corey function can be determined from gas-aqueous retention data. Ice saturation, as a function of temperature using the Brooks and Corey soil moisture retention function, is shown graphically in Figure 4.24, for an apparent aqueous saturation of 0.9 and unfrozen solute concentrations of 0.0, 1.0, and 2.0 mol/L. The graphs in Figure 4.24 were generated by fixing the apparent aqueous saturation and the unfrozen or base solute concentration. Solute concentrations in the aqueous phase increased with increasing ice saturation, because of a lack of solute absorption within the ice phase. Solute concentrations in the aqueous phase, as a function of temperature for unfrozen solute concentrations of 1.0 and 2.0 mol/L, are shown graphically in Figure 4.25.

$$\bar{\bar{s}}_l = \left[\frac{\beta_{g\ell}\left(\frac{P_g - P_\ell}{\bar{\rho}_\ell g}\right)}{\psi}\right]^{-\lambda}, \quad for \ \beta_{g\ell}\left(P_g - P_\ell\right) \ge \psi \tag{4.10.26}$$

$$\bar{\bar{s}}_l = 1, \quad for \ \beta_{g\ell}\left(P_g - P_\ell\right) < \psi$$

$$s_{uf} = \left[\frac{\beta_{i\ell}\left(\frac{P_i - P_\ell}{\bar{\rho}_\ell g}\right)}{\psi}\right]^{-\lambda}, \quad for \ \beta_{i\ell}\left(P_i - P_\ell\right) \ge \psi \tag{4.10.27}$$

$$s_{uf} = 1, \quad for \ \beta_{i\ell}\left(P_i - P_\ell\right) < \psi$$

4.10.3 Aqueous-NAPL-Gas Systems

The following sections describe nonhysteretic and hysteretic nonwetting-fluid entrapment soil-moisture retention functions for aqueous-NAPL-gas systems. The functions described herein follow the simplified theory by Kaluarachchi and Parker [1992] of the theoretical models of Parker and Lenhard [1987]. Saturations are defined as functions of water-equivalent scaled capillary heads, that are computed from differences in pressure across phase-pair interfaces. For aqueous-NAPL-gas systems, three interfacial capillary heads are defined (i.e., gas-aqueous, gas-NAPL, and NAPL-aqueous), according to Equations (4.10.28) through (4.10.30), where the wettability order decreases from aqueous to NAPL to gas. Phase scaling factors are computed from the ratio of interfacial tensions according to the theory of Lenhard [1994], as shown in Equation (4.10.31), where the gas-aqueous is chosen as the reference fluid.

$$h_{g\ell} = \frac{\left(P_g - P_\ell\right)}{\overline{\rho}_\ell \, g} \tag{4.10.28}$$

$$h_{gn} = \frac{\left(P_g - P_n\right)}{\overline{\rho}_\ell \, g} \tag{4.10.29}$$

$$h_{n\ell} = \frac{\left(P_n - P_\ell\right)}{\overline{\rho}_\ell \, g} \tag{4.10.30}$$

$$\beta_{ij} = \frac{\sigma_{ij}}{\sigma_{g\ell}} \tag{4.10.31}$$

The Parker and Lenhard [1987] theory distinguishes between actual, effective, and apparent saturations. Actual saturations are defined as the ratio of fluid volume to diffusive pore volume. Effective saturations represent normalized actual saturations based on the pore volumes above the irreducible or minimum saturation of the wetting fluid (i.e., aqueous phase liquid). Effective saturations for the aqueous-phase, NAPL, gas-phase, and total liquid, are defined according to Equations (4.10.32) through (4.10.35), respectively. Apparent saturations are defined in terms of effective saturations. Apparent saturations represent the effective saturation of the fluid plus the effective saturations of fluids of lesser wettability trapped within the fluid for the aqueous-phase, NAPL, and total liquid, according to Equations (4.10.36) through (4.10.38). Trapped fluids refer to discontinuous islands or ganglia of fluid occluded within another fluid of greater wettability. The theory of Lenhard and Parker [1987] assumes that

trapped fluids are immobile. Effective saturations can be defined in terms of trapped and free fluids, as shown in Equations (4.10.39) and (4.10.40), for the NAPL and gas phases, where free fluids refer to continuous phases that move convectively.

$$\bar{s}_\ell = \frac{s_\ell - s_m}{1 - s_m} \tag{4.10.32}$$

$$\bar{s}_n = \frac{s_n}{1 - s_m} \tag{4.10.33}$$

$$\bar{s}_g = \frac{s_g}{1 - s_m} \tag{4.10.34}$$

$$\bar{s}_t = \frac{s_\ell + s_n - s_m}{1 - s_m} \tag{4.10.35}$$

$$\bar{\bar{s}}_\ell = \bar{s}_\ell + \bar{s}_{n_t} + \bar{s}_{g_{t\ell}} \tag{4.10.36}$$

$$\bar{\bar{s}}_n = \bar{s}_n + \bar{s}_{g_{tn}} \tag{4.10.37}$$

$$\bar{\bar{s}}_t = \bar{s}_\ell + \bar{s}_n + \bar{s}_{g_{t\ell}} + \bar{s}_{g_{tn}} \tag{4.10.38}$$

$$\bar{s}_n = \bar{s}_{n_f} + \bar{s}_{n_t} \tag{4.10.39}$$

$$\bar{s}_g = \bar{s}_{g_f} + \bar{s}_{g_{t\ell}} + \bar{s}_{g_{tn}} \tag{4.10.40}$$

In the absence of hysteretic and fluid entrapment effects, fluid saturations are considered as unique functions of fluid-gas capillary heads. The Parker and Lenhard [1987] theory accommodates the effects of fluid entrapment by relating fluid-gas capillary heads to apparent saturations rather than effective saturations. The fundamental assumption related to the theory of Parker and Lenhard [1987] is that the functions relating fluid saturation to fluid-gas interfacial pressure differences can be expressed with a single soil-moisture retention function, for a given porous medium, by scaling the fluid-gas capillary heads. For aqueous-NAPL-gas systems, two functions relating fluid saturation with fluid-gas capillary head are required. The total-liquid saturation is related to the gas-NAPL capillary head, and the aqueous saturation is related to the oil-aqueous capillary head, as shown in Equations (4.10.41) and (4.10.42), respectively.

$$\bar{\bar{s}}_t = s\left(\beta_{gn}\, h_{gn}\right) \tag{4.10.41}$$

$$\bar{\bar{s}}_\ell = s\left(\beta_{n\ell}\, h_{n\ell}\right) \tag{4.10.42}$$

4.10.3.1 Van Genuchten Function

The van Genuchten function [van Genuchten 1980] relates fluid saturation to capillary head through two soil dependent correlation parameters. The n and m correlation parameters for the van Genuchten function can be related depending on the chosen function for relative permeability. Expressions for the effective total-liquid saturation as a function of scaled gas-NAPL capillary head and the effective aqueous saturation as a function of scaled oil-aqueous capillary head are shown in Equations (4.10.43) and (4.10.44), using the van Genuchten soil-moisture retention function. The van Genuchten function is shown graphically in Figure 4.17.

$$\bar{s}_t = \left[1 + \left(\alpha\, \beta_{gn}\, h_{gn}\right)^n\right]^{-m}, \quad for \;\; h_{gn} > 0 \tag{4.10.43}$$

where,

$$\bar{s}_t = 1, \quad for \;\; h_{gn} \le 0$$

$$\bar{s}_\ell = \left[1 + \left(\alpha\, \beta_{n\ell}\, h_{n\ell}\right)^n\right]^{-m}, \quad for \;\; h_{n\ell} > 0 \tag{4.10.44}$$

where,

$$\bar{s}_\ell = 1, \quad for \;\; h_{n\ell} \le 0$$

4.10.3.2 Brooks and Corey Function

The Brooks and Corey function [Brooks and Corey 1966] relates fluid saturation to capillary head through two soil dependent correlation parameters. The first parameter, ψ, is referred to as the entry head and equals the minimum drainage capillary head for which a continuous nonwetting phase (e.g., gas phase) exits. The second parameter, λ, is related to the pore-size distribution within the porous media. Expressions for the effective total-liquid saturation as a function of scaled gas-NAPL capillary head and the effective aqueous saturation as a function of scaled oil-aqueous capillary head are shown in Equations (4.10.45) and (4.10.46), using the Brooks and Corey soil-moisture retention function. The Brooks and Corey function is shown graphically in Figure 4.18.

$$\bar{s}_t = \left[\frac{\beta_{gn}\, h_{gn}}{\psi}\right]^{-\lambda}, \quad for \;\; \beta_{gn}\, h_{gn} > \psi \tag{4.10.45}$$

where,

$$\bar{s}_t = 1, \quad for \;\; \beta_{gn}\, h_{gn} \le \psi$$

$$\bar{s}_\ell = \left[\frac{\beta_{n\ell}\, h_{n\ell}}{\psi}\right]^{-\lambda}, \quad for \;\; \beta_{n\ell}\, h_{n\ell} > \psi \tag{4.10.46}$$

where,

$$\bar{s}_\ell = 1, \quad for \;\; \beta_{n\ell}\, h_{n\ell} \le \psi$$

4.10.3.3 Capillary Pressure Saturation Functions for Systems with Fluid Entrapment

Fluid entrapment effects in the functions for fluid saturation are accommodated in the theory of Parker and Lenhard [1987] from the assumption that fluid entrapment phenomena for aqueous-NAPL-gas systems can be predicted from fluid-gas systems (e.g., gas-aqueous, gas-NAPL, NAPL-aqueous). Fluids of lesser wettability are assumed to be trapped by fluids of greater wettability; therefore, gas can be entrapped by NAPL or aqueous phase and NAPL can be entrapped by the aqueous phase. For no free-NAPL conditions, the effective trapped NAPL saturation equals the effective NAPL saturation, according to Equation (4.10.47). For free-NAPL conditions, a simplified entrapment theory is used [Kaluarachchi and Parker 1992] in which the effective trapped NAPL saturation is a function of the apparent aqueous saturation, according to Equation (4.10.48). This relation recognizes that entrapped NAPL cannot exceed the NAPL present.

$$\bar{s}_{n_t} = \bar{s}_n \tag{4.10.47}$$

$$\bar{s}_{n_t} = \min\left[\frac{1-\bar{s}_l^{\min}}{1+L_n\left(1-\bar{s}_l^{\min}\right)} - \frac{1-\bar{s}_l}{1+L_n\left(1-\bar{s}_l\right)},\; \bar{s}_n\right], \quad for \;\; \bar{s}_\ell > \bar{s}_l^{\min} \tag{4.10.48}$$

where,

$$L_n = \frac{1}{i\bar{s}_{n_r}} - 1$$

Gas entrapment is complicated by the fact that both NAPL and aqueous fluids have greater wettabilities than gas and can contain entrapped gas. In the absence of free NAPL, gas entrapment is occurs by advancing gas-aqueous interface, according to the theory for aqueous-gas systems. In the presence of free NAPL, gas entrapment occurs in response to advancing gas-NAPL interfaces, corresponding to increasing apparent total liquid saturation. Release of entrapped gas follows either gas-aqueous or gas-NAPL interfaces, depending on the occurrence of free NAPL. Gas, initially trapped by one wetting fluid, transfers to the other according to the position of the oil-aqueous interface, tracked by the apparent aqueous saturation. For no free-NAPL conditions, the effective residual saturations for gas trapped by the aqueous phase are computed according to Equation (4.10.15). For free-NAPL conditions, the effective residual saturations for gas trapped by NAPL are computed according to Equation (4.10.49).

$$\bar{s}_{g_r} = \frac{\left(1 - \bar{s}_t^{\min}\right)}{1 + L_g\left(1 - \bar{s}_t^{\min}\right)} \qquad (4.10.49)$$

where,

$$L_g = \frac{1}{i\bar{s}_{g_r}} - 1$$

The distribution of entrapped gas within a aqueous-NAPL-gas system depends on the positions of the gas-NAPL and oil-aqueous interfaces, as tracked by the apparent aqueous and total liquid saturations. The distribution additionally depends on the minimum pore size into which gas-NAPL interfaces have receded since the inception of free-NAPL conditions, as tracked by the minimum value of the apparent total-liquid saturation and on the apparent aqueous saturation at the inception of free-NAPL conditions. To compute entrapped gas saturations, three conditions are distingushed

In the first case, there is no trapped or free NAPL present. Gas is only entrapped by the aqueous phase and the entrapped gas saturation is computed according to Equation (4.10.50).

$$\bar{s}_{g_{tl}} = \min\left[\left(\frac{1-\bar{s}_t^{\min}}{1+L_g\left(1-\bar{s}_t^{\min}\right)} - \frac{1-\bar{\bar{s}}_l}{1+L_g\left(1-\bar{\bar{s}}_l\right)}\right), \bar{s}_g\right] \tag{4.10.50}$$

where,

$$L_g = \frac{1}{\bar{s}_{g_r}} - 1$$

In the second case, no free NAPL is present and gas is, again, only entrapped by the aqueous phase according to Equation (4.10.51).

$$\bar{s}_{g_{tl}} = \min\left[\left(\frac{1-\bar{s}_t^{\min}}{1+L_g\left(1-\bar{s}_t^{\min}\right)} - \frac{1-\bar{\bar{s}}_l}{1+L_g\left(1-\bar{\bar{s}}_l\right)}\right), \bar{s}_g\right] \tag{4.10.51}$$

where,

$$L_g = \frac{1}{\bar{s}_{g_r}} - 1$$

The third case describes entrapment of the gas phase by both the aqueous and NAPL phases according to Equation (4.10.52) and (4.10.53) respectively.

$$\bar{s}_{g_{tl}} = \left(\frac{1-\bar{s}_t^{\min}}{1+L_g\left(1-\bar{s}_t^{\min}\right)} - \frac{1-\bar{\bar{s}}_l}{1+L_g\left(1-\bar{\bar{s}}_l\right)}\right) \tag{4.10.52}$$

$$\bar{s}_{g_{tn}} = \left(\frac{1-\bar{\bar{s}}_l}{1+L_g\left(1-\bar{\bar{s}}_l\right)} - \frac{1-\bar{\bar{s}}_t}{1+L_g\left(1-\bar{\bar{s}}_t\right)}\right) \tag{4.10.53}$$

where,

$$L_g = \frac{1}{\bar{s}_{g_r}} - 1$$

4.11 Relative Permeability

Relative permeability for fluid phases are computed for both nonhysteretic and hysteretic nonwetting-fluid entrapment systems. Three distinct fluid systems are recognized: water-air, water-ice-air, and water-oil-air. Relative permeabilities for water-air systems are computed for the aqueous- and gas-phase fluids. The functions for fluid phase relative permeability follow the simplified Kaluarachchi and Parker [1992] model which is based on the theory of Lenhard and Parker [1987]. Fluid entrapment effects are computed following the method of Land [1968]. Relative permeabilities for water-ice-air systems are computed for the aqueous- and gas-phase fluids. Only nonhysteretic systems are addressed where fluid phase relative permeabilities are unique functions of phase saturations. The relative permeability functions for water-ice-air systems follow the theory of White [1995]. Relative permeabilities for water-oil-air systems are computed for the aqueous-phase, NAPL, and gas-phase. The theory for relative permeability [Lenhard and Parker 1987] predicts mild hysteretic effects for the aqueous fluid, except at high saturations, pronounced hysteretic effects for the gas phase, negligible hysteretic effects for NAPL for low aqueous saturations, and marked hysteretic effects for NAPL with increasing aqueous saturations.

4.11.1 Aqueous-Gas Systems

For nonhysteretic systems several empirical functions are available in the STOMP simulator for computing fluid phase relative permeabilities from effective fluid saturations. For systems with gas entrapment, expressions according to a simplified theory [Kaluarachchi and Parker 1992] are used.

4.11.1.1 Burdine Relative Permeability Functions

Aqueous- and gas-phase relative permeability can be computed as a function of aqueous saturation from knowledge of the soil-moisture retention function and the pore distribution model of Burdine [1953]. If the van Genuchten and Brooks and Corey soil-moisture retention functions are used, closed-form expressions for fluid phase relative permeability can be derived. Using the van Genuchten soil-moisture retention function, the aqueous- and gas-phase relative permeabilities appear as shown in Equations (4.11.1) and (4.11.2), respectively. Using the Brooks and Corey soil-moisture retention function, the aqueous- and gas-phase relative permeabilities appear as shown in Equations (4.11.3) and (4.11.4), respectively. Examples of the Burdine relative permeability functions for water-air systems are shown graphically in Figures 4.26 and 4.27 with the van Genuchten and Brooks and Corey soil-moisture retention functions, respectively.

$$k_{r\ell} = \left(\bar{s}_\ell\right)^2 \left[1 - \left(1 - \left(\bar{s}_\ell\right)^{1/m}\right)^m\right] \tag{4.11.1}$$

$$k_{rg} = \left(\bar{s}_g\right)^2 \left(1 - \left(\bar{s}_\ell\right)^{1/m}\right)^m \tag{4.11.2}$$

$$k_{r\ell} = \left(\bar{s}_\ell\right)^{\left(3 + 2/\lambda\right)} \tag{4.11.3}$$

$$k_{rg} = \left(\bar{s}_g\right)^2 \left[1 - \left(\bar{s}_\ell\right)^{\left(1 + 2/\lambda\right)}\right] \tag{4.11.4}$$

4.11.1.2 Mualem Relative Permeability Functions

Aqueous- and gas-phase relative permeability can be computed as a function of aqueous saturation from knowledge of the soil-moisture retention function and the pore distribution model of Mualem [1976]. If the van Genuchten and Brooks and Corey soil-moisture retention functions are used, closed-form expressions for fluid phase relative permeability can be derived. Using the van Genuchten soil-moisture retention function, the aqueous- and gas-phase relative permeabilities appear as shown in Equations (4.11.5) and (4.11.6), respectively. Using the Brooks and Corey soil-moisture retention function, the aqueous- and gas-phase relative permeabilities appear as shown in Equations (4.11.7) and (4.11.8), respectively. Examples of the Mualem relative permeability functions for water-air systems are shown graphically in Figures 4.26 and 4.27 with the van Genuchten and Brooks and Corey soil-moisture retention functions, respectively.

$$k_{r\ell} = \left(\bar{s}_\ell\right)^{1/2} \left[1 - \left(1 - \left(\bar{s}_\ell\right)^{1/m}\right)^m\right]^2 \tag{4.11.5}$$

$$k_{rg} = \left(\bar{s}_g\right)^{1/2} \left[\left(1 - \left(\bar{s}_\ell\right)^{1/m}\right)^m\right]^2 \tag{4.11.6}$$

$$k_{r\ell} = \left(\bar{s}_\ell\right)^{\left(5/2 + 2/\lambda\right)} \tag{4.11.7}$$

$$k_{rg} = \left(\bar{s}_g\right)^{1/2} \left[1 - \left(\bar{s}_\ell\right)^{\left(1 + 1/\lambda\right)}\right]^2 \tag{4.11.8}$$

4.11.1.3 Corey Relative Permeability Functions

Aqueous- and gas-phase relative permeability can be computed from modified expressions for effective aqueous saturation according to the empirical model of Corey [1977]. The model of Corey accounts for trapped air through a modification to the definition of the effective aqueous saturation according to Equation (4.11.9). The Corey functions for aqueous- and gas-phase relative permeability are computed according to Equations (4.11.10) and (4.11.11), respectively. Examples of these functions are shown graphically in Figure 4.28.

$$\dot{s}_l = \frac{s_l - s_m}{1 - s_m - s_{g_{tl}}} \tag{4.11.9}$$

$$k_{r\ell} = \left(\bar{s}_\ell\right)^4 \tag{4.11.10}$$

$$k_{rg} = \left(1 - \bar{s}_\ell\right)^2 \left(1 - \left(\bar{s}_\ell\right)^2\right) \tag{4.11.11}$$

4.11.1.4 Fatt and Klikoff Relative Permeability Function

Aqueous- and gas-phase relative permeability are computed according to the Fatt and Klikoff [1959] models from the conventionally defined effective aqueous saturation according to Equations (4.11.12) and (4.11.13), respectively. Examples of these functions are shown graphically in Figure 4.28.

$$k_{r\ell} = \left(\bar{s}_\ell\right)^3 \tag{4.11.12}$$

$$k_{rg} = \left(1 - \bar{s}_\ell\right)^3 \tag{4.11.13}$$

4.11.1.5 Dual Porosity Relative Permeability Functions

Dual porosity functions or equivalent continuum models [Klavetter and Peters 1986; Nitao 1988] relate bulk fluid phase relative permeabilities to the those for the fracture and matrix according to Equations (4.11.14) and (4.11.15). Dual porosity models require the assumption that fracture and matrix fluid pressures are in equilibrium, which inherently neglects transient fracture-matrix interactions. Fracture and matrix relative permeabilities are computed from either the Burdine or Mualem models using either the van Genuchten or Brooks and Corey soil-moisture retention functions. In these functions the effective aqueous and gas saturations are replaced with the corresponding values for the fracture and matrix components of the soil. For

example the fracture and matrix aqueous relative permeabilities for the Burdine model with the Brooks and Corey soil-moisture retention function are shown in Equations (4.11.16) and (4.11.17), respectively. Examples of the dual porosity function for aqueous- and gas-phase relative permeability using the Burdine relative permeability function are shown graphically in Figures 4.29 and 4.30, respectively for the van Genuchten and Brooks and Corey soil moisture retention functions. Bulk, matrix, and fraction saturation values for the curves shown in Figures 4.29 and 4.30 were obtained from the dual porosity functions shown in Figures 4.20 and 4.21.

$$k_{r\ell_b} = \frac{k_f \, k_{r\ell_f} \, n_{D_f} + k_m \, k_{r\ell_m} \, n_{D_m}}{k_f \, n_{D_f} + k_m \, n_{D_m}} \tag{4.11.14}$$

$$k_{rg_b} = \frac{k_f \, k_{rg_f} \, n_{D_f} + k_m \, k_{rg_m} \, n_{D_m}}{k_f \, n_{D_f} + k_m \, n_{D_m}} \tag{4.11.15}$$

$$k_{r\ell_f} = \left(\bar{s}_{\ell_f}\right)^{\left(3 + 2/\lambda\right)} \tag{4.11.16}$$

$$k_{r\ell_m} = \left(\bar{s}_{\ell_m}\right)^{\left(3 + 2/\lambda\right)} \tag{4.11.17}$$

4.11.1.6 Relative Permeability Functions for Systems with Gas Entrapment

Gas entrapment affects the aqueous permeability by displacing water into larger pores. Parker and Lenhard [1987] have shown that this effect is small. In the STOMP model, we assume that the aqueous phase permeability is a single-valued function of aqueous phase saturation. Hysteresis in gas relative permeability for aqueous-gas systems also occurs as a result of gas entrapment, where the net effect is to reduce the pore space available for gas flow. Therefore, the only changes required in the gas relative permeability functions are to replace the effective aqueous saturations with the apparent aqueous saturations in the pore size integrals and to replace total gas saturation with free gas saturation in the tortuosity terms.

Aqueous- and gas-phase relative permeability can be computed as a function of aqueous saturation from knowledge of the soil-moisture retention function and the pore distribution model of Burdine [1953]. If the van Genuchten and Brooks and Corey soil-moisture retention functions are used, closed-form expressions for fluid phase relative permeability can be derived. Using the van Genuchten soil-moisture retention function, the aqueous- and gas-phase relative permeabilities appear as shown in Equations (4.11.18) and (4.11.19), respectively. Using the Brooks and Corey soil-moisture retention function, the aqueous- and gas-phase relative permeabilities appear as shown in Equations (4.11.20) and (4.11.21), respectively.

$$k_{r\ell} = \left(\bar{s}_\ell\right)^2 \left[1 - \left(1 - \left(\bar{s}_\ell\right)^{1/m}\right)^m\right] \tag{4.11.19}$$

$$k_{rg} = \left(\bar{s}_{g_f}\right)^2 \left(1 - \bar{s}_\ell^{\,1/m}\right)^m \tag{4.11.19}$$

$$k_{r\ell} = \left(\bar{s}_\ell\right)^{(3 + 2/\lambda)} \tag{4.11.20}$$

$$k_{rg} = \left(\bar{s}_{g_f}\right)^2 \left[1 - \left(\bar{s}_\ell\right)^{(1 + 2/\lambda)}\right] \tag{4.11.21}$$

Aqueous- and gas-phase relative permeability can be computed as a function of aqueous saturation from knowledge of the soil-moisture retention function and the pore distribution model of Mualem [1976]. If the van Genuchten and Brooks and Corey soil-moisture retention functions are used, closed-form expressions for fluid phase relative permeability can be derived. Using the van Genuchten soil-moisture retention function, the aqueous- and gas-phase relative permeabilities appear as shown in Equations (4.11.22) and (4.11.23), respectively. Using the Brooks and Corey soil-moisture retention function, the aqueous- and gas-phase relative permeabilities appear as shown in Equations (4.11.24) and (4.11.25), respectively.

$$k_{r\ell} = \left(\bar{s}_\ell\right)^{1/2} \left[1 - \left(1 - \left(\bar{s}_\ell\right)^{1/m}\right)^m\right]^2 \tag{4.11.22}$$

$$k_{rg} = \left(\bar{s}_{g_f}\right)^{1/2} \left[\left(1 - \bar{s}_\ell^{\,1/m}\right)^m\right]^2 \tag{4.11.23}$$

$$k_{r\ell} = \left(\bar{s}_\ell\right)^{(5/2 + 2/\lambda)} \tag{4.11.24}$$

$$k_{rg} = \left(\bar{s}_{g_f}\right)^{1/2} \left[1 - \left(\bar{s}_\ell\right)^{(1 + 1/\lambda)}\right]^2 \tag{4.11.25}$$

4.11.2 Aqueous-Ice-Gas Systems

Relative permeability for aqueous-air-gas systems are computed for nonhysteretic systems following the theory of White [1995]. This model assumes that liquid water completely occludes ice and that no direct ice-gas interfaces occur. Occluded ice is further assumed to behave

similar to occluded air in hysteretic aqueous-gas systems by obstructing the flow of liquid water and displacing water into larger pore spaces. Relative permeability functions for the aqueous and gas phases are derived from modified versions of the Burdine [1953] and Mualem [1976] functions. Both functions are modified to include the effects of occluded ice.

4.11.2.1 Burdine Relative Permeability Functions

Aqueous- and gas-phase relative permeabilities are computed as a function of effective aqueous saturations from knowledge of the soil-moisture retention function and the pore distribution model of Burdine [1953]. If the van Genuchten and Brooks and Corey soil-moisture retention functions are used, closed-form expressions for fluid relative permeability can be derived. For the van Genuchten soil-moisture retention function, the aqueous and gas relative permeabilities appear as shown in Equations (4.11.26) and (4.11.27), respectively. For the Brooks and Corey soil-moisture retention function, the aqueous and gas relative permeabilities appear as shown in Equations (4.11.28) and (4.11.29), respectively. Examples of the Burdine relative permeability functions for water-ice-air systems are shown graphically in Figure 4.31 for the van Genuchten and Brooks and Corey soil-moisture retention functions. This figure shows aqueous relative permeability as a function of ice saturation for a totally saturated system (i.e., $\bar{s}_\ell + \bar{s}_i = 1$).

$$k_{r\ell} = \left(\bar{s}_\ell\right)^2 \left[1 - \left(1 - \left(\bar{s}_\ell\right)^{1/m}\right)^m\right] \tag{4.11.26}$$

$$k_{rg} = \left(\bar{s}_g\right)^2 \left(1 - \left(\bar{s}_\ell\right)^{1/m}\right)^m \tag{4.11.27}$$

$$k_{r\ell} = \left(\bar{s}_\ell\right)^{\left(3 + 2/\lambda\right)} \tag{4.11.28}$$

$$k_{rg} = \left(\bar{s}_g\right)^2 \left[1 - \left(\bar{s}_\ell\right)^{\left(1 + 2/\lambda\right)}\right] \tag{4.11.29}$$

4.11.2.1 Mualem Relative Permeability Functions

Aqueous- and gas-phase relative permeabilities are computed as a function of effective aqueous saturations from knowledge of the soil-moisture retention function and the pore distribution model of Mualem [1976]. If the van Genuchten and Brooks and Corey soil-moisture retention functions are used, closed-form expressions for fluid relative permeability can be derived. For the van Genuchten soil-moisture retention function the aqueous and gas relative permeabilities appear as shown in Equations (4.11.30) and (4.11.31), respectively. For the

Brooks and Corey soil-moisture retention function, the aqueous and gas relative permeabilities appear as shown in Equations (4.11.32) and (4.11.33), respectively. Examples of the Mualem relative permeability functions for water-ice-air systems are shown graphically in Figures 4.31, for the van Genuchten and Brooks and Corey soil-moisture retention functions. This figure shows aqueous relative permeability as a function of ice saturation for a totally saturated system (i.e., $\bar{s}_\ell + \bar{s}_i = 1$).

$$k_{r\ell} = \left(\bar{s}_\ell\right)^{1/2} \left[1 - \left(1 - \left(\bar{s}_\ell\right)^{1/m}\right)^m\right]^2 \tag{4.11.30}$$

$$k_{rg} = \left(\bar{s}_g\right)^{1/2} \left[\left(1 - \left(\bar{s}_\ell\right)^{1/m}\right)^m\right]^2 \tag{4.11.31}$$

$$k_{r\ell} = \left(\bar{s}_\ell\right)^{(5/2 + 2/\lambda)} \tag{4.11.32}$$

$$k_{rg} = \left(\bar{s}_g\right)^{1/2} \left[1 - \left(\bar{s}_\ell\right)^{(1 + 1/\lambda)}\right]^2 \tag{4.11.33}$$

4.11.3 Aqueous-NAPL-Gas Systems

For nonhysteretic systems several empirical functions are available in the STOMP simulator for computing fluid phase relative permeabilities from effective fluid saturations. For systems with nonwetting fluid entrapment, expressions according to a simplified theory [Kaluarachchi and Parker 1992] are used.

4.11.3.1 Burdine Relative Permeability Functions

Aqueous, NAPL, and gas relative permeability can be computed as a function of fluid phase saturations from modified forms of the Burdine [1953] relative permeability model, integrated with certain forms of the soil-moisture retention function. If the van Genuchten and Brooks and Corey soil-moisture retention functions are used, closed-form expressions for fluid phase relative-permeability can be derived. Using the van Genuchten soil-moisture retention function, the aqueous, NAPL, and gas relative permeabilities appear as shown in Equations (4.11.34) through (4.11.36), respectively. Using the Brooks-Corey soil-moisture retention function, the aqueous, NAPL, and gas relative permeabilities appear as shown in Equations (4.11.37) through (4.11.39), respectively.

$$k_{r\ell} = \left(\bar{s}_\ell\right)^2 \left[1 - \left(1 - \bar{s}_\ell^{\,1/m}\right)^m\right] \tag{4.11.34}$$

$$k_{rn} = \left(\bar{s}_n\right)^2 \left[\left(1 - \left(\bar{s}_\ell\right)^{1/m}\right)^m - \left(1 - \left(\bar{s}_t\right)^{1/m}\right)^m\right] \tag{4.11.35}$$

$$k_{rg} = \left(\bar{s}_g\right)^2 \left[1 - \left(\bar{s}_t\right)^{1/m}\right]^m \tag{4.11.36}$$

$$k_{r\ell} = \left(\bar{s}_\ell\right)^{\left(3 + 2/\lambda\right)} \tag{4.11.37}$$

$$k_{rn} = \left(\bar{s}_n\right)^2 \left[\left(\bar{s}_t\right)^{\left(1 + 2/\lambda\right)} - \left(\bar{s}_\ell\right)^{\left(1 + 2/\lambda\right)}\right] \tag{4.11.38}$$

$$k_{rg} = \left(\bar{s}_g\right)^2 \left[1 - \left(\bar{s}_t\right)^{\left(1 + 2/\lambda\right)}\right] \tag{4.11.39}$$

4.11.3.2 Mualem Relative Permeability Functions

Aqueous, NAPL, and gas relative permeability can be computed as a function of fluid phase saturations from modified forms of the Mualem [1976] relative permeability model, integrated with certain forms of the soil-moisture retention function. If the van Genuchten and Brooks and Corey soil-moisture retention functions are used, closed-form expressions for fluid phase relative-permeability can be derived. Using the van Genuchten soil-moisture retention function, the aqueous, NAPL, and gas relative permeabilities appear as shown in Equations (4.11.40) through (4.11.42), respectively. Using the Brooks-Corey soil-moisture retention function, the aqueous, NAPL, and gas relative permeabilities appear as shown in Equations (4.11.43) through (4.11.45), respectively.

$$k_{r\ell} = \left(\bar{s}_\ell\right)^{1/2} \left[1 - \left(1 - \bar{s}_\ell^{\,1/m}\right)^m\right]^2 \tag{4.11.40}$$

$$k_{rn} = \left(\bar{s}_n\right)^{1/2} \left[\left(1 - \left(\bar{s}_\ell\right)^{1/m}\right)^m - \left(1 - \left(\bar{s}_t\right)^{1/m}\right)^m\right]^2 \tag{4.11.41}$$

$$k_{rg} = \left(\bar{s}_g\right)^{1/2} \left[1 - \left(\bar{s}_t\right)^{1/m}\right]^{2m} \tag{4.11.42}$$

$$k_{r\ell} = \left(\bar{s}_\ell\right)^{\left(5/2 + 2/\lambda\right)} \tag{4.11.43}$$

$$k_{rn} = \left(\bar{s}_n\right)^{1/2} \left[\left(\bar{s}_t\right)^{\left(1 + 1/\lambda\right)} - \left(\bar{s}_\ell\right)^{\left(1 + 1/\lambda\right)}\right]^2 \tag{4.11.44}$$

$$k_{rg} = \left(\bar{s}_g\right)^{1/2} \left[1 - \left(\bar{s}_t\right)^{\left(1 + 1/\lambda\right)}\right]^2 \tag{4.11.45}$$

4.11.3.3 Relative Permeability Functions for Systems with Fluid Entrapment

Nonwetting fluid entrapment affects the aqueous permeability by displacing water into larger pores. Parker and Lenhard [1987] have shown that this effect is small. In the STOMP model, we employ simplified permeability relations according to the theory by Kaluarachchi and Parker [1992]. Aqueous phase relative permeabilities are single-valued functions of the aqueous phase saturation. NAPL relative permeabilities are computed with the assumption that only free NAPL is continuous. Hysteresis in gas relative permeability for aqueous-gas systems also occurs as a result of gas entrapment, where the net effect is to reduce the pore space available for gas flow. Therefore, the only changes required in the gas relative permeability functions are to replace the effective aqueous saturations with the apparent aqueous saturations in the pore size integrals and to replace total gas saturation with free gas saturation in the tortuosity terms.

Aqueous, NAPL, and gas relative permeability can be computed as a function of fluid phase saturations from modified forms of the Burdine [1953] relative permeability model, integrated with certain forms of the soil-moisture retention function. If the van Genuchten and Brooks and Corey soil-moisture retention functions are used, closed-form expressions for fluid phase relative-permeability can be derived. Using the van Genuchten soil-moisture retention function, the aqueous, NAPL, and gas relative permeabilities appear as shown in Equations (4.11.46) through (4.11.48), respectively. Using the Brooks-Corey soil-moisture retention function, the aqueous, NAPL, and gas relative permeabilities appear as shown in Equations (4.11.49) through (4.11.51), respectively.

$$k_{r\ell} = \left(\bar{s}_\ell\right)^2 \left[1 - \left(1 - \bar{s}_\ell^{\,1/m}\right)^m\right] \tag{4.11.46}$$

$$k_{rn} = \left(\bar{s}_n\right)^2 \left[\left(1 - \left(\bar{s}_\ell\right)^{1/m}\right)^m - \left(1 - \bar{s}_t^{\,1/m}\right)^m\right] \tag{4.11.47}$$

$$k_{rg} = \left(\bar{s}_{g_f}\right)^2 \left[1 - \left(\bar{s}_t\right)^{1/m}\right]^m \tag{4.11.48}$$

$$k_{r\ell} = \left(\bar{s}_\ell\right)^{(3+2/\lambda)} \tag{4.11.49}$$

$$k_{rn} = \left(\bar{s}_n\right)^2 \left[\left(\bar{s}_t\right)^{(1+2/\lambda)} - \left(\bar{s}_\ell\right)^{(1+2/\lambda)}\right] \tag{4.11.50}$$

$$k_{rg} = \left(\bar{s}_{g_t}\right)^2 \left[1 - \left(\bar{s}_t\right)^{(1+2/\lambda)}\right] \tag{4.11.51}$$

Aqueous, NAPL, and gas relative permeability can be computed as a function of fluid phase saturations from modified forms of the Mualem [1976] relative permeability model, integrated with certain forms of the soil-moisture retention function. If the van Genuchten and Brooks and Corey soil-moisture retention functions are used, closed-form expressions for fluid phase relative-permeability can be derived. Using the van Genuchten soil-moisture retention function the aqueous, NAPL, and gas relative permeabilities appear as shown in Equations (4.11.52) through (4.11.54), respectively. Using the Brooks-Corey soil-moisture retention function, the aqueous, NAPL, and gas relative permeabilities appear as shown in Equations (4.11.55) through (4.11.57), respectively.

$$k_{r\ell} = \left(\bar{s}_\ell\right)^{1/2} \left[1 - \left(1 - \bar{s}_\ell^{\,1/m}\right)^m\right]^2 \tag{4.11.52}$$

$$k_{rn} = \left(\bar{s}_n\right)^{1/2} \left[\left(1 - \left(\bar{s}_\ell\right)^{1/m}\right)^m - \left(1 - \bar{s}_t^{\,1/m}\right)^m\right]^2 \tag{4.11.53}$$

$$k_{rg} = \left(\bar{s}_{g_f}\right)^{1/2} \left[1 - \left(\bar{s}_t\right)^{1/m}\right]^{2m} \tag{4.11.54}$$

$$k_{r\ell} = \left(\bar{s}_\ell\right)^{(5/2+2/\lambda)} \tag{4.11.55}$$

$$k_{rn} = \left(\bar{s}_n\right)^{1/2} \left[\left(\bar{s}_t\right)^{(1+1/\lambda)} - \left(\bar{s}_l\right)^{(1+1/\lambda)}\right]^2 \tag{4.11.56}$$

$$k_{rg} = \left(\bar{s}_{g_f}\right)^{1/2} \left[1 - \left(\bar{s}_t\right)^{(1+1/\lambda)}\right]^2 \tag{4.11.57}$$

4.12 Mechanical Dispersion

Hydraulic dispersion of transported solutes occurs in porous media because of variations in fluid velocity on the pore scale. With the assumption of relatively fast mixing times for solutes along a direction normal to the mean convection flow direction, a special case of convective-dispersive transport occurs. Under these conditions, the variations in pore velocity produce a hydrodynamic dispersion of which may mathematically be described in a form identical to diffusive flux [Bear 1972]. Additionally, because of the identical forms the coefficients of diffusion and mechanical dispersion can be combined to yield a single diffusion-dispersion coefficient. The hydrodynamic dispersion coefficient relates the dispersion flux of a dissolved solute to the gradient in solute concentration in the advective fluid and is a second-order symmetric tensor, which is a function of the porous media and fluid phase. Components of the hydrodynamic dispersion coefficient are computed from the principal fluid Darcy velocity flux components and two empirical parameters related to the porous media, according to Equations (4.12.1) through (4.12.3)

$$D_{h\gamma_x} = \alpha_L \hat{V}'_{\gamma x} + \alpha_T \left(\hat{V}'_{\gamma y} + \hat{V}'_{\gamma z}\right) \tag{4.12.1}$$

$$D_{h\gamma_y} = \alpha_L \hat{V}'_{\gamma y} + \alpha_T \left(\hat{V}'_{\gamma z} + \hat{V}'_{\gamma x}\right) \tag{4.12.2}$$

$$D_{h\gamma_z} = \alpha_L \hat{V}'_{\gamma z} + \alpha_T \left(\hat{V}'_{\gamma x} + \hat{V}'_{\gamma y}\right) \tag{4.12.3}$$

where,

$$\hat{V}'_{\gamma x} = \frac{\hat{V}_{\gamma x}}{\sqrt{\left(\hat{V}_{\gamma x}\right)^2 + \left(\hat{V}_{\gamma y}\right)^2 + \left(\hat{V}_{\gamma z}\right)^2}}$$

$$\hat{V}'_{\gamma y} = \frac{\hat{V}_{\gamma y}}{\sqrt{\left(\hat{V}_{\gamma x}\right)^2 + \left(\hat{V}_{\gamma y}\right)^2 + \left(\hat{V}_{\gamma z}\right)^2}}$$

$$\hat{V}'_{\gamma z} = \frac{\hat{V}_{\gamma z}}{\sqrt{\left(\hat{V}_{\gamma x}\right)^2 + \left(\hat{V}_{\gamma y}\right)^2 + \left(\hat{V}_{\gamma z}\right)^2}}$$

4.13 Partition Coefficients

Equilibrium conditions are assumed for computing salt and/or solute phase distributions. Salt occurs either dissolved in the aqueous phase or sorbed onto the porous media according to linear or nonlinear isotherm models. Salts concentrations in the gas and ice phases are neglected. Solutes are assumed either dissolved in a fluid phase or sorbed onto the porous media according to linear isotherm models. Solute concentrations in the ice phase is neglected.

4.13.1 Salt Partition Coefficients

Equilibrium concentrations for salts are computed using either a linear isotherm model, the nonlinear Freundlich model, or the nonlinear Langmuir model, according to Equations (4.13.1) through (4.13.3), respectively.

$$\frac{S_s}{\rho_s} = K_{s\ell}\, S_\ell \tag{4.13.1}$$

$$\frac{S_s}{\rho_s} = K_{s\ell}\left(S_\ell\right)^n \tag{4.13.2}$$

$$\frac{S_s}{\rho_s} = \frac{\bar{S}_s\, K_{s\ell}^S\, S_\ell}{\left(1 + K_{s\ell}^S\, S_\ell\right)} \tag{4.13.3}$$

4.13.2 Surfactant Partition Coefficients

Equilibrium concentrations for surfactants in the Water-Oil-Dissolved Oil-Surfactant operational mode are computed using either a linear isotherm model, the nonlinear Langmuir model, or the nonlinear Freundlich model, according to Equations (4.13.4) through (4.13.6), respectively.

$$\left(1 - n_T\right)\omega_s^{sf}\rho_s = K_{sl}^{sf}[1]\omega_l^{sf}\rho_l \tag{4.13.4}$$

$$\left(1-n_T\right)\omega_s^{sf}\rho_s = K_{sl}^{sf}[1]\left(\omega_l^{sf}\rho_l\right)^{K_{sl}^{sf}[2]} \tag{4.13.5}$$

$$\left(1-n_T\right)\omega_s^{sf}\rho_s = \frac{K_{sl}^{sf}[3]\omega_l^{sf}\rho_l}{\left(1+K_{sl}^{sf}[4]\omega_l^{sf}\rho_l\right)} \tag{4.13.6}$$

4.13.3 Dissolved-Oil Partition Coefficients

Equilibrium concentrations for dissolved oil in the Water-Oil-Dissolved Oil and the Water-Oil-Dissolved Oil-Surfactant operational modes are computed using either a linear isotherm model, the nonlinear Langmuir model, or the nonlinear Freundlich model, according to Equations (4.13.7) through (4.13.9), respectively.

$$\left(1-n_T\right)\omega_s^{do}\rho_s = K_{sl}^{do}[1]\omega_l^{do}\rho_l \tag{4.13.7}$$

$$\left(1-n_T\right)\omega_s^{do}\rho_s = K_{sl}^{do}[1]\left(\omega_l^{do}\rho_l\right)^{K_{sl}^{do}[2]} \tag{4.13.8}$$

$$\left(1-n_T\right)\omega_s^{do}\rho_s = \frac{K_{sl}^{do}[3]\omega_l^{do}\rho_l}{\left(1+K_{sl}^{do}[4]\omega_l^{do}\rho_l\right)} \tag{4.13.9}$$

4.13.4 Solute Partition Coefficients

With the equilibrium assumption, solute concentrations can be expressed with respect to either volumetric or phase concentrations. The volumetric solute concentration is related to phase concentrations according to Equation (4.13.10). Equilibrium concentrations for solutes are computed using either a linear isotherm model, the nonlinear Freundlich model, or the nonlinear Langmuir model.

Linear partitioning of solutes between the porous media and aqueous phase is expressed through the solid-aqueous distribution coefficient defined in Equation (4.13.11). The gas-aqueous distribution coefficient, which can be computed as a function temperature, defines the partitioning of dissolved solutes between the gas and aqueous phases according to Equation (4.13.12). The aqueous-NAPL distribution coefficient defines the partitioning of dissolved solutes between the aqueous and NAPL phases according to Equation (4.13.13). Equations

(4.13.10) through (4.13.13) are used to derive expressions for volumetric phase concentrations as a function of the total volumetric solute concentration and phase saturations according to Equations (4.13.14) through (4.13.17), for the aqueous, gas, NAPL, and solid phases, respectively. For the Water operational mode, the retardation coefficient, which represents the ratio between aqueous fluid migration velocity and solute migration velocity, is defined according to Equation (4.13.18).

$$C = \sum_{\gamma = \ell,g,n} n_D \, s_\gamma \, C_\gamma + \left(1 - n_T\right) C_s \tag{4.13.10}$$

$$K_{s\ell} = \frac{C_s}{C_\ell \, \rho_s} \tag{4.13.11}$$

$$K_{g\ell} = \frac{C_g}{C_\ell} = \tilde{a} + \frac{\tilde{b}}{T} + \tilde{c} \ln\left(T\right) + \tilde{d} \, T + \tilde{e} \, T^2 \tag{4.13.12}$$

$$K_{\ell n} = \frac{C_\ell}{C_n} \tag{4.13.13}$$

$$C_\ell = \frac{C}{n_D \, s_\ell + n_D \, s_g \, K_{g\ell} + \frac{n_D \, s_n}{K_{\ell n}} + \left(1 - n_T\right) \rho_s \, K_{s\ell}} \tag{4.13.14}$$

$$C_g = \frac{C}{\frac{n_D \, s_\ell}{K_{g\ell}} + n_D \, s_g + \frac{n_D \, s_n}{K_{\ell n} \, K_{g\ell}} + \frac{\left(1 - n_T\right) \rho_s \, K_{s\ell}}{K_{g\ell}}} \tag{4.13.15}$$

$$C_n = \frac{C}{n_D \, s_\ell \, K_{\ell n} + n_D \, s_g \, K_{g\ell} \, K_{\ell n} + n_D \, s_n + \left(1 - n_T\right) \rho_s \, K_{s\ell} \, K_{\ell n}} \tag{4.13.16}$$

$$C_s = \frac{C}{\frac{n_D \, s_\ell}{\rho_s \, K_{s\ell}} + \frac{n_D \, s_g \, K_{g\ell}}{\rho_s \, K_{s\ell}} + \frac{n_D \, s_n}{\rho_s \, K_{s\ell} \, K_{\ell n}} + \left(1 - n_T\right)} \tag{4.13.17}$$

$$R_D = 1 + \frac{\left(1 - n_T\right) \rho_s \, K_{s\ell}}{n_D \, s_\ell} \tag{4.13.18}$$

For the Water and Water-Air operational modes, an additional model for describing solute distribution is available, which differs from the above model in the extent of the wetting surface for unsaturated conditions. The above model contains the inherent assumption that all of the soil surfaces remain wetted regardless of the aqueous saturation. Another approach involves scaling the wetted surface with saturation, which yields an expression for the solid-aqueous distribution coefficient according to Equation (4.13.19). Using this expression for the solid-aqueous distribution coefficient yields expressions for aqueous-, gas-, and solid-volumetric concentrations, as shown in Equations (4.13.20) through (4.13.22), respectively. The retardation coefficient for the water mode is computed according to (4.13.23).

$$K_{s\ell} = \frac{C_s}{C_\ell \, \rho_s \, s_\ell} \tag{4.13.19}$$

$$C_\ell = \frac{C}{n_D \, s_\ell + n_D \, s_g \, K_{g\ell} + \left(1 - n_T\right) \rho_s \, s_\ell \, K_{s\ell}} \tag{4.13.20}$$

$$C_g = \frac{C}{\frac{n_D \, s_\ell}{K_{g\ell}} + n_D \, s_g + \frac{\left(1 - n_T\right) \rho_s \, s_\ell \, K_{s\ell}}{K_{g\ell}}} \tag{4.13.21}$$

$$C_s = \frac{C}{\frac{n_D}{\rho_s \, K_{s\ell}} + \frac{n_D \, s_g \, K_{g\ell}}{\rho_s \, s_\ell \, K_{s\ell}} + \left(1 - n_T\right)} \tag{4.13.22}$$

$$R_D = 1 + \frac{\left(1 - n_T\right) \rho_s \, K_{s\ell}}{n_D} \tag{4.13.23}$$

For the nonlinear Freundlich and Langmuir isotherms, the associated retardation coefficients are expressed in Equation (4.13.24) and (4.13.25), respectively.

$$R_D = \left[1 + \frac{K_{sl}[2] K_{sl}[1] C_l^{K_{sl}[2]}}{s_l n_D}\right] \tag{4.13.24}$$

$$R_D = \left[1 + \frac{K_{sl}[3]}{s_l n_D \left(1 + K_{sl}[4] C_l\right)^2}\right] \tag{4.13.25}$$

4.14 Solute Diffusion Coefficients

Solute diffusion coefficients are computed with the assumption of infinite dilution. The present version of the simulator additionally ignores phase compositional effects. The effects of temperature and pressure on solute diffusion coefficients, however, are considered. Aqueous diffusivity is expressed as a function of temperature and solvent viscosity following the theory of Wilke and Chang [Reid et al. 1987] according to Equation (4.14.1). Reference values for diffusion coefficients in liquid solvents can be estimated from the method of Wilke and Chang [Reid et al. 1987] according to Equation (4.14.2). For diffusion of solutes through the gas phase, the diffusivity is expressed as a function of temperature and pressure following the model of Fuller [Reid et al. 1987], according to Equation (4.14.3). Reference values for diffusion coefficients in gas solvents can be estimated from the method of Slattery and Bird [1958] according to Equation (4.14.4). NAPL diffusivity is expressed as a function of temperature and solvent viscosity following the theory of Wilke and Chang [Reid et al. 1987] according to Equation (4.14.5).

$$D_\ell^C = \overline{D}_\ell^C \frac{T}{\overline{T}} \frac{\overline{\mu}_\ell}{\mu_\ell} \tag{4.14.1}$$

$$\overline{D}_\gamma^C = \frac{7.4\ x\ 10^{-9} \left(\phi_\gamma\ M_\gamma\right)^{1/2} T}{\mu_\gamma \left(\upsilon_b^C\right)^{0.6}}, \quad for\ \gamma = \ell, n \tag{4.14.2}$$

where,

$\phi_\ell = 2.6$ *for water*, $\phi_n = 1.9$ *for methanol*,
$\phi_n = 1.6$ *for ethanol*, *and* $\phi_n = 1.0$ *for unassociated*

$$D_g^C = \overline{D}_g^C \frac{\overline{P}}{P} \left(\frac{T}{\overline{T}}\right)^{1.75} \tag{4.14.3}$$

$$D_g^C = 2.745\ x\ 10^{-4} \left[\frac{\left(\frac{P_c^C\ P_c^g}{\left(P_{atm}\right)^2}\right)^{1/3} \left(T_c^C\ T_c^g\right)^{5/12} \left(\frac{1}{M^C} + \frac{1}{M_g}\right)^{1/2}}{\left(\frac{P}{P_{atm}}\right)}\right] \left[\frac{T}{\sqrt{T_c^C\ T_c^g}}\right]^{1.823} \tag{4.14.4}$$

$$D_n^C = \overline{D}_n^C \frac{T}{\overline{T}} \frac{\overline{\mu}_n}{\mu_n} \tag{4.14.5}$$

For the Two-Phase Nonvolatile operational mode an alternate expression for aqueous-phase diffusion is available. The effective aqueous diffusion coefficient is defined according Equation (4.14.6) and represents the aqueous diffusivity for variably saturated porous media. An alternate expression for the effective aqueous diffusion coefficient, which is dependent on soil-solute combinations, is shown in Equation (4.14.7).

$$D_{\ell e}^C = \tau_\ell \, s_\ell \, n_D \, D_\ell^C \tag{4.14.6}$$

$$D_{\ell e}^C = D_\ell^C \, a_s^C \exp\left(n_D \, s_\ell \, b_s^C\right) \tag{4.14.7}$$

4.15 Solute Chain Decay

Decay or generation of solutes occurs in the STOMP simulator through an Arrhenius type kinetic reaction according to Equation (4.15.1). The decay-rate constant can be related to the radionuclide half-life according to Equation (4.15.2). Production of progeny solutes from parent solutes is computed through an Arrhenius type kinetic reaction according to Equation (4.15.3), where the chain decay fraction is a function of the parent-progeny pair, and the subscripts j and k indicate parent and progeny solutes respectively.

$$\frac{\partial C}{\partial t} = -\lambda^C \, C \tag{4.15.1}$$

$$\lambda^C = \frac{\ln(2)}{T_{1/2}^C} \tag{4.15.2}$$

$$\frac{\partial C^k}{\partial t} = \lambda^j \, F^{jk} \, C^j \tag{4.15.3}$$

4.16 First-Order Reactions

The first-order and Monod chemical reaction model incorporated into the STOMP simulator solves a series of chemical reactions of the general form shown in Equation (4.16.1)

$$N_{pr} A_{pr} + \sum_{\text{reactants}} N_r A_r \qquad \sum_{\text{products}} N_p A_p \tag{4.16.1}$$

For first-order reactions, the reaction rate for each chemical reaction is dependent on the molar concentration of the primary reactant according to Equations (4.16.2) through (4.16.4)

$$\frac{dC_{pr}}{dt} = -\frac{C_{pr} \ln(2)}{t_{pr}^{1/2}} \tag{4.16.2}$$

$$\frac{dC_r}{dt} = -\frac{C_{pr} \ln(2) N_r f_{pr}}{t_{pr}^{1/2} N_{pr}} \tag{4.16.3}$$

$$\frac{dC_p}{dt} = \frac{C_{pr} \ln(2) N_p f_{pr}}{t_{pr}^{1/2} N_{pr}} \tag{4.16.4}$$

The reaction rate factor is a function of the primary and secondary reactant molar concentrations, equation stoichiometry, reaction half-life, and simulation time step according to Equations (4.16.5) and (4.16.6):

$$f_{pr} = \left[1 + \left(g_{pr}\right)^2\right]^{-1/2} \tag{4.16.5}$$

$$g_{pr} = \max\left[\frac{C_{pr} \ln(2) N_r \Delta t}{t_{pr}^{1/2} C_r N_{pr}}\right] \tag{4.16.6}$$

The right-hand-side of Equation (4.16.6) represents the ratio of the molar amount of secondary reactant which could be consumed over the amount of secondary reactant available. The reaction rate function, see Equation (4.16.5), has the effect of modulating the reaction rate from first-order kinetics under conditions for which at least one of the secondary reactants nears being totally consumed.

4.17 Kinetic Dissolution/Solubilization of Oil

Several theoretical and experimental studies have shown that the aqueous-phase concentrations of dissolved oil can be significantly lower than equilibrium conditions for relatively large entrapped NAPL ganglia, high groundwater velocities, or low NAPL saturations [e.g., Mayer and Miller 1996]. These studies often yield formulations for mass transfer

correlations between the NAPL and aqueous phases, that relate the mass transfer coefficient, in dimensionless form as the Sherwood number *Sh,* to other system properties. Two general forms of these correlations have been incorporated into the Water-Oil-Dissolved Oil and the Water-Oil-Dissolved Oil-Surfactant operational modes. The first form, shown in Equation (4.17.1), is based on the Gilland-Sherwood formulation, which is typically applied to describing mass transport through liquid boundary layers for laminar flows.

$$Sh = \frac{k_{n,\ell}^{do} d_p^{\,2}}{D_{m\ell}^{do}} = a + bRe^m\, Sc^n \tag{4.17.1}$$

where the parameters *a, b, m,* and *n* are determined empirically. The second form, as shown in Equation (4.17.2) depends on the NAPL saturation as

$$Sh = \frac{k_{n,l}^{do} d_p^2}{D_{ml}^{do}} = a + bRe^m \left(n_D s_n\right)^n \tag{4.17.2}$$

where the Schmidt number *Sc* is replaced by the NAPL content. Implementation of Equations (4.17.1) and (4.17.2) indicate that similar mass transfer relations are assumed for oil dissolution and micellar solubilization although Abriola et al. [1993] stated that, based on detailed experiments, the mechanisms governing both processes are probably fundamentally different. Since more appropriate equations for micellar solubilization are currently lacking, it was decided to compute oil dissolution and micellar solubilization using similar relations.

Several authors [e.g., Pennell et al., 1993] have shown that the equilibrium concentration of solubilized oil in the aqueous phase is a linear function of the surfactant concentration above the critical micellar concentration (CMC). The following linear expression is used in the simulator to relate the equilibrium concentration of dissolved oil with dissolved surfactant concentration

$$\overline{C}_\ell^{\,do} = a + b \max\left[\left(C_\ell^s - CMC\right), 0\right] \tag{4.17.3}$$

4.18 Mobilization of Nonaqueous Phase Liquids

Mobilization of entrapped NAPL has been shown to be depending on viscous, buoyancy and capillary forces through the total trapping number [Pennell et al. 1996] defined as

$$N_t = \sqrt{N_c^2 + 2N_c N_b \sin\varphi + N_b^2} \tag{4.18.1}$$

where the angle φ refers to the flow angle with respect to the horizontal (measured counter-clockwise). The capillary number is defined in terms of the magnitude of the aqueous flow and NAPL-aqueous interfacial tension as

$$N_c = \frac{|\mathbf{u}_l|\mu_l}{\sigma_{nl}\cos\theta} \tag{4.18.2}$$

and the he Bond number in terms of the NAPL-aqueous interfacial tension is defined as

$$N_b = \frac{(\rho_n - \rho_l) g k_{rl} \mathbf{k}_z}{\sigma_{nl}\cos\theta} \tag{4.18.3}$$

Effective residual NAPL saturation is computed as a function of the trapping number using the empirical correlation shown in Equation (4.18.4)

$$\bar{s}_{nr}^{max} = \min\left[s_n \frac{\bar{s}_{nr}^{max}\big|_{N_t=0}}{1 + \left(N_t / N_t^c\right)} \right] \tag{4.18.4}$$

Changes in the trapping number (e.g., via changes in the interfacial tension or aqueous flow rates) result in changes to the effective residual NAPL saturation, which in turn can alter the volumes of free and entrapped NAPL. Converting entrapped NAPL to free NAPL through this processes effectively mobilizes a portion of the entrapped NAPL. This type of relationship has been used by Delshad et al. [1996] in the UTCHEM code and has experimentally been verified by Pennell et al. [1996]. Introducing surfactants into aqueous phase liquids in three-phase systems reduces the interfacial tension between two phase pairs (i.e., gas-aqueous and NAPL-aqueous). Water is the primary constituent in the aqueous phase, but in the Water-Oil-Dissolved Oil-Surfactant operational mode it may also include dissolved amounts of surfactant, oil, and air. Changes in interfacial tension with surfactant concentration affect the mobilization of free and trapped NAPLs. These effects are modeled in the simulator through modifications to the saturation-capillary pressure (*s*-*P*) scaling factors and in the residual NAPL saturations.

To provide continuity between two-phase (aqueous-gas) and three-phase (aqueous-NAPL-gas) saturation systems the scaling factors are defined as [Lenhard 1994; Lenhard and Parker 1987]

$$\beta_{gn} = \frac{\bar{\sigma}_{ij}}{\sigma_{gn}}, \beta_{nl} = \frac{\bar{\sigma}_{ij}}{\sigma_{nl}}, \beta_{gl} = \frac{\bar{\sigma}_{ij}}{\sigma_{gl}} \tag{4.18.5}$$

where the interfacial tension between fluid pair *ij* refers to the fluid pair used to determine the s-P relation, which is typically the gas-aqueous pair. The s-P scaling factors are related by

$$\frac{1}{\beta_{gn}} + \frac{1}{\beta_{nl}} = \frac{1}{\beta_{gl}} \tag{4.18.6}$$

which implies the following relationship among the interfacial tensions

$$\sigma_{gn} + \sigma_{nl} = \sigma_{gl} \tag{4.18.7}$$

Adding surfactant to the aqueous phase produces a reduction in the interfacial tension of the gas-aqueous and NAPL-aqueous fluid pairs, which directly correspond to increases in the gas-aqueous and NAPL-aqueous s-P scaling factors. Continuity of saturation between two- and three-phase systems is achieved by using the saturation functions for both systems, and restricting the NAPL pressure to values greater than or equal to the critical NAPL pressure defined as

$$P_n^c = \max\left[\frac{\beta_{gn} P_g + \beta_{nl} P_l}{\beta_{gn} + \beta_{nl}}\right] \tag{4.18.8}$$

4.10.1 Aqueous-Gas Systems

The following sections describe nonhysteretic and hysteretic soil moisture retention functions for aqueous-gas systems. Beyond the listed functions, the STOMP simulator also allows the description of the saturation function for aqueous-gas systems through tabular data. Unless specifically stated, the described functions refer to nonhysteretic systems. For aqueous-gas systems, actual aqueous saturations are computed in terms of effective aqueous saturations, according to Equation (4.10.1), where the effective minimum aqueous saturation is computed as a function of aqueous-gas capillary pressure, as shown in Equation (4.10.2), according to Fayer and Simmons [1995].

$$s_\ell = \bar{s}_\ell \left(1 - \bar{s}_m\right) + \bar{s}_m \tag{4.10.1}$$

$$\bar{s}_m = \left[1 - \frac{\ln\left(\frac{P_g - P_\ell}{\bar{\rho}_\ell \, g}\right)}{\ln\left(h_{od}\right)}\right] s_m \tag{4.10.2}$$

4.10.1.1 Van Genuchten Function

The van Genuchten function [van Genuchten 1980] relates the gas-aqueous capillary pressure to the effective aqueous saturation through two correlation parameters, according to Equation (4.10.3). The n and m correlation parameters for the van Genuchten function can be related depending on the chosen function for relative permeability. Typically, these parameters are related, as shown in Equation (4.10.3). An example of the van Genuchten function is shown graphically in Figure 4.18.

$$\bar{s}_\ell = \left[1 + \left(\alpha \left|\frac{P_g - P_\ell}{\bar{\rho}_\ell \, g}\right|\right)^n\right]^{-m} \quad for \left[P_g - P_\ell\right] > 0 \tag{4.10.3}$$

$$\bar{s}_\ell = 1 \quad for \left[P_g - P_\ell\right] \leq 0$$

where,

$$m = 1 - \frac{1}{n}$$

4.10.1.2 Brooks and Corey Function

The Brooks and Corey function [Brooks and Corey 1966] for aqueous-gas systems relates the gas-aqueous capillary pressure to the effective aqueous saturation with two correlation parameters, according to Equation (4.10.4). The first parameter, ψ , is referred to as the entry head and equals the minimum drainage capillary head for which a continuous nonwetting phase (e.g., gas phase) exits. The second parameter, λ , is related to the pore-size distribution within the porous media. An example of the Brooks and Corey function for aqueous-gas systems is shown graphically in Figure 4.19.

$$\bar{s}_\ell = \left[\frac{P_g - P_\ell}{\bar{\rho}_\ell \, g \, \psi} \right]^{-\lambda} \quad for \left(P_g - P_\ell \right) \geq \psi \tag{4.10.4}$$

$$\bar{s}_\ell = 1 \quad for \left(P_g - P_\ell \right) < \psi$$

4.10.1.3 Dual Porosity Functions

Dual porosity functions or equivalent continuum models for aqueous-gas systems relate the gas-aqueous capillary pressure to the bulk aqueous saturation for fractured geologic media through two functions [Klavetter and Peters 1986; Nitao 1988]. One function relates the gas-aqueous capillary pressure to the matrix aqueous saturation and the other relates the gas-aqueous capillary pressure to the fracture aqueous saturation. The pivotal assumption associated with the dual porosity function is that the fracture and matrix pressures are in equilibrium. This assumption neglects transient fracture-matrix interactions. Fracture and matrix effective saturations can be computed with either van Genuchten or Brooks and Corey functions (Sections 4.10.1.1 and 4.10.1.2). The bulk aqueous saturation is computed by combining the fracture and matrix aqueous saturations and diffusive porosities, as shown in Equation (4.10.5), where the actual saturations are computed from effective saturations, according to Equations (4.10.6) and (4.10.7). An example of a dual porosity function, using the van Genuchten and Brooks and Corey saturation functions for aqueous-gas systems, is shown graphically in Figures 4.20 and 4.21, respectively.

$$s_\ell = \frac{s_{\ell f} \, n_{Df} + s_{\ell m} \left(1 - n_{Df} \right) n_{Dm}}{n_{Df} + \left(1 - n_{Df} \right) n_{Dm}} \tag{4.10.5}$$

$$s_{\ell_f} = \bar{s}_{\ell_f}\left(1 - s_{m_f}\right) + s_{m_f} \tag{4.10.6}$$

$$s_{\ell_m} = \bar{s}_{\ell_m}\left(1 - s_{m_m}\right) + s_{m_m} \tag{4.10.7}$$

4.10.1.4 Capillary Pressure-Saturation Functions for Systems with Gas Entrapment

A theoretical model for hysteretic saturation functions for aqueous-gas systems was developed by Parker and Lenhard [1987]. A simplified version of this model, analogous to Kaluarachchi and Parker [1992], has been implemented in the STOMP simulator. The model includes effects of gas entrapment during aqueous-phase imbibition paths. Gas entrapment during aqueous-phase imbibition will depend on the aqueous saturation and current saturation path. The amount of entrapped gas varies linearly between zero and the gas effective residual saturation with the apparent saturation, which varies between the reversal point from main drainage to one. Gas effective residual saturations are computed using an empirical relationship developed by Land [1968] for aqueous-NAPL systems. In this simplified hysteretic model for aqueous-gas systems, gas can be trapped or free, where free gas refers to continuous volumes which advect freely and trapped gas refers to discontinuous ganglia of gas occluded within the aqueous phase. Occluded gas is assumed to be immobile. The apparent aqueous saturation equals the effective aqueous saturation plus effective trapped gas saturation, as shown in Equation (4.10.8). The effective gas saturation equals the effective trapped and free gas saturations, as shown in Equation (4.10.9). In hysteretic systems, the residual saturation is independent of capillary pressure.

$$\bar{\bar{s}}_\ell = \bar{s}_\ell + \bar{s}_{g_{t\ell}} \tag{4.10.8}$$

where,

$$\bar{s}_\ell = \frac{s_\ell - s_m}{1 - s_m}$$

$$\bar{s}_g = \bar{s}_{g_f} + \bar{s}_{g_{t\ell}} = \frac{s_g}{1 - s_m} \tag{4.10.9}$$

The saturation functions relate gas-aqueous capillary pressure to apparent aqueous saturations, according to Equations (4.10.10) and (4.10.11), for the van Genuchten and Brooks and Corey functions, respectively. The effective trapped gas saturation is computed according to Equation (4.10.12), which recognizes that entrapped gas cannot exceed the gas present. Land's

parameter for gas-aqueous interfaces is computed according to Equation (4.10.13).

$$\bar{\bar{s}}_\ell = \left[1 + \left(\alpha \left[\frac{P_g - P_\ell}{\bar{\rho}_\ell\, g}\right]\right)^n\right]^{-m} \tag{4.10.10}$$

$$\bar{\bar{s}}_\ell = \left[\frac{\left(\frac{P_g - P_\ell}{\bar{\rho}_\ell\, g}\right)}{\psi}\right]^{-\lambda}, \quad for\ \left(P_g - P_\ell\right) \geq \psi \tag{4.10.11}$$

$$\bar{\bar{s}}_\ell = 1, \quad for\ \left(P_g - P_\ell\right) < \psi$$

$$\bar{s}_g = \min\left[\frac{1 - \bar{s}_l^{\min}}{1 + L_g\left(1 - \bar{s}_l^{\min}\right)} - \frac{1 - \bar{\bar{s}}_l}{1 + L_g\left(1 - \bar{\bar{s}}_l\right)}, \bar{s}_g\right], \quad for\ \bar{\bar{s}}_\ell > \bar{s}_l^{\min} \tag{4.10.12}$$

where,

$$L_g = \frac{1}{\bar{s}_{g_r}} - 1 \tag{4.10.13}$$

4.10.2 Aqueous-Ice-Gas Systems

The following sections describe nonhysteretic soil-moisture retention functions for aqueous-ice-gas systems. For these systems, ice is assumed to be occluded by the aqueous phase, with no gas-ice interfaces. The apparent aqueous saturation represents the ratio of free aqueous saturation to the normalized free pore volume, according to Equation (4.10.14). The unfrozen aqueous fraction is defined as the ratio of liquid aqueous saturation to total aqueous saturation, according to Equation (4.10.15). The effective irreducible aqueous saturation is

defined as a function of the actual irreducible aqueous saturation and the unfrozen aqueous fraction, according to Equation (4.10.16). The effective aqueous and gas saturations, used in the relative permeability functions, are defined according to Equations (4.10.17) and (4.10.18), respectively.

$$\bar{\bar{s}}_\ell = \frac{s_\ell - \bar{s}_m}{1 - s_i - \bar{s}_m} \tag{4.10.14}$$

$$s_{uf} = \frac{s_\ell}{s_\ell + s_i} \tag{4.10.15}$$

$$\bar{s}_m = s_{uf}\, s_m \tag{4.10.16}$$

$$\bar{s}_\ell = \frac{s_\ell - \bar{s}_m}{1 - \bar{s}_m} \tag{4.10.17}$$

$$\bar{s}_g = \frac{s_g}{1 - \bar{s}_m} \tag{4.10.18}$$

Under freezing conditions, an assumption is made that thermodynamic equilibrium exists between the ice and aqueous phases in porous media. An expression of thermodynamic equilibrium between the ice and aqueous phases in porous media, which accounts for the difference between the ice pressure and the total potential of the aqueous phase, has been developed by Loch [1977], according to Equation (4.10.19). The total potential of the aqueous phase is the pressure one would measure in a soil aqueous solution with a tensiometer, if the tensiometer cup were a perfect semipermeable membrane. The total pressure is defined as the difference between the aqueous phase pressure and the osmotic pressure, as shown in Equation (4.10.20). The osmotic pressure for dilute solutes is computed according to Equation (4.10.21). Combining Equations (4.10.19) through (4.10.21) yields an expression for the ice pressure as a function of temperature, aqueous pressure, and solute concentration, as shown in Equation (4.10.22).

$$v_i\, P_i - v_\ell\, P_{tp} = -h_{wi} \ln\left(1 + \frac{\left(T - T^w_{fp}\right)}{T^w_{fp}}\right) \tag{4.10.19}$$

$$P_{tp} = P_\ell - \pi \tag{4.10.20}$$

$$\pi = C_\ell \; R \; T \tag{4.10.21}$$

$$P_i = \rho_i \left[\frac{\left(P_\ell - C_\ell \, R \, T\right)}{\rho_\ell} - h_{wi} \ln\left(1 + \frac{\left(T - T_{fp}^{w}\right)}{T_{fp}^{w}}\right) \right] \tag{4.10.22}$$

The soil moisture retention function that relates gas-aqueous capillary pressures to aqueous saturations, can be used to predict the retention function of any two-phase interface by interfacial-tension dependent scaling of the capillary pressures. Under freezing conditions, the apparent aqueous saturation is computed from the gas-aqueous capillary pressure and the fraction of unfrozen water is computed from the scaled ice-aqueous capillary pressure [Panday and Corapcioglu 1994], where the scaling factor is computed from the ratios of interfacial tensions [Lenhard 1994], according to Equation (4.10.23).

$$\beta_{i\ell} = \frac{\sigma_{g\ell}}{\sigma_{i\ell}}, \quad \beta_{g\ell} = \frac{\sigma_{g\ell}}{\sigma_{g\ell}} = 1 \tag{4.10.23}$$

4.10.2.1 Van Genuchten Functions

For freezing conditions, the van Genuchten function relates the gas-aqueous capillary pressure to the apparent aqueous saturation and the scaled ice-aqueous capillary pressure to the unfrozen aqueous-phase fraction, according to Equations (4.10.24) and (4.10.25), respectively. The correlation parameters for the van Genuchten function can be determined from gas-aqueous retention data. Ice saturation, as a function of temperature using the van Genuchten soil moisture retention function, is shown graphically in Figure 4.22, for a constant total aqueous saturation of 0.9 and unfrozen solute concentrations of 0.0, 1.0, and 2.0 mol/L. The graphs in Figure 4.22 were generated by fixing the total aqueous saturation and the unfrozen or base solute concentration. Solute concentrations in the aqueous phase increased with increasing ice saturation, because of the a lack of solute absorption within the ice phase. Solute concentrations in the aqueous phase as a function of temperature for unfrozen solute concentrations of 1.0, and 2.0 mol/L, are shown graphically in Figure 4.23.

$$\bar{\bar{s}}_\ell = \left[1 + \left(\alpha \, \beta_{g\ell} \frac{P_g - P_\ell}{\bar{\rho}_\ell \, g}\right)^{n}\right]^{-m}, \quad for \left[P_g - P_\ell\right] > 0 \tag{4.10.24}$$

$$\bar{\bar{s}}_\ell = 1, \quad for \left[P_g - P_\ell\right] \le 0$$

$$s_{uf} = \left[1 + \left(\alpha \beta_{i\ell} \left[\frac{P_i - P_\ell}{\bar{\rho}_\ell g}\right]\right)^n\right]^{-m}, \quad for \left[P_i - P_\ell\right] > 0 \tag{4.10.25}$$

$$s_{uf} = 1, \quad for \left[P_i - P_\ell\right] \le 0$$

4.10.2.2 Brooks and Corey Functions

For freezing conditions, the Brooks and Corey function relates the gas-aqueous capillary pressure to the apparent aqueous saturation and the scaled ice-aqueous capillary pressure to the unfrozen aqueous fraction, according to Equations (4.10.26) and (4.10.27), respectively. The correlation parameters for the Brooks and Corey function can be determined from gas-aqueous retention data. Ice saturation, as a function of temperature using the Brooks and Corey soil moisture retention function, is shown graphically in Figure 4.24, for an apparent aqueous saturation of 0.9 and unfrozen solute concentrations of 0.0, 1.0, and 2.0 mol/L. The graphs in Figure 4.24 were generated by fixing the apparent aqueous saturation and the unfrozen or base solute concentration. Solute concentrations in the aqueous phase increased with increasing ice saturation, because of a lack of solute absorption within the ice phase. Solute concentrations in the aqueous phase, as a function of temperature for unfrozen solute concentrations of 1.0 and 2.0 mol/L, are shown graphically in Figure 4.25.

$$\bar{\bar{s}}_l = \left[\frac{\beta_{g\ell}\left(\frac{P_g - P_\ell}{\bar{\rho}_\ell g}\right)}{\psi}\right]^{-\lambda}, \quad for \ \beta_{g\ell}\left(P_g - P_\ell\right) \ge \psi \tag{4.10.26}$$

$$\bar{\bar{s}}_l = 1, \quad for \ \beta_{g\ell}\left(P_g - P_\ell\right) < \psi$$

$$s_{uf} = \left[\frac{\beta_{i\ell}\left(\frac{P_i - P_\ell}{\bar{\rho}_\ell g}\right)}{\psi}\right]^{-\lambda}, \quad for \ \beta_{i\ell}\left(P_i - P_\ell\right) \ge \psi \tag{4.10.27}$$

$$s_{uf} = 1, \quad for \ \beta_{i\ell}\left(P_i - P_\ell\right) < \psi$$

4.10.3 Aqueous-NAPL-Gas Systems

The following sections describe nonhysteretic and hysteretic nonwetting-fluid entrapment soil-moisture retention functions for aqueous-NAPL-gas systems. The functions described herein follow the simplified theory by Kaluarachchi and Parker [1992] of the theoretical models of Parker and Lenhard [1987]. Saturations are defined as functions of water-equivalent scaled capillary heads, that are computed from differences in pressure across phase-pair interfaces. For aqueous-NAPL-gas systems, three interfacial capillary heads are defined (i.e., gas-aqueous, gas-NAPL, and NAPL-aqueous), according to Equations (4.10.28) through (4.10.30), where the wettability order decreases from aqueous to NAPL to gas. Phase scaling factors are computed from the ratio of interfacial tensions according to the theory of Lenhard [1994], as shown in Equation (4.10.31), where the gas-aqueous is chosen as the reference fluid.

$$h_{g\ell} = \frac{\left(P_g - P_\ell\right)}{\overline{\rho}_\ell \, g} \tag{4.10.28}$$

$$h_{gn} = \frac{\left(P_g - P_n\right)}{\overline{\rho}_\ell \, g} \tag{4.10.29}$$

$$h_{n\ell} = \frac{\left(P_n - P_\ell\right)}{\overline{\rho}_\ell \, g} \tag{4.10.30}$$

$$\beta_{ij} = \frac{\sigma_{ij}}{\sigma_{g\ell}} \tag{4.10.31}$$

The Parker and Lenhard [1987] theory distinguishes between actual, effective, and apparent saturations. Actual saturations are defined as the ratio of fluid volume to diffusive pore volume. Effective saturations represent normalized actual saturations based on the pore volumes above the irreducible or minimum saturation of the wetting fluid (i.e., aqueous phase liquid). Effective saturations for the aqueous-phase, NAPL, gas-phase, and total liquid, are defined according to Equations (4.10.32) through (4.10.35), respectively. Apparent saturations are defined in terms of effective saturations. Apparent saturations represent the effective saturation of the fluid plus the effective saturations of fluids of lesser wettability trapped within the fluid for the aqueous-phase, NAPL, and total liquid, according to Equations (4.10.36) through (4.10.38). Trapped fluids refer to discontinuous islands or ganglia of fluid occluded within another fluid of greater wettability. The theory of Lenhard and Parker [1987] assumes that

trapped fluids are immobile. Effective saturations can be defined in terms of trapped and free fluids, as shown in Equations (4.10.39) and (4.10.40), for the NAPL and gas phases, where free fluids refer to continuous phases that move convectively.

$$\bar{s}_\ell = \frac{s_\ell - s_m}{1 - s_m} \tag{4.10.32}$$

$$\bar{s}_n = \frac{s_n}{1 - s_m} \tag{4.10.33}$$

$$\bar{s}_g = \frac{s_g}{1 - s_m} \tag{4.10.34}$$

$$\bar{s}_t = \frac{s_\ell + s_n - s_m}{1 - s_m} \tag{4.10.35}$$

$$\bar{\bar{s}}_\ell = \bar{s}_\ell + \bar{s}_{n_t} + \bar{s}_{g_{t\ell}} \tag{4.10.36}$$

$$\bar{\bar{s}}_n = \bar{s}_n + \bar{s}_{g_{tn}} \tag{4.10.37}$$

$$\bar{\bar{s}}_t = \bar{s}_\ell + \bar{s}_n + \bar{s}_{g_{t\ell}} + \bar{s}_{g_{tn}} \tag{4.10.38}$$

$$\bar{s}_n = \bar{s}_{n_f} + \bar{s}_{n_t} \tag{4.10.39}$$

$$\bar{s}_g = \bar{s}_{g_f} + \bar{s}_{g_{t\ell}} + \bar{s}_{g_{tn}} \tag{4.10.40}$$

In the absence of hysteretic and fluid entrapment effects, fluid saturations are considered as unique functions of fluid-gas capillary heads. The Parker and Lenhard [1987] theory accommodates the effects of fluid entrapment by relating fluid-gas capillary heads to apparent saturations rather than effective saturations. The fundamental assumption related to the theory of Parker and Lenhard [1987] is that the functions relating fluid saturation to fluid-gas interfacial pressure differences can be expressed with a single soil-moisture retention function, for a given porous medium, by scaling the fluid-gas capillary heads. For aqueous-NAPL-gas systems, two functions relating fluid saturation with fluid-gas capillary head are required. The total-liquid saturation is related to the gas-NAPL capillary head, and the aqueous saturation is related to the oil-aqueous capillary head, as shown in Equations (4.10.41) and (4.10.42), respectively.

$$\bar{\bar{s}}_t = s\left(\beta_{gn}\, h_{gn}\right) \tag{4.10.41}$$

$$\bar{\bar{s}}_\ell = s\left(\beta_{n\ell}\, h_{n\ell}\right) \tag{4.10.42}$$

4.10.3.1 Van Genuchten Function

The van Genuchten function [van Genuchten 1980] relates fluid saturation to capillary head through two soil dependent correlation parameters. The n and m correlation parameters for the van Genuchten function can be related depending on the chosen function for relative permeability. Expressions for the effective total-liquid saturation as a function of scaled gas-NAPL capillary head and the effective aqueous saturation as a function of scaled oil-aqueous capillary head are shown in Equations (4.10.43) and (4.10.44), using the van Genuchten soil-moisture retention function. The van Genuchten function is shown graphically in Figure 4.17.

$$\bar{s}_t = \left[1 + \left(\alpha\, \beta_{gn}\, h_{gn}\right)^n\right]^{-m}, \quad for \;\; h_{gn} > 0 \tag{4.10.43}$$

where,

$$\bar{s}_t = 1, \quad for \;\; h_{gn} \le 0$$

$$\bar{s}_\ell = \left[1 + \left(\alpha\, \beta_{n\ell}\, h_{n\ell}\right)^n\right]^{-m}, \quad for \;\; h_{n\ell} > 0 \tag{4.10.44}$$

where,

$$\bar{s}_\ell = 1, \quad for \;\; h_{n\ell} \le 0$$

4.10.3.2 Brooks and Corey Function

The Brooks and Corey function [Brooks and Corey 1966] relates fluid saturation to capillary head through two soil dependent correlation parameters. The first parameter, ψ, is referred to as the entry head and equals the minimum drainage capillary head for which a continuous nonwetting phase (e.g., gas phase) exits. The second parameter, λ, is related to the pore-size distribution within the porous media. Expressions for the effective total-liquid saturation as a function of scaled gas-NAPL capillary head and the effective aqueous saturation as a function of scaled oil-aqueous capillary head are shown in Equations (4.10.45) and (4.10.46), using the Brooks and Corey soil-moisture retention function. The Brooks and Corey function is shown graphically in Figure 4.18.

$$\bar{s}_t = \left[\frac{\beta_{gn}\, h_{gn}}{\psi}\right]^{-\lambda}, \quad for \;\; \beta_{gn}\, h_{gn} > \psi \tag{4.10.45}$$

where,

$$\bar{s}_t = 1, \quad for \;\; \beta_{gn}\, h_{gn} \le \psi$$

$$\bar{s}_\ell = \left[\frac{\beta_{n\ell}\, h_{n\ell}}{\psi}\right]^{-\lambda}, \quad for \;\; \beta_{n\ell}\, h_{n\ell} > \psi \tag{4.10.46}$$

where,

$$\bar{s}_\ell = 1, \quad for \;\; \beta_{n\ell}\, h_{n\ell} \le \psi$$

4.10.3.3 Capillary Pressure Saturation Functions for Systems with Fluid Entrapment

Fluid entrapment effects in the functions for fluid saturation are accommodated in the theory of Parker and Lenhard [1987] from the assumption that fluid entrapment phenomena for aqueous-NAPL-gas systems can be predicted from fluid-gas systems (e.g., gas-aqueous, gas-NAPL, NAPL-aqueous). Fluids of lesser wettability are assumed to be trapped by fluids of greater wettability; therefore, gas can be entrapped by NAPL or aqueous phase and NAPL can be entrapped by the aqueous phase. For no free-NAPL conditions, the effective trapped NAPL saturation equals the effective NAPL saturation, according to Equation (4.10.47). For free-NAPL conditions, a simplified entrapment theory is used [Kaluarachchi and Parker 1992] in which the effective trapped NAPL saturation is a function of the apparent aqueous saturation, according to Equation (4.10.48). This relation recognizes that entrapped NAPL cannot exceed the NAPL present.

$$\bar{s}_{n_t} = \bar{s}_n \tag{4.10.47}$$

$$\bar{s}_{n_t} = \min\left[\frac{1-\bar{s}_l^{\min}}{1+L_n\left(1-\bar{s}_l^{\min}\right)} - \frac{1-\bar{s}_l}{1+L_n\left(1-\bar{s}_l\right)},\; \bar{s}_n\right], \quad for \;\; \bar{s}_\ell > \bar{s}_l^{\min} \tag{4.10.48}$$

where,

$$L_n = \frac{1}{i\bar{s}_{n_r}} - 1$$

Gas entrapment is complicated by the fact that both NAPL and aqueous fluids have greater wettabilities than gas and can contain entrapped gas. In the absence of free NAPL, gas entrapment is occurs by advancing gas-aqueous interface, according to the theory for aqueous-gas systems. In the presence of free NAPL, gas entrapment occurs in response to advancing gas-NAPL interfaces, corresponding to increasing apparent total liquid saturation. Release of entrapped gas follows either gas-aqueous or gas-NAPL interfaces, depending on the occurrence of free NAPL. Gas, initially trapped by one wetting fluid, transfers to the other according to the position of the oil-aqueous interface, tracked by the apparent aqueous saturation. For no free-NAPL conditions, the effective residual saturations for gas trapped by the aqueous phase are computed according to Equation (4.10.15). For free-NAPL conditions, the effective residual saturations for gas trapped by NAPL are computed according to Equation (4.10.49).

$$\bar{s}_{g_r} = \frac{\left(1 - \bar{s}_t^{\min}\right)}{1 + L_g\left(1 - \bar{s}_t^{\min}\right)} \qquad (4.10.49)$$

where,

$$L_g = \frac{1}{i\bar{s}_{g_r}} - 1$$

The distribution of entrapped gas within a aqueous-NAPL-gas system depends on the positions of the gas-NAPL and oil-aqueous interfaces, as tracked by the apparent aqueous and total liquid saturations. The distribution additionally depends on the minimum pore size into which gas-NAPL interfaces have receded since the inception of free-NAPL conditions, as tracked by the minimum value of the apparent total-liquid saturation and on the apparent aqueous saturation at the inception of free-NAPL conditions. To compute entrapped gas saturations, three conditions are distingushed

In the first case, there is no trapped or free NAPL present. Gas is only entrapped by the aqueous phase and the entrapped gas saturation is computed according to Equation (4.10.50).

$$\bar{s}_{g_{tl}} = \min\left[\left(\frac{1-\bar{s}_t^{\min}}{1+L_g\left(1-\bar{s}_t^{\min}\right)} - \frac{1-\bar{\bar{s}}_l}{1+L_g\left(1-\bar{\bar{s}}_l\right)}\right), \bar{s}_g\right] \tag{4.10.50}$$

where,

$$L_g = \frac{1}{\bar{s}_{g_r}} - 1$$

In the second case, no free NAPL is present and gas is, again, only entrapped by the aqueous phase according to Equation (4.10.51).

$$\bar{s}_{g_{tl}} = \min\left[\left(\frac{1-\bar{s}_t^{\min}}{1+L_g\left(1-\bar{s}_t^{\min}\right)} - \frac{1-\bar{\bar{s}}_l}{1+L_g\left(1-\bar{\bar{s}}_l\right)}\right), \bar{s}_g\right] \tag{4.10.51}$$

where,

$$L_g = \frac{1}{\bar{s}_{g_r}} - 1$$

The third case describes entrapment of the gas phase by both the aqueous and NAPL phases according to Equation (4.10.52) and (4.10.53) respectively.

$$\bar{s}_{g_{tl}} = \left(\frac{1-\bar{s}_t^{\min}}{1+L_g\left(1-\bar{s}_t^{\min}\right)} - \frac{1-\bar{\bar{s}}_l}{1+L_g\left(1-\bar{\bar{s}}_l\right)}\right) \tag{4.10.52}$$

$$\bar{s}_{g_{tn}} = \left(\frac{1-\bar{\bar{s}}_l}{1+L_g\left(1-\bar{\bar{s}}_l\right)} - \frac{1-\bar{\bar{s}}_t}{1+L_g\left(1-\bar{\bar{s}}_t\right)}\right) \tag{4.10.53}$$

where,

$$L_g = \frac{1}{\bar{s}_{g_r}} - 1$$

4.11 Relative Permeability

Relative permeability for fluid phases are computed for both nonhysteretic and hysteretic nonwetting-fluid entrapment systems. Three distinct fluid systems are recognized: water-air, water-ice-air, and water-oil-air. Relative permeabilities for water-air systems are computed for the aqueous- and gas-phase fluids. The functions for fluid phase relative permeability follow the simplified Kaluarachchi and Parker [1992] model which is based on the theory of Lenhard and Parker [1987]. Fluid entrapment effects are computed following the method of Land [1968]. Relative permeabilities for water-ice-air systems are computed for the aqueous- and gas-phase fluids. Only nonhysteretic systems are addressed where fluid phase relative permeabilities are unique functions of phase saturations. The relative permeability functions for water-ice-air systems follow the theory of White [1995]. Relative permeabilities for water-oil-air systems are computed for the aqueous-phase, NAPL, and gas-phase. The theory for relative permeability [Lenhard and Parker 1987] predicts mild hysteretic effects for the aqueous fluid, except at high saturations, pronounced hysteretic effects for the gas phase, negligible hysteretic effects for NAPL for low aqueous saturations, and marked hysteretic effects for NAPL with increasing aqueous saturations.

4.11.1 Aqueous-Gas Systems

For nonhysteretic systems several empirical functions are available in the STOMP simulator for computing fluid phase relative permeabilities from effective fluid saturations. For systems with gas entrapment, expressions according to a simplified theory [Kaluarachchi and Parker 1992] are used.

4.11.1.1 Burdine Relative Permeability Functions

Aqueous- and gas-phase relative permeability can be computed as a function of aqueous saturation from knowledge of the soil-moisture retention function and the pore distribution model of Burdine [1953]. If the van Genuchten and Brooks and Corey soil-moisture retention functions are used, closed-form expressions for fluid phase relative permeability can be derived. Using the van Genuchten soil-moisture retention function, the aqueous- and gas-phase relative permeabilities appear as shown in Equations (4.11.1) and (4.11.2), respectively. Using the Brooks and Corey soil-moisture retention function, the aqueous- and gas-phase relative permeabilities appear as shown in Equations (4.11.3) and (4.11.4), respectively. Examples of the Burdine relative permeability functions for water-air systems are shown graphically in Figures 4.26 and 4.27 with the van Genuchten and Brooks and Corey soil-moisture retention functions, respectively.

$$k_{r\ell} = \left(\bar{s}_\ell\right)^2 \left[1 - \left(1 - \left(\bar{s}_\ell\right)^{1/m}\right)^m\right] \tag{4.11.1}$$

$$k_{rg} = \left(\bar{s}_g\right)^2 \left(1 - \left(\bar{s}_\ell\right)^{1/m}\right)^m \tag{4.11.2}$$

$$k_{r\ell} = \left(\bar{s}_\ell\right)^{\left(3 + 2/\lambda\right)} \tag{4.11.3}$$

$$k_{rg} = \left(\bar{s}_g\right)^2 \left[1 - \left(\bar{s}_\ell\right)^{\left(1 + 2/\lambda\right)}\right] \tag{4.11.4}$$

4.11.1.2 Mualem Relative Permeability Functions

Aqueous- and gas-phase relative permeability can be computed as a function of aqueous saturation from knowledge of the soil-moisture retention function and the pore distribution model of Mualem [1976]. If the van Genuchten and Brooks and Corey soil-moisture retention functions are used, closed-form expressions for fluid phase relative permeability can be derived. Using the van Genuchten soil-moisture retention function, the aqueous- and gas-phase relative permeabilities appear as shown in Equations (4.11.5) and (4.11.6), respectively. Using the Brooks and Corey soil-moisture retention function, the aqueous- and gas-phase relative permeabilities appear as shown in Equations (4.11.7) and (4.11.8), respectively. Examples of the Mualem relative permeability functions for water-air systems are shown graphically in Figures 4.26 and 4.27 with the van Genuchten and Brooks and Corey soil-moisture retention functions, respectively.

$$k_{r\ell} = \left(\bar{s}_\ell\right)^{1/2} \left[1 - \left(1 - \left(\bar{s}_\ell\right)^{1/m}\right)^m\right]^2 \tag{4.11.5}$$

$$k_{rg} = \left(\bar{s}_g\right)^{1/2} \left[\left(1 - \left(\bar{s}_\ell\right)^{1/m}\right)^m\right]^2 \tag{4.11.6}$$

$$k_{r\ell} = \left(\bar{s}_\ell\right)^{\left(5/2 + 2/\lambda\right)} \tag{4.11.7}$$

$$k_{rg} = \left(\bar{s}_g\right)^{1/2} \left[1 - \left(\bar{s}_\ell\right)^{\left(1 + 1/\lambda\right)}\right]^2 \tag{4.11.8}$$

4.11.1.3 Corey Relative Permeability Functions

Aqueous- and gas-phase relative permeability can be computed from modified expressions for effective aqueous saturation according to the empirical model of Corey [1977]. The model of Corey accounts for trapped air through a modification to the definition of the effective aqueous saturation according to Equation (4.11.9). The Corey functions for aqueous- and gas-phase relative permeability are computed according to Equations (4.11.10) and (4.11.11), respectively. Examples of these functions are shown graphically in Figure 4.28.

$$\dot{s}_l = \frac{s_l - s_m}{1 - s_m - s_{g_{tl}}} \tag{4.11.9}$$

$$k_{r\ell} = \left(\bar{s}_\ell\right)^4 \tag{4.11.10}$$

$$k_{rg} = \left(1 - \bar{s}_\ell\right)^2 \left(1 - \left(\bar{s}_\ell\right)^2\right) \tag{4.11.11}$$

4.11.1.4 Fatt and Klikoff Relative Permeability Function

Aqueous- and gas-phase relative permeability are computed according to the Fatt and Klikoff [1959] models from the conventionally defined effective aqueous saturation according to Equations (4.11.12) and (4.11.13), respectively. Examples of these functions are shown graphically in Figure 4.28.

$$k_{r\ell} = \left(\bar{s}_\ell\right)^3 \tag{4.11.12}$$

$$k_{rg} = \left(1 - \bar{s}_\ell\right)^3 \tag{4.11.13}$$

4.11.1.5 Dual Porosity Relative Permeability Functions

Dual porosity functions or equivalent continuum models [Klavetter and Peters 1986; Nitao 1988] relate bulk fluid phase relative permeabilities to the those for the fracture and matrix according to Equations (4.11.14) and (4.11.15). Dual porosity models require the assumption that fracture and matrix fluid pressures are in equilibrium, which inherently neglects transient fracture-matrix interactions. Fracture and matrix relative permeabilities are computed from either the Burdine or Mualem models using either the van Genuchten or Brooks and Corey soil-moisture retention functions. In these functions the effective aqueous and gas saturations are replaced with the corresponding values for the fracture and matrix components of the soil. For

example the fracture and matrix aqueous relative permeabilities for the Burdine model with the Brooks and Corey soil-moisture retention function are shown in Equations (4.11.16) and (4.11.17), respectively. Examples of the dual porosity function for aqueous- and gas-phase relative permeability using the Burdine relative permeability function are shown graphically in Figures 4.29 and 4.30, respectively for the van Genuchten and Brooks and Corey soil moisture retention functions. Bulk, matrix, and fraction saturation values for the curves shown in Figures 4.29 and 4.30 were obtained from the dual porosity functions shown in Figures 4.20 and 4.21.

$$k_{r\ell_b} = \frac{k_f \, k_{r\ell_f} \, n_{D_f} + k_m \, k_{r\ell_m} \, n_{D_m}}{k_f \, n_{D_f} + k_m \, n_{D_m}} \tag{4.11.14}$$

$$k_{rg_b} = \frac{k_f \, k_{rg_f} \, n_{D_f} + k_m \, k_{rg_m} \, n_{D_m}}{k_f \, n_{D_f} + k_m \, n_{D_m}} \tag{4.11.15}$$

$$k_{r\ell_f} = \left(\bar{s}_{\ell_f}\right)^{\left(3 + 2/\lambda\right)} \tag{4.11.16}$$

$$k_{r\ell_m} = \left(\bar{s}_{\ell_m}\right)^{\left(3 + 2/\lambda\right)} \tag{4.11.17}$$

4.11.1.6 Relative Permeability Functions for Systems with Gas Entrapment

Gas entrapment affects the aqueous permeability by displacing water into larger pores. Parker and Lenhard [1987] have shown that this effect is small. In the STOMP model, we assume that the aqueous phase permeability is a single-valued function of aqueous phase saturation. Hysteresis in gas relative permeability for aqueous-gas systems also occurs as a result of gas entrapment, where the net effect is to reduce the pore space available for gas flow. Therefore, the only changes required in the gas relative permeability functions are to replace the effective aqueous saturations with the apparent aqueous saturations in the pore size integrals and to replace total gas saturation with free gas saturation in the tortuosity terms.

Aqueous- and gas-phase relative permeability can be computed as a function of aqueous saturation from knowledge of the soil-moisture retention function and the pore distribution model of Burdine [1953]. If the van Genuchten and Brooks and Corey soil-moisture retention functions are used, closed-form expressions for fluid phase relative permeability can be derived. Using the van Genuchten soil-moisture retention function, the aqueous- and gas-phase relative permeabilities appear as shown in Equations (4.11.18) and (4.11.19), respectively. Using the Brooks and Corey soil-moisture retention function, the aqueous- and gas-phase relative permeabilities appear as shown in Equations (4.11.20) and (4.11.21), respectively.

$$k_{r\ell} = \left(\bar{s}_\ell\right)^2 \left[1 - \left(1 - \left(\bar{s}_\ell\right)^{1/m}\right)^m\right] \tag{4.11.19}$$

$$k_{rg} = \left(\bar{s}_{g_f}\right)^2 \left(1 - \bar{s}_\ell^{\,1/m}\right)^m \tag{4.11.19}$$

$$k_{r\ell} = \left(\bar{s}_\ell\right)^{(3 + 2/\lambda)} \tag{4.11.20}$$

$$k_{rg} = \left(\bar{s}_{g_f}\right)^2 \left[1 - \left(\bar{s}_\ell\right)^{(1 + 2/\lambda)}\right] \tag{4.11.21}$$

Aqueous- and gas-phase relative permeability can be computed as a function of aqueous saturation from knowledge of the soil-moisture retention function and the pore distribution model of Mualem [1976]. If the van Genuchten and Brooks and Corey soil-moisture retention functions are used, closed-form expressions for fluid phase relative permeability can be derived. Using the van Genuchten soil-moisture retention function, the aqueous- and gas-phase relative permeabilities appear as shown in Equations (4.11.22) and (4.11.23), respectively. Using the Brooks and Corey soil-moisture retention function, the aqueous- and gas-phase relative permeabilities appear as shown in Equations (4.11.24) and (4.11.25), respectively.

$$k_{r\ell} = \left(\bar{s}_\ell\right)^{1/2} \left[1 - \left(1 - \left(\bar{s}_\ell\right)^{1/m}\right)^m\right]^2 \tag{4.11.22}$$

$$k_{rg} = \left(\bar{s}_{g_f}\right)^{1/2} \left[\left(1 - \bar{s}_\ell^{\,1/m}\right)^m\right]^2 \tag{4.11.23}$$

$$k_{r\ell} = \left(\bar{s}_\ell\right)^{(5/2 + 2/\lambda)} \tag{4.11.24}$$

$$k_{rg} = \left(\bar{s}_{g_f}\right)^{1/2} \left[1 - \left(\bar{s}_\ell\right)^{(1 + 1/\lambda)}\right]^2 \tag{4.11.25}$$

4.11.2 Aqueous-Ice-Gas Systems

Relative permeability for aqueous-air-gas systems are computed for nonhysteretic systems following the theory of White [1995]. This model assumes that liquid water completely occludes ice and that no direct ice-gas interfaces occur. Occluded ice is further assumed to behave

similar to occluded air in hysteretic aqueous-gas systems by obstructing the flow of liquid water and displacing water into larger pore spaces. Relative permeability functions for the aqueous and gas phases are derived from modified versions of the Burdine [1953] and Mualem [1976] functions. Both functions are modified to include the effects of occluded ice.

4.11.2.1 Burdine Relative Permeability Functions

Aqueous- and gas-phase relative permeabilities are computed as a function of effective aqueous saturations from knowledge of the soil-moisture retention function and the pore distribution model of Burdine [1953]. If the van Genuchten and Brooks and Corey soil-moisture retention functions are used, closed-form expressions for fluid relative permeability can be derived. For the van Genuchten soil-moisture retention function, the aqueous and gas relative permeabilities appear as shown in Equations (4.11.26) and (4.11.27), respectively. For the Brooks and Corey soil-moisture retention function, the aqueous and gas relative permeabilities appear as shown in Equations (4.11.28) and (4.11.29), respectively. Examples of the Burdine relative permeability functions for water-ice-air systems are shown graphically in Figure 4.31 for the van Genuchten and Brooks and Corey soil-moisture retention functions. This figure shows aqueous relative permeability as a function of ice saturation for a totally saturated system (i.e., $\bar{s}_\ell + \bar{s}_i = 1$).

$$k_{r\ell} = \left(\bar{s}_\ell\right)^2 \left[1 - \left(1 - \left(\bar{s}_\ell\right)^{1/m}\right)^m\right] \tag{4.11.26}$$

$$k_{rg} = \left(\bar{s}_g\right)^2 \left(1 - \left(\bar{s}_\ell\right)^{1/m}\right)^m \tag{4.11.27}$$

$$k_{r\ell} = \left(\bar{s}_\ell\right)^{\left(3 + 2/\lambda\right)} \tag{4.11.28}$$

$$k_{rg} = \left(\bar{s}_g\right)^2 \left[1 - \left(\bar{s}_\ell\right)^{\left(1 + 2/\lambda\right)}\right] \tag{4.11.29}$$

4.11.2.1 Mualem Relative Permeability Functions

Aqueous- and gas-phase relative permeabilities are computed as a function of effective aqueous saturations from knowledge of the soil-moisture retention function and the pore distribution model of Mualem [1976]. If the van Genuchten and Brooks and Corey soil-moisture retention functions are used, closed-form expressions for fluid relative permeability can be derived. For the van Genuchten soil-moisture retention function the aqueous and gas relative permeabilities appear as shown in Equations (4.11.30) and (4.11.31), respectively. For the

Brooks and Corey soil-moisture retention function, the aqueous and gas relative permeabilities appear as shown in Equations (4.11.32) and (4.11.33), respectively. Examples of the Mualem relative permeability functions for water-ice-air systems are shown graphically in Figures 4.31, for the van Genuchten and Brooks and Corey soil-moisture retention functions. This figure shows aqueous relative permeability as a function of ice saturation for a totally saturated system (i.e., $\bar{s}_\ell + \bar{s}_i = 1$).

$$k_{r\ell} = \left(\bar{s}_\ell\right)^{1/2} \left[1 - \left(1 - \left(\bar{s}_\ell\right)^{1/m}\right)^m\right]^2 \tag{4.11.30}$$

$$k_{rg} = \left(\bar{s}_g\right)^{1/2} \left[\left(1 - \left(\bar{s}_\ell\right)^{1/m}\right)^m\right]^2 \tag{4.11.31}$$

$$k_{r\ell} = \left(\bar{s}_\ell\right)^{(5/2 + 2/\lambda)} \tag{4.11.32}$$

$$k_{rg} = \left(\bar{s}_g\right)^{1/2} \left[1 - \left(\bar{s}_\ell\right)^{(1 + 1/\lambda)}\right]^2 \tag{4.11.33}$$

4.11.3 Aqueous-NAPL-Gas Systems

For nonhysteretic systems several empirical functions are available in the STOMP simulator for computing fluid phase relative permeabilities from effective fluid saturations. For systems with nonwetting fluid entrapment, expressions according to a simplified theory [Kaluarachchi and Parker 1992] are used.

4.11.3.1 Burdine Relative Permeability Functions

Aqueous, NAPL, and gas relative permeability can be computed as a function of fluid phase saturations from modified forms of the Burdine [1953] relative permeability model, integrated with certain forms of the soil-moisture retention function. If the van Genuchten and Brooks and Corey soil-moisture retention functions are used, closed-form expressions for fluid phase relative-permeability can be derived. Using the van Genuchten soil-moisture retention function, the aqueous, NAPL, and gas relative permeabilities appear as shown in Equations (4.11.34) through (4.11.36), respectively. Using the Brooks-Corey soil-moisture retention function, the aqueous, NAPL, and gas relative permeabilities appear as shown in Equations (4.11.37) through (4.11.39), respectively.

$$k_{r\ell} = \left(\bar{s}_\ell\right)^2 \left[1 - \left(1 - \bar{s}_\ell^{\,1/m}\right)^m\right] \tag{4.11.34}$$

$$k_{rn} = \left(\bar{s}_n\right)^2 \left[\left(1 - \left(\bar{s}_\ell\right)^{1/m}\right)^m - \left(1 - \left(\bar{s}_t\right)^{1/m}\right)^m\right] \tag{4.11.35}$$

$$k_{rg} = \left(\bar{s}_g\right)^2 \left[1 - \left(\bar{s}_t\right)^{1/m}\right]^m \tag{4.11.36}$$

$$k_{r\ell} = \left(\bar{s}_\ell\right)^{\left(3 + 2/\lambda\right)} \tag{4.11.37}$$

$$k_{rn} = \left(\bar{s}_n\right)^2 \left[\left(\bar{s}_t\right)^{\left(1 + 2/\lambda\right)} - \left(\bar{s}_\ell\right)^{\left(1 + 2/\lambda\right)}\right] \tag{4.11.38}$$

$$k_{rg} = \left(\bar{s}_g\right)^2 \left[1 - \left(\bar{s}_t\right)^{\left(1 + 2/\lambda\right)}\right] \tag{4.11.39}$$

4.11.3.2 Mualem Relative Permeability Functions

Aqueous, NAPL, and gas relative permeability can be computed as a function of fluid phase saturations from modified forms of the Mualem [1976] relative permeability model, integrated with certain forms of the soil-moisture retention function. If the van Genuchten and Brooks and Corey soil-moisture retention functions are used, closed-form expressions for fluid phase relative-permeability can be derived. Using the van Genuchten soil-moisture retention function, the aqueous, NAPL, and gas relative permeabilities appear as shown in Equations (4.11.40) through (4.11.42), respectively. Using the Brooks-Corey soil-moisture retention function, the aqueous, NAPL, and gas relative permeabilities appear as shown in Equations (4.11.43) through (4.11.45), respectively.

$$k_{r\ell} = \left(\bar{s}_\ell\right)^{1/2} \left[1 - \left(1 - \bar{s}_\ell^{\,1/m}\right)^m\right]^2 \tag{4.11.40}$$

$$k_{rn} = \left(\bar{s}_n\right)^{1/2} \left[\left(1 - \left(\bar{s}_\ell\right)^{1/m}\right)^m - \left(1 - \left(\bar{s}_t\right)^{1/m}\right)^m\right]^2 \tag{4.11.41}$$

$$k_{rg} = \left(\bar{s}_g\right)^{1/2} \left[1 - \left(\bar{s}_t\right)^{1/m}\right]^{2m} \tag{4.11.42}$$

$$k_{r\ell} = \left(\bar{s}_\ell\right)^{\left(5/2 + 2/\lambda\right)} \tag{4.11.43}$$

$$k_{rn} = \left(\bar{s}_n\right)^{1/2} \left[\left(\bar{s}_t\right)^{\left(1 + 1/\lambda\right)} - \left(\bar{s}_\ell\right)^{\left(1 + 1/\lambda\right)}\right]^2 \tag{4.11.44}$$

$$k_{rg} = \left(\bar{s}_g\right)^{1/2} \left[1 - \left(\bar{s}_t\right)^{\left(1 + 1/\lambda\right)}\right]^2 \tag{4.11.45}$$

4.11.3.3 Relative Permeability Functions for Systems with Fluid Entrapment

Nonwetting fluid entrapment affects the aqueous permeability by displacing water into larger pores. Parker and Lenhard [1987] have shown that this effect is small. In the STOMP model, we employ simplified permeability relations according to the theory by Kaluarachchi and Parker [1992]. Aqueous phase relative permeabilities are single-valued functions of the aqueous phase saturation. NAPL relative permeabilities are computed with the assumption that only free NAPL is continuous. Hysteresis in gas relative permeability for aqueous-gas systems also occurs as a result of gas entrapment, where the net effect is to reduce the pore space available for gas flow. Therefore, the only changes required in the gas relative permeability functions are to replace the effective aqueous saturations with the apparent aqueous saturations in the pore size integrals and to replace total gas saturation with free gas saturation in the tortuosity terms.

Aqueous, NAPL, and gas relative permeability can be computed as a function of fluid phase saturations from modified forms of the Burdine [1953] relative permeability model, integrated with certain forms of the soil-moisture retention function. If the van Genuchten and Brooks and Corey soil-moisture retention functions are used, closed-form expressions for fluid phase relative-permeability can be derived. Using the van Genuchten soil-moisture retention function, the aqueous, NAPL, and gas relative permeabilities appear as shown in Equations (4.11.46) through (4.11.48), respectively. Using the Brooks-Corey soil-moisture retention function, the aqueous, NAPL, and gas relative permeabilities appear as shown in Equations (4.11.49) through (4.11.51), respectively.

$$k_{r\ell} = \left(\bar{s}_\ell\right)^2 \left[1 - \left(1 - \bar{s}_\ell^{\,1/m}\right)^m\right] \tag{4.11.46}$$

$$k_{rn} = \left(\bar{s}_n\right)^2 \left[\left(1 - \left(\bar{s}_\ell\right)^{1/m}\right)^m - \left(1 - \bar{s}_t^{\,1/m}\right)^m\right] \tag{4.11.47}$$

$$k_{rg} = \left(\bar{s}_{g_f}\right)^2 \left[1 - \left(\bar{s}_t\right)^{1/m}\right]^m \tag{4.11.48}$$

$$k_{r\ell} = \left(\bar{s}_\ell\right)^{(3+2/\lambda)} \tag{4.11.49}$$

$$k_{rn} = \left(\bar{s}_n\right)^2 \left[\left(\bar{s}_t\right)^{(1+2/\lambda)} - \left(\bar{s}_\ell\right)^{(1+2/\lambda)}\right] \tag{4.11.50}$$

$$k_{rg} = \left(\bar{s}_{g_t}\right)^2 \left[1 - \left(\bar{s}_t\right)^{(1+2/\lambda)}\right] \tag{4.11.51}$$

Aqueous, NAPL, and gas relative permeability can be computed as a function of fluid phase saturations from modified forms of the Mualem [1976] relative permeability model, integrated with certain forms of the soil-moisture retention function. If the van Genuchten and Brooks and Corey soil-moisture retention functions are used, closed-form expressions for fluid phase relative-permeability can be derived. Using the van Genuchten soil-moisture retention function the aqueous, NAPL, and gas relative permeabilities appear as shown in Equations (4.11.52) through (4.11.54), respectively. Using the Brooks-Corey soil-moisture retention function, the aqueous, NAPL, and gas relative permeabilities appear as shown in Equations (4.11.55) through (4.11.57), respectively.

$$k_{r\ell} = \left(\bar{s}_\ell\right)^{1/2} \left[1 - \left(1 - \bar{s}_\ell^{\,1/m}\right)^m\right]^2 \tag{4.11.52}$$

$$k_{rn} = \left(\bar{s}_n\right)^{1/2} \left[\left(1 - \left(\bar{s}_\ell\right)^{1/m}\right)^m - \left(1 - \bar{s}_t^{\,1/m}\right)^m\right]^2 \tag{4.11.53}$$

$$k_{rg} = \left(\bar{s}_{g_f}\right)^{1/2} \left[1 - \left(\bar{s}_t\right)^{1/m}\right]^{2m} \tag{4.11.54}$$

$$k_{r\ell} = \left(\bar{s}_\ell\right)^{(5/2+2/\lambda)} \tag{4.11.55}$$

$$k_{rn} = \left(\bar{s}_n\right)^{1/2} \left[\left(\bar{s}_t\right)^{(1+1/\lambda)} - \left(\bar{s}_l\right)^{(1+1/\lambda)}\right]^2 \tag{4.11.56}$$

$$k_{rg} = \left(\bar{s}_{g_f}\right)^{1/2} \left[1 - \left(\bar{s}_t\right)^{(1+1/\lambda)}\right]^2 \tag{4.11.57}$$

4.12 Mechanical Dispersion

Hydraulic dispersion of transported solutes occurs in porous media because of variations in fluid velocity on the pore scale. With the assumption of relatively fast mixing times for solutes along a direction normal to the mean convection flow direction, a special case of convective-dispersive transport occurs. Under these conditions, the variations in pore velocity produce a hydrodynamic dispersion of which may mathematically be described in a form identical to diffusive flux [Bear 1972]. Additionally, because of the identical forms the coefficients of diffusion and mechanical dispersion can be combined to yield a single diffusion-dispersion coefficient. The hydrodynamic dispersion coefficient relates the dispersion flux of a dissolved solute to the gradient in solute concentration in the advective fluid and is a second-order symmetric tensor, which is a function of the porous media and fluid phase. Components of the hydrodynamic dispersion coefficient are computed from the principal fluid Darcy velocity flux components and two empirical parameters related to the porous media, according to Equations (4.12.1) through (4.12.3)

$$D_{h\gamma_x} = \alpha_L \hat{V}'_{\gamma x} + \alpha_T \left(\hat{V}'_{\gamma y} + \hat{V}'_{\gamma z}\right) \tag{4.12.1}$$

$$D_{h\gamma_y} = \alpha_L \hat{V}'_{\gamma y} + \alpha_T \left(\hat{V}'_{\gamma z} + \hat{V}'_{\gamma x}\right) \tag{4.12.2}$$

$$D_{h\gamma_z} = \alpha_L \hat{V}'_{\gamma z} + \alpha_T \left(\hat{V}'_{\gamma x} + \hat{V}'_{\gamma y}\right) \tag{4.12.3}$$

where,

$$\hat{V}'_{\gamma x} = \frac{\hat{V}_{\gamma x}}{\sqrt{\left(\hat{V}_{\gamma x}\right)^2 + \left(\hat{V}_{\gamma y}\right)^2 + \left(\hat{V}_{\gamma z}\right)^2}}$$

$$\hat{V}'_{\gamma y} = \frac{\hat{V}_{\gamma y}}{\sqrt{\left(\hat{V}_{\gamma x}\right)^2 + \left(\hat{V}_{\gamma y}\right)^2 + \left(\hat{V}_{\gamma z}\right)^2}}$$

$$\hat{V}'_{\gamma z} = \frac{\hat{V}_{\gamma z}}{\sqrt{\left(\hat{V}_{\gamma x}\right)^2 + \left(\hat{V}_{\gamma y}\right)^2 + \left(\hat{V}_{\gamma z}\right)^2}}$$

4.13 Partition Coefficients

Equilibrium conditions are assumed for computing salt and/or solute phase distributions. Salt occurs either dissolved in the aqueous phase or sorbed onto the porous media according to linear or nonlinear isotherm models. Salts concentrations in the gas and ice phases are neglected. Solutes are assumed either dissolved in a fluid phase or sorbed onto the porous media according to linear isotherm models. Solute concentrations in the ice phase is neglected.

4.13.1 Salt Partition Coefficients

Equilibrium concentrations for salts are computed using either a linear isotherm model, the nonlinear Freundlich model, or the nonlinear Langmuir model, according to Equations (4.13.1) through (4.13.3), respectively.

$$\frac{S_s}{\rho_s} = K_{s\ell}\, S_\ell \tag{4.13.1}$$

$$\frac{S_s}{\rho_s} = K_{s\ell}\left(S_\ell\right)^n \tag{4.13.2}$$

$$\frac{S_s}{\rho_s} = \frac{\bar{S}_s\, K_{s\ell}^S\, S_\ell}{\left(1 + K_{s\ell}^S\, S_\ell\right)} \tag{4.13.3}$$

4.13.2 Surfactant Partition Coefficients

Equilibrium concentrations for surfactants in the Water-Oil-Dissolved Oil-Surfactant operational mode are computed using either a linear isotherm model, the nonlinear Langmuir model, or the nonlinear Freundlich model, according to Equations (4.13.4) through (4.13.6), respectively.

$$\left(1 - n_T\right)\omega_s^{sf}\rho_s = K_{sl}^{sf}[1]\omega_l^{sf}\rho_l \tag{4.13.4}$$

$$\left(1-n_T\right)\omega_s^{sf}\rho_s = K_{sl}^{sf}[1]\left(\omega_l^{sf}\rho_l\right)^{K_{sl}^{sf}[2]} \tag{4.13.5}$$

$$\left(1-n_T\right)\omega_s^{sf}\rho_s = \frac{K_{sl}^{sf}[3]\omega_l^{sf}\rho_l}{\left(1+K_{sl}^{sf}[4]\omega_l^{sf}\rho_l\right)} \tag{4.13.6}$$

4.13.3 Dissolved-Oil Partition Coefficients

Equilibrium concentrations for dissolved oil in the Water-Oil-Dissolved Oil and the Water-Oil-Dissolved Oil-Surfactant operational modes are computed using either a linear isotherm model, the nonlinear Langmuir model, or the nonlinear Freundlich model, according to Equations (4.13.7) through (4.13.9), respectively.

$$\left(1-n_T\right)\omega_s^{do}\rho_s = K_{sl}^{do}[1]\omega_l^{do}\rho_l \tag{4.13.7}$$

$$\left(1-n_T\right)\omega_s^{do}\rho_s = K_{sl}^{do}[1]\left(\omega_l^{do}\rho_l\right)^{K_{sl}^{do}[2]} \tag{4.13.8}$$

$$\left(1-n_T\right)\omega_s^{do}\rho_s = \frac{K_{sl}^{do}[3]\omega_l^{do}\rho_l}{\left(1+K_{sl}^{do}[4]\omega_l^{do}\rho_l\right)} \tag{4.13.9}$$

4.13.4 Solute Partition Coefficients

With the equilibrium assumption, solute concentrations can be expressed with respect to either volumetric or phase concentrations. The volumetric solute concentration is related to phase concentrations according to Equation (4.13.10). Equilibrium concentrations for solutes are computed using either a linear isotherm model, the nonlinear Freundlich model, or the nonlinear Langmuir model.

Linear partitioning of solutes between the porous media and aqueous phase is expressed through the solid-aqueous distribution coefficient defined in Equation (4.13.11). The gas-aqueous distribution coefficient, which can be computed as a function temperature, defines the partitioning of dissolved solutes between the gas and aqueous phases according to Equation (4.13.12). The aqueous-NAPL distribution coefficient defines the partitioning of dissolved solutes between the aqueous and NAPL phases according to Equation (4.13.13). Equations

(4.13.10) through (4.13.13) are used to derive expressions for volumetric phase concentrations as a function of the total volumetric solute concentration and phase saturations according to Equations (4.13.14) through (4.13.17), for the aqueous, gas, NAPL, and solid phases, respectively. For the Water operational mode, the retardation coefficient, which represents the ratio between aqueous fluid migration velocity and solute migration velocity, is defined according to Equation (4.13.18).

$$C = \sum_{\gamma = \ell,g,n} n_D \, s_\gamma \, C_\gamma + \left(1 - n_T\right) C_s \tag{4.13.10}$$

$$K_{s\ell} = \frac{C_s}{C_\ell \, \rho_s} \tag{4.13.11}$$

$$K_{g\ell} = \frac{C_g}{C_\ell} = \tilde{a} + \frac{\tilde{b}}{T} + \tilde{c} \ln\left(T\right) + \tilde{d} \, T + \tilde{e} \, T^2 \tag{4.13.12}$$

$$K_{\ell n} = \frac{C_\ell}{C_n} \tag{4.13.13}$$

$$C_\ell = \frac{C}{n_D \, s_\ell + n_D \, s_g \, K_{g\ell} + \frac{n_D \, s_n}{K_{\ell n}} + \left(1 - n_T\right) \rho_s \, K_{s\ell}} \tag{4.13.14}$$

$$C_g = \frac{C}{\frac{n_D \, s_\ell}{K_{g\ell}} + n_D \, s_g + \frac{n_D \, s_n}{K_{\ell n} \, K_{g\ell}} + \frac{\left(1 - n_T\right) \rho_s \, K_{s\ell}}{K_{g\ell}}} \tag{4.13.15}$$

$$C_n = \frac{C}{n_D \, s_\ell \, K_{\ell n} + n_D \, s_g \, K_{g\ell} \, K_{\ell n} + n_D \, s_n + \left(1 - n_T\right) \rho_s \, K_{s\ell} \, K_{\ell n}} \tag{4.13.16}$$

$$C_s = \frac{C}{\frac{n_D \, s_\ell}{\rho_s \, K_{s\ell}} + \frac{n_D \, s_g \, K_{g\ell}}{\rho_s \, K_{s\ell}} + \frac{n_D \, s_n}{\rho_s \, K_{s\ell} \, K_{\ell n}} + \left(1 - n_T\right)} \tag{4.13.17}$$

$$R_D = 1 + \frac{\left(1 - n_T\right) \rho_s \, K_{s\ell}}{n_D \, s_\ell} \tag{4.13.18}$$

For the Water and Water-Air operational modes, an additional model for describing solute distribution is available, which differs from the above model in the extent of the wetting surface for unsaturated conditions. The above model contains the inherent assumption that all of the soil surfaces remain wetted regardless of the aqueous saturation. Another approach involves scaling the wetted surface with saturation, which yields an expression for the solid-aqueous distribution coefficient according to Equation (4.13.19). Using this expression for the solid-aqueous distribution coefficient yields expressions for aqueous-, gas-, and solid-volumetric concentrations, as shown in Equations (4.13.20) through (4.13.22), respectively. The retardation coefficient for the water mode is computed according to (4.13.23).

$$K_{s\ell} = \frac{C_s}{C_\ell \, \rho_s \, s_\ell} \tag{4.13.19}$$

$$C_\ell = \frac{C}{n_D \, s_\ell + n_D \, s_g \, K_{g\ell} + \left(1 - n_T\right) \rho_s \, s_\ell \, K_{s\ell}} \tag{4.13.20}$$

$$C_g = \frac{C}{\frac{n_D \, s_\ell}{K_{g\ell}} + n_D \, s_g + \frac{\left(1 - n_T\right) \rho_s \, s_\ell \, K_{s\ell}}{K_{g\ell}}} \tag{4.13.21}$$

$$C_s = \frac{C}{\frac{n_D}{\rho_s \, K_{s\ell}} + \frac{n_D \, s_g \, K_{g\ell}}{\rho_s \, s_\ell \, K_{s\ell}} + \left(1 - n_T\right)} \tag{4.13.22}$$

$$R_D = 1 + \frac{\left(1 - n_T\right) \rho_s \, K_{s\ell}}{n_D} \tag{4.13.23}$$

For the nonlinear Freundlich and Langmuir isotherms, the associated retardation coefficients are expressed in Equation (4.13.24) and (4.13.25), respectively.

$$R_D = \left[1 + \frac{K_{sl}[2] K_{sl}[1] C_l^{K_{sl}[2]}}{s_l n_D}\right] \tag{4.13.24}$$

$$R_D = \left[1 + \frac{K_{sl}[3]}{s_l n_D \left(1 + K_{sl}[4] C_l\right)^2}\right] \tag{4.13.25}$$

4.14 Solute Diffusion Coefficients

Solute diffusion coefficients are computed with the assumption of infinite dilution. The present version of the simulator additionally ignores phase compositional effects. The effects of temperature and pressure on solute diffusion coefficients, however, are considered. Aqueous diffusivity is expressed as a function of temperature and solvent viscosity following the theory of Wilke and Chang [Reid et al. 1987] according to Equation (4.14.1). Reference values for diffusion coefficients in liquid solvents can be estimated from the method of Wilke and Chang [Reid et al. 1987] according to Equation (4.14.2). For diffusion of solutes through the gas phase, the diffusivity is expressed as a function of temperature and pressure following the model of Fuller [Reid et al. 1987], according to Equation (4.14.3). Reference values for diffusion coefficients in gas solvents can be estimated from the method of Slattery and Bird [1958] according to Equation (4.14.4). NAPL diffusivity is expressed as a function of temperature and solvent viscosity following the theory of Wilke and Chang [Reid et al. 1987] according to Equation (4.14.5).

$$D_\ell^C = \overline{D}_\ell^C \frac{T}{\overline{T}} \frac{\overline{\mu}_\ell}{\mu_\ell} \tag{4.14.1}$$

$$\overline{D}_\gamma^C = \frac{7.4\ x\ 10^{-9} \left(\phi_\gamma\ M_\gamma\right)^{1/2} T}{\mu_\gamma \left(\upsilon_b^C\right)^{0.6}}, \quad for\ \gamma = \ell, n \tag{4.14.2}$$

where,

$\phi_\ell = 2.6$ *for water*, $\phi_n = 1.9$ *for methanol*,
$\phi_n = 1.6$ *for ethanol*, *and* $\phi_n = 1.0$ *for unassociated*

$$D_g^C = \overline{D}_g^C \frac{\overline{P}}{P} \left(\frac{T}{\overline{T}}\right)^{1.75} \tag{4.14.3}$$

$$D_g^C = 2.745\ x\ 10^{-4} \left[\frac{\left(\frac{P_c^C\ P_c^g}{\left(P_{atm}\right)^2}\right)^{1/3} \left(T_c^C\ T_c^g\right)^{5/12} \left(\frac{1}{M^C} + \frac{1}{M_g}\right)^{1/2}}{\left(\frac{P}{P_{atm}}\right)}\right] \left[\frac{T}{\sqrt{T_c^C\ T_c^g}}\right]^{1.823} \tag{4.14.4}$$

$$D_n^C = \overline{D}_n^C \frac{T}{\overline{T}} \frac{\overline{\mu}_n}{\mu_n} \tag{4.14.5}$$

For the Two-Phase Nonvolatile operational mode an alternate expression for aqueous-phase diffusion is available. The effective aqueous diffusion coefficient is defined according Equation (4.14.6) and represents the aqueous diffusivity for variably saturated porous media. An alternate expression for the effective aqueous diffusion coefficient, which is dependent on soil-solute combinations, is shown in Equation (4.14.7).

$$D_{\ell e}^C = \tau_\ell \, s_\ell \, n_D \, D_\ell^C \tag{4.14.6}$$

$$D_{\ell e}^C = D_\ell^C \, a_s^C \exp\left(n_D \, s_\ell \, b_s^C\right) \tag{4.14.7}$$

4.15 Solute Chain Decay

Decay or generation of solutes occurs in the STOMP simulator through an Arrhenius type kinetic reaction according to Equation (4.15.1). The decay-rate constant can be related to the radionuclide half-life according to Equation (4.15.2). Production of progeny solutes from parent solutes is computed through an Arrhenius type kinetic reaction according to Equation (4.15.3), where the chain decay fraction is a function of the parent-progeny pair, and the subscripts j and k indicate parent and progeny solutes respectively.

$$\frac{\partial C}{\partial t} = -\lambda^C \, C \tag{4.15.1}$$

$$\lambda^C = \frac{\ln(2)}{T_{1/2}^C} \tag{4.15.2}$$

$$\frac{\partial C^k}{\partial t} = \lambda^j \, F^{jk} \, C^j \tag{4.15.3}$$

4.16 First-Order Reactions

The first-order and Monod chemical reaction model incorporated into the STOMP simulator solves a series of chemical reactions of the general form shown in Equation (4.16.1)

$$N_{pr} A_{pr} + \sum_{\text{reactants}} N_r A_r \qquad \sum_{\text{products}} N_p A_p \tag{4.16.1}$$

For first-order reactions, the reaction rate for each chemical reaction is dependent on the molar concentration of the primary reactant according to Equations (4.16.2) through (4.16.4)

$$\frac{dC_{pr}}{dt} = -\frac{C_{pr} \ln(2)}{t_{pr}^{1/2}} \tag{4.16.2}$$

$$\frac{dC_r}{dt} = -\frac{C_{pr} \ln(2) N_r f_{pr}}{t_{pr}^{1/2} N_{pr}} \tag{4.16.3}$$

$$\frac{dC_p}{dt} = \frac{C_{pr} \ln(2) N_p f_{pr}}{t_{pr}^{1/2} N_{pr}} \tag{4.16.4}$$

The reaction rate factor is a function of the primary and secondary reactant molar concentrations, equation stoichiometry, reaction half-life, and simulation time step according to Equations (4.16.5) and (4.16.6):

$$f_{pr} = \left[1 + \left(g_{pr}\right)^2\right]^{-1/2} \tag{4.16.5}$$

$$g_{pr} = \max\left[\frac{C_{pr} \ln(2) N_r \Delta t}{t_{pr}^{1/2} C_r N_{pr}}\right] \tag{4.16.6}$$

The right-hand-side of Equation (4.16.6) represents the ratio of the molar amount of secondary reactant which could be consumed over the amount of secondary reactant available. The reaction rate function, see Equation (4.16.5), has the effect of modulating the reaction rate from first-order kinetics under conditions for which at least one of the secondary reactants nears being totally consumed.

4.17 Kinetic Dissolution/Solubilization of Oil

Several theoretical and experimental studies have shown that the aqueous-phase concentrations of dissolved oil can be significantly lower than equilibrium conditions for relatively large entrapped NAPL ganglia, high groundwater velocities, or low NAPL saturations [e.g., Mayer and Miller 1996]. These studies often yield formulations for mass transfer

correlations between the NAPL and aqueous phases, that relate the mass transfer coefficient, in dimensionless form as the Sherwood number *Sh,* to other system properties. Two general forms of these correlations have been incorporated into the Water-Oil-Dissolved Oil and the Water-Oil-Dissolved Oil-Surfactant operational modes. The first form, shown in Equation (4.17.1), is based on the Gilland-Sherwood formulation, which is typically applied to describing mass transport through liquid boundary layers for laminar flows.

$$Sh = \frac{k_{n,\ell}^{do} d_p^{\,2}}{D_{m\ell}^{do}} = a + bRe^m\, Sc^n \tag{4.17.1}$$

where the parameters *a, b, m,* and *n* are determined empirically. The second form, as shown in Equation (4.17.2) depends on the NAPL saturation as

$$Sh = \frac{k_{n,l}^{do} d_p^2}{D_{ml}^{do}} = a + bRe^m \left(n_D s_n\right)^n \tag{4.17.2}$$

where the Schmidt number *Sc* is replaced by the NAPL content. Implementation of Equations (4.17.1) and (4.17.2) indicate that similar mass transfer relations are assumed for oil dissolution and micellar solubilization although Abriola et al. [1993] stated that, based on detailed experiments, the mechanisms governing both processes are probably fundamentally different. Since more appropriate equations for micellar solubilization are currently lacking, it was decided to compute oil dissolution and micellar solubilization using similar relations.

Several authors [e.g., Pennell et al., 1993] have shown that the equilibrium concentration of solubilized oil in the aqueous phase is a linear function of the surfactant concentration above the critical micellar concentration (CMC). The following linear expression is used in the simulator to relate the equilibrium concentration of dissolved oil with dissolved surfactant concentration

$$\overline{C}_\ell^{\,do} = a + b \max\left[\left(C_\ell^s - CMC\right), 0\right] \tag{4.17.3}$$

4.18 Mobilization of Nonaqueous Phase Liquids

Mobilization of entrapped NAPL has been shown to be depending on viscous, buoyancy and capillary forces through the total trapping number [Pennell et al. 1996] defined as

$$N_t = \sqrt{N_c^2 + 2N_c N_b \sin\varphi + N_b^2} \tag{4.18.1}$$

where the angle φ refers to the flow angle with respect to the horizontal (measured counter-clockwise). The capillary number is defined in terms of the magnitude of the aqueous flow and NAPL-aqueous interfacial tension as

$$N_c = \frac{|\mathbf{u}_l|\mu_l}{\sigma_{nl}\cos\theta} \tag{4.18.2}$$

and the he Bond number in terms of the NAPL-aqueous interfacial tension is defined as

$$N_b = \frac{(\rho_n - \rho_l) g k_{rl} \mathbf{k}_z}{\sigma_{nl}\cos\theta} \tag{4.18.3}$$

Effective residual NAPL saturation is computed as a function of the trapping number using the empirical correlation shown in Equation (4.18.4)

$$\bar{s}_{nr}^{max} = \min\left[s_n \frac{\bar{s}_{nr}^{max}\big|_{N_t=0}}{1 + \left(N_t / N_t^c\right)} \right] \tag{4.18.4}$$

Changes in the trapping number (e.g., via changes in the interfacial tension or aqueous flow rates) result in changes to the effective residual NAPL saturation, which in turn can alter the volumes of free and entrapped NAPL. Converting entrapped NAPL to free NAPL through this processes effectively mobilizes a portion of the entrapped NAPL. This type of relationship has been used by Delshad et al. [1996] in the UTCHEM code and has experimentally been verified by Pennell et al. [1996]. Introducing surfactants into aqueous phase liquids in three-phase systems reduces the interfacial tension between two phase pairs (i.e., gas-aqueous and NAPL-aqueous). Water is the primary constituent in the aqueous phase, but in the Water-Oil-Dissolved Oil-Surfactant operational mode it may also include dissolved amounts of surfactant, oil, and air. Changes in interfacial tension with surfactant concentration affect the mobilization of free and trapped NAPLs. These effects are modeled in the simulator through modifications to the saturation-capillary pressure (*s*-*P*) scaling factors and in the residual NAPL saturations.

To provide continuity between two-phase (aqueous-gas) and three-phase (aqueous-NAPL-gas) saturation systems the scaling factors are defined as [Lenhard 1994; Lenhard and Parker 1987]

$$\beta_{gn} = \frac{\bar{\sigma}_{ij}}{\sigma_{gn}}, \beta_{nl} = \frac{\bar{\sigma}_{ij}}{\sigma_{nl}}, \beta_{gl} = \frac{\bar{\sigma}_{ij}}{\sigma_{gl}} \tag{4.18.5}$$

where the interfacial tension between fluid pair *ij* refers to the fluid pair used to determine the s-P relation, which is typically the gas-aqueous pair. The s-P scaling factors are related by

$$\frac{1}{\beta_{gn}} + \frac{1}{\beta_{nl}} = \frac{1}{\beta_{gl}} \tag{4.18.6}$$

which implies the following relationship among the interfacial tensions

$$\sigma_{gn} + \sigma_{nl} = \sigma_{gl} \tag{4.18.7}$$

Adding surfactant to the aqueous phase produces a reduction in the interfacial tension of the gas-aqueous and NAPL-aqueous fluid pairs, which directly correspond to increases in the gas-aqueous and NAPL-aqueous s-P scaling factors. Continuity of saturation between two- and three-phase systems is achieved by using the saturation functions for both systems, and restricting the NAPL pressure to values greater than or equal to the critical NAPL pressure defined as

$$P_n^c = \max\left[\frac{\beta_{gn} P_g + \beta_{nl} P_l}{\beta_{gn} + \beta_{nl}}\right] \tag{4.18.8}$$

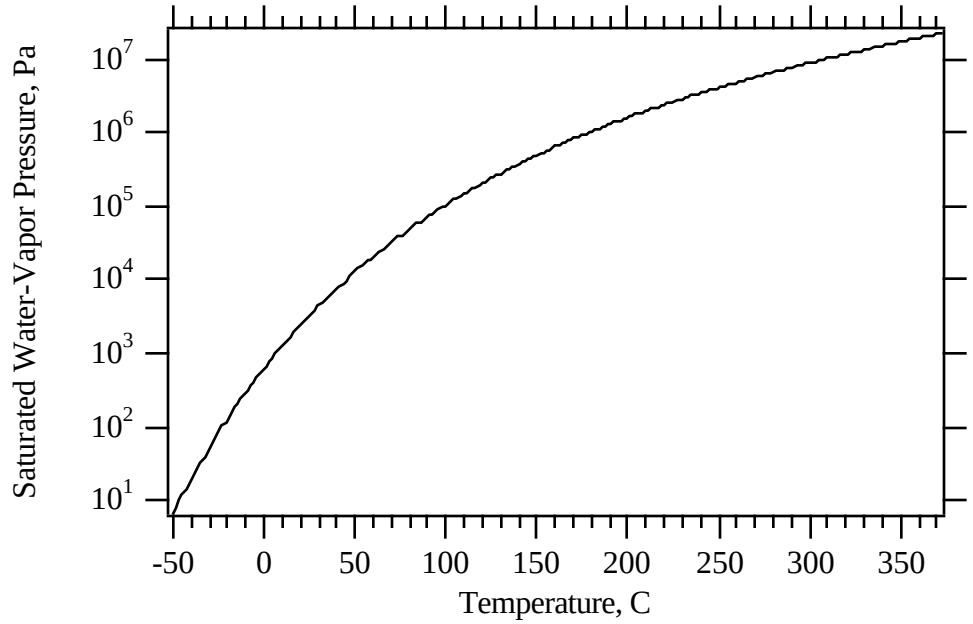

Figure 4.1. Saturated Vapor Pressure for Water

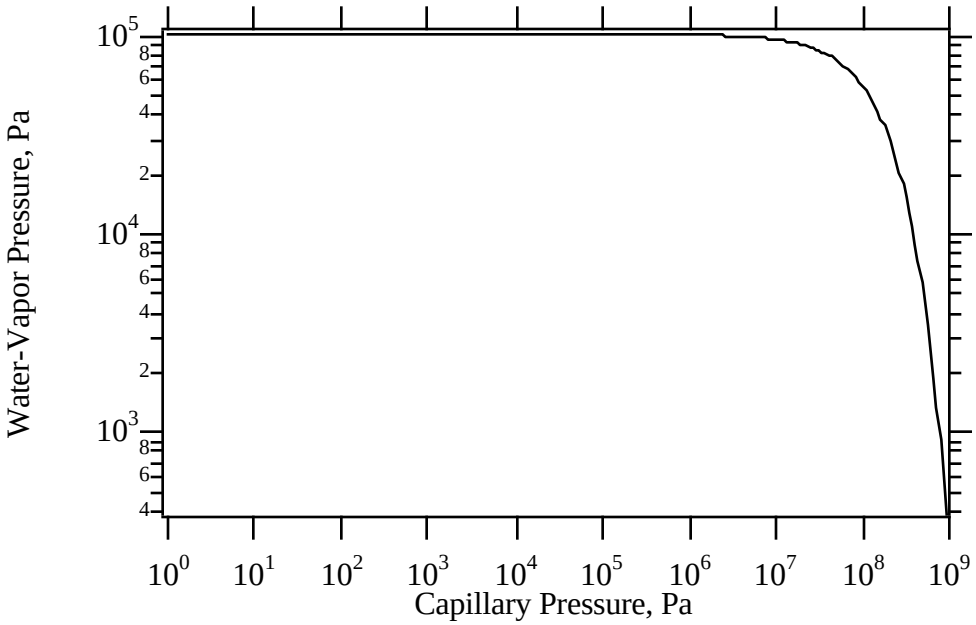

Figure 4.2. Vapor Pressure Lowering for Water @ 100 C

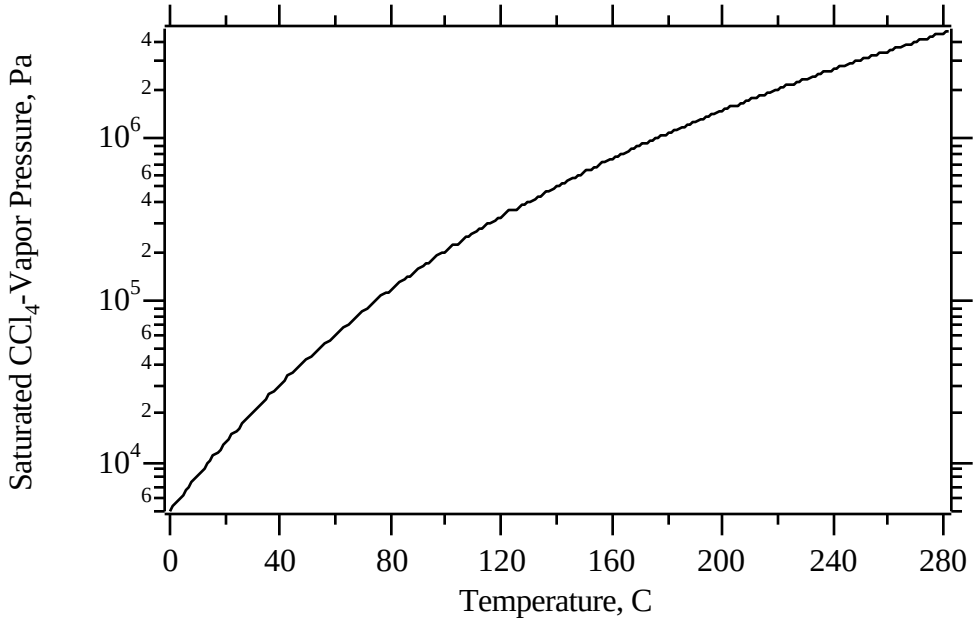

Figure 4.3. Saturated Vapor Pressure for Carbon Tetrachloride

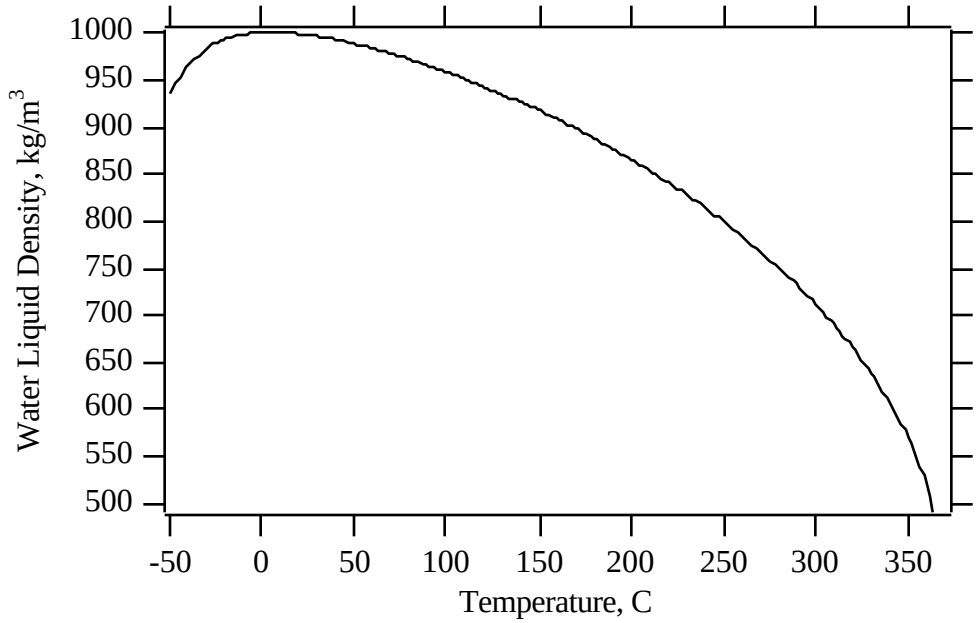

Figure 4.4. Saturated Liquid Density for Water

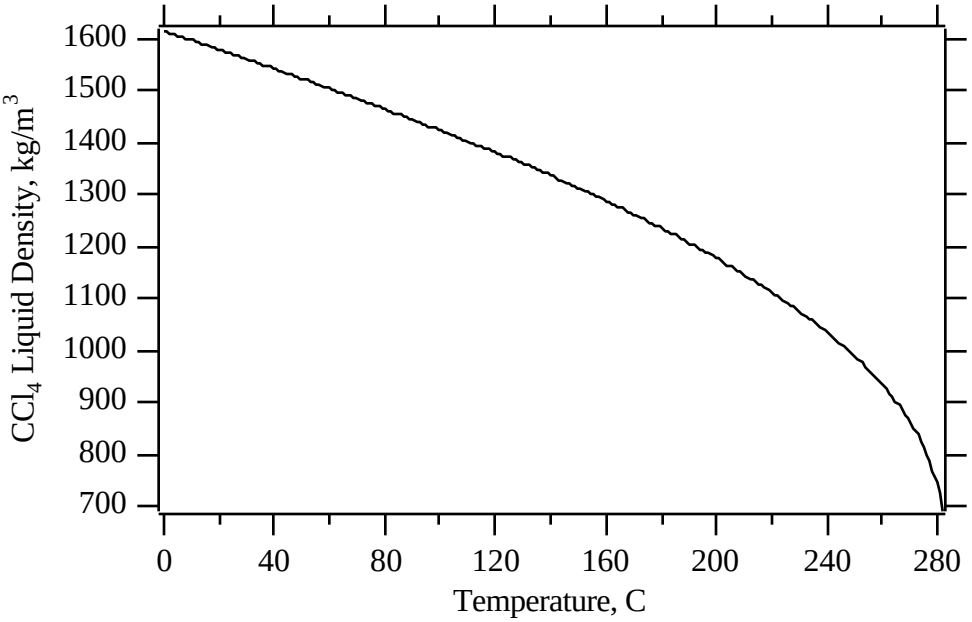

Figure 4.5. Saturated Liquid Density for Carbon Tetrachloride

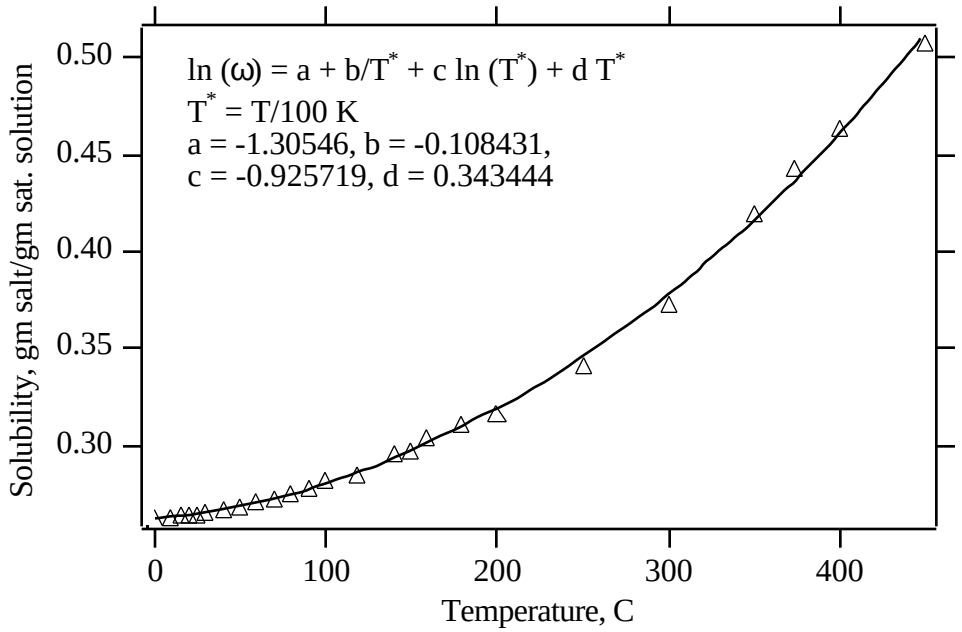

Figure 4.6. Solubility of Sodium Chloride in Water

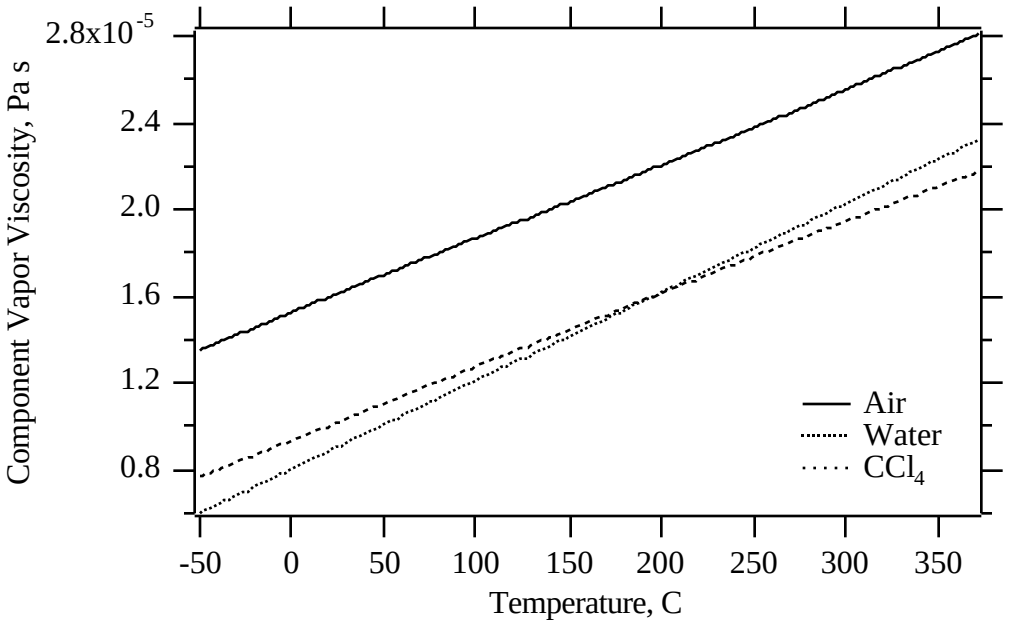

Figure 4.7. Component Vapor Viscosity for Air, Water, and Carbon Tetrachloride

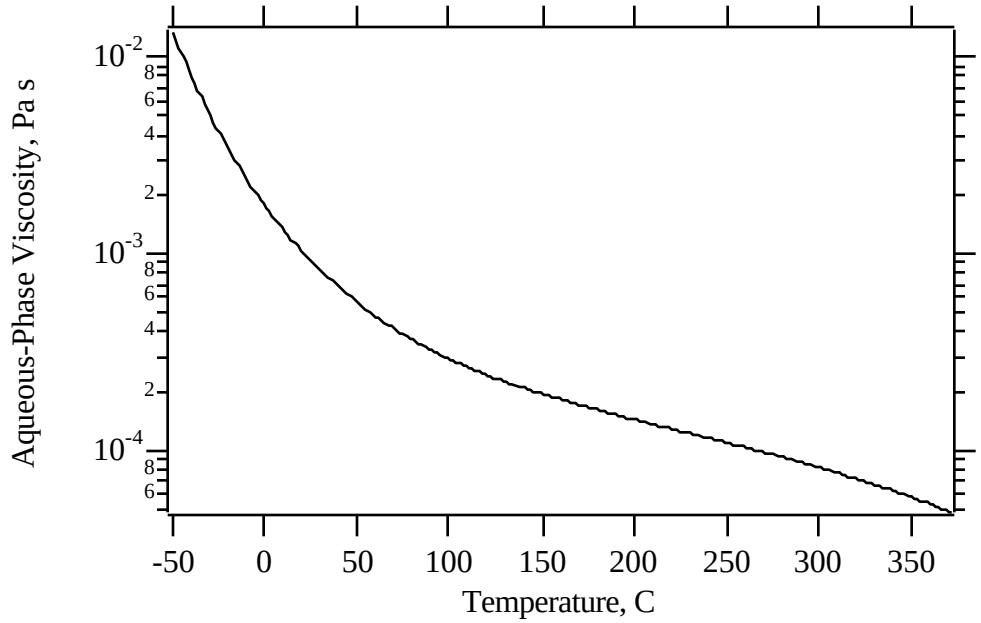

Figure 4.8. Saturated Liquid Viscosity for Water

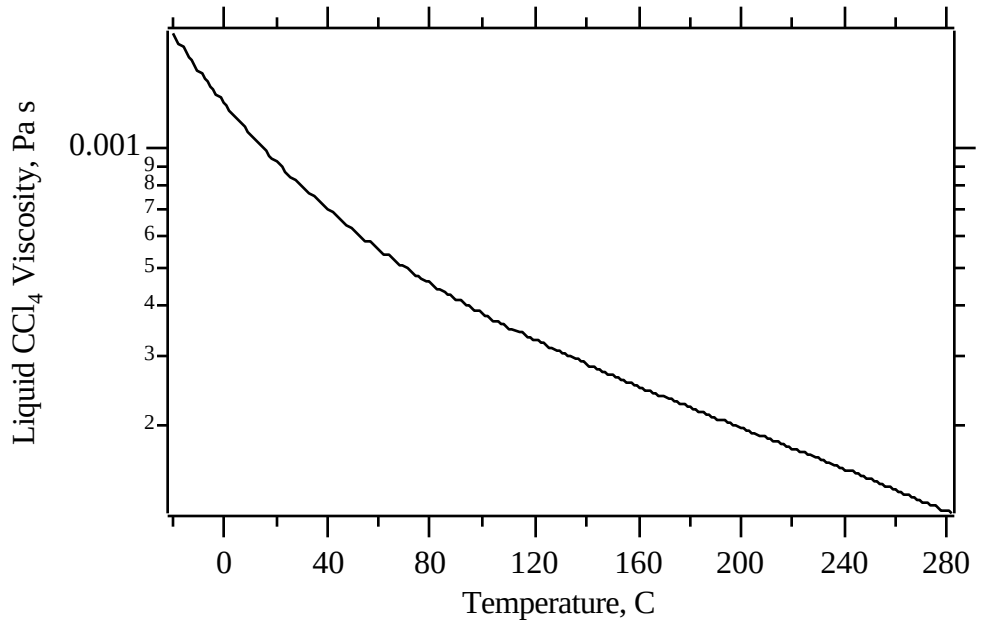

Figure 4.9. Saturated Liquid Viscosity for Carbon Tetrachloride

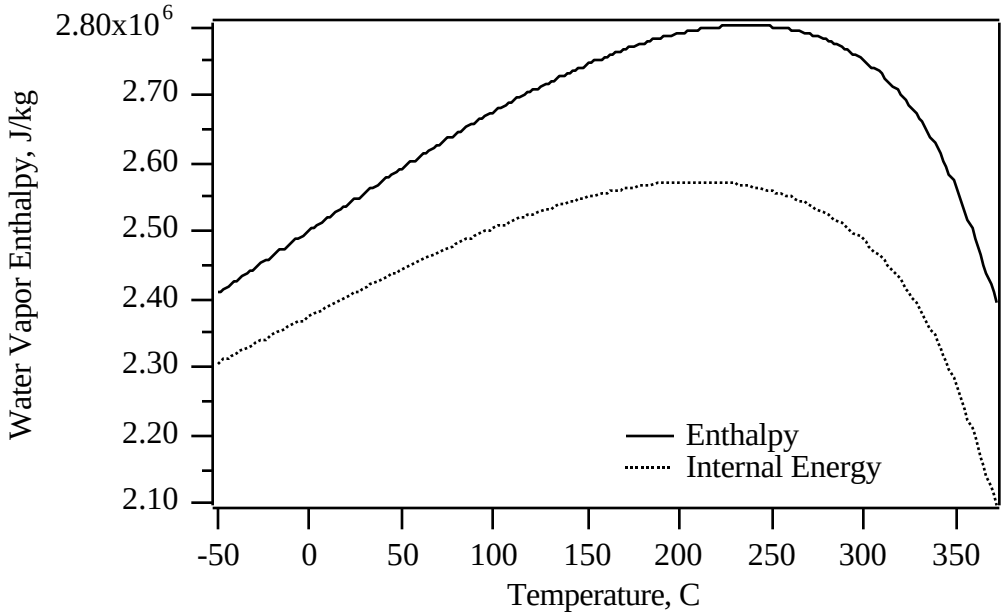

Figure 4.10. Saturated Vapor Enthalpy and Internal Energy for Water

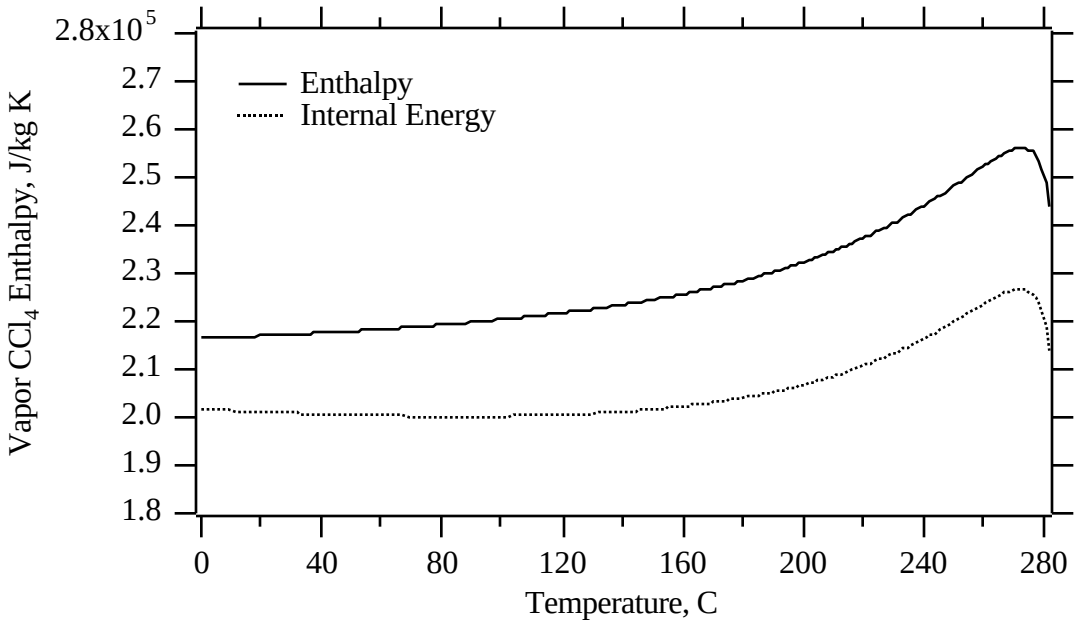

Figure 4.11. Vapor Enthalpy and Internal Energy for Carbon Tetrachloride

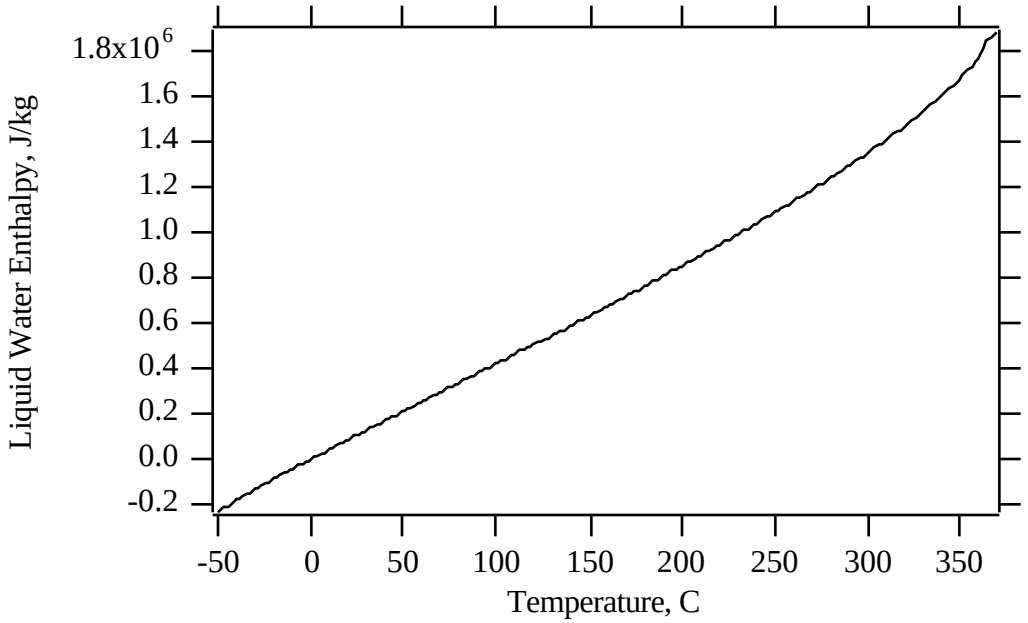

Figure 4.12. Saturated Liquid Enthalpy for Water

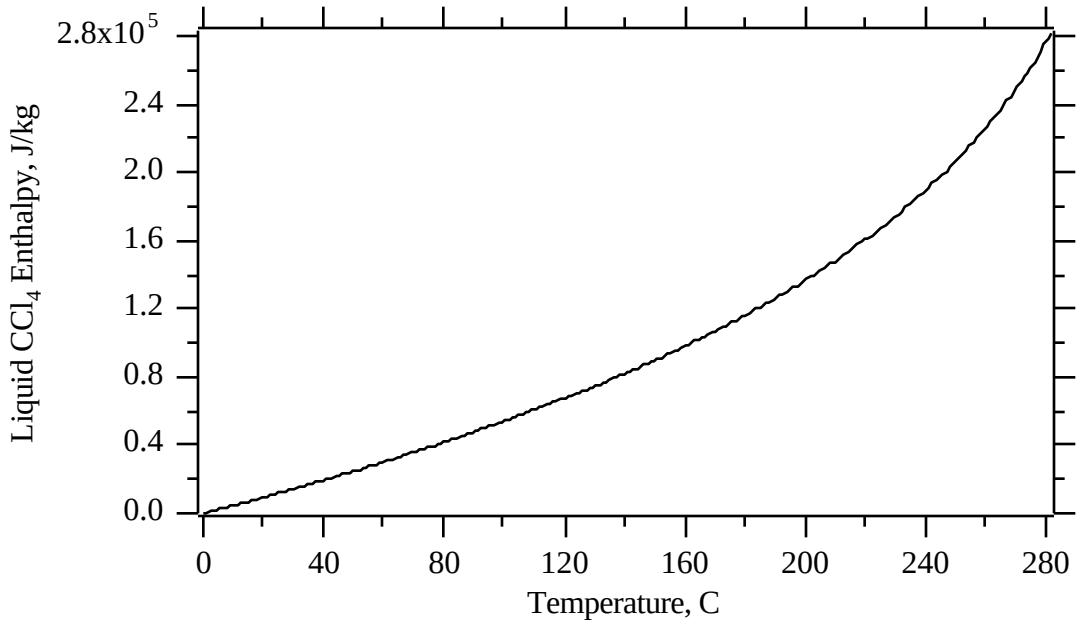

Figure 4.13. Saturated Liquid Enthalpy for Carbon Tetrachloride

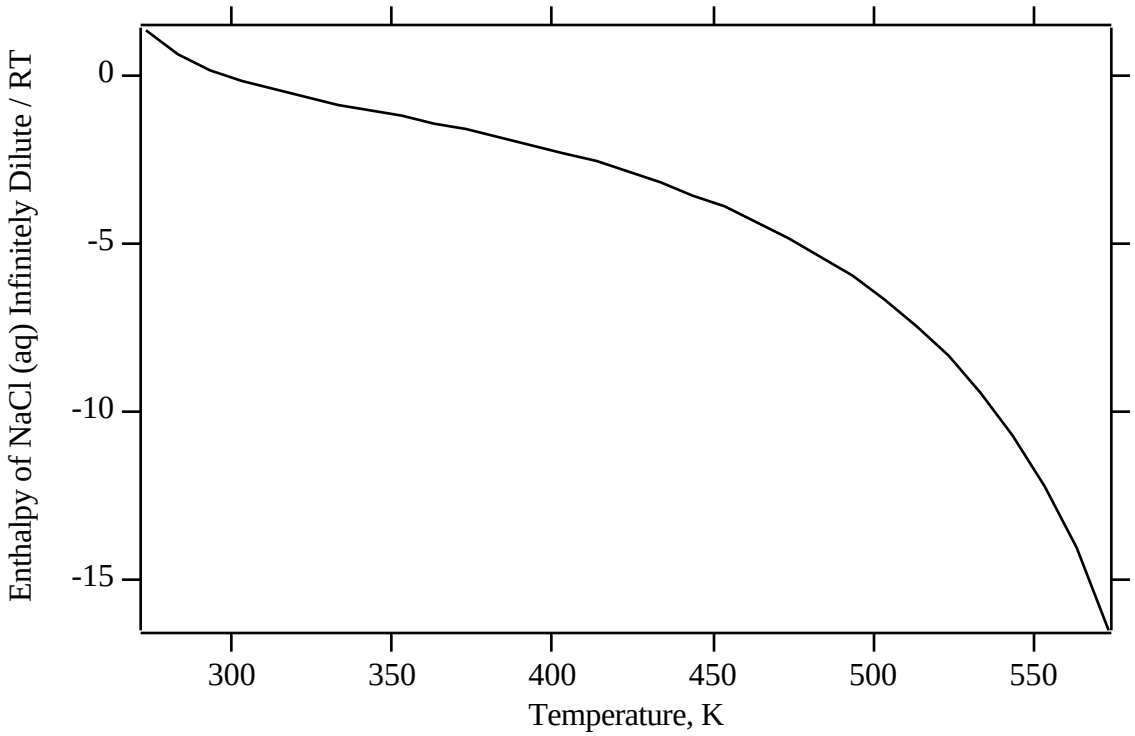

Figure 4.14. Enthalpy of Infinitely Dilute Aqueous Solutions of Salt (NaCl)

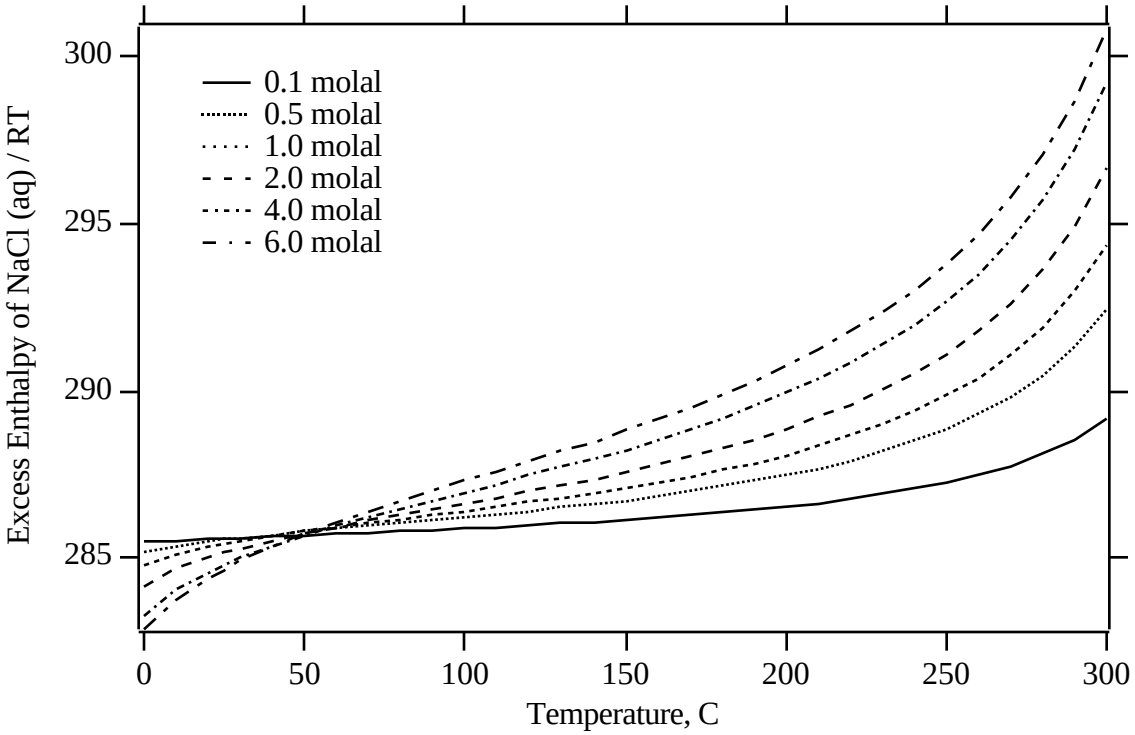

Figure 4.15. Excess Enthalpy of Aqueous Solutions of Salt (NaCl)

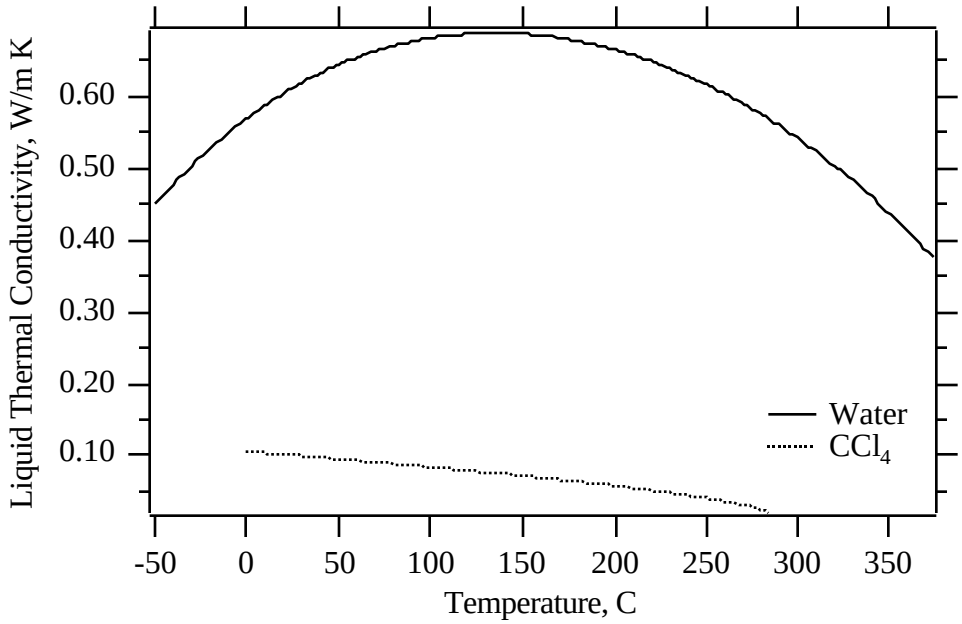

Figure 4.16. Saturated Liquid Thermal Conductivity for Water and Carbon Tetrachloride

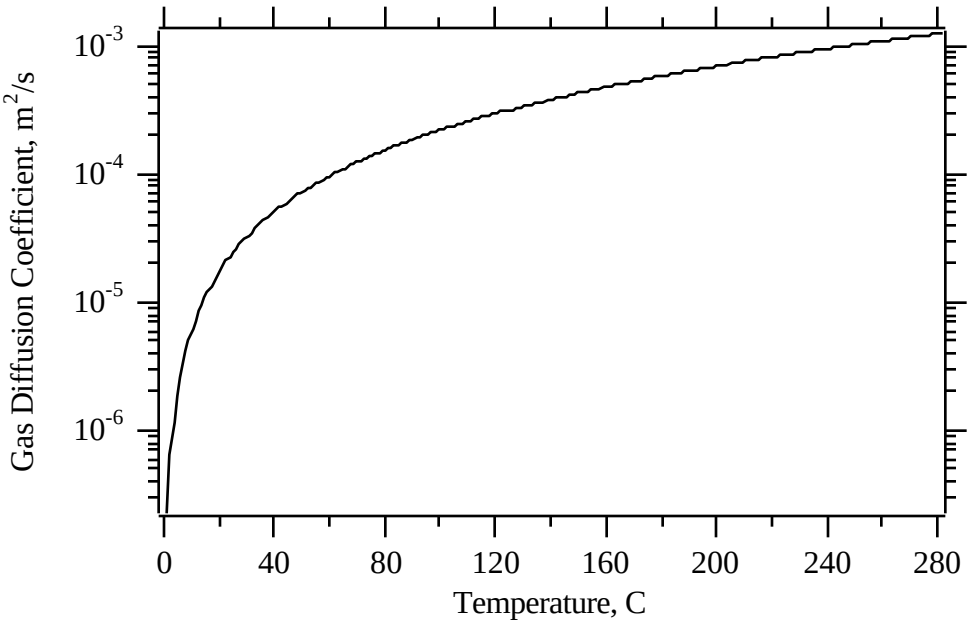

Figure 4.17. Binary Gas Diffusion Coefficient for Water and Carbon Tetrachloride

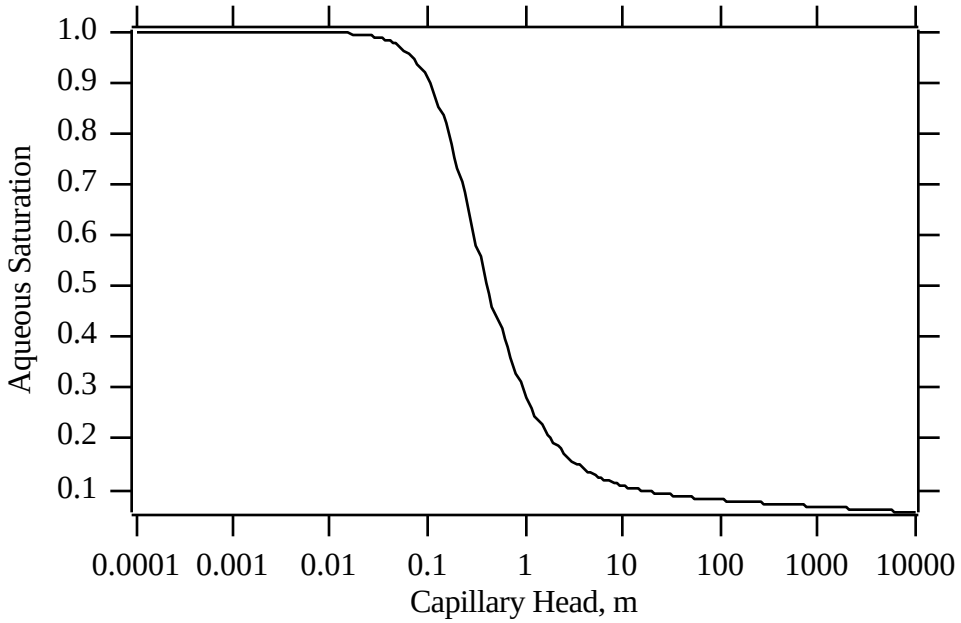

Figure 4.18. van Genuchten Saturation Function
$\alpha = 5\ m^{-1},\ n = 2,\ m = 2,\ s_m = 0.1$

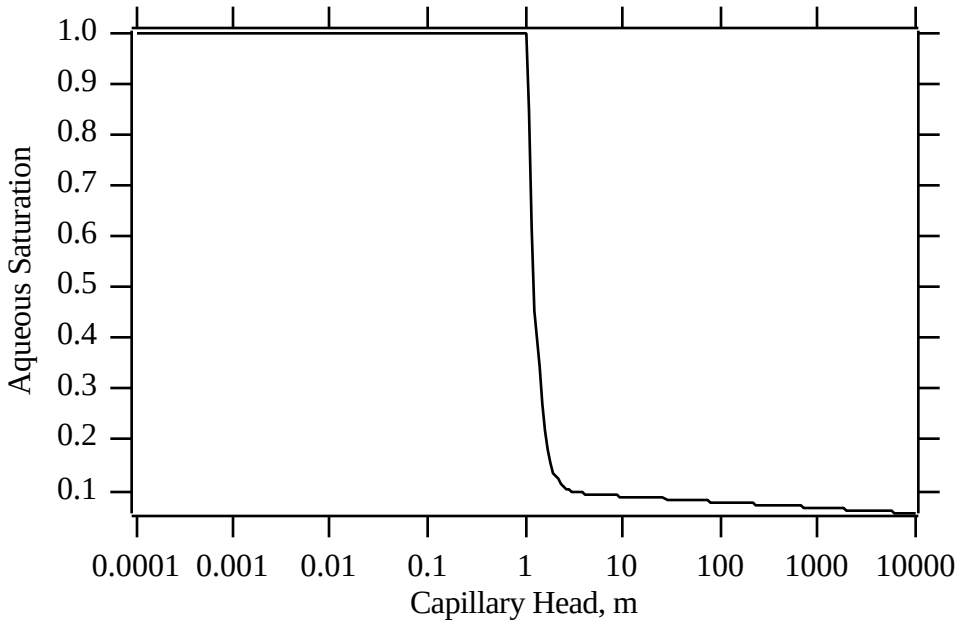

Figure 4.19. Brooks and Corey Saturation Function
$\psi = 1\ m,\ \lambda = 5,\ s_m = 0.1$

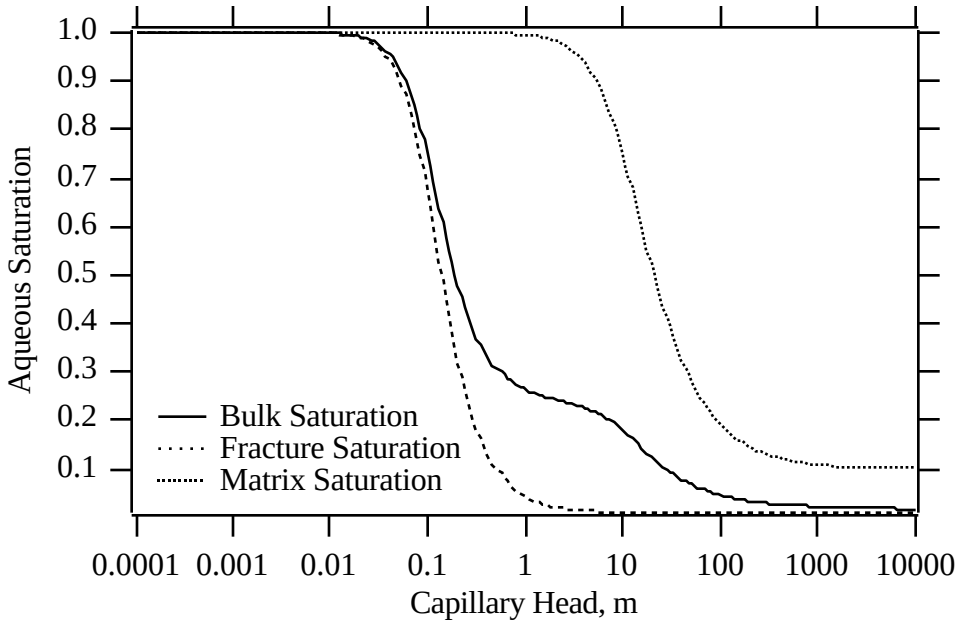

Figure 4.20. van Genuchten Dual Porosity Saturation Function
$n_{Df} = 0.25,\ \alpha_f = 10\ m^{-1},\ n_f = 2.5,\ s_{mf} = 0.01$
$n_{Dm} = 0.1,\ \alpha_m = 0.1\ m^{-1},\ n_m = 2.0,\ s_{mm} = 0.1$

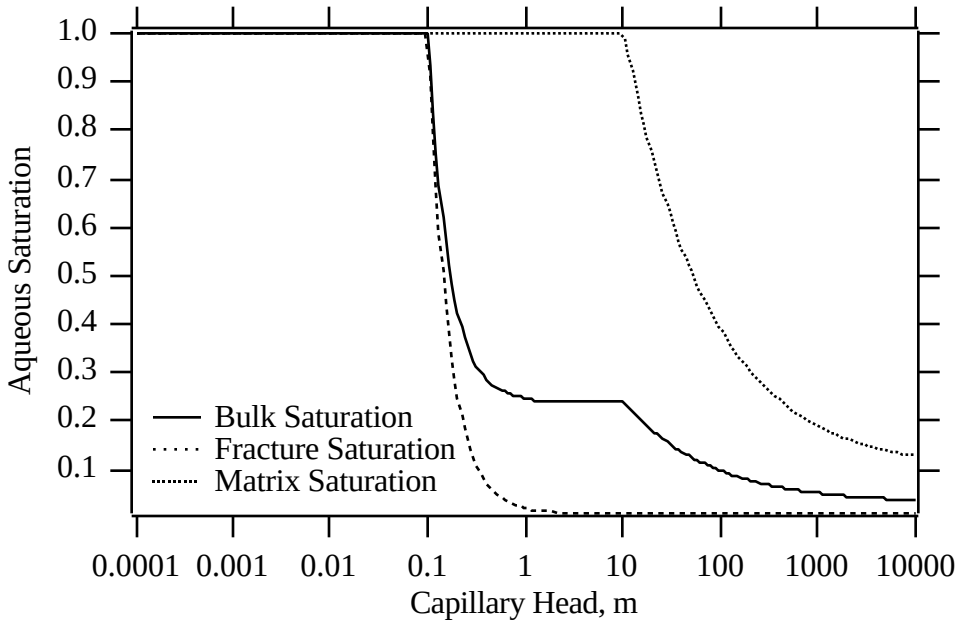

Figure 4.21. Brooks and Corey Dual Porosity Saturation Function
$n_{Df} = 0.25,\ \psi_f = 0.1\ m,\ \lambda_f = 2.0,\ s_{mf} = 0.01$
$n_{Dm} = 0.1,\ \psi_m = 10.0\ m,\ \lambda_m = 0.5,\ s_{mm} = 0.1$

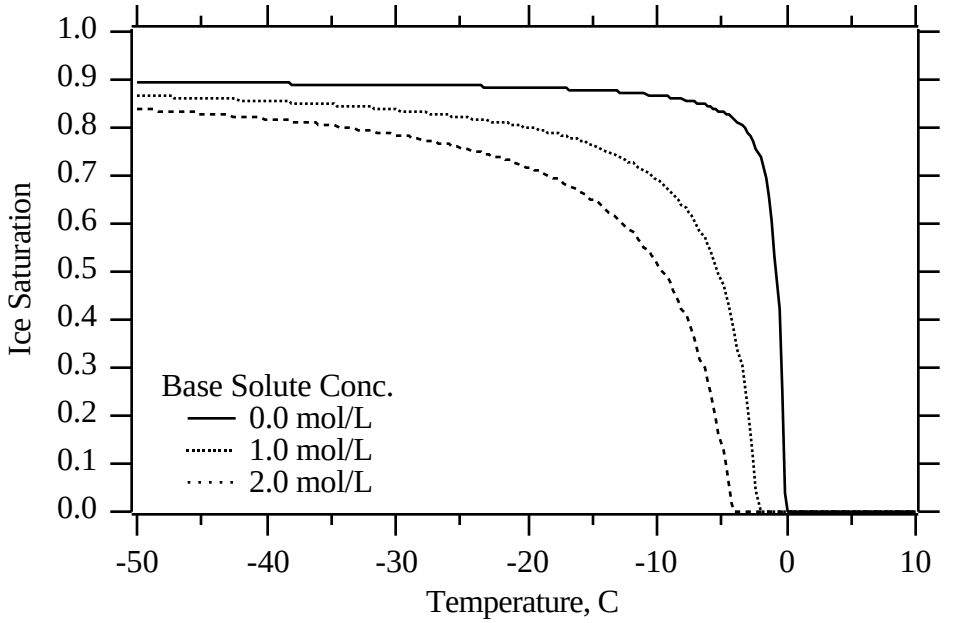

Figure 4.22. Ice Saturation for van Genuchten Saturation Function
$\alpha = 0.01\ m^{-1},\ n = 2,\ m = 1 - 1/n,\ s_\ell + s_i = 0.9,\ s_m = 0.1$

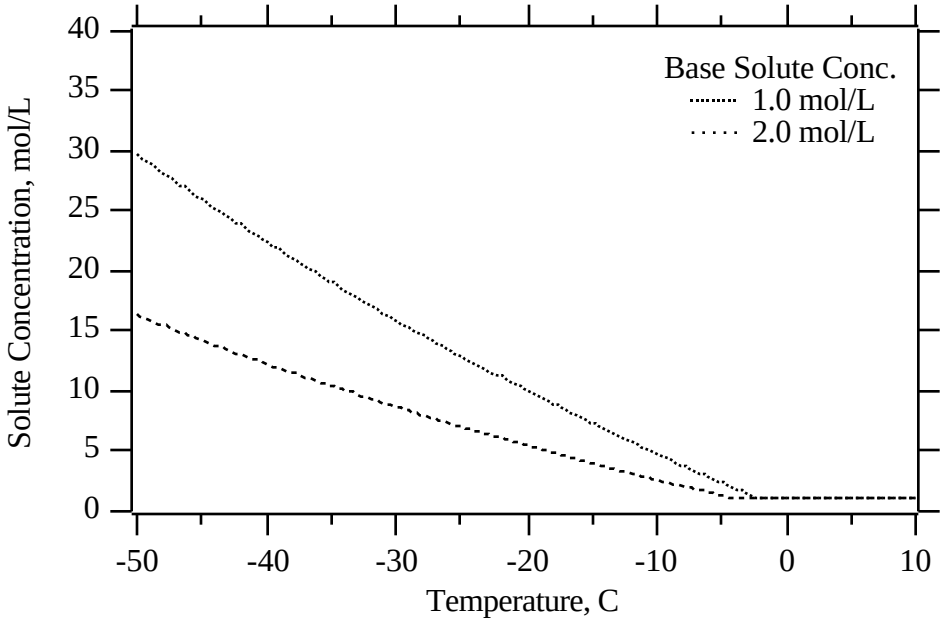

Figure 4.23. Solute Concentration for van Genuchten Saturation Function
$\alpha = 0.01\ m^{-1},\ n = 2,\ m = 1 - 1/n,\ s_\ell + s_i = 0.9,\ s_m = 0.1$

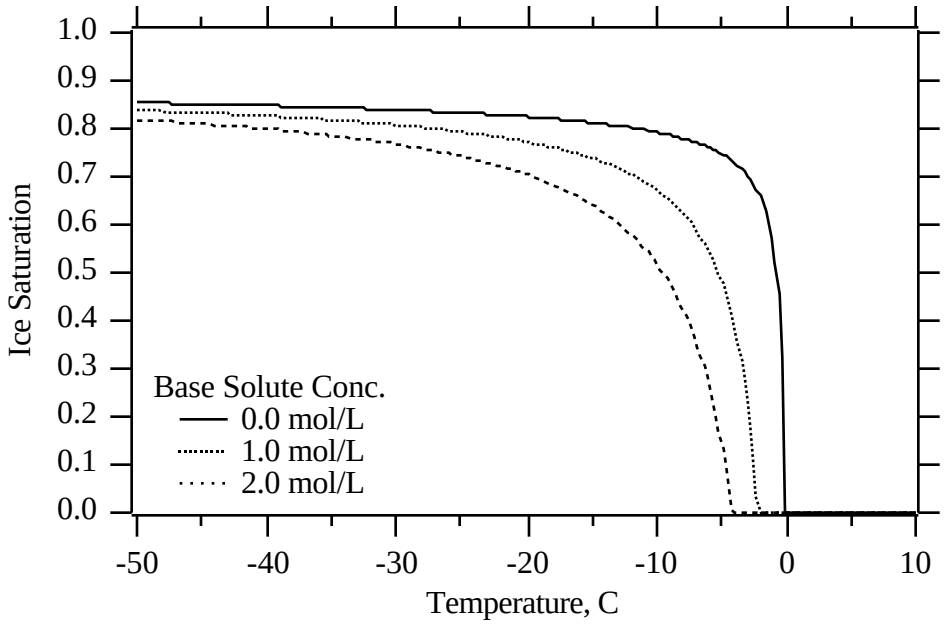

Figure 4.24. Ice Saturation for Brooks and Corey Saturation Function
$\psi = 39.23\ m,\ \lambda = 0.5,\ s_\ell + s_i = 0.9,\ s_m = 0.1$

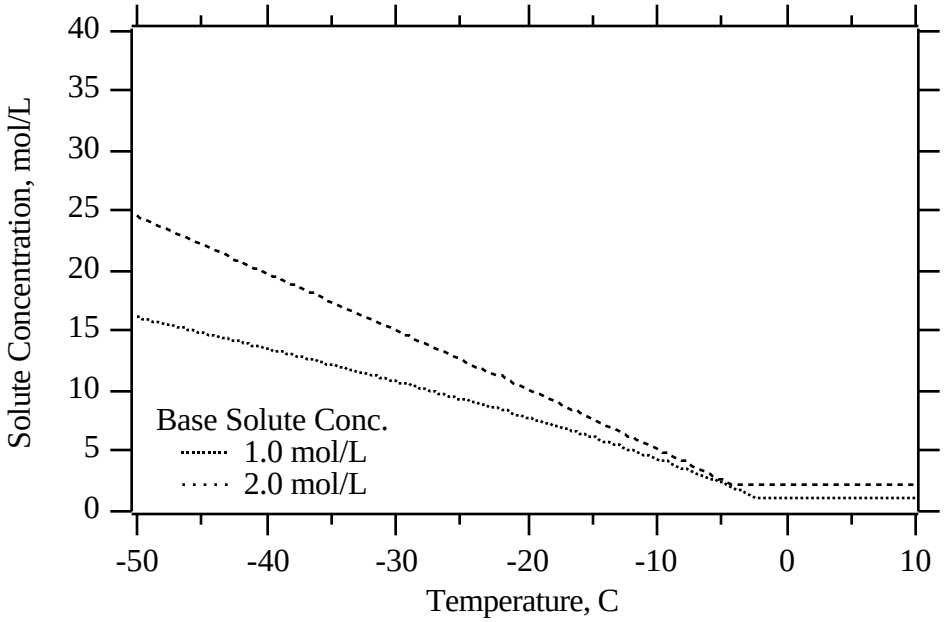

Figure 4.25. Solute Concentration for Brooks and Corey Saturation Function

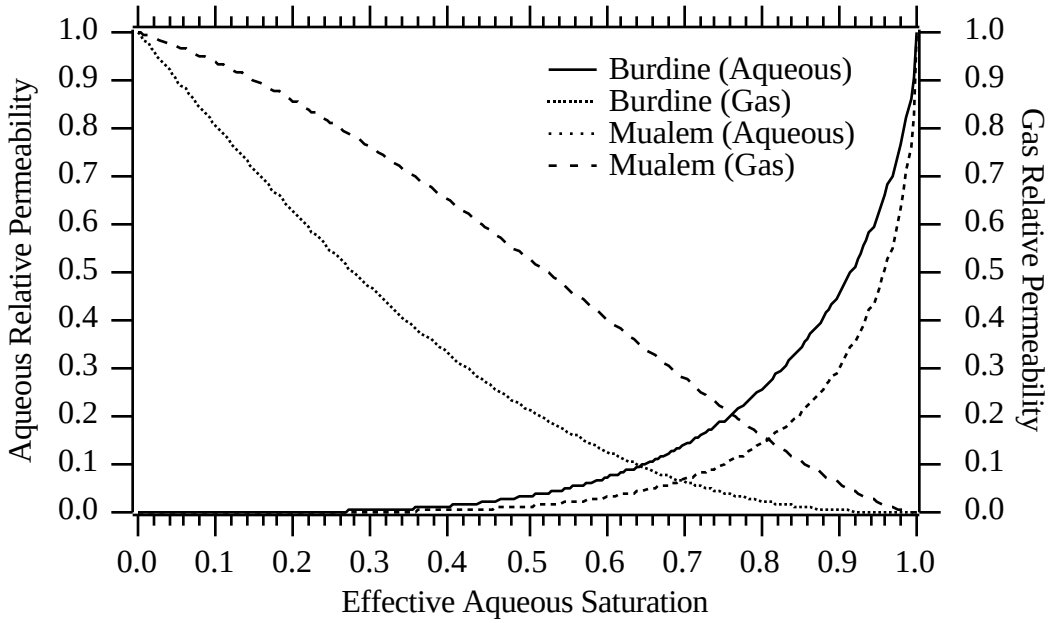

Figure 4.26. Aqueous and Gas Relative Permeability with van Genuchten Retention Function $m = 0.5$

5.0 Primary Variables and Phase Transitions

5.1 Introduction

Each governing conservation equation in the STOMP simulator is solved for one independent primary variable. For systems with multiple phases, the primary variable for a particular governing equation can vary between nodes within the computational domain, where primary variables are chosen by the simulator according to the local phase condition. This numerical solution scheme is frequently referred to as primary variable switching. The Gibbs phase rule [Wark, 1995], shown in Equation (5.1.1), states that the number of independent intensive properties required to fix the intensive state of a system equals the number of components plus two minus the number of phases. The number of independent intensive properties is frequently referred to as the degrees of freedom for the system. The thermodymanic and hydrologic state of a porous media system is specified when the number of independent intensive properties equals the number of degrees of freedom according to the phase rule. The number of solved conservation equations in the STOMP simulator equals the number of independent intensive properties less the number of intensive properties fixed through assumptions.

$$F = C + 2 - P \tag{5.1.1}$$

Phase transitions (i.e., phase appearances and disappearances) are characteristic phenomena of multiple phase systems, which require special numerical techniques to resolve. Historically, phase transitions have been handled by restricting phases from completely disappearing and/or through the application of primary variable switching schemes, where the solved primary variables change with the appearance or disappearance of a phase. The STOMP simulator uses a combination of these two techniques. For all operational modes and phase systems, the aqueous phase is restricted from completely disappearing. The aqueous-phase saturation is restricted to values greater than zero through the application of a vapor-pressure lowering scheme and the soil moisture-retention function. For nonisothermal systems, the aqueous-phase saturation is not artificially restricted to values above the residual or irreducible moisture content, but it is restricted to positive non-zero values. For operational modes involving the gas phase, no restrictions are placed on the appearance or disappearance of the gas phase. Gas-phase transitions are treated by switching the primary variable (unknown) for the air-mass conservation equation. Similarly, for operational modes involving NAPL, no restrictions are applied to the appearance or disappearance of NAPL. NAPL transitions are numerically treated with a switch in the primary variable for the oil-mass conservation equation.

5.2 Water-Air Systems

With the assumption that the aqueous-phase never completely disappears, phase transitions for water-air systems only involve the appearance, total entrapment, and disappearance of the gas-phase. Total entrapment of the gas phase is recognized only for hysteretic saturation functions. Under this condition, the apparent aqueous saturation equals one and the entrapped gas saturation becomes the unknown primary variable for the air-mass conservation equation. For two-phase porous media systems, phase saturations increase the number of degrees of freedom according to Equation (5.2.1).

$$F = C + 3 - P \tag{5.2.1}$$

The Water operational mode computes aqueous-phase flow and transport under the assumption of a passive gas phase. This operational mode involves one component (water) and one phase (aqueous); therefore, there are three degrees of freedom or three independent intensive variables which must be specified to fix the thermodynamic and hydrologic state of the system. The assumptions of isothermal conditions and a passive gas phase equate to a fixed temperature and gas pressure, which yields only one independent intensive variable to be solved. Because of the assumption that the aqueous phase never totally disappears, no phase transitions are associated with the Water operational mode and the water-mass conservation equation is solved for a single unknown: the aqueous pressure.

The Water-Air operational mode computes aqueous- and gas-phase flow and transport. This operational mode involves two components (water and air) and two phases (aqueous and gas); therefore, there are three degrees of freedom. The assumption of isothermal conditions fixes the temperature, which yields two independent intensive variables to be solved. Two-phase conditions are recognized with this operational mode: aqueous-phase saturated and unsaturated. Saturation functions with gas entrapment add an additional phase condition: aqueous-phase saturated, with entrapped gas. In the unsaturated state, aqueous and gas phases exist in equilibrium and the two primary variables are the aqueous and gas pressures. In the saturated state, the gas-phase has completely disappeared and the two primary variables become the aqueous pressure and mole-fraction of air dissolved in the aqueous phase. For saturation functions with gas entrapment, a phase condition is recognized which is characterized with an apparent aqueous saturation of one and total entrapment of the gas phase. In this phase, condition the entrapped gas and aqueous phase are in equilibrium and the primary variables become the aqueous pressure and entrapped gas saturation. These primary variable sets and phase condition descriptions are summarized in Table 5.1.

The Water-Air-Energy operational mode computes aqueous phase, gas phase, and energy flow and transport. This operational mode is similar to the Water-Air operational mode, with the exception that the system temperature becomes an additional independent variable, which

requires the solution of the energy conservation equation. As with the Water-Air operational mode, two- and three-phase conditions and associated primary variable sets are recognized, respectively, for nonhysteretic and hysteretic saturation functions. The primary variable sets and phase conditions for the Water-Air-Energy operational mode are summarized in Table 5.1.

Table 5.1. Water-Air System Primary Variables

Water Mode

Description	Primary Variable Set
Aqueous	P_ℓ
Aqueous w/ Entrapped Gas	P_ℓ

Water-Air Mode

Description	Primary Variable Set
Aqueous w/ Dissolved Air	P_ℓ, χ_ℓ^a
Aqueous w/ Entrapped Gas	P_ℓ, s_g
Aqueous-Gas	P_ℓ, P_g

Water-Air-Energy Mode

Description	Primary Variable Set
Aqueous w/ Dissolved Air	T, P_ℓ, χ_ℓ^a
Aqueous w/ Entrapped Gas	T, P_ℓ, s_g
Aqueous-Gas	T, P_ℓ, P_g

5.3 Water-Ice-Air Systems

Flow and transport in water-ice-air systems are computed by the Water-Air-Energy operational mode of the STOMP simulator. For water-ice-air systems, this operational mode involves two components (water and air) and three phases (aqueous, ice, and gas). Three-phase systems in porous media require two saturation-capillary pressure functions which adds two

additional constraints to the Gibbs phase rule as shown in Equation (5.3.1). The water-ice-air system, therefore, has three degrees of freedom and requires the solution of three conservation equations, water mass, air mass, and energy. Only nonhysteretic saturation functions are recognized by this operational mode for water-ice-air systems. With the assumption that the aqueous phase never completely disappears, important phase transitions are those between saturated and unsaturated conditions for the apparent aqueous saturation. No primary variable switching occurs for ice phase appearances and/or disappearances. The primary variable sets and phase condition descriptions for water-ice-air systems are shown in Table 5.2.

$$F = C + 4 - P \tag{5.3.1}$$

Table 5.2. Water-Ice-Air System Primary Variables

Water-Air-Energy Mode

Description	Primary Variable Set
Aqueous w/ Dissolved Air	T, P_ℓ, χ_ℓ^a
Aqueous-Gas	T, P_ℓ, P_g

5.4 Water-Oil Systems

The water-oil systems comprise five operational modes: Water-Oil, Water-Air-Oil, Water-Air-Oil-Dissolved Oil, Water-Oil-Dissolved Oil-Surfactant and Water-Air-Oil-Energy. With the assumption that the aqueous-phase never completely disappears, phase transitions for water-oil systems involve the appearance, total entrapment, and disappearance of both the NAPL and gas phase. The wettability order for these operational modes is assumed to decrease in the order of water to oil to air. Total entrapment of the nonwetting phases is recognized only for hysteretic saturation functions. The total entrapment and dissolution of nonwetting fluids represents two-phase condition transitions. During the transition from partial to total entrapment of a nonwetting fluid, a primary variable switch is made from pressure to saturation for the entrapped fluid. During the transition from total entrapment to total dissolution, a primary variable switch is made from saturation to mole fraction in the aqueous phase of a principal component. Three-phase systems in porous media require two saturation-capillary pressure functions, which adds two additional constraints to the Gibbs phase rule as shown in Equation (5.4.1).

$$F = C + 4 - P \tag{5.4.1}$$

The Water-Oil operational mode computes aqueous-phase and NAPL flow and transport under the assumption of a passive gas phase. This operational mode involves two components (water and oil) and two phases (aqueous and NAPL). Therefore, according to Equation (5.4.1), there are four degrees of freedom (independent intensive variables) which must be specified to fix the thermodynamic and hydrologic state of the system. The assumptions of isothermal conditions and a passive gas phase equate to a fixed temperature and gas pressure, yielding only two independent intensive variable to be solved. For nonhysteretic saturation functions, phase transitions are associated with the appearance and disappearance of NAPL. When the NAPL saturation is greater than zero, the primary unknown for one oil mass conservation equation is the NAPL pressure. When the NAPL saturation equals zero the primary unknowns for the oil mass conservation equation is the mole fraction of oil dissolved in the aqueous phase. For saturation functions with NAPL entrapment, additional phase transitions are recognized that involve the total entrapment of the NAPL by the aqueous phase. This phase condition represents and intermediate condition between free NAPL and dissolved oil. For this phase condition, the primary unknown for one oil mass conservation equation is the entrapped NAPL saturation. Primary variable sets and phase conditions for the Water-Oil operational mode are summarized in Table 5.3.

The Water-Oil-Air operational mode computes aqueous-phase, gas-phase, and NAPL flow and transport. This operational mode involves three components (water, air, and oils) and three phases (aqueous, gas, and NAPL). Therefore, according to Equation (5.4.1) there are four degrees of freedom (independent intensive variables) that must be specified to fix the thermodynamic and hydrologic state of the system. The assumption of isothermal conditions equates to a fixed temperature that leaves three independent intensive variables to be solved. For nonhysteretic saturation functions, phase transitions are associated with the appearance and disappearance of the gas phase and NAPL. When the total liquid saturation is less than one, the primary unknown for the air mass conservation equation is the gas pressure. For saturated total liquid conditions the primary unknown for the air mass equation switches to the mole fraction of air dissolved in the aqueous phase. Similarly, for the NAPL transitions, when the NAPL saturation is greater than zero the primary unknown for the oil mass conservation equation is the NAPL pressure. For NAPL saturations equal to zero, the primary unknown for the oil mass conservation equation is the component mole fractions dissolved in the aqueous phase. For saturation functions with fluid entrapment, additional phase transitions are recognized that involve the total entrapment of gas and NAPL by fluids of greater wettability. Total fluid entrapment conditions represent intermediate phase conditions between free-phase and aqueous-dissolved conditions. Under total fluid entrapment conditions the primary unknown variable becomes the saturation of the entrapped fluid. Primary variable sets and phase condition descriptions for the Water-Oil-Air operational mode are summarized in Table 5.3.

The Water-Oil-Air-Energy operational mode computes aqueous-, and gas-phase, NAPL and energy flow and transport. This operational mode is similar to the Water-Oil-Air operational mode, with the exception that the system temperature becomes an additional independent variable, which requires the solution of the energy conservation equation. As with the Water-Oil-Air operational mode, two- and three-phase conditions and associated primary variable sets are recognized, respectively, for nonhysteretic and nonwetting fluid entrapment saturation functions. The primary variable sets and phase conditions for the Water-Oil-Air-Energy operational mode are summarized in Table 5.3.

The Water-Oil-Dissolved Oil operational mode computes aqueous-phase, oil, and dissolved oil flow and transport. The dissolution process is assumed to be of kinetic nature. This operational mode involves three components (water, oil, and dissolved oil) and three phases (aqueous, gas, and NAPL). Therefore, according to Equation (5.4.1) there are four degrees of freedom (independent intensive variables) that must be specified to fix the thermodynamic and hydrologic state of the system. The assumption of isothermal conditions equates to a fixed temperature that leaves three intensive variables to be solved. For nonhysteretic saturation functions, phase transitions are associated with the appearance and disappearance of the gas phase and NAPL. For the NAPL transitions, when the NAPL saturation is greater than zero the primary unknown for the oil continuity equation is the NAPL pressure. The primary unknown for the dissolved oil mass conservation equation is always the mole fraction dissolved in the aqueous phase. For saturation functions with fluid entrapment, additional phase transitions are recognized that involve the total entrapment of gas and NAPL by fluids of greater wettability. Total fluid entrapment conditions represent intermediate phase conditions between free-phase and aqueous-dissolved conditions. Under total fluid entrapment conditions the primary unknown variable becomes the saturation of the entrapped NAPL. Primary variable sets and phase condition descriptions for the Water-Oil-Dissolved Oil operational mode are summarized in Table 5.3.

The Water-Oil-Dissolved Oil-Surfactant operational mode computes aqueous-phase, oil, dissolved oil, and surfactant flow and transport. The dissolution and solubilization processes are assumed to be of kinetic nature. This operational mode involves four components (water, oil, dissolved oil and surfactant) and three phases (aqueous, gas, and NAPL). Therefore, according to Equation (5.4.1) there are five degrees of freedom (independent intensive variables) that must be specified to fix the thermodynamic and hydrologic state of the system. The assumption of isothermal conditions equates to a fixed temperature that leaves four intensive variables to be solved. For nonhysteretic saturation functions, phase transitions are associated with the appearance and disappearance of the gas phase and NAPL. For the NAPL transitions, when the NAPL saturation is greater than zero the primary unknown for the oil continuity equation is the NAPL pressure. The primary unknown for the dissolved oil mass conservation equation is always the mole fraction dissolved in the aqueous phase. For the surfactant mass conservation equation, the primary unknow is always the surfactant mole fraction. For saturation functions

with fluid entrapment, additional phase transitions are recognized that involve the total entrapment of gas and NAPL by fluids of greater wettability. Total fluid entrapment conditions represent intermediate phase conditions between free-phase and aqueous-dissolved conditions. Under total fluid entrapment conditions the primary unknown variable becomes the saturation of the entrapped NAPL. Primary variable sets and phase condition descriptions for the Water-Oil-Dissolved Oil-Surfactant operational mode are summarized in Table 5.3.

Table 5.3. Water-Oil-Air System Primary Variables

Water-Oil Mode

Description	Primary Variable Set
Aqueous w/ Dissolved Oil	P_l, χ_l^o
Aqueous w/ Trapped NAPL	P_l, s_n
Aqueous-Gas w/ Dissolved Oil	P_l, χ_l^o
Aqueous-Gas w/ Trapped NAPL	P_l, s_n
Aqueous-NAPL	P_l, P_n
Aqueous-NAPL-Gas	P_l, P_n

Water-Oil-Air Mode

Description	Primary Variable Set
Aqueous w/ Dissolved Oil w/ Dissolved Air	P_l, χ_l^o, χ_l^a
Aqueous w/ Dissolved Oil w/ Trapped Gas	P_l, χ_l^o, s_g
Aqueous w/ Trapped NAPL w/ Dissolved Air	P_l, s_n, χ_l^a
Aqueous w/ Trapped NAPL w/ Trapped Gas	P_l, s_n, χ_l^a
Aqueous-Gas w/ Dissolved Oil	P_l, χ_l^o, P_g
Aqueous-Gas w/ Trapped NAPL	P_l, s_n, P_g
Aqueous-NAPL w/ Dissolved Air	P_l, P_n, χ_l^a
Aqueous-NAPL w/ Trapped Gas	P_l, P_n, s_g
Aqueous-NAPL-Gas	P_l, P_n, P_g

Water-Oil-Air-Energy Mode

Description	Primary Variable Set
Aqueous w/ Dissolved Oil w/ Dissolved Air	$T, P_l, \chi_l^o, \chi_l^a$
Aqueous w/ Dissolved Oil w/ Trapped Gas	T, P_l, χ_l^o, s_g
Aqueous w/ Trapped NAPL w/ Dissolved Air	T, P_l, s_n, χ_l^a
Aqueous w/ Trapped NAPL w/ Trapped Gas	T, P_l, s_n, χ_l^a
Aqueous-Gas w/ Dissolved Oil	T, P_l, χ_l^o, P_g
Aqueous-Gas w/ Trapped NAPL	T, P_l, s_n, P_g
Aqueous-NAPL w/ Dissolved Air	T, P_l, P_n, χ_l^a
Aqueous-NAPL w/ Trapped Gas	T, P_l, P_n, χ_l^a
Aqueous-NAPL-Gas	T, P_l, P_n, P_g

Water-Oil-Dissolved Oil Mode

Description	Primary Variable Set
Aqueous w/ Dissolved Oil	P_l, P_n, χ_l^o
Aqueous w/ Trapped NAPL w/ Dissolved Oil	P_l, s_n, χ_l^o
Aqueous-Gas w/ Dissolved Oil	P_l, P_n, χ_l^o
Aqueous-Gas w/ Trapped NAPL w/ Dissolved Oil	P_l, s_n, χ_l^o
Aqueous-NAPL w/ Dissolved Oil	P_l, s_n, χ_l^o
Aqueous-NAPL-Gas	P_l, s_n, χ_l^o

Water-Oil-Dissolved Oil-Surfactant Mode

Description	Primary Variable Set
Aqueous	$P_l, P_n, \chi_l^o, \chi_l^s$
Aqueous w/ Trapped NAPL	$P_l, s_n, \chi_l^o, \chi_l^s$
Aqueous-Gas	$P_l, P_n, \chi_l^o, \chi_l^s$
Aqueous-Gas w/ Trapped NAPL	$P_l, s_n, \chi_l^o, \chi_l^s$
Aqueous-NAPL	$P_l, P_n, \chi_l^o, \chi_l^s$
Aqueous-NAPL-Gas	$P_l, P_n, \chi_l^o, \chi_l^s$

6.0 Numerical Solution Theory

6.1 Introduction

The STOMP simulator solves the governing-conservation equations and constitutive functions using numerical techniques for nonlinear systems. This section documents the transformation of the governing-conservation equations from partial-differential form to algebraic form, algebraic expression of boundary conditions, linearization of the conservation equations and constitutive functions, and solution of linear systems.

The governing conservation equations are discretized to algebraic form following the integrated-finite-difference method of Patankar [1980]. This transformation requires that the physical domain be spatially discretized into an orthogonal computational domain which comprises nonoverlapping volumes (nodes). Each volume can have a maximum of two neighboring nodes for each dimensional direction. Intrinsic properties are assumed to be uniform over the volume domain and are defined for a node point at the geometric center of the volume. Flux quantities are defined at the geometric center of the surfaces between node volumes and along a direction parallel to the surface normal. Fluxes across node surfaces between neighboring inactive nodes and/or adjacent to the domain boundary are controlled through boundary conditions. Solution of the governing-conservation equations in time requires discretization of the time domain. The method of Patankar [1980] is implicit using backward Euler time differencing. The expressions that result from discretizing the governing equations are nonlinear algebraic equations.

The STOMP simulator considers two-orthogonal grid systems: Cartesian and cylindrical. Coordinate directions for Cartesian systems follow the “right-hand” rule from the “x” to “y” to “z” directions. Positive and negative directions along the “x,” “y,” and “z” coordinates are referred to as “east,” “west,” “north,” “south,” “top,” and “bottom,” respectively. The gravitational vector can be aligned arbitrarily with respect to the Cartesian directions. Coordinate directions for cylindrical systems are referred to as “r” for radial, “Θ” for azimuthal, and “z” for vertical. The gravity vector for the cylindrical system is always aligned with the “z” coordinate direction.

The system of algebraic equations that include the discretized governing-conservation equations and the constitutive functions are nonlinear. Nonlinearities in the soil-moisture retention functions, relative permeability functions, and physical properties near phase transitions are the primary contributors. Conversion of the algebraic equations from nonlinear to linear form follows the iterative Newton-Raphson [Kreyszig 1979] technique for multiple variables. The technique typically yields quadratic convergence of the residuals, given sufficiently close estimates of the primary unknowns. Each iteration loop requires the solution

of a system of linear equations in terms of the equation residuals. Because only orthogonal grid systems are considered, the system of linear equations will have a block-banded structure.

6.2 Governing Equation Discretization

The governing-conservation equations are discretized following the integrated finite difference of Patankar [1980], which is locally and globally conserving. Mass conservation equations for water, air, and VOC components are nearly identical in form, and therefore result in similar algebraic forms. The conservation equation for energy differs from the mass conservation equations having diffusive-dispersive and advective components. Discretization of combined diffusive and advective transport requires donor-cell weighting of the transport components, therefore yielding differ algebraic forms than those for the mass conservation equations. The conservation equation for solute or salt transport is similar in form to that of the energy conservation equation but its discretization uses a different donor-cell weighting scheme, therefore resulting in a separate algebraic form.

6.2.1 Mass Conservation Equation

The mass conservation equations, shown in Equations (3.2.1) through (3.4.1), are discretized by assuming a piecewise profile to express the variation in primary variables between node points and integrating over the node volume. The accumulation terms (i.e., left-hand-side terms) are integrated over the node volume according to Equation (6.2.1), where the specific terms for the water, air, and oil mass conservation equations appear as shown in Equations (6.2.2) through (6.2.4), respectively. Intrinsic properties for the node volume are represented by properties at the node centroid. Source terms are similarly integrated over the node volume according to Equation (6.2.5).

$$\frac{\partial}{\partial t}\left[\int_{\bar{V}} \bar{M}^{j}\, d\bar{V}\right] = \frac{\partial}{\partial t}\left[\bar{M}^{j}\,\bar{V}\right] \quad for\ j = w, a, o \tag{6.2.1}$$

$$\frac{\partial}{\partial t}\left[\bar{M}^{w}\,\bar{V}\right] = \frac{\partial}{\partial t}\left[\bar{V}\sum_{\gamma=\ell,g,i}\left(n_D\,\omega_{\gamma}^{w}\,\rho_{\gamma}\,s_{\gamma}\right)\right] \tag{6.2.2}$$

$$\frac{\partial}{\partial t}\left[\bar{M}^{a}\,\bar{V}\right] = \frac{\partial}{\partial t}\left[\bar{V}\sum_{\gamma=\ell,g}\left(n_D\,\omega_{\gamma}^{a}\,\rho_{\gamma}\,s_{\gamma}\right)\right] \tag{6.2.3}$$

$$\frac{\partial}{\partial t}\left[\overline{M}^{o}\,\overline{V}\right] = \frac{\partial}{\partial t}\left[\overline{V}\sum_{\gamma=\ell,g,n}\left(n_D\,\omega_\gamma^o\,\rho_\gamma\,s_\gamma\right)+\left(1-n_T\right)\omega_s^o\,\rho_s\right] \tag{6.2.4}$$

$$\int_{\overline{V}} \dot{m}^j\, d\overline{V} = \dot{m}^j\,\overline{V} \quad \textit{for } j = w, a, o \tag{6.2.5}$$

Flux terms are evaluated on the node surfaces and for the mass conservation equations comprise advective and diffusive components. Integration of the flux terms over the node volume proceeds by first converting the volumetric integral of flux over a control volume to a surface integral through Green's theorem [Kreyszig 1979] according to Equation (6.2.6). Discretizing the control volume surfaces into node surfaces and defining flux directions parallel to the surface normal allows the surface integrals to be converted to summations over all node surfaces, according to Equation (6.2.7). This transformation strictly requires an orthogonal grid system for the flux directions to be aligned with the surface normals. Nonorthogonal systems will yield mass balance errors. Darcy fluxes are discretized, in the six coordinated directions, using upwind interfacial averaging for the component mass fraction, phase density, and relative permeability and harmonic averaging for the intrinsic permeability and phase viscosity according to Equation (6.2.7). These default interfacial averaging schemes can be altered through user input. Diffusive fluxes are discretized, in the six coordinate directions, using harmonic averaging for the combination of terms which comprise an effective diffusion coefficient. The default interfacial averaging scheme can be altered for each parameter through user input. Geometric variables for a Cartesian coordinate system are shown in Figures 6.1 and 6.2 for the X-Z and Y-Z coordinate planes, respectively. Geometric variables for a cylindrical coordinate system are shown in Figures 6.3 and 6.4 for the R-Z and R-Θ coordinate planes, respectively.

$$\int_{\overline{V}}\left[\sum_{\gamma=\ell,g,n}\left(\mathbf{F}_\gamma^j + \mathbf{J}_\gamma^j\right)\right] d\overline{V} = \int_{\Gamma}\left[\sum_{\gamma=\ell,g,n}\left(\mathbf{F}_\gamma^j + \mathbf{J}_\gamma^j\right)\right]\mathbf{n}\, d\Gamma \quad \textit{for } j = w, a, o \tag{6.2.6}$$

where,

$$\mathbf{F}_\gamma^j = -\frac{\omega_\gamma^j\,\rho_\gamma\,k_{r\gamma}\,\mathbf{k}}{\mu_\gamma}\left(P_\gamma + \rho_\gamma\, g\,\mathbf{z}_g\right) \quad \textit{for } \gamma = \ell, g, n \textit{ and } j = w, a, o$$

$$\mathbf{J}_\gamma^j = -\tau_\gamma\, n_D\,\rho_\gamma\, s_\gamma\,\frac{M^j}{M_\gamma}\, D_\gamma^j \quad \chi_\gamma^j \quad \textit{for } \gamma = \ell, g, n \textit{ and } j = w, a, o$$

$$\int_{\Gamma} \left[\sum_{\gamma=\ell,g,n} \left(\mathbf{F}_{\gamma}^{j} + \mathbf{J}_{\gamma}^{j} \right) \right] \mathbf{n}\, d\Gamma = \sum_{\substack{\varsigma=W,E,S,\\ N,T,B}} \left[\sum_{\gamma=\ell,g,n} \left(F_{\gamma_\varsigma}^{j} + J_{\gamma_\varsigma}^{j} \right) \right] A_{\varsigma} \quad \text{for } j = w, a, o \tag{6.2.7}$$

where,

$$F_{\gamma_\varsigma}^{j} = -\frac{\left\langle \omega_{\gamma}^{j}\ \rho_{\gamma}\ k_{r\gamma} \right\rangle_{\varsigma}^{uw} \langle \mathbf{k} \rangle_{\varsigma}^{h}}{\left\langle \mu_{\gamma} \right\rangle_{\varsigma}^{h}} \left(\frac{P_{\gamma_{\varsigma^+}} - P_{\gamma_{\varsigma^-}}}{\delta x_{\varsigma}} + \left\langle \rho_{\gamma}\ g \right\rangle_{\varsigma}^{a} z_{g_{\varsigma}} \right)$$

for $\gamma = \ell, g, n$; $j = w, a, o$; *and* $\varsigma = E, W, S, N, B, T$

$$J_{\gamma_\varsigma}^{j} = -\left\langle \tau_{\gamma}\ n_D\ \rho_{\gamma}\ s_{\gamma}\ \frac{M^{j}}{M_{\gamma}}\ D_{\gamma}^{j} \right\rangle_{\varsigma}^{h} \frac{\chi_{\gamma_{\varsigma^+}}^{j} - \chi_{\gamma_{\varsigma^-}}^{j}}{\delta x_{\varsigma}}$$

for $\gamma = \ell, g, n$; $j = w, a, o$; *and* $\varsigma = E, W, S, N, B, T$

The mass conservation equations are discretized in time using a fully implicit scheme according to Equation (6.2.8), where the time levels are indicated with superscripts. The primary unknowns for the mass conservation equations are intrinsic properties at node volume centroids (node grid point) for time level $t+\delta t$. Converting Equation (6.2.8) to residual form yields the expression shown in Equation (6.2.9).

$$\begin{aligned} \bar{V}\left[\frac{\left\{ \bar{M}^{j} \right\}^{t+\delta t} - \left\{ \bar{M}^{j} \right\}^{t}}{\delta t} \right] &= \bar{V} \left\{ \dot{m}^{j} \right\}^{t+\frac{\delta t}{2}} \\ &- \sum_{\varsigma=W,E,S,N,T,B} \left[\sum_{\gamma=\ell,g,n} \left(\left[F_{\gamma_\varsigma}^{j} \right]^{t+\delta t} + \left[J_{\gamma_\varsigma}^{j} \right]^{t+\delta t} \right) \right] A_{\varsigma} \quad \text{for } j = w, a, o \end{aligned} \tag{6.2.8}$$

$$\begin{aligned} \left\{ \bar{R}^{j} \right\}^{t+\delta t} &= \bar{V}\left[\frac{\left\{ \bar{M}^{j} \right\}^{t+\delta t} - \left\{ \bar{M}^{j} \right\}^{t}}{\delta t} \right] - \bar{V} \left\{ \dot{m}^{j} \right\}^{t+\frac{\delta t}{2}} \\ &+ \sum_{\varsigma=W,E,S,N,T,B} \left[\sum_{\gamma=\ell,g,n} \left(\left[F_{\gamma_\varsigma}^{j} \right]^{t+\delta t} + \left[J_{\gamma_\varsigma}^{j} \right]^{t+\delta t} \right) \right] A_{\varsigma} \quad \text{for } j = w, a, o \end{aligned} \tag{6.2.9}$$

6.2.2 Energy Conservation Equation

The energy conservation equation, shown in Equation (3.5.1), is discretized by assuming a piecewise profile to express the variation in primary variables between node points and integrating over the node volume. The thermal capacitance terms (i.e., left-hand-side terms) and energy source terms are integrated over the node volume according to Equations (6.2.10) and (6.2.11), respectively.

$$\frac{\partial}{\partial t}\left[\int_{\bar{V}} \bar{E}\, d\bar{V}\right] = \frac{\partial}{\partial t}\left[\bar{E}\ \bar{V}\right] \tag{6.2.10}$$

where,

$$\bar{E} = \sum_{\gamma=\ell,g,n,i} \left(n_D\, \rho_\gamma\ s_\gamma\ u_\gamma\right) + \left(1 - n_T\right) \rho_s\, u_s + \left(n_T - n_D\right) \rho_\ell\, u_\ell$$

$$\int_{\bar{V}} \left[\sum_{j=w,a,o} \left(h^j\ \dot{m}^j\right) + \dot{q}\right] d\bar{V} = \left[\sum_{j=w,a,o} \left(h^j\ \dot{m}^j\right) + \dot{q}\right] \bar{V} \tag{6.2.11}$$

Thermal energy is transferred through advection and diffusion. Spatial discretization of the advective and diffusive thermal flux proceeds by first converting the volumetric integral of flux over a control volume to a surface integral using Green's theorem [Kreysig 1979], according to Equation (6.2.12). Surface integrals are approximated by discretizing the control volume surfaces into node surfaces and summing the contributions to heat flux over the node surfaces, according to Equation (6.2.13).

$$\begin{aligned} &\int_{\bar{V}} \left[-\sum_{\gamma=\ell,g,n} \left(\rho_\gamma\ h_\gamma\ \mathbf{V}_\gamma + \sum_{j=w,a,o} \left(h^j\ \mathbf{J}_\gamma^j\right)\right) + \left(\mathbf{k}_e \quad T\right)\right] d\bar{V} \\ &= \int_{\Gamma} \left[-\sum_{\gamma=\ell,g,n} \left(\rho_\gamma\ h_\gamma\ \mathbf{V}_\gamma + \sum_{j=w,a,o} \left(h^j\ \mathbf{J}_\gamma^j\right)\right) + \left(\mathbf{k}_e \quad T\right)\right] \mathbf{n}\, d\Gamma \end{aligned} \tag{6.2.12}$$

where,

$$\mathbf{V}_\gamma = -\frac{k_{r\gamma}\ \mathbf{k}}{\mu_\gamma}\left(P_\gamma + \rho_\gamma\ g\ \mathbf{z}_g\right) \quad for\ \gamma = \ell, g, n$$

$$\mathbf{J}_\gamma^j = -\tau_\gamma\ n_D\ \rho_\gamma\ s_\gamma\ \frac{M^j}{M_\gamma}\ D_\gamma^j \quad \chi_\gamma^j \quad \text{for } \gamma = \ell, g, n \text{ and } j = w, a, o$$

$$\int_\Gamma \left[-\sum_{\gamma=\ell,g,n} \left(\rho_\gamma\ h_\gamma\ \mathbf{V}_\gamma + \sum_{j=w,a,o} \left(h^j\ \mathbf{J}_\gamma^j \right) \right) + \left(\mathbf{k}_e \quad T \right) \right] \mathbf{n}\, d\Gamma$$
$$= \sum_{\varsigma=W,E,S,N,B,T} \left[-\sum_{\gamma=\ell,g,n} \left(\rho_\gamma\ h_\gamma\ V_\gamma \right)_\varsigma + \sum_{j=w,a,o} \left(h^j\ J_\gamma^j \right)_\varsigma + \left(\mathbf{k}_e \quad T \right)_\varsigma \right] A_\varsigma \qquad (6.2.13)$$

where,

$$V_{\gamma_\varsigma} = -\frac{\left\langle k_{r\gamma} \right\rangle_\varsigma^{uw} \left\langle \mathbf{k} \right\rangle_\varsigma^h}{\left\langle \mu_\gamma \right\rangle_\varsigma^h} \left[\frac{P_{\gamma_{\varsigma^+}} - P_{\gamma_{\varsigma^-}}}{\delta x_\varsigma} + \left\langle \rho_\gamma\ g \right\rangle_\varsigma^a z_{g_\varsigma} \right]$$

for $\gamma = \ell, g, n$ *and* $\varsigma = E, W, S, N, B, T$

$$J_{\gamma_\varsigma}^j = -\left\langle \tau_\gamma\ n_D\ \rho_\gamma\ s_\gamma\ \frac{M^j}{M_\gamma}\ D_\gamma^j \right\rangle_\varsigma^h \frac{\chi_{\gamma_{\varsigma^+}}^j - \chi_{\gamma_{\varsigma^-}}^j}{\delta x_\varsigma}$$

for $\gamma = \ell, g, n$; $j = w, a, o$; *and* $\varsigma = E, W, S, N, B, T$

The diffusive term of Equation (6.2.13) is computed using a user-defined interfacial average for the effective thermal conductivity, where the default form is harmonic averaging, according to Equation (6.2.14). The advective components of Equation (6.2.13) are computed using upwind (donor cell) averaging, according to Equations (6.2.15) and (6.2.16).

$$\left(\mathbf{k}_e \quad T \right)_\varsigma = \left\langle \mathbf{k}_e \right\rangle_\varsigma^h \frac{T_{\varsigma^+} - T_{\varsigma^-}}{\delta x_\varsigma} \quad \text{for } \varsigma = E, W, S, N, B, T \qquad (6.2.14)$$

$$\left(\rho_\gamma\ h_\gamma\ V_\gamma \right)_\varsigma = \left(\rho_\gamma\ h_\gamma \right)_{\varsigma^-} \max\left[V_{\gamma_{\varsigma^-}}, 0 \right] - \left(\rho_\gamma\ h_\gamma \right)_{\varsigma^+} \max\left[-V_{\gamma_{\varsigma^+}}, 0 \right] \qquad (6.2.15)$$

for $\gamma = \ell, g, o$ *and* $\varsigma = E, W, S, N, B, T$

$$\left(h^j\ J^j_\gamma\right)_\varsigma = \left(h^j\right)_{\varsigma^-} \max\left[J^j_{\gamma\,\varsigma^-}, 0\right] - \left(h^j\right)_{\varsigma^+} \max\left[-J^j_{\gamma\,\varsigma^+}, 0\right] \qquad (6.2.16)$$

for $\gamma = \ell, g, o$; $j = w, a, o$; *and* $\varsigma = E, W, S, N, B, T$

As with the mass conservation equations, the energy conservation equations are discretized in time using a fully implicit scheme, according to Equation (6.2.17), where the time levels are indicated with superscripts. The primary unknowns for the energy equation are the temperatures at the node centroids (node grid points) for time level $t + \delta t$. In residual form, Equation (6.2.17) appears as shown in Equation (6.2.18).

$$\begin{aligned}
\bar{V}\left[\frac{\left\{\bar{E}\right\}^{t+\delta t} - \left\{\bar{E}\right\}^{t}}{\delta t}\right] &= \bar{V}\left[\sum_{j=w,a,o}\left(h^j\ \dot{m}^j\right) + \dot{q}\right]^{t+\frac{\delta t}{2}} = \sum_{\substack{\varsigma=W,E,S,\\ N,B,T}}\left[\left\{\left(\mathbf{k}_e \quad T\right)_\varsigma\right\}^{t+\delta t} A_\varsigma\right] \\
&- \sum_{\substack{\varsigma=W,E,S,\\ N,B,T}}\left[\sum_{\gamma=\ell,g,n}\left(\rho_\gamma\ h_\gamma\ V_\gamma\right)_\varsigma^{t+\delta t} - \sum_{j=w,a,o}\left(h^j\ J^j_\gamma\right)_\varsigma^{t+\delta t}\right] A_\varsigma
\end{aligned} \qquad (6.2.17)$$

$$\begin{aligned}
\left\{\bar{R}^e\right\}^{t+\delta t} &= \bar{V}\left[\frac{\left\{\bar{E}\right\}^{t+\delta t} - \left\{\bar{E}\right\}^{t}}{\delta t}\right] - \bar{V}\left[\sum_{j=w,a,o}\left(h^j\ \dot{m}^j\right) + \dot{q}\right]^{t+\frac{\delta t}{2}} \\
&- \sum_{\substack{\varsigma=W,E,S,\\ N,B,T}}\left[\left\{\left(\mathbf{k}_e \quad T\right)_\varsigma\right\}^{t+\delta t} A_\varsigma\right] \\
&+ \sum_{\substack{\varsigma=W,E,S,\\ N,B,T}}\left[\sum_{\gamma=\ell,g,n}\left(\rho_\gamma\ h_\gamma\ V_\gamma\right)_\varsigma^{t+\delta t} - \sum_{j=w,a,o}\left(h^j\ J^j_\gamma\right)_\varsigma^{t+\delta t}\right] A_\varsigma
\end{aligned} \qquad (6.2.18)$$

6.2.3 Salt Conservation Equation

The salt mass conservation equation, shown in Equation (3.6.1), is discretized by assuming a piecewise profile for the salt concentration between node points and integrating over the node volume. The advection and diffusion-dispersion transport terms of the salt mass conservation equation are combined following the power-law scheme of Patankar [1980].

Integration of the accumulation, source, and decay terms for salt mass over the node volume proceeds according to Equation (6.2.19).

$$\int_{\bar{V}} \left(\frac{\partial S}{\partial t} - \dot{m}^S \right) d\bar{V} \;=\; \frac{\partial S}{\partial t}\,\bar{V} - \dot{m}^S\,\bar{V} \tag{6.2.19}$$

Salt transport fluxes are computed between node points and comprise advective and diffusive-dispersive components. Integration of the flux terms proceeds by converting volumetric integrals to surface integrals following Green's theorem [Kreyszig 1979], according to Equation (6.2.20). Surface integrals are approximated by discretizing the control volume surfaces into node surfaces and summing the contributions to salt transport over the node surfaces, according to Equation (6.2.21). The diffusive-dispersive term of Equation (6.2.21) is computed using a user-defined interfacial average for the effective diffusion-dispersion coefficient, where the default scheme is harmonic averaging, according to Equation (6.2.22).

$$\begin{aligned} &\int_{\bar{V}} \left[-\left[S_\ell\, \mathbf{V}_\ell \right] + \left[\left(\left(\tau_\ell\, s_\ell\, n_D\, D_\ell^S + s_\ell\, n_D\, \mathbf{D}_{\mathrm{h}\ell} \right) \quad S_\ell \right) \right] \right] d\bar{V} \\ &= \int_{\Gamma} \left[-\left(S_\ell\, \mathbf{V}_\ell \right) + \left(\left(\tau_\ell\, s_\ell\, n_D\, D_\ell^S + s_\ell\, n_D\, \mathbf{D}_{\mathrm{h}\ell} \right) \quad S_\ell \right) \right] \mathbf{n}\, d\Gamma \end{aligned} \tag{6.2.20}$$

where,

$$\mathbf{V}_\ell \;=\; -\frac{k_{r\ell}\,\mathbf{k}}{\mu_\ell} \left(\nabla P_\ell + \rho_\ell\, g\, \nabla z_g \right)$$

$$\begin{aligned} &\int_{\Gamma} \left[-\left(S_\ell\, \mathbf{V}_\ell \right) + \left(\left(\tau_\ell\, s_\ell\, n_D\, D_\ell^S + s_\ell\, n_D\, \mathbf{D}_{\mathrm{h}\ell} \right) \quad S_\ell \right) \right] \mathbf{n}\, d\Gamma \\ &= \sum_{\varsigma = W,E,S,N,B,T} \left[-\left(S_\ell\, V_\ell \right)_\varsigma + \left(\left(\tau_\ell\, s_\ell\, n_D\, D_\ell^S + s_\ell\, n_D\, \mathbf{D}_{\mathrm{h}\ell} \right) \quad S_\ell \right)_\varsigma \right] A_\varsigma \end{aligned} \tag{6.2.21}$$

where,

$$V_{\ell_\varsigma} \;=\; -\frac{\langle k_{r\ell} \rangle_\varsigma^{uw}\, \langle \mathbf{k} \rangle_\varsigma^{h}}{\langle \mu_\ell \rangle_\varsigma^{h}} \left[\frac{\left(P_{\ell_{\varsigma^+}} - P_{\ell_{\varsigma^-}} \right)}{\delta x_\varsigma} + \langle \rho_\ell\, g \rangle_\varsigma^{a} z_{g_\varsigma} \right]$$

for $\varsigma = E, W, S, N, B, T$

$$\left(\left(\tau_\ell \; s_\ell \; n_D \; D_\ell^S + s_\ell \; n_D \; \mathbf{D}_{\mathrm{h}\ell}\right) \quad S_\ell\right)_\varsigma$$
$$= \left\langle \tau_\ell \; s_\ell \; n_D \; D_\ell^S + s_\ell \; n_D \; \mathbf{D}_{\mathrm{h}\ell} \right\rangle_\varsigma^h \frac{\left(S_{\ell_{\varsigma^+}} - S_{\ell_{\varsigma^-}}\right)}{\delta x_\varsigma} \quad \textit{for} \;\; \varsigma = E, W, S, N, B, T \tag{6.2.22}$$

Solution of the salt transport equation depends on the local Peclet number, which represents the ratio of advective transport to diffusive-dispersive transport, according to Equation (6.2.23). The power law scheme is based on the salt concentration profile for steady conditions with no sources nor decay. For a Peclet number of zero, diffusion-dispersion transport dominates and a linear profile of salt concentration occurs between two spacial points. For a Peclet number of one, advection and diffusion-dispersion equally contribute to salt transport and the salt concentration profile will be skewed towards an upstream salt concentration. For large Peclet numbers, advection transport dominates and the upstream salt concentration defines the salt concentration profile between two spacial points. The power-law scheme closely approximates the exact solution for steady conditions without excessive computational expense. Salt flux from combined advective and diffusive-dispersive transport can be expressed using the power-law scheme according to Equation (6.2.24).

$$Pe_{\ell_\varsigma} = \frac{V_{\ell_\varsigma} \; \delta x_\varsigma}{\left\langle \tau_\ell \; s_\ell \; n_D \; D_\ell^S + s_\ell \; n_D \; \mathbf{D}_{\mathrm{h}\ell} \right\rangle_\varsigma^h} \tag{6.2.23}$$

$$G_{\ell_\varsigma}^S = -S_{\ell_{\varsigma^+}} \left[\max\left(-V_{\ell_\varsigma}, 0\right) + \left(\mathbf{D}_{\ell e}^S\right)_\varsigma \max\left[0, \left(1 - \frac{0.1\left|V_{\ell_\varsigma}\right|}{\left(\mathbf{D}_{\ell e}^S\right)_\varsigma}\right)^5\right] \right]$$
$$+ S_{\ell_{\varsigma^-}} \left[\max\left(V_{\ell_\varsigma}, 0\right) + \left(\mathbf{D}_{\ell e}^S\right)_\varsigma \max\left[0, \left(1 - \frac{0.1\left|V_{\ell_\varsigma}\right|}{\left(\mathbf{D}_{\ell e}^S\right)_\varsigma}\right)^5\right] \right] \tag{6.2.24}$$
$$\textit{for} \;\; \varsigma = W, E, S, N, B, T$$

where,

$$\left(\mathbf{D}_{\ell e}^S\right)_\varsigma = \frac{\left\langle \tau_\ell \; s_\ell \; n_D \; D_\ell^S + s_\ell \; n_D \; \mathbf{D}_{\mathrm{h}\ell} \right\rangle_\varsigma^h}{\delta x_\varsigma}$$

The salt conservation equation is discretized in time using a fully implicit scheme, according to Equation (6.2.25), where the time levels are indicated with superscripts. The primary unknowns for the salt conservation equation are the salt volumetric mass concentrations at the node centroids (node grid points) for time level $t + \delta t$. In residual form, Equation (6.2.25) appears as shown in Equation (6.2.26).

$$\bar{V}\left[\frac{\{S\}^{t+\delta t} - \{S\}^{t}}{\delta t}\right] = \bar{V}\left\{\dot{m}^{S}\right\}^{t+\frac{\delta t}{2}} + G^{S}_{\ell\,W} - G^{S}_{\ell\,E} + G^{S}_{\ell\,S} - G^{S}_{\ell\,N} + G^{S}_{\ell\,B} - G^{S}_{\ell\,T} \tag{6.2.25}$$

$$\left\{\bar{R}^{S}\right\}^{t+\delta t} = \bar{V}\left[\frac{\{S\}^{t+\delta t} - \{S\}^{t}}{\delta t}\right] - \bar{V}\left\{\dot{m}^{S}\right\}^{t+\frac{\delta t}{2}} - G^{S}_{\ell\,W} + G^{S}_{\ell\,E} - G^{S}_{\ell\,S} + G^{S}_{\ell\,N} - G^{S}_{\ell\,B} + G^{S}_{\ell\,T} \tag{6.2.26}$$

6.2.4 Solute Conservation Equation

The solute mass conservation equation, shown in Equation (3.7.1), is discretized by assuming a piecewise profile for the solute concentration between node points and integrating over the node volume. Integration of the accumulation, source, and decay terms for solute mass over the node volume proceeds according to Equation (6.2.27).

$$\int_{\bar{V}}\left(\frac{\partial C}{\partial t} - \dot{m}^{C} - \dot{R}^{C}\,C\right)d\bar{V} = \frac{\partial C}{\partial t}\,\bar{V} - \dot{m}^{C}\,\bar{V} - \dot{R}^{C}\,C\,\bar{V} \tag{6.2.27}$$

Solute transport fluxes are computed between node points and comprise advective and diffusive-dispersive components. Integration of the flux terms proceeds by converting volumetric integrals to surface integrals following Green's theorem [Kreyszig 1979], according to Equation (6.2.28). Surface integrals are approximated by discretizing the control volume surfaces into node surfaces and summing the contributions to solute transport over the node surfaces, according to Equation (6.2.29). The diffusive-dispersive term of Equation (6.2.29) is computed using a user-defined interfacial average for the effective diffusion-dispersion coefficient, where the default scheme is harmonic averaging, according to Equation (6.2.30).

$$\int_{\bar{V}} \left[\sum_{\gamma=\ell,g,n} \left(\left[C_\gamma \ \mathbf{V}_\gamma \right] \right) + \sum_{\gamma=\ell,g,n} \left[\left(\tau_\gamma \ s_\gamma \ n_D \ D_\gamma^C + s_\gamma \ n_D \ \mathbf{D}_{h\gamma} \right) \quad C_\gamma \right] \right] d\bar{V}$$
$$= \int_{\Gamma} \left[\sum_{\gamma=\ell,g,n} \left(C_\gamma \ \mathbf{V}_\gamma \right) + \sum_{\gamma=\ell,g,n} \left(\left(\tau_\gamma \ s_\gamma \ n_D \ D_\gamma^C + s_\gamma \ n_D \ \mathbf{D}_{h\gamma} \right) \quad C_\gamma \right) \right] \mathbf{n} \ d\Gamma \tag{6.2.28}$$

where,

$$\mathbf{V}_\gamma \ = \ - \frac{k_{r\gamma} \ \mathbf{k}}{\mu_\gamma} \left(\quad P_\gamma \ + \rho_\gamma \ g \ \mathbf{z}_g \right) \quad for \ \gamma = \ell, g, n$$

$$\int_{\Gamma} \left[\sum_{\gamma=\ell,g,n} \left(C_\gamma \ \mathbf{V}_\gamma \right) - \sum_{\gamma=\ell,g,n} \left(\left(\tau_\gamma \ s_\gamma \ n_D \ D_\gamma^C + s_\gamma \ n_D \ \mathbf{D}_{h\gamma} \right) \quad C_\gamma \right) \right] \mathbf{n} \ d\Gamma$$
$$= \sum_{\substack{\varsigma = W,E,S, \\ N,B,T}} \left[\sum_{\gamma=\ell,g,n} \left(C_\gamma \ V_\gamma \right)_\varsigma - \sum_{\gamma=\ell,g,n} \left(\left(\tau_\gamma \ s_\gamma \ n_D \ D_\gamma^C + s_\gamma \ n_D \ \mathbf{D}_{h\gamma} \right) \quad C_\gamma \right)_\varsigma \right] A_\varsigma \tag{6.2.29}$$

where,

$$V_{\gamma_\varsigma} \ = \ - \frac{\left\langle k_{r\gamma} \right\rangle_\varsigma^{uw} \left\langle \mathbf{k} \right\rangle_\varsigma^h}{\left\langle \mu_\gamma \right\rangle_\varsigma^h} \left[\frac{\left(P_{\gamma_{\varsigma^+}} - P_{\gamma_{\varsigma^-}} \right)}{\delta x_\varsigma} + \left\langle \rho_\gamma \ g \right\rangle_\varsigma^a z_{g_\varsigma} \right]$$

$$for \ \gamma = \ell, g, n \ \ and \ \ \varsigma = E, W, S, N, B, T$$

$$\left(\left(\tau_\gamma \ s_\gamma \ n_D \ D_\gamma^C + s_\gamma \ n_D \ \mathbf{D}_{h\gamma} \right) \quad C_\gamma \right)_\varsigma$$
$$= \left\langle \tau_\gamma \ s_\gamma \ n_D \ D_\gamma^C + s_\gamma \ n_D \ \mathbf{D}_{h\gamma} \right\rangle_\varsigma^h \frac{\left(C_{\gamma_{\varsigma^+}} - C_{\gamma_{\varsigma^-}} \right)}{\delta x_\varsigma} \tag{6.2.30}$$

$$for \ \ \gamma = \ell, g, n \ \ and \ \ \varsigma = E, W, S, N, B, T$$

The transport terms of the solute mass conservation equation are resolved with either the power-law scheme of Patankar [1980] or with a third-order scheme using Total Variation Diminishing (TVD) criteria [Datta Gupta et al., 1992].

6.2.4.1 Patankar's [1980] Power Law Scheme

Solution of the solute transport equation depends on the local Peclet number, which represents the ratio of advective transport to diffusive-dispersive transport, according to Equation (6.2.31). The power law scheme is based on the solute concentration profile for steady conditions with no sources nor decay. For a Peclet number of zero, diffusion-dispersion transport dominates and a linear profile of solute concentration occurs between two spacial points. For a Peclet number of one, advection and diffusion-dispersion equally contribute to solute transport and the solute concentration profile will be skewed towards an upstream solute concentration. For large Peclet numbers, advection transport dominates and the upstream solute concentration defines the solute concentration profile between two spacial points. The power-law scheme closely approximates the exact solution for steady conditions without excessive computational expense. Solute flux from combined advective and diffusive-dispersive transport can be expressed using the power-law scheme according to Equation (6.2.32).

$$Pe_{\gamma\varsigma} = \frac{V_{\gamma\varsigma}\,\delta x_{\varsigma}}{\left\langle \tau_{\gamma}\; s_{\gamma}\; n_D\, D_{\gamma}^{C} + s_{\gamma}\; n_D\, \mathbf{D}_{h\gamma} \right\rangle_{\varsigma}^{h}} \tag{6.2.31}$$

$$\begin{aligned} G_{\gamma\varsigma}^{C} = & -C_{\gamma\varsigma}\left[\max\left(-V_{\gamma\varsigma},\, 0\right) + \left(\mathbf{D}_{\gamma e}^{C}\right)_{\varsigma} \max\left[0,\, \left(1 - \frac{0.1\left|V_{\gamma\varsigma}\right|}{\left(\mathbf{D}_{\gamma e}^{C}\right)_{\varsigma}}\right)^{5}\right]\right] \\ & + C_{\gamma\varsigma-}\left[\max\left(V_{\gamma\varsigma},\, 0\right) + \left(\mathbf{D}_{\gamma e}^{C}\right)_{\varsigma} \max\left[0,\, \left(1 - \frac{0.1\left|V_{\gamma\varsigma}\right|}{\left(\mathbf{D}_{\gamma e}^{C}\right)_{\varsigma}}\right)^{5}\right]\right] \end{aligned} \tag{6.2.32}$$

for $\gamma = \ell, g, n$ *and* $\varsigma = W, E, S, N, B, T$

where,

$$\left(\mathbf{D}_{\gamma e}^{C}\right)_{\varsigma} = \frac{\left\langle \tau_{\gamma}\; s_{\gamma}\; n_D\, D_{\gamma}^{C} + s_{\gamma}\; n_D\, \mathbf{D}_{h\gamma} \right\rangle_{\varsigma}^{h}}{\delta x_{\varsigma}}$$

The discretized solute concentration equation can be written in two compact forms. The first form uses the expressions of solute flux according to Equation (6.2.33). The second form uses a linear system format with coefficients for the solute concentrations according to Equation (6.2.34).

$$\sum_{\gamma=\ell,g,n}\left(G^C_{\gamma\,W}-G^C_{\gamma\,E}+G^C_{\gamma\,S}-G^C_{\gamma\,N}+G^C_{\gamma\,B}-G^C_{\gamma\,T}\right)=\frac{\partial C}{\partial t}\,\overline{V}-\dot{m}^C\,\overline{V}-\dot{R}^C\,C\,\overline{V} \quad (6.2.33)$$

$$a_P\,C_P-\sum_{\varsigma=W,E,S,N,B,T}a_\varsigma\,C_\varsigma=\frac{\partial C}{\partial t}\,\overline{V}-\dot{m}^C\,\overline{V}-\dot{R}^C\,C\,\overline{V} \quad (6.2.34)$$

where,

$$a_\varsigma=\sum_{\gamma=\ell,g,n}a_{\gamma\varsigma}$$

$$a_{\gamma P}=\sum_{\varsigma=W,E,S,N,B,T}a_{\gamma\varsigma}+\sum_{\varsigma=E,N,T}V_{\gamma\varsigma}-\sum_{\varsigma=W,S,B}V_{\gamma\varsigma}$$

$$a_{\gamma\varsigma}=\left(\mathbf{D}^C_{\mathrm{e}\,\gamma}\right)_\varsigma\max\left[1-\frac{0.1\left|V_{\gamma\varsigma}\right|}{\left(\mathbf{D}^C_{\mathrm{e}\,\gamma}\right)_\varsigma},\,0\right]^5+\max\left[V_{\gamma\varsigma},\,0\right]$$

for $\varsigma = W, S, B$ *and* $\gamma = \ell, g, n$

$$a_{\gamma\varsigma}=\left(\mathbf{D}^C_{\mathrm{e}\,\gamma}\right)_\varsigma\max\left[1-\frac{0.1\left|V_{\gamma\varsigma}\right|}{\left(\mathbf{D}^C_{\mathrm{e}\,\gamma}\right)_\varsigma},\,0\right]^5+\max\left[-V_{\gamma\varsigma},\,0\right]$$

for $\varsigma = E, N, T$ *and* $\gamma = \ell, g, n$

The solute mass conservation equation is discretized in time using a fully implicit scheme, according to Equation (6.2.35), in linear system format, where time levels are indicated with superscripts.

$$\sum_{\varsigma=P,W,E,S,N,B,T} a_\varsigma \left\{C_\varsigma\right\}^{t+\delta t} = \frac{\left\{C_P\right\}^t}{\partial t}\bar{V} - \dot{m}^C \bar{V} \qquad (6.2.35)$$

where,

$$a_\varsigma = \sum_{\gamma=\ell,g,n} a_{\gamma\varsigma}$$

$$a_{\gamma P} = \sum_{\varsigma=W,E,S,N,B,T} a_{\gamma\varsigma} + \sum_{\varsigma=E,N,T} V_{\gamma\varsigma} - \sum_{\varsigma=W,S,B} V_{\gamma\varsigma} + \frac{\bar{V}}{\delta t} + \dot{R}^C \bar{V}$$

$$a_{\gamma\varsigma} = \left(\mathbf{D}_{\mathrm{e}\,\gamma}^C\right)_\varsigma \max\left[\left(1 - \frac{0.1\left|V_{\gamma\varsigma}\right|}{\left(\mathbf{D}_{\mathrm{e}\,\gamma}^C\right)_\varsigma}\right)^5, 0\right] + \max\left[V_{\gamma\varsigma}, 0\right]$$

for $\varsigma = W, S, B$ *and* $\gamma = \ell, g, n$

$$a_{\gamma\varsigma} = \left(\mathbf{D}_{\mathrm{e}\,\gamma}^C\right)_\varsigma \max\left[\left(1 - \frac{0.1\left|V_{\gamma\varsigma}\right|}{\left(\mathbf{D}_{\mathrm{e}\,\gamma}^C\right)_\varsigma}\right)^5, 0\right] + \max\left[-V_{\gamma\varsigma}, 0\right]$$

for $\varsigma = E, N, T$ *and* $\gamma = \ell, g, n$

6.2.4.2 TVD Transport

For advection-dominated flow (high Peclet numbers), users have the option to employ a third-order scheme using a TVD technique [Datta Gupta et al. 1991]. Conventional techniques, like the one discussed by Patankar [1980], suffer from artificial diffusion that smears otherwise sharp fronts. The smearing is a result of the first-order approximation of the advective term in the transport equation. Datta Gupta et al. [1991] proposed and succesfully tested a third-order diferencing scheme with an appropriate flux limiting funtion which significantly minimizes numerical diffusion while, at the same time, avoiding oscillations that commonly affect classical higher-order schemes.

The third-order TVD technique is best described following an example outlined by Datta Gupta et al. [1991]. Assume solute transport according to the hyperbolic conservation equation

$$\frac{\partial C}{\partial t} = -\sum_{\gamma=l,g,n}\left(\left[C_\gamma \mathbf{V}_\gamma\right]\right) \tag{6.2.36}$$

When only aqueous transport is considered in the x-direction, Equation (6.2.36) reduces to

$$\frac{\partial C_l}{\partial t} = \frac{\partial\left(C_l \mathbf{V}_l\right)}{\partial x} \tag{6.2.37}$$

With $\mathbf{V}_l$ taken to be a positive constant, Equation (6.2.37) can be discretized over a mesh cell i and time step interval [n,n+1} to yield

$$\frac{C_{l,i}^{n+1} - C_{l,i}^{n}}{\Delta t} = \frac{\mathbf{V}_l\left(\overline{C}_{l,i+1/2} - \overline{C}_{l,i-1/2}\right)}{\Delta x} \tag{6.2.38}$$

The time-averaged fluxes can be approximated as follows

$$\overline{C}_{l,i+1/2} = C_{l,i}^{n} + 1/2(1-\lambda)F_i\Delta x \tag{6.2.39}$$

where

$$\lambda = \mathbf{V}_l \frac{\Delta t}{\Delta x}$$

and F_i is the concentration gradient of the upwind cell. The STOMP simulator uses the Leonard [1979] scheme to obtain third-order accuracy

$$F_i = \frac{2-\lambda}{3}\frac{C_{l,i+1}^{n} - C_{l,i}^{n}}{\Delta x} + \frac{1-\lambda}{3}\frac{C_{l,i}^{n} - C_{l,i-1}^{n}}{\Delta x} \tag{6.2.40}$$

The TVD scheme is constructed by combining lower and higher-order fluxes and by imposing limiter functions on the higher-order flux to prevent oscillations. Equation (6.2.39) can be rewritten in a first-order flux plus a corrective term

$$\overline{C}_{l,i+1/2} = C_{l,i}^{n} + \phi(r)\frac{(C_{l,i+1}^{n} - C_{l,i}^{n})}{2}(1-\lambda) \tag{6.2.41}$$

where $\phi(r)$ is the flux-limiting function and r is a measure of data smoothness [Datta Gupta et al. 1991]. For Leonard's scheme with positive velocities

$$\phi(r) = \frac{2-\lambda}{3} + \frac{1+\lambda}{3} r \qquad (6.2.42)$$

where

$$r = \frac{C^n_{l,i} - C^n_{l,i-1}}{C^n_{l,i+1} - C^n_{l,i}}, \text{for } \bar{C}_{l,i+1/2}$$

and

$$r = \frac{C^n_{l,i-1} - C^n_{l,i-2}}{C^n_{l,i} - C^n_{l,i-1}}, \text{for } \bar{C}_{l,i-1/2}$$

To ensure that the limited antidiffusive flux is maximized in amplitude subject to the scheme being TVD, the following limiter is used in the STOMP code

$$\phi(r) = \max\left[0, \min\left(2, 2r, \frac{2+r}{3}\right)\right] \qquad (6.2.43)$$

6.3 Boundary Conditions

The discretization methods described above for the mass, energy, and solute mass conservation equations strictly applied to interior nodes (i.e., nodes surrounded by neighboring nodes). For nodes adjacent to a domain boundary or an inactive node the discretized forms of the governing equations are modified according to the user specified boundary conditions. Zero flux boundary conditions are applied whenever no boundary condition is specified for a boundary surface. Boundary conditions which can be specified for a boundary surface are varied, depend on the operational mode, and other associated boundary conditions.

Eight boundary conditions are appropriate for flow boundaries and are applicable to the conservation equations for water, air, and oil mass: Dirichlet, Neumann, zero flux, initial condition, saturated, unit gradient, hydraulic gradient, and free gradient. The Dirichlet boundary condition specifies the value of intrinsic properties on the boundary surfaces (e.g., aqueous pressure, gas pressure, NAPL pressure). The Neumann boundary condition specifies a surface flux on the boundary surface (e.g., aqueous Darcy velocity, gas Darcy velocity, NAPL Darcy velocity). The zero flux boundary condition specifies an impermeable boundary for flow or transport and serves as the default condition for undeclared boundary surfaces (e.g., zero fluid flow). The initial condition boundary condition uses the initial conditions in the nodes adjacent to a boundary surface to fix the intrinsic properties on the boundary surface. The saturated

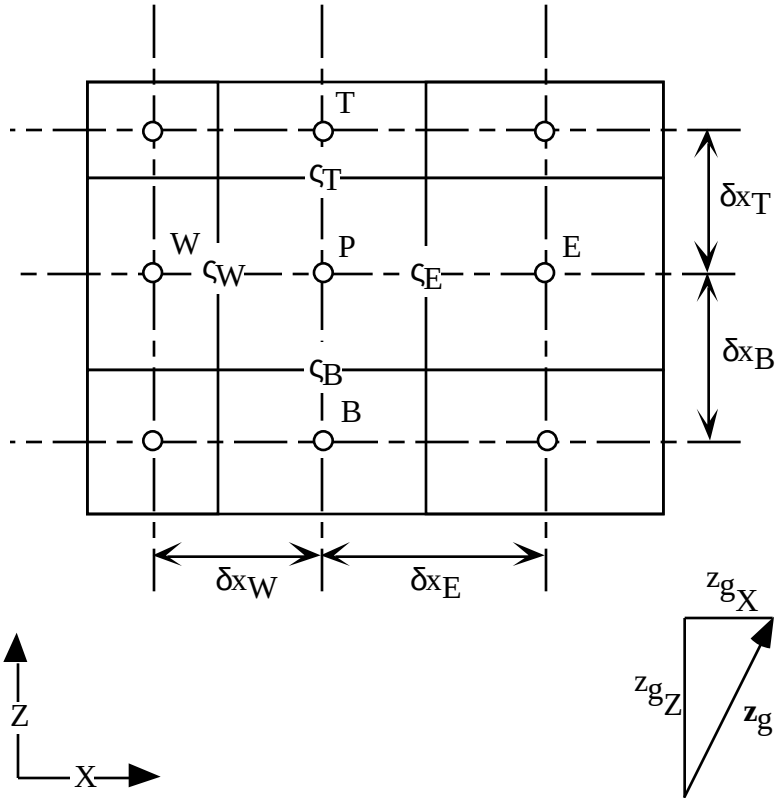

Figure 6.1. X-Z Coordinate Plane for Cartesian Systems

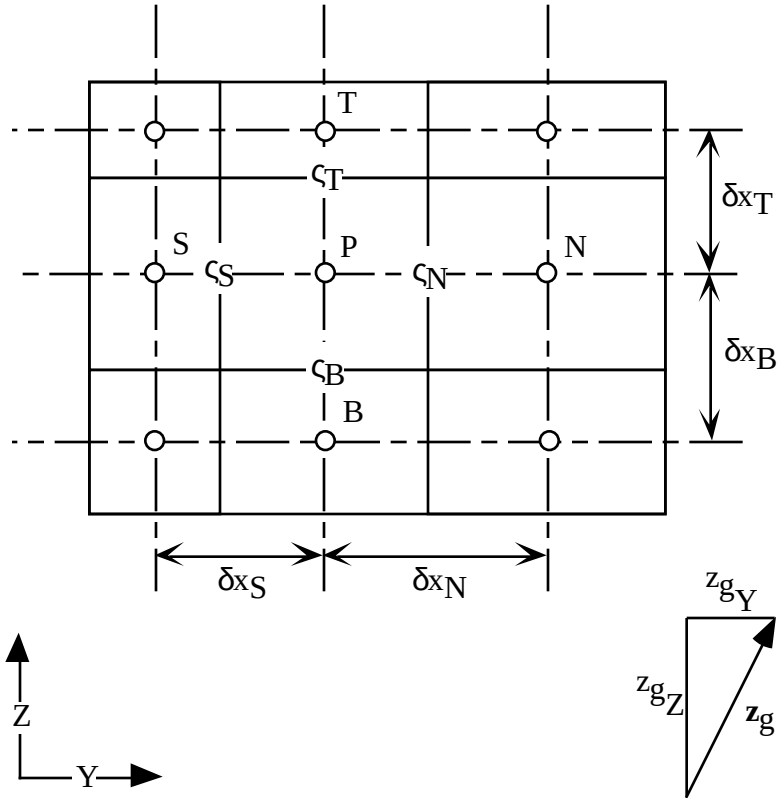

Figure 6.2. Y-Z Coordinate Plane for Cartesian Systems

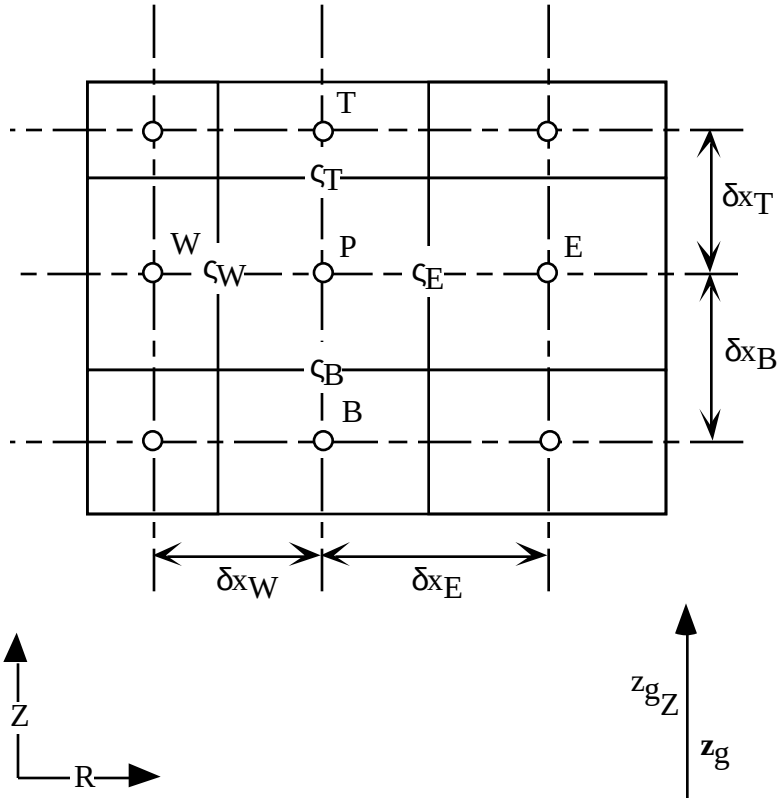

Figure 6.3. R-Z Coordinate Plane for Cylindrical Systems

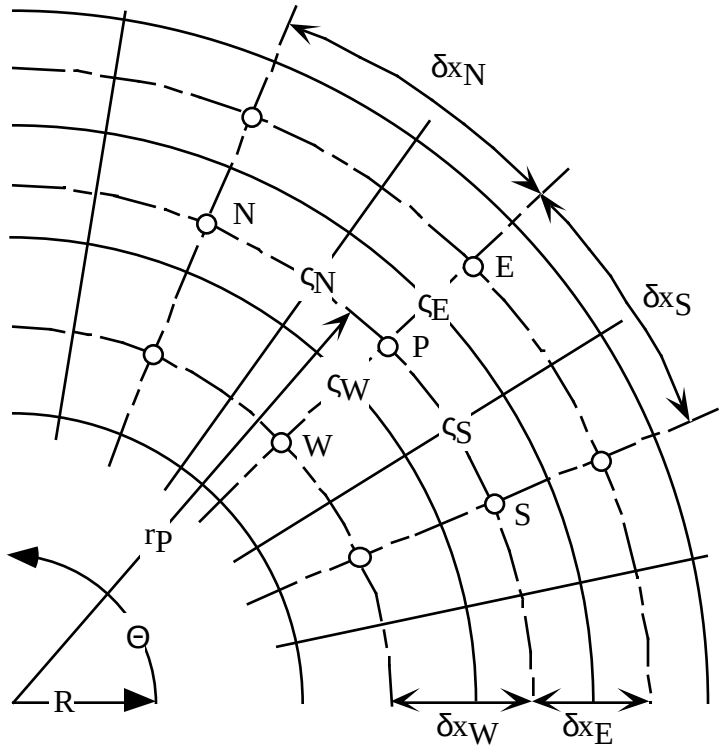

Figure 6.4. R-Θ Coordinate Plane for Cylindrical Systems

boundary condition is appropriate for fluid flow boundaries for two-phase systems and establishes zero capillary pressure conditions on the boundary surface. The unit gradient boundary condition is appropriate for fluid flow boundaries and establishes a fluid pressure on the boundary surface equal to the fluid pressure at the adjacent node modified by the hydraulic gradient for the fluid. The free gradient boundary condition is appropriate for fluid flow boundaries for two-phase systems and establishes a fluid pressure on the boundary surface by extrapolating the local pressure gradient within the computational domain to the boundary surface. The hydraulic gradient boundary condition is appropriate for fluid flow boundaries and establishes a series of boundary pressures according to the local hydraulic gradient for the fluid.

Five boundary conditions are appropriate for transport boundaries and are applicable to the conservation equations for energy and solute mass: Dirichlet, zero flux, initial condition, outflow and inflow. The Dirichlet boundary condition specifies the value of intrinsic properties on the boundary surfaces (e.g., temperature, or solute concentration). The zero flux boundary condition specifies an impermeable boundary for flow or transport and serves as the default condition for undeclared boundary surfaces (e.g., zero heat flux, or zero solute flux). The initial condition boundary condition uses the initial conditions in the nodes adjacent to a boundary surface to fix the intrinsic properties on the boundary surface. The outflow boundary condition considers transport out of the computational domain by advection only, no diffusive transport occurs. This boundary conditions will not transport energy or solute mass into the domain. The inflow boundary condition considers transport into the computational domain only by advection; no diffusive transport occurs. This boundary condition will not transport energy or solute mass out of the domain.

In general, boundary conditions for simulations that involve the solution of multiple governing equations can be combined in a variety of ways, one major restriction. Specification of a Neumann boundary condition for the energy equation on a boundary surface, other than the zero flux condition, requires that the flow equation boundary conditions for that boundary surface be specified as zero flux. Nonzero fluid flow and heat transport can be achieved for boundary nodes through a combination of flow boundary conditions, a zero flux energy boundary, and energy sources for the boundary nodes. Regardless of the boundary condition or combination of boundary conditions a sufficient number of independent intensive variables must be declared to specify the thermodynamic and hydrologic state on the boundary surface. Definitions for geometric parameters for nodes with boundary surfaces on the “west” side are shown in Figures 6.5 and 6.6 for the X-Z and X-Y Cartesian coordinate planes and in Figures 6.7 and 6.8 for the R-Z and R-Θ cylindrical coordinate planes, respectively.

6.3.1 Dirichlet Boundary Condition

The Dirichlet boundary condition is equivalent to specifying the value for the primary unknown on the boundary surface. Assigned values of primary variables are used to compute secondary variables for the boundary surface. Average properties for transport between a boundary surface and the adjacent node are computed using user specified averaging schemes between the values of the properties on the boundary surface and adjacent node. For example, the discretized forms for Darcy mass flux and diffusive mass flux rates of water, Equation (6.2.7), are modified for a Dirichlet aqueous phase boundary condition on a "west" boundary surface, according to Equations (6.3.1) and (6.3.2), respectively. For the salt and solute mass conservation equations, a Dirichlet boundary condition on the "west" surface produces a modification to the discretized conservation equation, Equations (6.2.26) and (6.2.35), according to Equation (6.3.3) and (6.3.4), respectively.

$$F^{w}_{\ell\,WB} = -\frac{\left\langle \omega^{w}_{\ell}\,\rho_{\ell}\,k_{r\ell}\right\rangle^{uw}_{WB}\,\langle \mathbf{k}\rangle^{h}_{WB}}{\langle \mu_{\ell}\rangle^{h}_{WB}}\left(\frac{\left(P_{\ell P}-P_{\ell WB}\right)}{\delta x_{WB}}+\langle \rho_{\ell}\,g\rangle^{a}_{WB} z_{g_{WB}}\right) \tag{6.3.1}$$

$$J^{w}_{\ell\,WB} = -\left\langle \tau_{\ell}\,n_{D}\,\rho_{\ell}\,s_{\ell}\,\frac{M^{w}}{M_{\ell}}\,\mathbf{D}^{w}_{\ell}\right\rangle^{h}_{WB}\frac{\left(\chi^{w}_{\ell\,P}-\chi^{w}_{\ell\,WB}\right)}{\delta x_{WB}} \tag{6.3.2}$$

$$a_{P}\,S_{P}-\sum_{\varsigma=E,S,N,B,T}a_{\varsigma}\,S_{\varsigma} = \frac{\partial S}{\partial t}\,\bar{V}-\dot{m}^{S}\,\bar{V}+a_{WB}\,S_{WB} \tag{6.3.3}$$

$$a_{P}\,C_{P}-\sum_{\varsigma=E,S,N,B,T}a_{\varsigma}\,C_{\varsigma} = \frac{\partial C}{\partial t}\,\bar{V}-\dot{m}^{C}\,\bar{V}-\dot{R}^{C}\,C\,\bar{V}+a_{WB}\,C_{WB} \tag{6.3.4}$$

6.3.2 Neumann Boundary Condition

The Neumann boundary condition is equivalent to specifying the flux on a boundary surface. Fluxes which may be specified are aqueous volumetric, gas volumetric, NAPL volumetric, energy, and solute mass. For example, the discretized form for Darcy mass flux of water, Equation (6.2.7), is modified for a Neumann boundary condition on a "west" boundary surface, according to Equation (6.3.5). Sufficient information is needed to fix the thermodynamic and hydrologic state on the boundary surface. Calculation of phase pressures from phase volumetric flow rates requires an iterative solution because averaged values of properties (e.g., relative permeability) are nonlinear functions of the phase pressure on the boundary. To avoid an iterative solution of the phase pressure on the boundary phase pressures are computed

assuming a unit relative permeability, according to Equation (6.3.6) for a “west” boundary surface.

$$F^{w}_{\ell\,WB} = \left\langle \omega^{w}_{\ell}\, \rho_{\ell} \right\rangle^{uw}_{WB} V_{\ell WB} \tag{6.3.5}$$

$$P_{\ell WB} = \delta x_{WB} \left(\frac{V^{w}_{\ell\,WB} \left\langle \mu_{\ell} \right\rangle^{h}_{WB}}{\left\langle \mathbf{k} \right\rangle^{h}_{WB}} + \left\langle \rho_{\ell}\, g \right\rangle^{a}_{WB} z_{g_{WB}} \right) + P_{\ell P} \tag{6.3.6}$$

6.3.3 Zero Flux Boundary Condition

The zero flux boundary condition is the default boundary condition and is equivalent to specifying zero flow and/or transport across the boundary surface. Complex boundary conditions, which involve multiple specifications on a single boundary surface, require that sufficient information be specified to fix the thermodynamic and hydrologic state on the boundary surface. For example, a recognized boundary condition combination for an water-air system (i.e., Two-Phase Volatile operational mode) is a Dirichlet aqueous boundary and zero flux gas boundary. Isothermal water-air systems require two independent intensive variables to fix the thermodynamic and hydrologic state of the system. For this boundary system the Dirichlet aqueous boundary assigns a value to the aqueous pressure. The gas pressure can be specified through user input or be computed using zero flux boundary conditions and solving Equation (6.2.7) for the gas pressure, according to Equation (6.3.7) for a “west” boundary surface.

$$P_{g_{WB}} = \delta x_{WB} \left\langle \rho_{g}\, g \right\rangle^{a}_{WB} z_{g_{WB}} + P_{g_P} \tag{6.3.7}$$

6.3.4 Initial Condition Boundary Condition

The initial condition boundary condition is identical in application to the Dirichlet boundary condition, with the exception that the primary variable is fixed to the initial value at the adjacent node. No user input is required for this type boundary condition because boundary values are obtained through the initial condition specifications. Initial boundary pressures are computed once at the start of a simulation.

6.3.5 Saturated Boundary Condition

The saturated boundary condition is recognized for water-air systems and perform as dynamic Dirichlet boundary conditions, where zero capillary pressure is maintained on the boundary surface. The saturated boundary condition fixes the aqueous pressure equal to the gas pressure on a boundary surface regardless of the boundary condition for the gas pressure. For a single-phase system, the gas pressure is fixed through the initial conditions and the aqueous pressure is maintained on a saturated boundary equal to this gas pressure. For a two-phase system, the gas pressure on a boundary surface is user specified according to the gas-phase boundary conditions. The saturated boundary condition for the aqueous phase fixes the aqueous pressure at the boundary surface equal to the gas pressure. Saturated boundary pressures are computed with each Newton-Raphson iteration.

6.3.6 Unit Gradient Boundary Condition

The unit gradient boundary condition is recognized for aqueous-phase, gas-phase, and NAPL boundary conditions and maintains a unit gradient in the phase hydraulic head. A unit gradient in the phase hydraulic head is equivalent to setting the normalized Darcy velocity equal to minus one, according to Equation (6.3.8) for a "west" boundary surface. Phase pressure on the boundary surface is computed by solving Equation (6.3.8) for the boundary pressure, according to Equation (6.3.9), for a "west" boundary surface. Unit gradient boundary pressures are computed with each Newton-Raphson iteration.

$$\frac{V_{\gamma\,WB}\left\langle \mu_\gamma \right\rangle_{WB}^{h}}{\left\langle k_{r\gamma} \right\rangle_{WB}^{uw}\langle \mathbf{k} \rangle_{WB}^{h}} = -1 = -\left(\frac{\left(P_{\gamma\,P} - P_{\gamma\,WB}\right)}{\delta x_{WB}} + \left\langle \rho_\gamma\ g \right\rangle_{WB}^{a} z_{g_{WB}}\right) \quad \text{for } \gamma = \ell, g, n \tag{6.3.8}$$

$$P_{\gamma\,WB} = P_{\gamma\,P} + \delta x_{WB}\left(\left\langle \rho_\gamma\ g \right\rangle_{WB}^{a} z_{g_{WB}}\right) \quad \text{for } \gamma = \ell, g, n \tag{6.3.9}$$

6.3.7 Free Gradient Boundary Condition

The free gradient boundary condition is recognized for aqueous-phase, gas-phase, and NAPL boundary conditions. This boundary condition is essentially a dynamic Dirichlet-type boundary, where the pressure on the boundary surface is set to maintain the gradient in pressure in the interior nodes adjacent to the boundary surface. This boundary type requires, as a minimum, two active nodes adjacent to the boundary surface. The gradient in phase pressure is

linearly extrapolated from the interior nodes to the boundary surface to determine the boundary pressure. Free gradient boundary pressures are computed with each Newton-Raphson iteration.

6.3.8 Outflow Boundary Condition

The outflow boundary condition is recognized for transport boundaries (e.g., energy transport, solute transport). This boundary conditions allows transported quantities to be transported out across a boundary surface by advection only. Transport by diffusion or transport in across the boundary surface is prohibited. Energy flux across an outflow boundary surface on a "west" boundary is computed according to Equation (6.3.10). Solute flux across an outflow boundary surface on a "west" boundary is computed according to Equation (6.3.11).

$$Q_{\gamma\,WB} = -\left(\rho_\gamma\ h_\gamma\right)_P \max\left[-V_{\gamma\,WB}, 0\right] \quad for\ \ \gamma = \ell, g, n \tag{6.3.10}$$

$$G^C_{\gamma\,WB} = -C_{\gamma\,P} \max\left[-V_{\gamma\,WB}, 0\right] \quad for\ \ \gamma = \ell, g, n \tag{6.3.11}$$

6.3.9 Inflow Boundary Condition

The inflow boundary condition is recognized for transport boundaries (e.g., energy transport, solute transport). This boundary conditions allows transported quantities to be transported in across a boundary surface by advection only. Transport by diffusion or transport out across the boundary surface is prohibited. Energy flux across an inflow boundary surface on a "west" boundary is computed according to Equation (6.3.12). Solute flux across an inflow boundary surface on a "west" boundary is computed according to Equation (6.3.13).

$$Q_{\gamma\,WB} = \left(\rho_\gamma\ h_\gamma\right)_{WB} \max\left[V_{\gamma\,WB}, 0\right] \quad for\ \ \gamma = \ell, g, n \tag{6.3.12}$$

$$G^C_{\gamma\,WB} = C_{\gamma\,WB} \max\left[V_{\gamma\,WB}, 0\right] \quad for\ \ \gamma = \ell, g, n \tag{6.3.13}$$

6.3.10 Falling-Head/Pond Boundary Condition

The falling-head boundary condition computes the phase pressure on a single boundary surface assuming the surface is supplied with a ponded fluid source. Fluid fluxes into the computational domain will deplete the fluid source; whereas, fluid fluxes from the computational domain will increase the source. The falling-head boundary can be applied to all boundary

surface orientations, however, the ponded fluid is always assumed to drain with the gravitational vector. Boundary pressures computed for the falling-head type boundary condition are those for the current time step, therefore will vary with iteration. The falling-pond boundary condition is analogous to the falling-head boundary condition with two exceptions. This boundary condition can be applied over multiple boundary surfaces, which are connected to a single ponded source of fluid, and the boundary pressure remains constant between iterations, computed from previous time step conditions. The falling-pond boundary condition will typically over estimate infiltration rates compared with the more accurate falling-head boundary condition. The falling-pond boundary condition, however, is required for multiple boundary surfaces connected to a common ponded fluid source.

The falling-head and falling-pond boundary conditions are intended to compute the pressure on a boundary surface assuming the surface is connected to ponded fluid. The pressure at the boundary surface is computed as the hydrostatic pressure for the column of ponded fluid. The fluid density of the ponded column is assumed to be constant at the density of the node adjacent to the boundary surface. The height of fluid in the ponded column varies with flux across the boundary surface, where flux into the system reduces the column height.

For the falling-pond boundary, the pressure at the boundary surface is computed from the height of fluid in the ponded column, according to Equation (6.3.14)

$$P_{\ell b} = \left[h - A_r \left(\frac{\sum_{s_b} \left(V_\ell A \Delta t \right)}{\sum_{s_b} A} \right) \right] \rho_\ell g + P_{g_b} \Bigg|^{t-} \tag{6.3.14}$$

For the falling-head boundary condition, the pressure at the boundary surface is computed for the current time step according to Equation (6.3.15) and (6.3.16)

$$P_{\ell b} = \left(h - V_\ell A_r \Delta t \right) \rho_\ell g + P_{g_b} \tag{6.3.15}$$

$$V_\ell = \frac{k_\ell \left[\frac{\left(P_{\ell b} - P_\ell \right)}{\Delta x} \pm \rho_\ell g \mathbf{z}_g \right]}{\mu_\ell} \tag{6.3.16}$$

Combining Equations (6.3.15) and (6.3.16) yields an expression for the aqueous-phase boundary pressure, according to Equation (6.3.17).

$$P_{l_b} = \frac{\dfrac{k_\ell}{\mu_\ell}\left(\dfrac{P_\ell}{\Delta x} \pm \rho_\ell g \mathbf{z}_g\right) + \dfrac{\left(h \rho_\ell g + P_{g_b}\right)}{A_r \Delta t \rho_\ell g}}{\left(\dfrac{1}{A_r \Delta t \rho_\ell g} + \dfrac{k_\ell}{\Delta x \mu_\ell}\right)} \qquad (6.3.17)$$

6.4 Newton-Raphson Linearization

The discretized governing equations for component mass conservation, salt mass, and energy conservation, Equations (6.2.9) and (6.2.18), form a nonlinear set of algebraic equations. Nonlinearites arise from the dependence of secondary variables on the primary unknowns. Cross dependencies of secondary variables in one governing equation with the primary unknown in other governing equations requires that this system of nonlinear equations be solved simultaneously. A primary assumption associated with the solute mass conservation equation is that the solute concentrations are infinitely dilute. This assumption implies that fluid properties are independent of solute concentrations, which allows the solution of the solute conservation equations to be solved separately from the coupled flow and energy transport solutions. The discretized governing equations for solute mass conservation, Equation (6.26a), form a linear set of algebraic equations, which are solved directly following the solution of the coupled flow and energy transport system. The nonlinearities in the coupled flow and energy transport system of equations are resolved through the application of the iterative Newton-Raphson technique.

The Newton-Raphson linearization technique is an iterative method for solving nonlinear algebraic equations of the form shown in Equation (6.4.1), where $f(x)$ is differentiable in x. The linearization concept approximates $f(x)$ with suitable tangents. Each iteration yields a new estimate of x as the intersection of the tangent to the function $f(x)$ at the previous estimate of x and the abscissa axis, according to Equation (6.4.2) in mathematical form. In this formulation $f(x)$ is considered the equation residual. For convergent systems, the residual decreases in a quadratically with iteration. In multiple variable systems, as with the coupled flow and energy transport system, the scalar function, $f(x)$, is replaced with a vector function $\mathbf{R}(\mathbf{x})$, according to Equation (6.4.3). The vector function, $\mathbf{R}(\mathbf{x})$, represents the system of nonlinear algebraic equations produced from discretizing the conservation equations for component mass and energy, Equations (6.2.9) and (6.2.18). The vector of unknowns, $\mathbf{x}$, represents the set of primary variables for the system, which are determined by the operational mode and phase conditions. Equation (6.4.3) can be rewritten in terms of increments to the primary variables, according to Equation (6.4.4). The partial derivatives shown in Equation (6.4.4) form the Jacobian matrix.

$$f(x) = 0 \tag{6.4.1}$$

$$x^{n+1} = x^n - \frac{f(x)}{f'(x)} \tag{6.4.2}$$

$$\mathbf{x}^{n+1} = \mathbf{x}^n - \frac{\mathbf{R}(\mathbf{x})}{\mathbf{R}'(\mathbf{x})} \tag{6.4.3}$$

$$\frac{\partial \mathbf{R}(\mathbf{x})}{\partial \mathbf{x}} \Delta\mathbf{x} = -\mathbf{R}(\mathbf{x}) \tag{6.4.4}$$

To simplify these discussions a one-dimensional system involving the solution of the water mass, air mass, and energy conservation equations will be considered. The system of linear equations that result from applying the Newton-Raphson linearization technique to this system of nonlinear algebraic equations is shown in Equation (6.4.5) for a computational domain with "n" nodes. In Equation (6.4.5) each Jacobian matrix element represents a block matrix of order three, according to Equation (6.4.6); each unknown vector element represents a vector of increments to the primary variables of order three, according to Equation (6.4.7); and each solution vector element represents a vector of equation residuals of order three, according to Equation (6.4.8).

$$\begin{vmatrix}
\frac{\partial \mathbf{R}_1}{\partial \mathbf{x}_1} & \frac{\partial \mathbf{R}_1}{\partial \mathbf{x}_2} & 0 & 0 & 0 & 0 & 0 \\
\frac{\partial \mathbf{R}_2}{\partial \mathbf{x}_1} & \frac{\partial \mathbf{R}_2}{\partial \mathbf{x}_2} & \frac{\partial \mathbf{R}_2}{\partial \mathbf{x}_3} & 0 & 0 & 0 & 0 \\
0 & \frac{\partial \mathbf{R}_3}{\partial \mathbf{x}_2} & \frac{\partial \mathbf{R}_3}{\partial \mathbf{x}_3} & \frac{\partial \mathbf{R}_3}{\partial \mathbf{x}_4} & 0 & 0 & 0 \\
0 & 0 & \frac{\partial \mathbf{R}_4}{\partial \mathbf{x}_3} & \frac{\partial \mathbf{R}_4}{\partial \mathbf{x}_4} & 0 & 0 & 0 \\
0 & 0 & 0 & 0 & \frac{\partial \mathbf{R}_{n-2}}{\partial \mathbf{x}_{n-2}} & \frac{\partial \mathbf{R}_{n-2}}{\partial \mathbf{x}_{n-1}} & 0 \\
0 & 0 & 0 & 0 & \frac{\partial \mathbf{R}_{n-1}}{\partial \mathbf{x}_{n-2}} & \frac{\partial \mathbf{R}_{n-1}}{\partial \mathbf{x}_{n-1}} & \frac{\partial \mathbf{R}_{n-1}}{\partial \mathbf{x}_n} \\
0 & 0 & 0 & 0 & 0 & \frac{\partial \mathbf{R}_n}{\partial \mathbf{x}_1} & \frac{\partial \mathbf{R}_n}{\partial \mathbf{x}_n}
\end{vmatrix}
\begin{vmatrix} \mathbf{x}_1 \\ \mathbf{x}_2 \\ \mathbf{x}_3 \\ \mathbf{x}_4 \\ \\ \mathbf{x}_{n-2} \\ \mathbf{x}_{n-1} \\ \mathbf{x}_n \end{vmatrix}
=
\begin{vmatrix} -\mathbf{R}_1 \\ -\mathbf{R}_2 \\ -\mathbf{R}_3 \\ -\mathbf{R}_4 \\ \\ -\mathbf{R}_{n-2} \\ -\mathbf{R}_{n-1} \\ -\mathbf{R}_n \end{vmatrix} \tag{6.4.5}$$

$$\frac{\partial \mathbf{R}_k}{\partial \mathbf{x}_l} = \begin{vmatrix} \frac{\partial R_k^w}{\partial PV_l^w} & \frac{\partial R_k^w}{\partial PV_l^a} & \frac{\partial R_k^w}{\partial PV_l^e} \\ \frac{\partial R_k^a}{\partial PV_l^w} & \frac{\partial R_k^a}{\partial PV_l^a} & \frac{\partial R_k^a}{\partial PV_l^e} \\ \frac{\partial R_k^e}{\partial PV_l^w} & \frac{\partial R_k^e}{\partial PV_l^a} & \frac{\partial R_k^e}{\partial PV_l^e} \end{vmatrix} \tag{6.4.6}$$

$$\mathbf{x}_l = \begin{vmatrix} \Delta PV_l^w \\ \Delta PV_l^a \\ \Delta PV_l^e \end{vmatrix} \tag{6.4.7}$$

$$-\mathbf{R}_k = \begin{vmatrix} -R_k^w \\ -R_k^a \\ -R_k^e \end{vmatrix} \tag{6.4.8}$$

For a two-dimensional system involving the solution of the water mass, air mass, and energy conservation equations, the Jacobian matrix would contain two extra bands of block matrices: one below and one above the diagonal band. These extra bands would be located one half-band width from the main diagonal band, where the half-band width equaled the lesser of the number of nodes per row or column for a two-dimensional grid. A three-dimensional grid would contain four extra bands of block matrices, two below and two above the diagonal band. The furthest bands would be located one half-band width from the main diagonal band, where the half-band width equaled the least number of nodes in a plane. For example, a three-dimensional Cartesian grid with 20 nodes in the “X” coordinate direction, 30 nodes in the “Y” coordinate direction, and 40 nodes in the “Z” coordinate direction, would have a half-band width of 600.

The Newton-Raphson scheme has two major computational components. The first component involves computing the Jacobian matrix and solution vector elements; the second component involves solving the resulting linear system of equations. Both components are required during each iteration. The Jacobian matrix elements are essentially partial derivatives of the equation residuals with respect to the primary variables. These partially derivatives are computed numerically as exemplified in Equation (6.4.9). Numerical evaluation of these partial derivatives was chosen over analytical evaluation because its robustness and directness in coding. The numerical evaluation scheme requires that the equation residuals be evaluated with the most current values of the primary variables and with each primary variable slightly incremented. Increments to the primary variables are critical parameters for implementing the Newton-Raphson linearization scheme using numerical derivatives. Excessively large increments can lead

to nonconvergent solutions because the tangents to the residual equations are computed incorrectly. In contrast, excessively small increments can result to changes in the equation residuals, which are below the precision limit.

$$\frac{\partial R_k^j}{\partial PV_l^i} \quad \frac{R_k^j \Big|^{PV_l^i + \Delta PV_l^i} - R_k^j \Big|^{PV_l^i}}{\Delta PV_l^i} \tag{6.4.9}$$

Each Newton-Raphson iteration procedure begins with the start of a new time step or after a convergence failure and reduction in time step. Each iteration begins by executing logic algorithms that determine the primary variable set from phase conditions and fix the primary variable increments. The next step is to calculate all secondary variables with the current primary variables and with each primary variable incremented. Following this, all flux variables are evaluated with the current primary and associated secondary variables and then repeated with the incremented primary and associated secondary variables. With the secondary variables and fluxes evaluated, the residuals to the governing equations are computed using current and incremented values of the primary, secondary, and flux variables. The current and incremented equations residuals are then used to compute the partial derivatives that comprise the Jacobian matrix and the solution vector.

The resulting system of linear equations is then solved with either a direct or iterative linear system solver, with the unknowns being increments to the primary variables. Converged solutions are recognized by comparing the maximum normalized increment to the primary variables against a convergence criterion (i.e., user specified limit). A Newton-Raphson iteration ends by updating the primary variables with the latest computed primary increments. If the largest normalized primary variable increment exceeds the convergence limit, then another iteration is executed. If the solution is convergent, then the solute transport equations are solved or a new time step is initiated. In the case of a nonconvergent solution, the time step is reduced, the primary variables are reset to the most recent converged values, and the time step is reinitiated.

6.5 Linear System Solvers

The system of linear equations that results from the discretization of the governing partial differential equations over a particular computational domain always has a banded structure, where the number of off diagonal bands equals the dimensionality of the computational domain. Elements within the Jacobian coefficient are actually submatrices, where the submatrix order equals the number of solved coupled governing equations. For example, the solution of

only the water conservation equation produces single element submatrices; whereas, the solution of the three mass conservation equations simultaneously with the energy equation yields four-by-four submatrices. These structured Jacobian coefficient matrices arise from the element sequencing scheme incorporated into the Arid-ID engineering simulator and limitations on the computational domain structures. The matrix sequencing or numbering algorithms are designed to minimize the largest half-band width for a given computational domain and solution option combination. The sequencing algorithms are designed for orthogonal grid systems that are six-surfaced in three dimensions or four-sided in two dimensions.

Two linear equation solvers are available within the Arid-ID engineering simulator a direct banded matrix algorithm and an iterative conjugate gradient algorithm. The banded matrix algorithm is generally more appropriate for small to moderately sized Jacobian matrices (order less than 35,000); whereas, the conjugate gradient algorithm appears more appropriate for larger order Jacobian matrices. In general, the banded matrix algorithm requires more memory than the conjugate gradient algorithm, which uses an efficient sparse matrix storage scheme. The banded matrix algorithm is computationally more efficient on small to moderately sized problems; however, for larger problems the conjugate gradient algorithm becomes the better performer. Both linear equation solution algorithms were obtained from publicly available software packages.

The banded matrix solution algorithm was extracted from the LINPACK subroutines (Dongarra et al. 1980) for general nonsymmetric band matrices. The algorithm operates on band matrices by decomposing the matrix into an upper triangular and lower triangular matrix. The matrix product of the lower triangular matrix with the upper triangular matrix equals the original band matrix (i.e., $\mathbf{A} = \mathbf{L}\,\mathbf{U}$, where $\mathbf{A}$ is the band matrix, $\mathbf{L}$ is the lower triangular matrix and $\mathbf{U}$ is the upper triangular matrix). The system of linear equations, $\mathbf{A}\,\mathbf{x} = \mathbf{b}$, is solved with the above decomposition or factorization by solving successively $\mathbf{L}\,(\mathbf{U}\,\mathbf{x}) = \mathbf{b}$. This factorization procedure produces nonzero elements outside the bands of the original band matrix. If m_l equals the half-band width of the Jacobian coefficient matrix (the Arid-ID engineering simulator produces band matrices with equal lower and upper band widths), then the two triangular factors have band widths of m_l and $2m_l$. Storage must be provided for the extra m_l diagonals. This is illustrated for a one-dimensional problem of five nodes and two-solved mass conservation equations. The Jacobian coefficient matrix for this problem would appear as shown in Equation (6.5.1). The band storage requires $3\,m_l + 1 = 10$ rows of storage arranged as shown in Equation (6.5.2). The * indicates elements which are never referenced but storage space must be provided. The + indicates elements which may be occupied during the factorization process. The original Jacobian coefficient matrix is referred to as $\mathbf{A}$ and its storage counterpart as $\mathbf{a}$; then the columns of $\mathbf{A}$ are stored in the columns of $\mathbf{a}$, and the diagonals of $\mathbf{A}$ are stored in the rows of $\mathbf{a}$, such that the principal diagonal is stored in row $2\,m_l + 1$ of $\mathbf{a}$.

$$\mathbf{A} = \begin{vmatrix} x_{1,1} & x_{1,2} & x_{1,3} & x_{1,4} & 0 & 0 & 0 & 0 & 0 & 0 \\ x_{2,1} & x_{2,2} & x_{2,3} & x_{2,4} & 0 & 0 & 0 & 0 & 0 & 0 \\ x_{3,1} & x_{3,2} & x_{3,3} & x_{3,4} & x_{3,5} & x_{3,6} & 0 & 0 & 0 & 0 \\ x_{4,1} & x_{4,2} & x_{4,3} & x_{4,4} & x_{4,5} & x_{4,6} & 0 & 0 & 0 & 0 \\ 0 & 0 & x_{5,3} & x_{5,4} & x_{5,5} & x_{5,6} & x_{5,7} & x_{5,8} & 0 & 0 \\ 0 & 0 & x_{6,3} & x_{6,4} & x_{6,5} & x_{6,6} & x_{6,7} & x_{6,8} & 0 & 0 \\ 0 & 0 & 0 & 0 & x_{7,5} & x_{7,6} & x_{7,7} & x_{7,8} & x_{7,9} & x_{7,10} \\ 0 & 0 & 0 & 0 & x_{8,5} & x_{8,6} & x_{8,7} & x_{8,8} & x_{8,9} & x_{8,10} \\ 0 & 0 & 0 & 0 & 0 & 0 & x_{9,7} & x_{9,8} & x_{9,9} & x_{9,10} \\ 0 & 0 & 0 & 0 & 0 & 0 & x_{10,7} & x_{10,8} & x_{10,9} & x_{10,10} \end{vmatrix} \tag{6.5.1}$$

$$\mathbf{a} = \begin{vmatrix} & & & & & & + & + & + & + \\ & & & & & + & + & + & + & + \\ & & & & + & + & + & + & + & + \\ & & & x_{1,4} & 0 & x_{3,6} & 0 & x_{5,8} & 0 & x_{7,10} \\ & & x_{1,3} & x_{2,4} & x_{3,5} & x_{4,6} & x_{5,7} & x_{6,8} & x_{7,9} & x_{8,10} \\ & x_{1,2} & x_{2,3} & x_{3,4} & x_{4,5} & x_{5,6} & x_{6,7} & x_{7,8} & x_{8,9} & x_{9,10} \\ x_{1,1} & x_{2,2} & x_{3,3} & x_{4,4} & x_{5,5} & x_{6,6} & x_{7,7} & x_{8,8} & x_{9,9} & x_{10,10} \\ x_{2,1} & x_{3,2} & x_{4,3} & x_{5,4} & x_{6,5} & x_{7,6} & x_{8,7} & x_{9,8} & x_{10,9} & \\ x_{3,1} & x_{4,2} & x_{5,3} & x_{6,4} & x_{7,5} & x_{8,6} & x_{9,7} & x_{10,8} & & \\ x_{4,1} & 0 & x_{6,3} & 0 & x_{8,5} & 0 & x_{10,7} & & & \end{vmatrix} \tag{6.5.2}$$

The conjugate gradient solution algorithm was extracted from the SPLIB package of subroutines intended for solving large sparse linear systems by iterative methods (Bramley and Wang 1995). This package of subroutines has various acceleration techniques and preconditioners available for solving large sparse linear systems. The reader is referred to the original reference for detailed information.

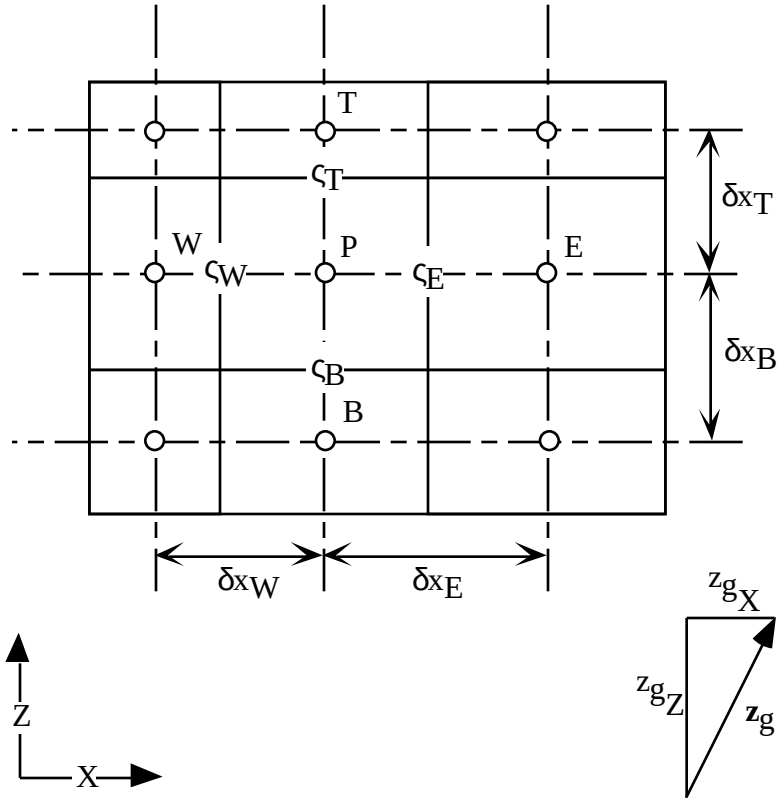

Figure 6.1. X-Z Coordinate Plane for Cartesian Systems

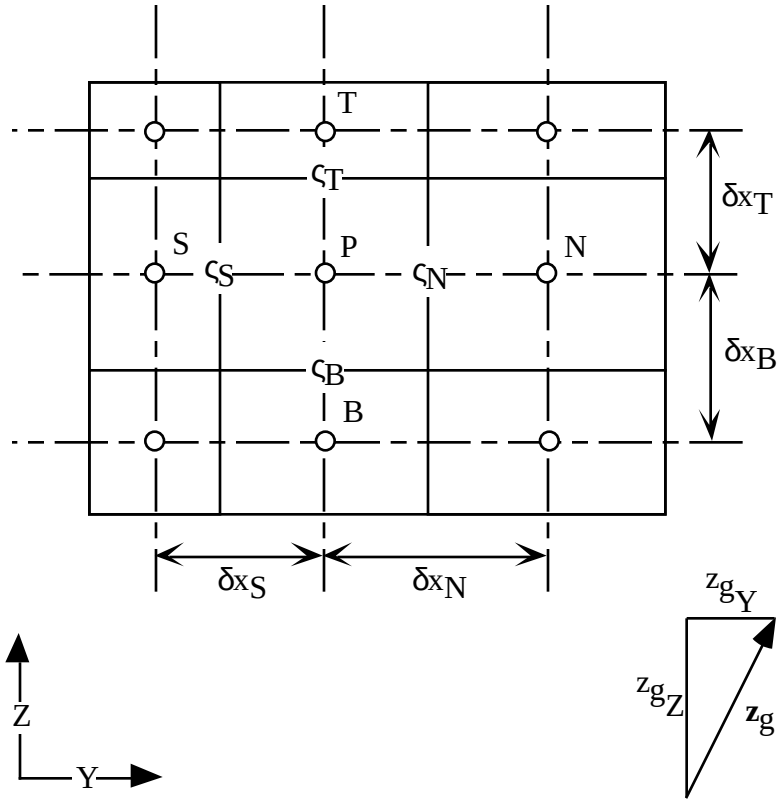

Figure 6.2. Y-Z Coordinate Plane for Cartesian Systems

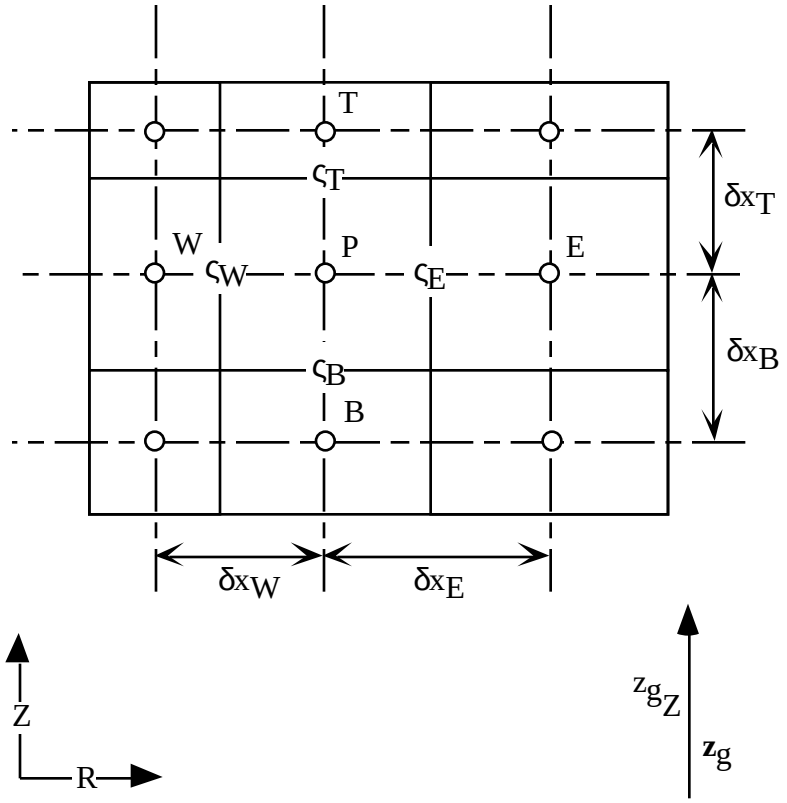

Figure 6.3. R-Z Coordinate Plane for Cylindrical Systems

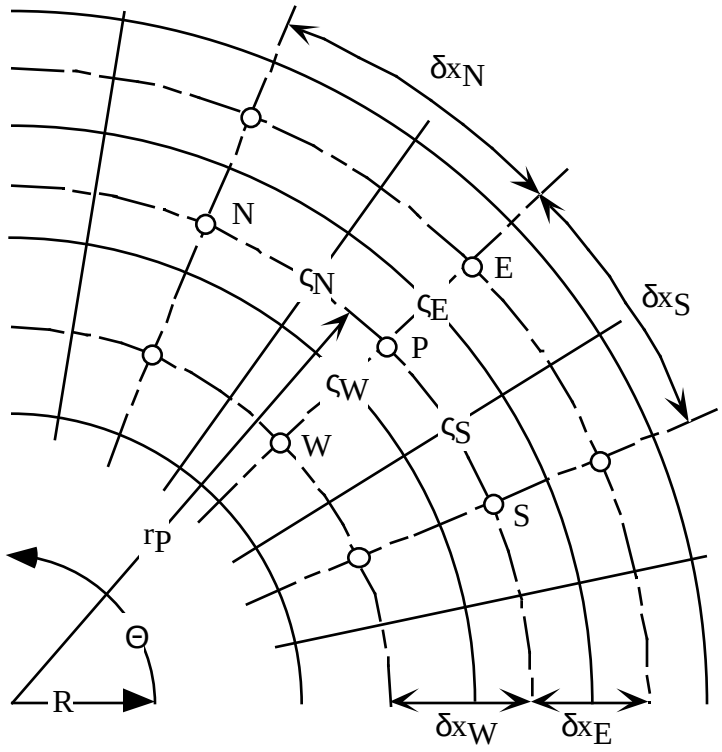

Figure 6.4. R-Θ Coordinate Plane for Cylindrical Systems

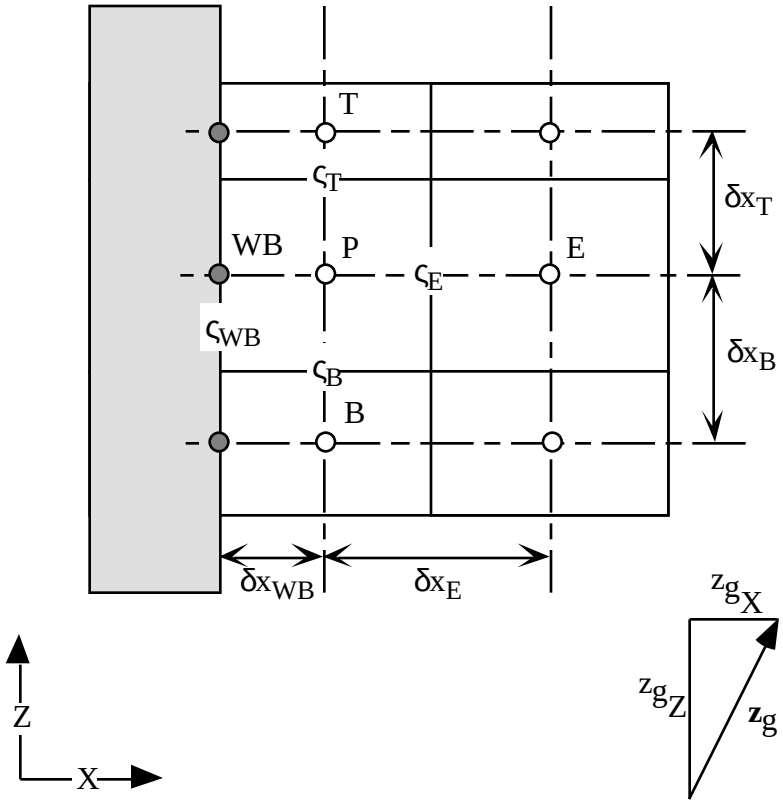

Figure 6.5. X-Z Cartesian Coordinate Plane for “West” Boundary

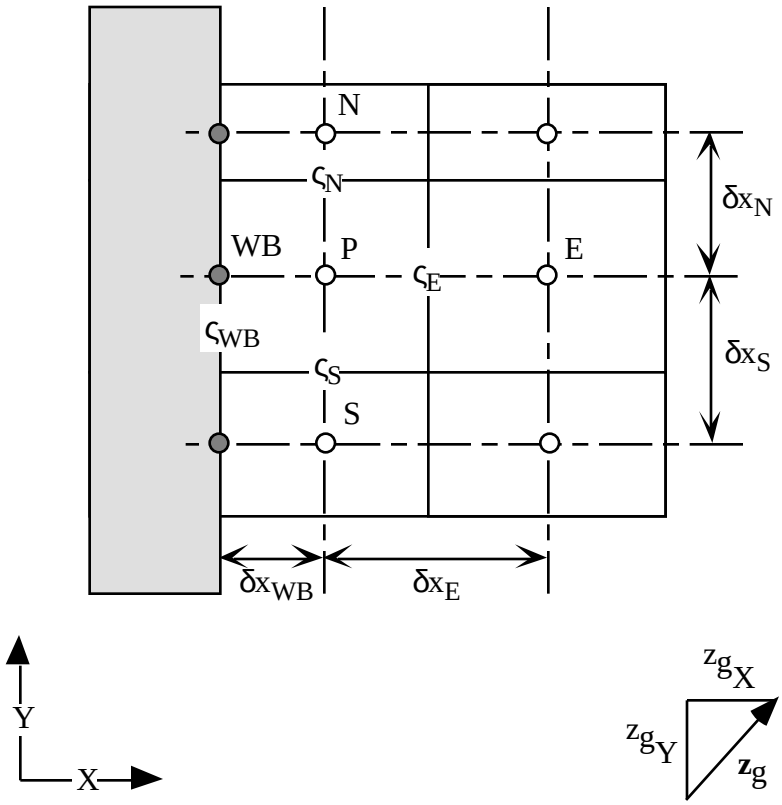

Figure 6.6. X-Y Cartesian Coordinate Plane for “West” Boundary

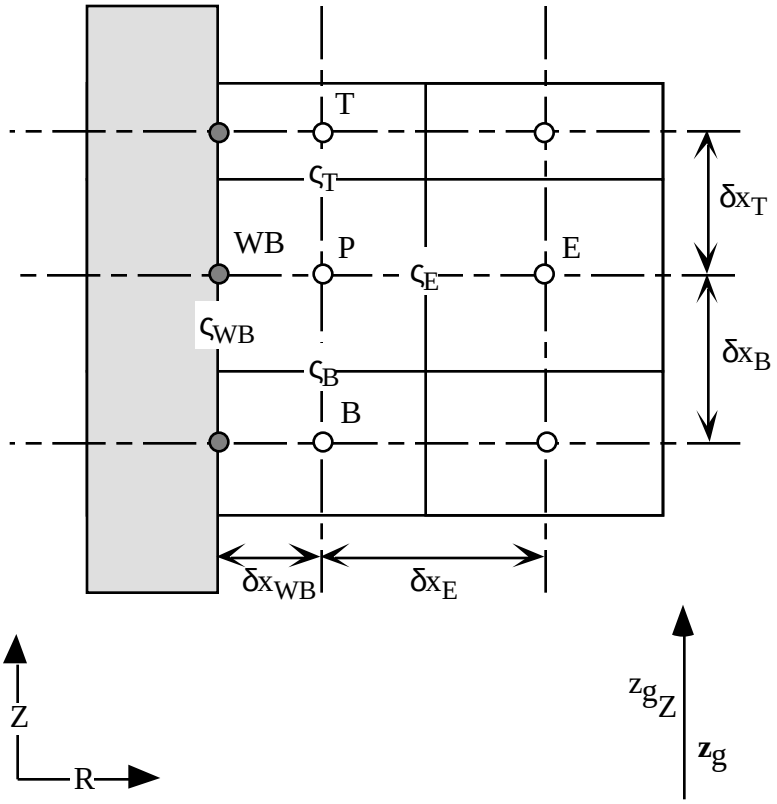

Figure 6.7. R-Z Cylindrical Coordinate Plane for "West" Boundary

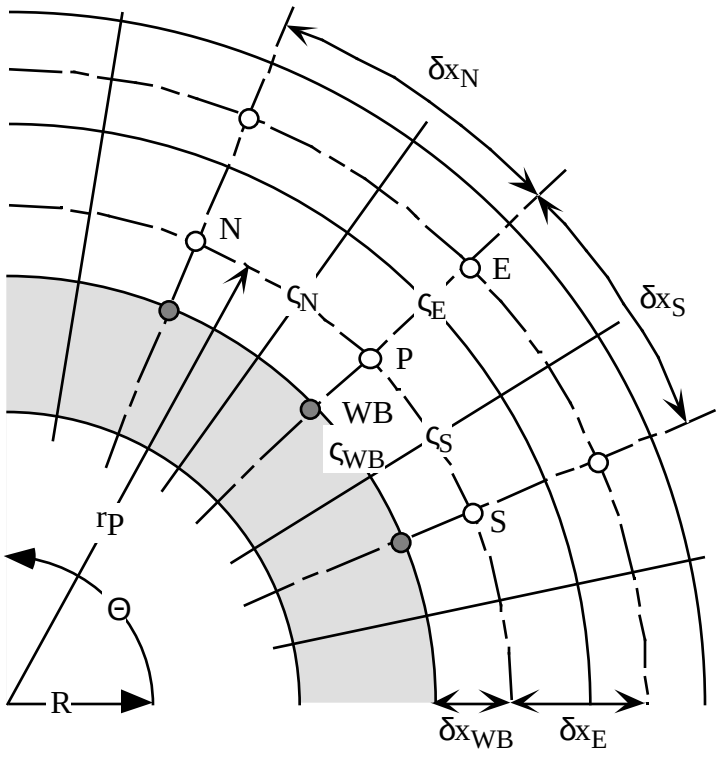

Figure 6.8. R-Θ Cylindrical Coordinate Plane for "West" Boundary

7.0 Code Architecture

7.1 Introduction

The primary design guides for the STOMP simulator have been modularity, computational efficiency, and readability. A modular code architecture is beneficial because of the ease of reading, maintaining, and modifying the algorithms and is essential to the variable configuration source code. Computational efficiency refers to both memory requirements and execution speed. The STOMP simulator has been designed with a variable configuration source code that allows the memory requirements and code algorithms to be partially customized to the computational problem. This approach offers considerable advantages with respect to achieving a computationally efficient code design. Within this source code framework, however, many design choices have been made that affect computational efficiency. Algorithm design often offers options between memory and speed. For example, to lessen memory requirements, a code designer may opt to repeatedly compute commonly used variables. Conversely, execution speed may be increased at the cost of increased memory requirements, by storing commonly used variables after their initial computation. Generally, the approach in the STOMP simulator has been to favor increased memory requirements to gain computational speed. This design approach has been chosen because of current state of computer architecture and capabilities. Because the STOMP simulator has been created as a scientific tool, algorithm readability has been an primary design guide. As a scientific tool, the simulator was never expected to remain unmodified, but rather a constantly changing package of software tools which could be applied to new or more complex problems. This design goal makes readability an essential feature of the code. Code readability has been achieved through an extensive use of comments, a modular design, a large group of common blocks, and minimal subroutine and function arguments.

7.2 Flow Path

The primary flow path for all operational modes of the STOMP simulator comprises three components; initialization, iteration, and closure. Control of the flow path at the primary level occurs from within the main program routine named “STOMP,” for all operational modes. A flow chart for the initialization, iteration, and closure components of the main program is shown in Figure 7.1. The initialization component of the program is executed once during a simulation. The routines in the initialization component are executed sequentially, as shown in Figure 7.1, from the program start to the start of the first time step. The iteration component of the program contains a pair of nested loops, one for time stepping and the other for Newton-Raphson linearization. Termination of the Newton-Raphson loop occurs with a successful convergence or with an iteration limit violation. Termination of the time-stepping loop occurs

with simulation limit or a time step reduction limit violation. Regardless of the termination cause, the closure routines are executed at the successful or unsuccessful completion of a simulation. The transport solution is shown as a single routine on the STOMP flow diagram. It comprises, however, several transport routines within a solute loop. The flow diagram for the solute transport portion of the iteration component is shown in Figure 7.2.

The initialization component of the program flow path begins with an initialization of the clocks and variables. All variables in the common blocks of the "commons" file are initialized at this point either to zero or default values. Unless specifically defaulted, integers are initialized to 0, real variables are initialized to 0.D+0, and character strings are initialized to blank. During the variable initializations, the "*input*" and "*output*" files are opened. The next routine prints the welcome statement, disclaimer, and banner to the standard output device (screen) and the output file. This is followed with the procedures for reading the "*input*" file. The "*input*" file is read using a predefined card order. After each card has been read, the "*input*" file is rewound and searched from the beginning for the next card to be read. This approach allows the user to order input cards in a random order. The predefined card read order is critical and should not be altered in the software. When appropriate "*restart*" files are read for input data information during these procedures. Input data is checked for saturation or thermodynamic state consistency in the "Check Physical States" routines. If an error is found in these routines the simulation will be terminated with an associated error message. If no errors in thermodynamic state are noted, then the program continues initializing variables with the Jacobian matrix pointers. The Jacobian matrix structure varies with operational mode and grid geometry. Refer to Section 6.0 for a description of the numerical methods and linear system solvers. Jacobian matrix pointers are integer arrays that relate primary variables for a particular node to a location in the Jacobian matrix. If the simulation does not involve dynamic domains, then these pointers are constants during the simulation and need to be computed only once. The next three initialization routines compute initial values for the secondary variables from the initial conditions specified through the "*input*" or "*restart*" files. These routines have been divided into three components (i.e., those for computing phase saturation related variables, thermodynamic properties, and solute concentrations).

The iteration component of the program flow path contains a pair of nested loops. The outer loop increments time and represents a single time step and the inner loop increments iterations of the Newton-Raphson linearization technique. During a single time increment loop (time step) both the flow and transport governing equation sets are solved. The Newton-Raphson linearization loop is applicable only to the solution of the mass and heat flow governing equations. The solute transport governing equations are solved directly (without iteration) and sequentially to the iterative flow solution. Each time step loop starts with a computation of the new time step and increments to the time and time step counter. Time steps are computed with an algorithm based on the previous complete time step, the time step acceleration factor, and the time to a transition point. Transition points occur with changes in execution period times,

boundary condition times, source times, and output times. Time steps always conclude on transition points, which commonly requires the time step to be temporarily reduced. The time step, following a temporary reduction to meet a transition point time, will resume the prior time stepping levels, except in the case of execution period transitions where a new initial or maximum time step has been declared. The next procedure involves loading the previous time step arrays for field variables. Field variables from the array location for the current field variable value are loaded into the array location for the previous time step field variable value. The next three routines, prior to starting a Newton-Raphson iteration loop, involve writing previous time step results to output. Simulation results are written to the "Reference Node Output Record," the standard input/output device (screen), a "*plot*" file, and/or a "*restart*" file, depending on the directives made by the user on the "Output Control" card.

The Newton-Raphson iteration loop solves the governing flow equations for component mass and energy. The first procedure within this loop involves the calculation of boundary surface properties. Each declared boundary surface, has associated field variables which are computed with the same algorithms as the node field variables, but only when the boundary condition is active. This approach eliminates the necessity for computing field variable values for disabled boundary surfaces. The next group of routines computes fluxes across interior surfaces (those surfaces between active nodes). Fluxes which are computed within these routines are dependent on the operational mode and include Darcy phase velocities, component diffusion-dispersion fluxes, thermal conductive flux, thermal advective flux, and thermal diffusion-dispersion fluxes. The same group of flux variables is computed in the next procedure for each active boundary surface. As with the procedure for computing field variables on boundary surfaces the approach of computing flux variables only for active boundary surfaces eliminates computing unused boundary flux variables. The next procedure computes source and/or sink contributions to each of the governing flow equations from the user specified inputs on the "Source" card. Source contributions are stored in arrays and subsequently used in computing the Jacobian matrix coefficients. At this point in the Newton-Raphson iteration loop, all field and surface flux variables have been computed, along with the source contributions. These variables compose the primary components of the governing flow equations.

Coefficients of Jacobian matrix and solution vector are computed in a multiple stage sequence. The first stage involves setting all of the previous coefficient arrays to zero. This stage is necessary because the nonzero elements of the Jacobian matrix will change with time step as various boundary condition transition between active and inactive states. The second stage involves computing the Jacobian matrix and solution vector with the assumption of zero flux boundary conditions for all boundary surfaces, including surfaces between active and inactive nodes. The Jacobian matrix loading procedure depends on the operational mode, but is sequenced according to governing partial differential equations. Coefficients for the water mass conservation equation are loaded first, followed by the air mass, oil mass, salt or surfactant mass, and energy conservation equations. The resulting system of equations represents the discretized and

linearized system of governing flow equations with zero flux boundary conditions imposed, where the source contributions have been incorporated. The final stage modifies this linear system according to the active user imposed boundary conditions. Boundary conditions will alter both the coefficient matrix and solution vector. With the Jacobian matrix and solution vector elements computed, the next procedure involves solving the linear system of equations. The linear system is solved either with a direct banded matrix solver or an iterative conjugate gradient solver. Both routines return corrections to the primary variables in the solution vector array.

Corrections to the primary variables, computed from the linear system solvers, are used to update the primary variables and determine convergence. The Newton-Raphson procedure computes corrections to the primary variable set with each iteration. The starting values for primary variables for each new time step are the previous time step values of the primary variables, as these values represent reasonable estimates of the future values. For a convergent iteration scheme, each successive iteration yields diminishing corrections to the primary variables. Phase transitions and primary variable switching schemes, however, can yield temporary increases in the correction to a particular primary variable. The two procedures that immediately follow the linear system solver procedures update the primary variables and determine convergence. Convergence occurs if the normalized values of the primary variable corrections for all unknowns falls below a user-defined value (typically $1.x10^{-6}$). The next three procedures, which include computing increments to the primary variables, computing saturation related properties, and computing thermodynamic properties, are executed independent of the convergence result. If convergence occurs, then these computed values represent the current values of secondary variables at the conclusion of the time step. Otherwise, they represent the current iterate values of the secondary variables. If convergence occurs, then the solution procedure continues with solute transport procedures. At the conclusion of nonconvergent iterations, two additional checks are made. If the iteration count does not exceed the user specified limit, then program proceeds with a new Newton-Raphson iteration loop. If the iteration count exceeds the limit, then a check is made on the count of successive time step reductions. If convergence has failed and resulted in a time step reduction four times in succession, then the simulation aborts and program execution is transferred to the closure routines. Otherwise, the time step is reduced, the program execution is transferred to the beginning of the time increment loop, and another attempt is made to reach a converged solution for the time step.

The transport solution procedure follows the iterative solution of the mass and heat flow equations and, although a direct solution scheme, involves looping over the number of solutes. A procedure flow diagram for the transport solution routines is shown in Figure 7.2. Before entering the solute loop, the interior-surface and boundary-surface flux procedures are called to obtain values of all flux variables at the conclusion of a time step. Flux values at the conclusion of a time step will typically vary from those computed during the last iteration of the current time step, because the primary and secondary variables will have been updated near the bottom

of the last Newton-Raphson iteration loop. The surface flux calculations within the Newton-Raphson loop differ from these surface calculations in that only the current unincremented value of the surface flux is computed.

The transport solution procedure loops over the number of solutes in the reverse order and they are defined on the "Solute/Fluid Interactions" card. A reverse looping order is used to compute progeny solutes before computing parent solutes. This approach allows sequential coupling between solutes that decay radioactively or chemically with first order reaction rates yielding solute products. The first step of the transport solution loop involves computing the equilibrium distribution of solute between the fluid and solid phases. The second step is to initialize the coefficient matrix and solution vector elements to zero. As with the flow solution scheme, the possibility for boundary conditions and sources that transition makes initializing the linear system elements mandatory. The third step of the transport solution loop is to compute the solute source and/or sink contributions. Solute source contributions are incorporated directly into the coefficient matrix and solution vector elements. The fourth step involves loading the coefficient matrix and solution vector. As with the flow solution scheme, the coefficient matrix and solution vector elements are computed assuming zero-flux conditions on all boundary surfaces. Element loading depends on the operational mode and occurs sequentially by phases, where the aqueous phase contributions are loaded first, followed by the gas phase and NAPL. Solid phase contributions are loaded with the first active fluid phase. The fifth step of the transport solution procedure is the solution of linear system of equations. Algorithms for solving the transport linear system of equations are identical to those for the flow solution, accept that the returned results for the transport solution are directly the volumetric solute concentrations. The sixth step of the transport solution is to update the solute concentrations with their newly computed values. The concluding steps for the transport solution compute solute fluxes and integrate the solute sources. Once the transport solution loop has been executed for every solute the program execution returns to the flow solution procedures. Time steps for the transport solution are by default equal to those used for the flow solution. Although not currently an option with the STOMP simulator, the transport solution could be advanced in fractional values of the flow solution time steps.

The closure routines are only executed once at the successful or unsuccessful conclusion of a simulation. These routines generate final "*plot*" files, "*restart*" files, and close all opened files. Upon successful conclusion to the simulation the final "*restart*" file will contain a record of the primary variables at the conclusion of the final time step. Conversely, if a simulation concludes unsuccessfully, because of a convergence failure or otherwise, the "*restart*" file will contain a record of the primary variables at the conclusion of the previous converged time step. The STOMP simulator is a once through program.

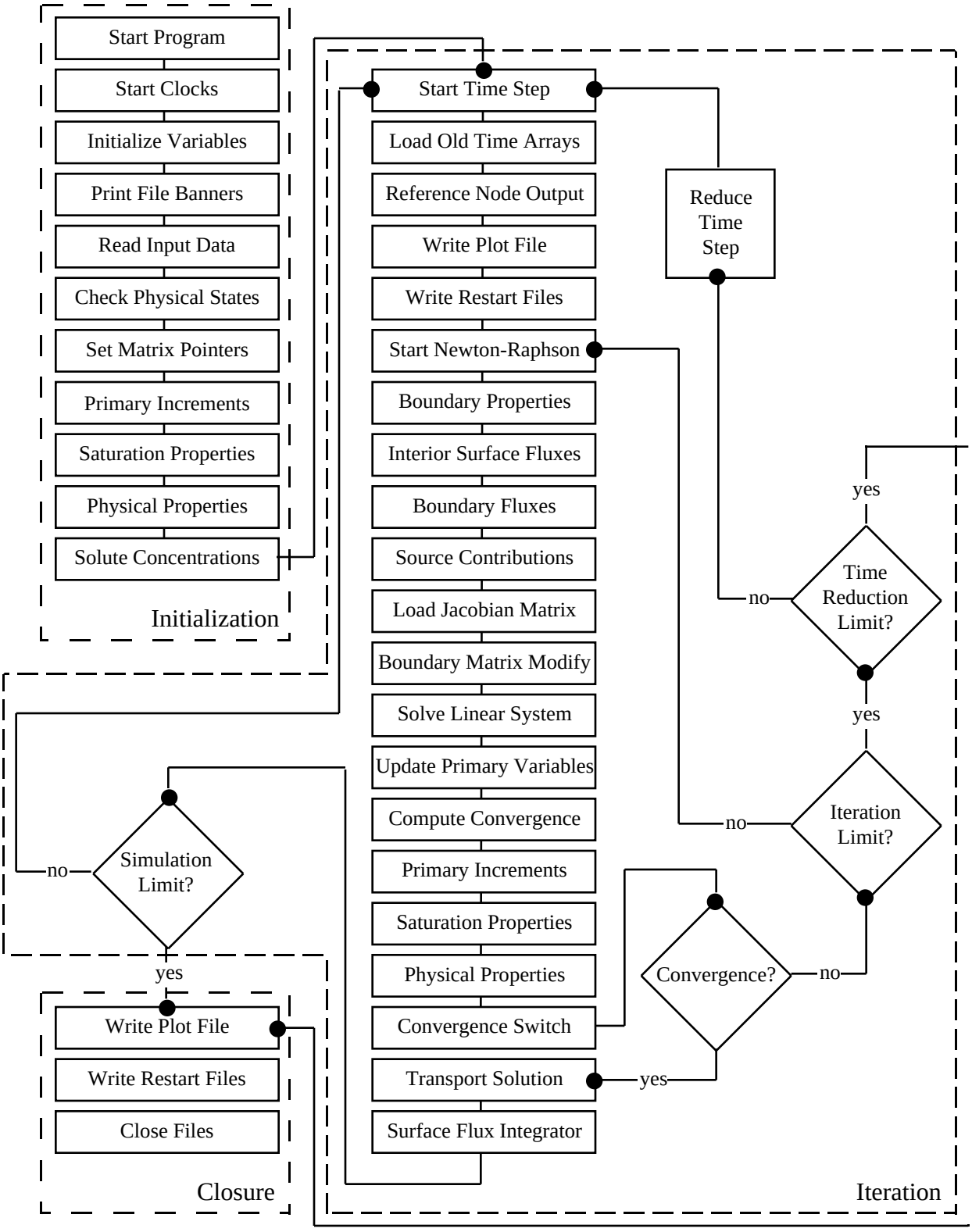

Figure 7.1. STOMP Flow Diagram

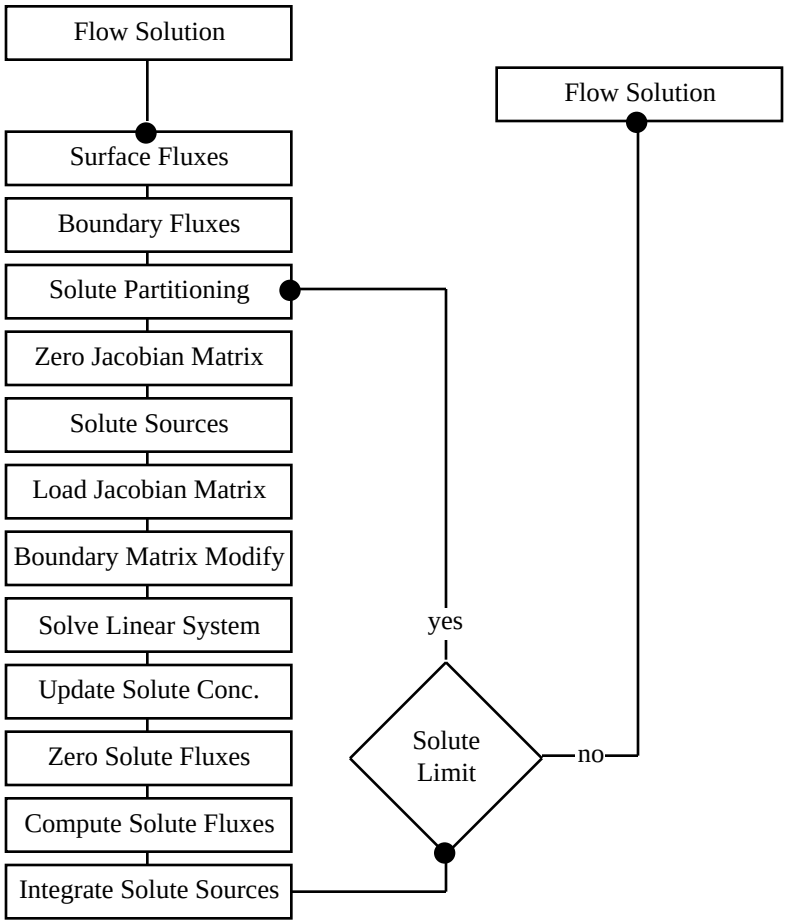

Figure 7.2. Transport Solution Flow Diagram

8.0 Engineered Systems

8.1. Dual-Screen Wells for In-Well Vapor-Stripping (IWVS)

The engineered component (i.e., air-lift pumping well) of the in-well vapor-stripping system was treated numerically in the STOMP simulator as a linked solute source model. In this model, a zone of surfaces is defined within the computational grid over which inlet fluxes of solute are summed. In the physical domain, this would represent the lower screened interval of the vapor-stripping well. Solute concentrations of the incoming water are reduced according to the thermodynamic equilibrium conditions at the separator plate. The fundamental assumption associated with this model is that sufficient interphase mass transport of the VOC has occurred between the water and air during the air-lift pumping to achieve nearly equilibrium conditions at the separator plate. The zone of surfaces is then linked to a zone of nodes in the computational domain that receives the solute at reduced concentration levels. In the physical domain, this would be equivalent to the separator plate and upper screened interval where water of lower dissolved TCE concentration is infiltrated into the hydrologic system.

Thermodynamic equilibrium of the VOC between the aqueous and gas phases during air-lift pumping is assumed to depend on the air-to-water volumetric flow ratio, well-head pressure, temperature, and solubility of the dissolved VOC. The mole fraction of dissolved solute in the returning water stream can be computed from a conservation equation for solute between the inlet and outlet of the vapor-stripping well, according to Equation (8.1.1).

$$\dot{C} = \frac{\chi_g^{voc} \rho_g \dot{q}_g}{M_g} + \frac{\chi_\ell^{voc} \rho_\ell \dot{q}_\ell}{M_\ell} \tag{8.1.1}$$

With the assumption of low VOC concentrations the gas and aqueous molecular weights can be expressed as functions of the water and air mole fractions, according to Equations (8.1.2)

$$M_g = \chi_g^a M^a + \chi_g^w M^w$$

$$M_\ell = M^w \tag{8.1.2}$$

Phase partitioning of the VOC between the aqueous and gas phases is expressed using Henry's Law, according to Equation (8.1.3)

$$\chi_g^{voc} = \frac{\chi_\ell^{voc} H_{g\ell}^{voc}}{P_g} \tag{8.1.3}$$

The mole fraction of dissolved VOC at the water-separator plate is computed by combining Equations (8.1.1-3), according to Equation (8.1.4).

$$\chi_{\ell}^{voc} = \frac{\dot{C}}{\dot{q}_{\ell}\left[\frac{H_{g\ell}^{voc}\,\rho_g\left(\dot{q}_g/\dot{q}_{\ell}\right)}{P_g\,M_g} + \frac{\rho_{\ell}}{M_{\ell}}\right]} \qquad (8.1.4)$$

9.0 References

Abriola, L.M., T.J. Dekker, and K.D. Pennell. 1993. "Surfactant enhanced solubilization of residual dodecane in soil columns. 2. Mathematical Modeling." *Environ. Sci. Technol.* 27: 2341-2351

ANSI. 1978. *American National Standard programming language FORTRAN.* X3.9-1978, ANSI, 1430 Broadway, New York.

ASHRAE. 1977. *ASHRAE handbook and product directory, 1977 fundamentals.* American Society of Heating, Refrigerating, and Air-Conditioning Engineers, Inc., New York.

ASME. 1967. *Thermodynamic and transport properties of steam.* The American Society of Mechanical Engineers, United Engineering Center, New York.

Bear, J. 1972. *Dynamics of fluids in porous media,* Elsevier, New York.

Bird, R. B., W. E. Stewart, and E. N. Lightfoot. 1960. *Transport phenomena.* John Wiley & Sons, Inc., New York.

Bramley, R., and X. Wang. 1995. SPLIB: A library of iterative methods for sparse linear systems.

Brooks, R. H., and A. T. Corey. 1966. "Properties of porous media affecting fluid flow." *Journal of Irrigation and Drainage Division* 93(3):61-88.

Burdine, N. T. 1953. "Relative permeability calculations from pore-size distribution data." *Petroleum Trans.* 198:71-77.

Carnahan, B., H. A. Luther, and J. O. Wilkes. 1969. *Applied numerical methods.* John Wiley & Sons, Inc., New York.

Corey, A. T. 1977. "Mechanics of heterogeneous fluids in porous media." *Water Resources Publications,* Fort Collins, Colorado.

Datta Gupta, A., L.W. Lake, G.A. Pope, and K. Sepehrnoori. 1991. "High-resolution monotonic schemes for reservoir fluid flow simulation." *In Situ* 15:289-317.

Delshad, M., G.A. Pope, and K. Sepehrnoori. 1996. "A compositional simulator for modeling surfactant enhanced aquifer remediation, 1 Formulation." *J. Contam. Hydrol.* 23:303-327.

De Vries, D. A. 1966. "Thermal Properties of Soils." In *Physics of plant environment*, edited by W. R. Van Wijk, pp. 210-235, North-Holland, Amsterdam.

Dickerson, R.W., D.K. Tressler, W.B. Van Arnsdel, and M.J. Copley. 1969. *Thermal properties of food, in the Freezing Preservation of Foods Vol. 2.* AVI Publishing Co., Westport, Conn.

Falta, R. W., K. Preuss, I. Javandel, and P. A. Witherspoon. 1990a. *Numerical modeling of steam injection for the removal of nonaqueous phase liquids from the subsurface: 1. Numerical Formulation.* LBL-29615, Lawrence Berkeley Laboratory, Berkeley, California.

Falta, R. W., K. Preuss, I. Javandel, and P. A. Witherspoon. 1990b. *Numerical modeling of steam injection for the removal of nonaqueous phase liquids from the subsurface: 2. Code validation and application.* LBL-29615, Lawrence Berkeley Laboratory, Berkeley, California.

Fayer, M.J. and C.S. Simmons. 1995. "Modified soil water retention functions for all matric suctions." *Water Resour. Res.* 31:1233-1238.

Jury, W. A., W. R. Gardner, and W. H. Gardner. 1991. *Soil physics.* John Wiley & Sons, Inc., New York.

Klavetter, E.A., and R. R. Peters. 1986. *Estimation of hydrologic properties of unsaturated fractured rock mass.* SAND84-2642, Sandia National Laboratories, Albuquerque, New Mexico.

Kreyszig, E. 1979. *Advanced engineering mathematics.* Fourth Edition. John Wiley & Sons, Inc., New York.

Kaluarachchi, J.J. and J.C. Parker. 1992. "Multiphase flow with a simplified model for oil entrapment." *Transport in Porous Media* 7:1-14.

Land, C. S. 1968. "Calculation of imbibition relative permeability for two- and three-phase flow from rock properties." *Trans. Am. Inst. Min. Metall. Pet. Eng.* 243:149-156.

Leijnse, A. 1992. *Three-dimensional modeling of coupled flow and transport in porous media.* Ph.D. Dissertation, Notre Dame, Indiana.

Lenhard, R. J. 1994. "Scaling fluid content-pressure relations of different fluid systems in porous media." In *Proc. of the Fourteenth Annual American Geophysical Union Hydrology Days,* Hydrology Days Publications, Atherton, California. pp. 223-235.

Lenhard, R. J., and J. C. Parker. 1987. "A model for hysteretic constitutive relations governing multiphase flow 2. Permeability-saturation relations." *Water Resources Research,* 23(12):2197-2206.

Leonard, B.P. 1988. "Universal limiter for transient interpolation modeling of the advective transport equations: The ultimate conservative difference scheme." NASA TM 100916, ICOMP-88-11.

Linke, W. F. 1965. *Solubilities inorganic and metal-organic compounds: a compilation of solubility data from the periodical literature.* Americal Chemical Society, Washington, D.C.

Loch, J. P. G. 1977. "Thermodynamic equilibrium between ice and water in porous media." *Soil Sci.,* 126:77-80.

Mayer, A.S. and C.T. Miller. 1996. "The influence of mass transfer characteristics and porous media heterogeneity on nonaqueous phase dissolution." *Water Resour. Res.* 32: 1551-1567.

Millington, R. J. and J. P. Quirk. 1959. "Permeability of porous media." *Nature* 183:387-388.

Mualem, Y. 1976. "A new model for predicting the hydraulic conductivity of unsaturated porous media." *Water Resources Research.,* 12:513-522.

Nichols, W. E., N. J. Aimo, M. Oostrom, and M. D. White. 2000. "*STOMP subsurface transport over multiple phases. Version 2.0. Application guide."* PNNL-12028, Pacific Northwest National Laboratory, Richland, Washington.

Nitao, J. J. 1988. *Numerical modeling of the thermal and hydrological environment around a nuclear waste package using the equivalent continuum approximation: horizontal emplacement.* UCID-2144, Lawrence Livermore National Laboratory, Livermore, California.

Panday, S., and M. Y. Corapcioglu. 1994. "Theory of phase-separate multicomponent contaminant transport in frozen soils." *J. Contam. Hyd.,* 16:235-269.

Parker, J. C. and R. J. Lenhard. 1987. "A model for hysteretic constitutive relations governing multiphase flow 1. Saturation-pressure relations." *Water Resources Research,* 23(12):2187-2196.

Patankar, S. V. 1980. *Numerical heat transfer and fluid flow.* Hemisphere Publishing Corporation, Washington, D. C.

Pennell, K.D., L.M. Abriola, and W.J. Weber, Jr. 1993. "Surfactant enhanced solubilization of residual dodecane in soil columns. 1. Experimental investigation." *Environ. Sci. Technol.* 27: 2332-2340.

Pennell, K.D., G.A. Pope, and L.M. Abriola. 1996. "Influence of viscous and buoyancy forces on the mobilization of residual tetrachlorethylene during surfactant flushing." *Envir. Science and Technol.* 30:1328-1335.

Pitzer, K. S., J. C. Peiper, and R. H. Busey. 1984. "Thermodynamic properties of aqueous sodium chloride solutions." *J. Phys. Chem. Ref. Data,* 13(1):1-102.

Reid, R. C., J. M. Prausnitz, and B. E. Poling. 1987. *The properties of gases and liquids.* Fourth edition, McGraw-Hill Book Company, New York.

Sandler, S. I. 1989. *Chemical and Engineering Thermodynamics.* John Wiley & Sons, Inc., New York.

Slattery, J. C., and R. B. Bird. 1958. "Calculation of the diffusion coefficient of dilute gases and of the self-diffusion coefficient of dense gases." *Am. Inst. Chem. Engr. J.* 4(2):137-142.

Somerton, W. H., A. H. El-shaarani, and S. M. Mobarak. 1974. "High temperature behavior of rocks associated with geothermal type reservoirs." Paper SPE-4897, presented at the 44th Annual California Regional Meeting of the Society of Petroleum Engineers, San Francisco, California.

Somerton, W. H., J. A. Keese, and S. L. Chu. 1973. "Thermal behavior of unconsolidated oil sands." Paper SPE-4506, presented at the 48th Annual Fall Meeting of the Society of Petroleum Engineers, Las Vegas, Nevada.

Talbott, S. 1988. *Managing projects with make.* O'Reilly and Associates, Inc., Newton, Massachusetts.

van Genuchten, M. Th. 1980. "A closed-form equation for predicting the hydraulic conductivity of unsaturated soils." *Soil Sci. Soc. Am. J.,* 44:892-898.

van Wylen, G. J. and R. E. Sonntag. 1978. *Fundamentals of classical thermodynamics.* 2nd edition, revised printing, John Wiley & Sons, Inc., New York.

Vargaftik, N. B. 1975. *Tables on the thermodynamic properties of liquids and gases.* Hemisphere Publishers, Inc., Washington, D. C.

Wark, K., Jr. 1995. *Advanced thermodynamics for engineers.* McGraw-Hill, Inc., New York.

Washburn, E. W., C. J. West, N. E. Dorsey, F. R. Bichowsky, and M. D. Ring. 1929. *International critical tables of numerical data, physics, chemistry, and technololgy.* National Research Council, McGraw-Hill Book Company, Inc., New York.

White, M. D. 1995. "Theory and numerical application of subsurface flow and transport for transient freezing conditions." In *Proc. of the Fifteenth Annual American Geophysical Union Hydrology Days*, Hydrology Days Publications, Atherton, California. pp. 339-352.

White, M.D. and M. Oostrom. 2000. *"STOMP subsurface transport over multiple phases, Version 2.0, User's guide."* PNNL 12034, Pacific Northwest National Laboratory, Richland, Washington. In Press.

Yaws, C. L., J. W. Miller, P. N. Shah, G. R. Schorr, and P. M. Patel. 1976. *Chem. Eng. Sci.* 83(25):153.

Appendix A

Numerical Constants

Appendix A

Table A.1. Water Critical Properties

Property	Numerical Value
T_c^w	647.3 K
P_c^w	2.212 x 10^7 Pa
v_c^w	3.17 x 10^{-3} m^3/kg
Z_c^w	0.235
ω_P^w	0.344

Table A.2. Water Vapor Pressure Function Constants

Constant	Numerical Value
k_1	-7.691 234 564
k_2	-2.608 023 696 x 10^1
k_3	-1.681 706 546 x 10^2
k_4	. 6.423 285 504 x 10^1
k_5	-1.189 646 225 x 10^2
k_6	. 4.167 117 320
k_7	. 2.097 506 760 x 10^1
k_8	. 1.0 x 10^9
k_9	. 6.0

Table A.3. Carbon Tetrachloride Vapor Pressure Constants and Critical Properties

Property	Numerical Value
$\tilde{a}$	-7.07139
$\tilde{b}$	1.71497
$\tilde{c}$	-2.8993
$\tilde{d}$	-2.49466
T_c^o	556.4 K
P_c^o	4.56 x 10^6 Pa
v_c^o	1.794 x 10^{-3} m^3/kg
Z_c^o	0.272
ω_P^o	0.193

Table A.4. Liquid-Water Primary Constants

Constant	Numerical Value
A_0	$6.824\ 687\ 741 \times 10^{3}$
A_1	$-5.422\ 063\ 673 \times 10^{2}$
A_2	$-2.096\ 666\ 205 \times 10^{4}$
A_3	$3.941\ 286\ 787 \times 10^{4}$
A_4	$-6.733\ 277\ 739 \times 10^{4}$
A_5	$9.902\ 381\ 028 \times 10^{4}$
A_6	$-1.093\ 911\ 774 \times 10^{5}$
A_7	$8.590\ 841\ 667 \times 10^{4}$
A_8	$-4.511\ 168\ 742 \times 10^{4}$
A_9	$1.418\ 138\ 926 \times 10^{4}$
A_{10}	$-2.017\ 271\ 113 \times 10^{3}$
A_{11}	$7.982\ 692\ 717 \times 10^{0}$
A_{12}	$-2.616\ 571\ 843 \times 10^{-2}$
A_{13}	$1.522\ 411\ 790 \times 10^{-3}$
A_{14}	$2.284\ 279\ 054 \times 10^{-2}$
A_{15}	$2.421\ 647\ 003 \times 10^{2}$
A_{16}	$1.269\ 716\ 088 \times 10^{-10}$
A_{17}	$2.074\ 838\ 328 \times 10^{-7}$
A_{18}	$2.174\ 020\ 350 \times 10^{-8}$
A_{19}	$1.105\ 710\ 498 \times 10^{-9}$
A_{20}	$1.293\ 441\ 934 \times 10^{1}$
A_{21}	$1.308\ 119\ 072 \times 10^{-5}$
A_{22}	$6.047\ 626\ 338 \times 10^{-14}$
a_1	$8.438\ 375\ 405 \times 10^{-1}$
a_2	$5.362\ 162\ 162 \times 10^{-4}$
a_3	$1.720\ 000\ 000 \times 10^{0}$
a_4	$7.342\ 278\ 489 \times 10^{-2}$
a_5	$4.975\ 858\ 870 \times 10^{-2}$
a_6	$6.537\ 154\ 300 \times 10^{-1}$
a_7	$1.150\ 000\ 000 \times 10^{-6}$
a_8	$1.510\ 800\ 000 \times 10^{-5}$
a_9	$1.418\ 800\ 000 \times 10^{-1}$
a_{10}	$7.002\ 753\ 165 \times 10^{0}$
a_{11}	$2.995\ 284\ 926 \times 10^{-4}$
a_{12}	$2.040\ 000\ 000 \times 10^{-1}$

Table A.5. Hankinson-Brobst-Thomson Liquid Density Function Constants

Constant	Numerical Value
h_1	-9.070 217
h_2	$6.245\ 326 \times 10^{1}$
h_4	$-1.351\ 102 \times 10^{2}$
h_6	4.795 940
h_7	$2.500\ 470 \times 10^{-1}$
h_8	1.141 880
h_{10}	$8.614\ 880 \times 10^{-2}$
h_{11}	$3.444\ 830 \times 10^{-2}$

Table A.6. Water-Vapor Primary Constants

Constant	Numerical Value
B_0	$1.683\ 599\ 274 \times 10^{1}$
B_{01}	$2.856\ 067\ 796 \times 10^{1}$
B_{02}	$-5.438\ 923\ 329 \times 10^{1}$
B_{03}	$4.330\ 662\ 834 \times 10^{-1}$
B_{04}	$-6.547\ 711\ 697 \times 10^{-1}$
B_{05}	$8.565\ 182\ 058 \times 10^{-2}$
B_{11}	$6.670\ 375\ 918 \times 10^{-2}$
B_{12}	$1.388\ 983\ 801 \times 10^{0}$
B_{21}	$8.390\ 104\ 328 \times 10^{-2}$
B_{22}	$2.614\ 670\ 893 \times 10^{-2}$
B_{23}	$-3.373\ 439\ 453 \times 10^{-2}$
B_{31}	$4.520\ 918\ 904 \times 10^{-1}$
B_{32}	$1.069\ 036\ 614 \times 10^{-1}$
B_{41}	$-5.975\ 336\ 707 \times 10^{-1}$
B_{42}	$-8.847\ 535\ 804 \times 10^{-2}$
B_{51}	$5.958\ 051\ 609 \times 10^{-1}$
B_{52}	$-5.159\ 303\ 373 \times 10^{-1}$
B_{53}	$2.075\ 021\ 122 \times 10^{-1}$
B_{61}	$1.190\ 610\ 271 \times 10^{-1}$
B_{62}	$-9.867\ 174\ 132 \times 10^{-2}$
B_{71}	$1.683\ 998\ 803 \times 10^{-1}$
B_{72}	$-5.809\ 438\ 001 \times 10^{-2}$
B_{81}	$6.552\ 390\ 126 \times 10^{-3}$
B_{82}	$5.710\ 218\ 649 \times 10^{-4}$

Table A.6. (contd)

Constant	Numerical Value
B_{90}	1.936 587 558 x 10^{2}
B_{91}	-1.388 522 425 x 10^{3}
B_{92}	4.126 607 219 x 10^{3}
B_{93}	-6.508 211 677 x 10^{3}
B_{94}	5.745 984 054 x 10^{3}
B_{95}	-2.693 088 365 x 10^{3}
B_{96}	5.235 718 623 x 10^{2}
b_{0}	7.633 333 333 x 10^{-1}
b_{61}	4.006 073 948 x 10^{-1}
b_{71}	8.636 081 627 x 10^{-2}
b_{81}	-8.532 322 921 x 10^{-1}
b_{82}	3.460 208 861 x 10^{-1}

Table A.7. Water-Vapor Derived Constants

Constant	Numerical Value
L_{0}	1.574 373 327 x 10^{1}
L_{1}	-3.417 061 978 x 10^{1}
L_{2}	1.931 380 707 x 10^{1}

Table A.8. ASME Water Property Function Indices

j	$n(j)$	$z(j,1)$	$z(j,2)$	$z(j,3)$	$l(j)$	$x(j,1)$	$x(j,2)$	j
1	2	13	3	–	–	–	–	1
2	3	18	2	1	–	–	–	2
3	2	18	10	–	–	–	–	3
4	2	25	14	–	–	–	–	4
5	3	32	28	24	–	–	–	5
6	2	12	11	–	1	14	–	6
7	2	24	18	–	1	19	–	7
8	2	24	14	–	2	54	27	8

Table A.9. Liquid Water Thermal Conductivity Constants

Constant	Numerical Value
c_{10}	-9.2247×10^{2}
c_{11}	2.8395×10^{3}
c_{12}	-1.8007×10^{3}
c_{13}	5.2577×10^{2}
c_{14}	7.344×10^{1}
c_{20}	9.4730×10^{-1}
c_{21}	2.5186
c_{22}	-2.0012
c_{23}	5.1536×10^{-1}
c_{30}	1.6563×10^{-3}
c_{31}	-3.8929×10^{-3}
c_{32}	2.9323×10^{-3}
c_{33}	-7.1693×10^{-4}
$\bar{T}$	2.7315×10^{2}